Metal-Organic Framework-Based Triboelectric Nanogenerators

Jiahao Ye

Wolfson College

University of Oxford

A thesis submitted for the degree of

Doctor of Philosophy

Hilary 2025

Preface

This thesis is submitted for the degree of Doctor of Philosophy in the University of Oxford, United Kingdom. The research presented in this work was carried out by the author between October 2021 and February 2025 in the Department of Engineering Science, under the supervision of Professor Jin-Chong Tan.

To the best of my knowledge, the work described in this dissertation is original, except where due reference has been made, acknowledging the work of others. Nothing has been included that is the outcome of work done in collaboration with others, except where explicitly noted. No part of this dissertation, or any similar to it, has been, or is currently being submitted for any degree at this, or any other university. This thesis is less than 250 pages in length.

The work presented herein has been partially published in the following journal papers:

1. **J. Ye** and J.C. Tan, "High-Performance Triboelectric Nanogenerators Incorporating Chlorinated Zeolitic Imidazolate Frameworks with Topologically Tunable Dielectric and Surface Adhesion Properties", *Nano Energy*, 114, 108687 (2023).
2. **J. Ye**, T. Xu, and J.C. Tan, "Triboelectric Nanogenerators Based on Composites of Zeolitic Imidazolate Frameworks Functionalized with Halogenated Ligands for Contact and Rotational Mechanical Energy Harvesting", *ACS Applied Nano Materials*, 8, 8, 3942–3953 (2025).
3. **J. Ye**, T. Xu, L. Germane, L. Lapcinskis, A. Šutka, and J.C. Tan, "Functionalized PDMS for Regulating Triboelectric Output of Nanogenerators: A Study of Charge Transfer Mechanisms", *Journal of Materials Chemistry C,* 13 (15), 7654-7663 (2025).
4. **J. Ye**, G. Cinque, L. Donà, and J.C. Tan, "Noncontact Triboelectric Nanogenerators Based on Fluorinated Metal-Organic Frameworks for

Rotational Energy Harvesting and Sensing", *APL Electronic Devices,* 1, 036109 (2025).

Other manuscripts were published during my DPhil but are not directly related to the work developed in this thesis:

1. T. Xu, **J. Ye**, and J.C. Tan, "Unravelling the Ageing Effects of PDMS-Based Triboelectric Nanogenerators", *Advanced Materials & Interfaces*, 2400094 (2024).
2. J. Chang, J. Li, **J. Ye**, B. Zhang, J. Chen, Y. Xia, J. Lei, T. Carlson, R. Loureiro, J.C. Tan*, H. Zhao*, "AI-Enabled Piezoelectric Wearable for Joint Torque Monitoring", *Nano-Micro Letters*, 17 (1), 1-20 (2025).
3. Y. Zhang, S. Mollick, M. Tricarico, **J. Ye**, D. A. Sherman, and J.C. Tan, "Turn-On Fluorescence Chemical Sensing through Transformation of Self-Trapped Exciton States at Room Temperature", *ACS Sensors* 7, 2338-2344 (2022).

Jiahao Ye
Oxford
February 2025

Acknowledgment

First and foremost, I would like to express my deepest gratitude to my supervisor, Professor Jin-Chong Tan, for his invaluable guidance, encouragement, and support throughout my DPhil journey at Oxford. His insights and mentorship have been instrumental in shaping my research and academic growth.

I would also like to thank all my collaborators, Dr Gianfelice Cinque from Diamond Light Source, Dr Lorenzo Donà from University of Turin, and Professor Andris Šutka from Riga Technical University. I would also like to thank Chim Chu from Oxford University Innovation for his assistance with patent applications.

I would like to thank all my colleagues in the Multifunctional Materials and Composites (MMC) Lab: Yang, Arun, Annika, Dylan, Samraj, Sujeet, Tao, Michele, Vishal, Tianhuai, Cyril, Ben, Yogesh, Jinke, Mehdi, Fatih, Chuzhan, Mounir, Harry, and Yiyi. The insightful scientific discussions and shared moments during group lunches, barbecues, and squash sessions have made this experience truly enriching.

Beyond the lab, I have been incredibly fortunate to meet so many wonderful friends at Oxford. To my Wolfson friends—Chenny, Sam, Zhao, Vincent, Alan, Yizhou, Luke, Ellen, Rustam, Vedika, Sarah, and Tien—thank you for all the tennis, squash, and dinners we have shared. To Cici, Sus, Yishan, Xianghe, Xiao, Claire, Feng, Jason, Zhaoxing, and Roxi—thank you for the countless hotpot gatherings and beers (despite my allergy). Your friendship has been a source of joy and support throughout this journey. I would also like to thank Wolfson College for providing accommodation, funding for conferences, and fostering a vibrant and friendly community. My time at Wolfson has been filled with memorable moments.

Lastly, I would like to express my deepest thanks to my family—to my younger brothers for the short but precious reunions; to my uncle who has always been directing and supporting me in my academic journey abroad; and most importantly, to my mom and dad, who provided me with unconditional love and encouragement through this journey. This accomplishment would not have been possible without your support.

Abstract

The growing demand for sensors in modern technologies has increased the necessity for efficient and sustainable energy harvesting technologies. Triboelectric nanogenerators (TENG), which operate based on contact electrification and electrostatic induction, have garnered significant attention over the past decade. However, the limited selection of high-performance materials remains a key challenge in advancing TENG technology. Metal-organic frameworks (MOF), with their exceptional tuneability in structure and properties, present excellent potential to develop next-generation TENG materials with enhanced triboelectric output. Beyond improving performance, MOFs provide a unique platform for studying the underlying charge transfer mechanisms. In this integrated thesis, the fundamental principles of TENG technology and recent advances in MOF-based TENGs are introduced in Chapter 1 and 2, followed by an overview of triboelectric testing setups and characterisation techniques in Chapter 3.

Chapter 4 to 7 explore different approaches to material and structural design to enhance TENG performance. Specifically, Chapter 4 examines the influence of MOF topology on triboelectric output, while Chapter 5 focuses on the effect of ligand functionalisation. The mechanisms behind these improvements are revealed by nano-scale chemical and mechanical characterisations, dielectric measurements, and computational simulations. Chapter 6 introduces a detailed investigation of a noncontact rotational TENG design, incorporating a fluorinated MOF to extend the practical applications of MOF-based TENGs. Chapter 7 explores a surface modification strategy for conventional polymer materials, providing deeper insights into the charge transfer mechanisms through various proposed models.

Overall, this thesis aims to facilitate the design of high-performance TENG devices through a materials-driven approach while expanding their potential applications. The findings are critically summarised in Chapter 8, with a discussion on future research directions in the field of MOF-based TENGs.

Table of Contents

List of Figures

List of Tables

List of Abbreviations

2-Br-Im	2-bromo-1H-imidazole
2-CF_3-Im	2-trifluoromethyl-1H-imidazole
2-Cl-Im	2-chloro-1H-imidazole
2D	two-dimensional
2-mIm	2-methylimidazole
3D	three-dimensional
AC	alternating current
AFM	atomic force microscopy
APTES	(3-aminopropyl)triethoxysilane
ATR	attenuated total reflection
BET	Brunauer-Emmett-Teller
CCDC	Cambridge Crystallographic Data Centre
CE	contact electrification
CF_3	trifluoromethyl
DC	direct current
dcIm	4,5-dichloroimidazole
DFT	density functional theory
DMF	dimethylformamide
EDS	energy-dispersive X-ray spectroscopy
ESP	electrostatic potential

far-IR	far infrared
FESEM	field-emission scanning electron microscope
FTIR	Fourier-transform infrared spectroscopy
HOMO	highest occupied molecular orbital
IoT	Internet of Things
ITO	indium tin oxide
KPFM	Kelvin probe force microscopy
LDPE	low-density polyethylene
LED	light-emitting diode
LUMO	lowest unoccupied molecular orbital
MCT	mercury cadmium telluride
MOF	metal-organic framework
MOP	metal-organic polyhedra
nano-FTIR	nanoscale Fourier Transform Infrared Spectroscopy
P(VDF-TrFE)	poly(vinylidene fluoride-trifluoroethylene)
PDMS	polydimethylsiloxane
PET	polyethylene terephthalate
PS	polystyrene
PTFE	polytetrafluoroethylene
PVDF	poly(vinylidene fluoride)
RH	relative humidity
SAM	self-assembled monolayer
SE	secondary electron

SEM	scanning electron microscopy
SR	synchrotron radiation
TENG	triboelectric nanogenerator
TFM	tip force microscopy
TMSPMA	3-(trimethoxysilyl)propyl methacrylate
UV	ultraviolet
VTMS	vinyltrimethoxysilane
XPS	X-ray photoelectron spectroscopy
XRD	X-ray diffraction
ZIF	zeolitic imidazolate framework
$Zn(NO_3)_2\cdot 6H_2O$	zinc nitrate
$Zn(OAc)_2\cdot 2H_2O$	zinc acetate
$Zn_5(CO_3)_2(OH)_6$	zinc carbonate basic
ZnO	zinc oxide

List of Symbols

θ	Angle
Å	Angstroms
cm	Centimetres
°C	Degrees Celsius
GΩ	Gigaohm
kg	Kilogram
kHz	Kilohertz
kΩ	Kiloohm
MHz	Megahertz
MΩ	Megaohm
MPa	Megapascal
µA	Microampere
µL	Microlitre
µm	Micrometres
mL	Millilitre
mm	Millimetres
mmol	Millimole
mN s^{-1}	Millinewton per second
Ms	Millisecond
mW m^{-2}	Milliwatt per square metre
nm	Nanometres

wt%	Percentage by mass
mol%	Percentage by molar
pJ	Picojoule
rpm	Revolutions per minute
V	Volt
cm^{-1}	Wavenumber

1

Introduction

1.1 Motivation

Throughout human history, technological advancements have always been closely related to the discovery and efficient utilisation of energy sources. Primitive methods such as generating fire by drilling wood marked the beginning of humanity's ability to harness energy. The subsequent discovery of coal as a fuel source and the invention of the steam engine catalysed the Industrial Revolution, driving significant industrial and societal transformation. Later, the development of electromagnetic generators and advancements in oil refinery further enabled large-scale electricity generation, revolutionising modern life. Today, in the 21st century, with the rapid expansion of the Internet of Things (IoT), a spurt in demand for micro-sensors and intelligent devices has raised more attention to alternative energy harvesting technologies that enable self-powered electronics. Currently, to meet the energy needs of these devices, conventional batteries remain the primary solution. However, their limited lifespan, environmental impact, and high maintenance costs pose significant challenges at scale. With over 100 billion sensors projected to be connected to the IoT by 2030 [1], there is growing interest in alternative energy harvesting technologies that can enable self-powered systems and reduce reliance on traditional power supplies [2,3].

Triboelectric nanogenerator (TENG), a technology for energy harvesting developed by Wang *et al.* in 2012 [4], has emerged as a promising candidate to meet the energy demand in self-powered sensors. Based on the coupling effect of contact electrification and electrostatic induction, TENG can convert mechanical motions into electric energy which offers a tremendous opportunity to develop green energy solutions in a variety of scenarios [5,6]. TENGs are considered promising substituents for conventional energy sources in sensors and small-scale electronics in numerous applications, as shown in Figure 1.1.

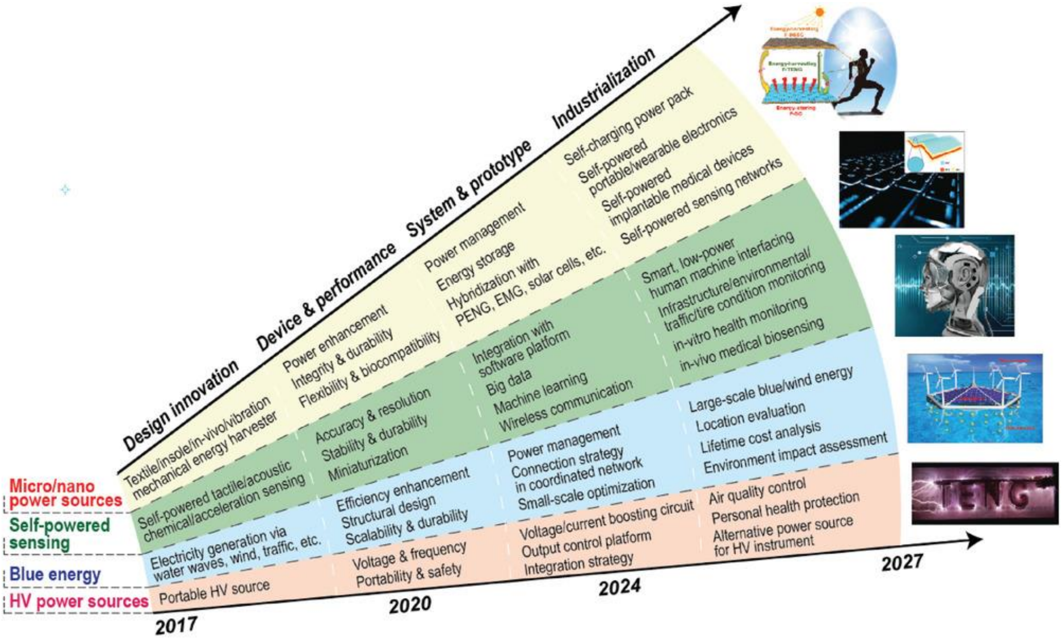

Figure 1.1. Applications of TENG and a road map for the development of TENG technologies. Adapted with permission from [7]. Copyright 2020 John Wiley and Sons.

1. Introduction

TENGs have outstanding efficiency in scavenging energy from low-frequency motions which are ubiquitous in daily activities but mostly wasted to the ambient background. Through intensive research during the past decade, TENG has been used to harvest mechanical energy from water waves [8,9], human motions, mechanical vibration, and wind [10,11]. Beyond energy harvesting, more applications of TENG have been explored in the field of self-powered sensors including stress variation detection, gas concentration monitoring, and vital signal inspection, demonstrating great potential in wearable electronics and healthcare devices [12]. Despite their advantages, TENGs face critical limitations, particularly in material selection and relatively low power output. Conventionally, the selection of TENG pair relies on triboelectric series ranked by the empirical results of material's ability to attract or repel electrons while contacting with another material. Although this series has expanded over time to include a broader range of materials, from conventional metals to natural products and polymers, there remains a need to develop new materials for TENG and establish a deeper understanding of the fundamental principles for material selection.

Recently, metal-organic frameworks (MOF), a class of highly crystalline porous materials, have shown great potential to enhance the triboelectric output of TENG devices. MOFs offer unique advantages, including excellent tuneablity with the constituting metal ion node and organic ligand, which allows for controllable structures and functional properties for specialised applications. Their tailorable pore size and high surface area further contribute to their application in TENG. The design flexibility of MOFs makes them ideal candidates for studying structure-property relationships, which can provide guidelines for the development of next-generation TENG materials with tailored properties for specific applications. In recent literature, MOFs can either be fabricated as thin films or incorporated as a filler material to introduce additional charges into the composite film. Since the first MOF-based TENG proposed by Khandelwal *et al.* in 2019 [13], research in this field is still in its early stages. Given the great versatility of MOF structures, there is a critical need to develop universal design criteria for their integration into TENG technology.

1.2 Research aims

The main objective of this DPhil thesis is to develop high-performance metal-organic framework-based triboelectric nanogenerators and broaden their scope of applications. Previous studies on MOF-based TENGs have focused on individual materials without comparing different MOFs [14-17], resulting in fragmented findings and lacking general trends or selection criteria. To close this knowledge gap, this thesis aims to study the underlying effects of MOF topology and the electron-withdrawing ability of the constituting organic ligands, in conjunction with advanced characterisation techniques, thereby establishing a set of universal selection criteria for MOF-based triboelectric materials. The work also contributes to a deeper understanding of the underlying mechanism of dielectric-to-metal type TENG. In addition, leveraging optimised MOF-TENG systems with superior triboelectric output, this thesis aims to explore advanced applications of MOF-based TENG.

1.3 Thesis structure

This integrated thesis is composed of 7 chapters. A summary of the thesis structure is presented in Figure 1.2.

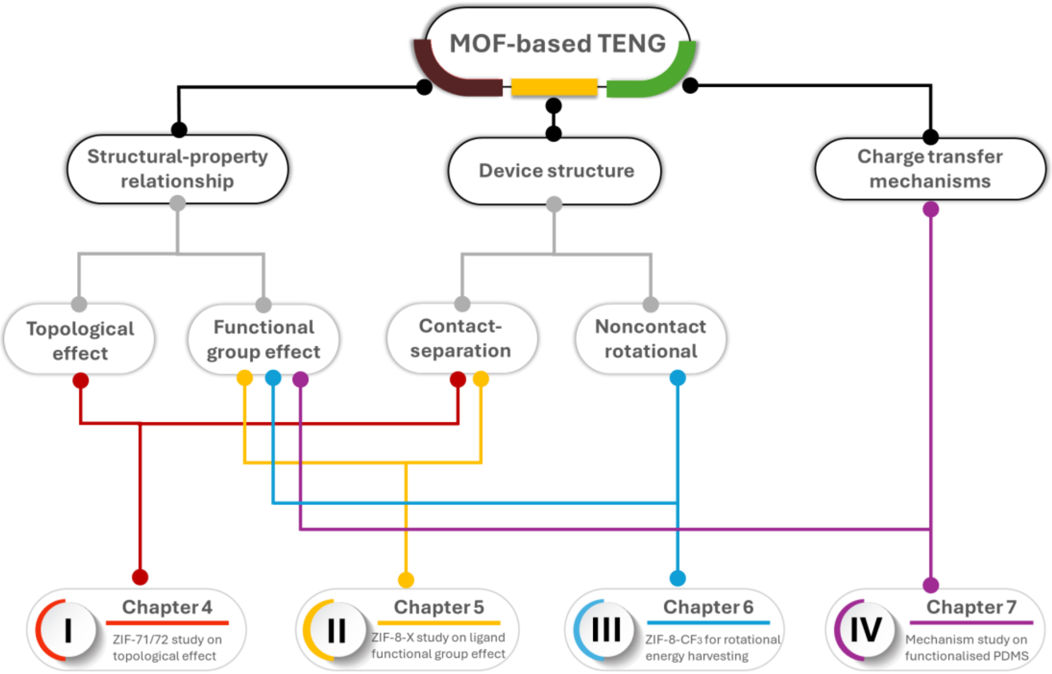

Figure 1.2. Overview of main chapters presented in this thesis.

The present chapter (Chapter 1) sets out the motivations and primary objectives of this DPhil thesis, focusing on the general scope of TENG devices enclosing MOFs. It provides an overview of the key challenges in energy harvesting and highlights the potential of MOF-based TENGs.

Chapter 2 provides a detailed background of the research, including a literature review on TENG technology and the potential of MOF-based TENG in energy harvesting. This chapter covers the fundamental principles of TENG operation, key properties of MOFs relevant to triboelectric applications, and the state of the art in MOF-based TENG research.

Chapter 3 outlines the experimental methodologies employed in this thesis. It provides a detailed description of the design and fabrication of triboelectric test rigs used for evaluating the triboelectric performance of prepared materials. The chapter also discusses the characterisation techniques employed in this study, including electrical, mechanical, morphological, and chemical analysis. Detailed experimental and simulation methods are also introduced.

The following chapters (Chapters 4 to 7) present individual research studies related to the general topic of MOF-based TENG, with a published paper or manuscript attached to the end of each chapter. The motivation and background of each paper are introduced, with a summary of key findings and additional insights based on the supplementary data.

Specifically, Chapter 4 studies the impact of MOF topology on the triboelectric output of MOF-based TENGs. Chlorinated zeolitic imidazolate frameworks, ZIF-71 (RHO topology) and ZIF-72 (LCS topology), which share identical chemical compositions but differ in topology, were incorporated in polydimethylsiloxane (PDMS) matrix as fillers for the fabrication of resilient TENG. This study demonstrates that the prepared ZIF-72/PDMS nanocomposite exhibited significant electrical output attributed to the high dielectric constant and surface adhesion of ZIF-72 LCS topology. With advanced characterisation approaches, specifically nanoscale Fourier transform infrared spectroscopy (nano-FTIR) and tip force microscopy (TFM), compositional variations at the near-surface layer of the ZIF-72 nanocomposite and high surface adhesion have been revealed, which collectively contribute to the promising triboelectric properties of ZIF-72 based TENG.

Chapter 5 then studies another critical parameter in the design of MOF-based TENGs—the influence of ligand functionalisation on triboelectric energy harvesting efficiency. The excellent tuneability of MOF materials provides an opportunity to enhance their triboelectric performance by tailoring ligand functional groups towards specific applications. This chapter investigates the functionalisation of ZIF-8 with various electron-withdrawing groups and evaluates the impact on triboelectric energy harvesting efficiencies within a poly(vinylidene fluoride) (PVDF) composite fibre matrix.

Chapter 6 extends the application of MOF-based TENG by exploring a non-contact rotational mode TENG. Building upon previous studies, ZIF-8 is functionalised with highly electronegative trifluoromethyl (CF_3) groups to yield ZIF-8-CF_3. The prepared composite is assembled into to TENG device capable of generating high-frequency and high-power output while significantly extending the device's lifespan due to its non-contact design. The potential applications of this device, including wind energy harvesting, wind speed sensing, and humidity sensing, are demonstrated in this chapter.

Chapter 7 focuses on the fundamental mechanisms of contact electrification (CE) in dielectric-to-metal TENGs. Developed based on the previous functionalisation approach introduced in Chapter 5, conventional PDMS membranes are surface functionalised with self-assembled monolayers (SAM). The underlying mechanisms of different triboelectric properties of functionalised samples are explained *via* both electron transfer and material transfer models, supported by nano spectroscopic techniques and fine-scale mechanical studies.

The final chapter (Chapter 8) provides a summary of the thesis, presenting the key results and conclusions. Perspectives and insights towards future research in the field of MOF-based TENG are also discussed.

2

Literature Reviews

2.1 Triboelectric nanogenerators

2.1.1 Operating Modes of TENGs

Triboelectric nanogenerators are a class of energy harvesting devices that operate based on the coupling effect of contact electrification and electrostatic induction [18]. While two materials come into contact, surface charge transfer occurs due to differences in their electron affinities, leading to the formation of positive and negative electrostatic charges. Upon separation, the opposite charges on the material surface induce an electrostatic potential difference between the electrodes attached to materials. If an external circuit is connected between the electrodes, this induced potential difference will drive electrons to flow between the electrodes, generating an electric current. Based on the same working principle but different device configurations, four primary operating modes of TENG have been developed to accommodate various application scenarios: (1) contact-separation mode, (2) lateral sliding mode, (3) single-electrode mode, and (4) free-standing mode.

2.1.1.1 Contact-separation mode

The contact-separation mode is one of the most extensively studied and widely applied operating modes of TENGs. It is often used as the standard configuration for evaluating the performance of different triboelectric materials. In a contact-separation mode TENG, two materials with differing electron affinities are periodically brought into and out of contact. During contact, triboelectric charges are generated as electron-donating (tribo-positive) material transfers electrons to the electron-withdrawing (tribo-negative) material. During separation, the induced electrical potential drives electrons to flow through the external circuit. The contact-separation mode TENG is one of the most important operating modes for performance evaluation in this thesis. The system can be modelled as the schematic shown in Figure 2.1.

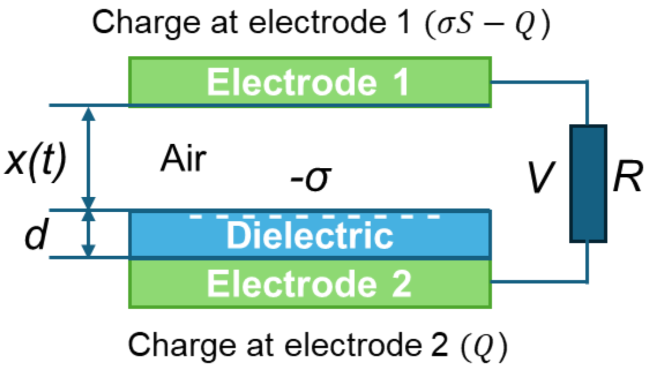

Figure 2.1. Schematic diagram for the modelling of a contact-separation mode TENG. Reproduced from ref [19]. Copyright 2013 Royal Society of Chemistry.

From fundamental electrostatics, the total charge transfer during contact is determined by the electrical flux between the two parallel surfaces, known as Gauss's Law [20]:

$$Q = \Phi\varepsilon_0 = ES\varepsilon_0\varepsilon_m \tag{1}$$

where Q is the electrical charge transferred between two electrodes and Φ is the electrical flux between the two parallel plates. As the electrical flux is always perpendicular to the surface of the plates, the total flux can be further expanded to ES, where E is the electrical field strength and S is the surface area of the electrode plate. ε_0 and ε_m are the permittivity of vacuum and the relative permittivity of the dielectric material, respectively. By applying Equation 1 to a parallel-plate capacitor model, the electric field strength created by the dielectric material and air can be written as [21]:

$$V = E_m d + E_{air} x(t) \tag{2}$$

$$E_m = \frac{Q}{S\varepsilon_0\varepsilon_m};\ E_{air} = \frac{\sigma S - Q}{S\varepsilon_0} \tag{3}$$

$$V = -\frac{Q}{S\varepsilon_0}\left(d_0 + x(t)\right) + \frac{\sigma x(t)}{\varepsilon_0} \tag{4}$$

where d is the thickness of the dielectric material, d_0 is the effective thickness constant ($d_0 = d/\varepsilon_m$), σ is the surface charge density, $x(t)$ is the distance between the plates as a function of time. Under open-circuit conditions ($Q = 0$), the open-circuit voltage of TENG can be simplified as:

$$V_{oc} = \frac{\sigma x(t)}{\varepsilon_0} \tag{5}$$

For short-circuit condition ($V = 0$), the short-circuit charge transfer Q_{sc} and short-circuit current I_{sc} can be derived as [22]:

$$Q_{sc} = \frac{S\sigma x(t)}{d_0 + x(t)};\ I_{sc} = \frac{dQ_{sc}}{dt} = \frac{dQ_{sc}}{dx(t)} \cdot \frac{dx(t)}{dt} = \frac{S\sigma d_0}{\left(d_0 + x(t)\right)^2} \cdot \frac{dx(t)}{dt} = \frac{S\sigma d_0 v(t)}{\left(d_0 + x(t)\right)^2} \tag{6}$$

where *v(t)* is the speed of the relative movement between tribo-layers. The charge density of material is considered a crucial limitation to generating a higher triboelectric output. These equations indicate that the improvement of surface charge density and contact area of a triboelectric layer will lead to enhanced current output.

2.1.1.2 Lateral sliding mode

In the lateral sliding mode TENG, charge transfer occurs due to the in-plane displacement of triboelectric layers. While the top dielectric layer slides over the bottom layer, the redistribution of surface charge induces a potential difference, driving the flow of electrons and creating a current flow in the external circuit. A continuous AC current can be generated from a periodic sliding motion [23]. The top layer could be either a dielectric material or a metal, as shown in Figure 2.2. The relationship between voltage, transferred charge, and electrode separation distance (*V-Q-x* relationship) for this type of TENG can be presented by:

$$V = -\frac{d_0}{w\varepsilon_0(l-x)}Q + \frac{\sigma x d_0}{\varepsilon_0(l-x)} \tag{7}$$

where w is the width of the device and l is the geometric size of dielectric in the longitudinal direction. As this operating mode does not require an air gap to separate the two surfaces, it facilitates a more compact device design, making it advantageous for packaging and integration. However, the cyclic sliding often leads to mechanical wear, reducing the durability and longevity of the device. Variants of this mode have been proposed with linear grating structures [24], segmentally structured disks [25], and cylindrical rotational designs [26], leading to higher energy conversion efficiencies.

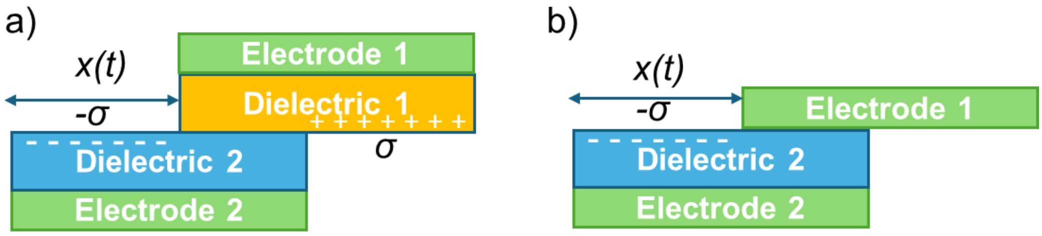

Figure 2.2. Theoretical models proposed for the (a) dielectric-to-dielectric sliding mode TENG and (b) conductor-to-dielectric sliding mode TENG. Reproduced from ref [23]. Copyright 2013 John Wiley and Sons.

2.1.1.3 Single electrode mode

The single electrode mode operates similarly to the contact-separation mode but utilises only one primary electrode. The other electrode works as a reference electrode for electric potential, which can be placed anywhere or simply grounded. During operation, a charge transfer from primary electrode to the dielectric layer will be induced by the contact between the dielectric materials. When the top dielectric surface is separated from the bottom surface, free electrons in the reference electrode will flow to the primary electrode in order to balance the potential difference. The voltage across a single electrode mode TENG can be represented as [27]:

$$V = -\frac{Q}{C} + \frac{\sigma w l C_2}{C_1 C_2 + C_2 C_3 + C_1 C_3} \tag{8}$$

where C_1, C_2 and C_3 are the constitutional capacitances of single electrode mode under open-circuit condition using an equivalent circuit model, as shown in Figure 2.3b. While this mode generates less energy compared to contact-separation mode due to the electrostatic shielding by the primary electrode, it offers significant advantages for harvesting energy from freely moving objects such as walking individuals or vehicles which does not require a direct electrical connection to both electrodes [28,29].

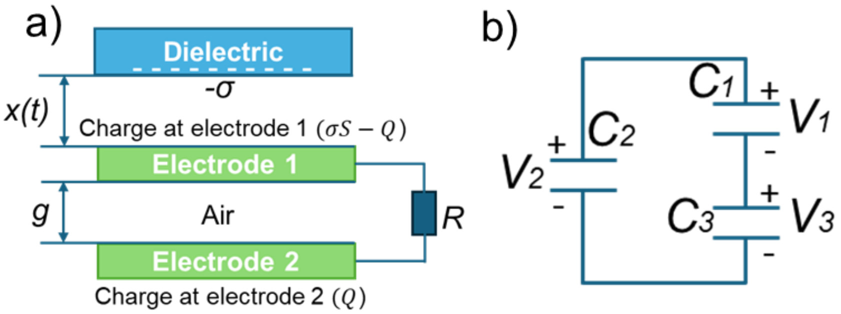

Figure 2.3. (a) Theoretical model of the single electrode mode TENG. b) Equivalent circuit model of the single electrode mode TENG in (a). Reproduced from ref [27]. Copyright 2014 John Wiley and Sons.

2.1.1.4 Free-standing mode

For a free-standing mode TENG, two stationary electrodes are positioned on the same plane with a gap in between, while a freestanding dielectric layer is placed above the electrodes. Triboelectric charges will be induced on the surfaces of electrodes when the dielectric layer is moving between the two electrodes, therefore resulting in charge flows across the two electrodes through the external circuit, as shown in Figure 2.4 [30,31]. Similar to single electrode mode, this configuration enables energy harvesting for a moving object, which does not require direct connection to the TENG system by wire. This mode is particularly advantageous for contact-free applications, reducing mechanical wear while enabling scalable configurations such as sliding [32], grating [33], and rolling structures [34]. Among these various designs, non-contact rotational TENG is one of the most attractive configurations of free-standing mode TENG, in which a precharged surface induces electrostatic induction in the electrodes without requiring direct physical contact. Compared with conventional electrostatic generators, which often require an external bias or continuous sliding of brushes to redistribute charges, TENGs uniquely couple triboelectric charge generation with electrostatic harvesting under contact-free operation. Once the dielectric surface has been initially charged by contact electrification, output current will be generated by the motion of charges on electrodes rather than the triboelectric materials. A critical challenge in non-contact devices is the decay of surface charges over time, caused by environmental leakage and charge recombination, meaning that the material needs to be periodically recharged to maintain performance [179]. Consequently, the development of strategies to sustain the surface charge of materials are essential for ensuring stable output and broadening the practical applicability of non-contact TENGs.

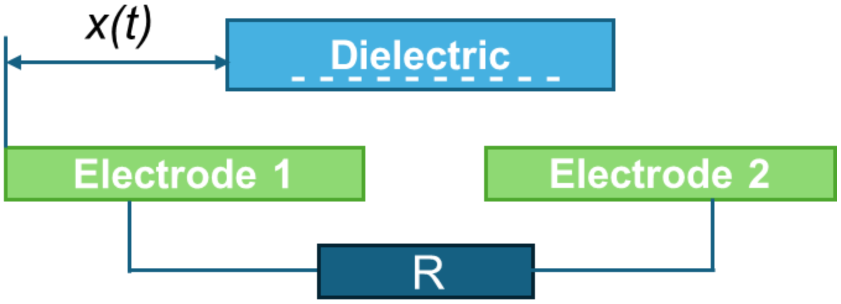

Figure 2.4. Theoretical model of free-standing mode TENG. Reproduced from ref [30]. Copyright 2015 Elsevier.

2.1.2 Contact electrification

Although triboelectric nanogenerator is a relatively recent invention, the phenomenon of contact electrification (CE) has been observed for over 2600 years and is a common occurrence in humans' daily activities. However, the fundamental mechanisms of CE remain debated due to limitations in the characterisation techniques [3]. With advancements in technology, CE has found applications in various fields such as charge-induced adhesion and electrostatic printing, while it can be undesirable in certain circumstances, such as electrostatic discharge in microelectronics [35]. Therefore, a thorough understanding of CE mechanisms is essential for optimising its applications. Over the years, three primary charge transfer mechanisms have been proposed to lead to the CE, including (1) electron transfer, (2) ion transfer, and (3) material transfer, as presented in Figure 2.5.

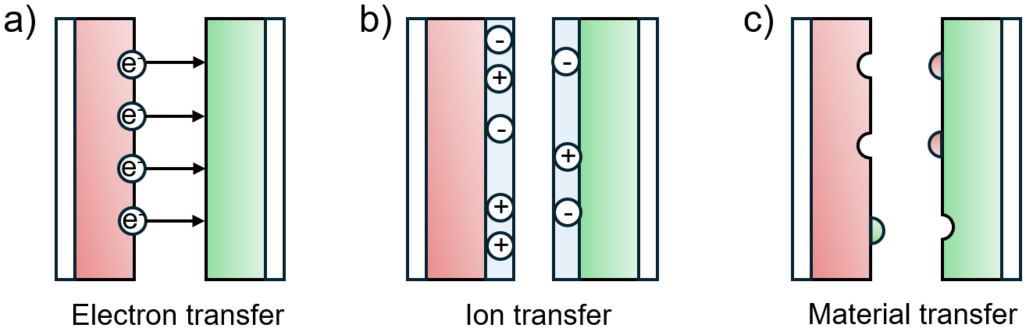

Figure 2.5. Schematic representation of contact electrification mechanisms. (a) Electron transfer, (b) ion transfer, and (c) material transfer.

Electron transfer is one of the primary explanations for charge generation in CE. This model suggests that charge transfer occurs in the form of electrons which is driven by the difference in materials' work functions or contact potential differences [36,37]. In general, electrons migrate from a material with a lower work function to one with a higher work function to achieve Fermi level equilibrium. A surface state model is often used to illustrate the electron transfer phenomena in materials whose electronic structures can be represented by a band diagram. For materials where such representations are not feasible, an electron cloud overlap model has been proposed to explain the charge transfer by electrons entering the repulsive region of another material's electron cloud under external force [38,39]. A correlation between the triboelectric output and the work function differences of contacting materials has been revealed to support the electron transfer mechanism [40,41]. Additionally, more evidence of electron transfer is demonstrated by Liu and Bard, showing that CE could drive various electrochemical reactions that typically require electrons [42,43]. However, this model is less convincing for explaining CE in insulators, as a high energy barrier needs to be overcome for electron transfer associated with their wide band gap. Moreover, the model fails to explain the observation that CE occurs between identical materials.

Ion transfer model proposes that charge transfer during CE is driven by asymmetrically separated mobile ions while contacting two materials [44,45]. This model suggests that all surfaces absorb water, leading to the formation of a layer of OH^- group, especially for ionic polymer and hydrophilic materials. Diaz *et al.* introduced the "water bridge" model, where a water layer is formed at the interface of non-ionic insulators [46]. The ions will be asymmetrically distributed due to the chemical potential difference at the water bridge, leading to the formation of charges. Furthermore, Diaz *et al.* conducted a semi-quantitative study that correlated the triboelectric series to the pK_b values of polymers. pK_b is a value that reflects the basicity of the polymer, providing a measure of the degree of protonation. The result suggested a consistent correlation between transferred charge and proton and ion transfer between the surfaces [47]. However, research from Baytekein *et al.* indicated that CE occurs even under environments with 0% relative humidity where no water molecule presents, although the amount of transfer has been largely reduced [48]. This research suggested that the role of water is significant to stabilise surface charges occurred during CE, but other mechanisms are also involved. The significance of ion transfer in CE likely depends on specific material properties and environmental factors.

Mass transfer is another mechanism that was initially not considered a dominant mechanism as CE is in general too reproducible to be attributed to a relatively random process as material transfer [36]. However, this mechanism has drawn more attention in recent years with the advancement of local surface characterisation techniques such as X-ray photoelectron spectroscopy (XPS), nanoscopic FTIR, and KPFM [3,49,50]. In 2011, Baytekin *et al.* observed a random mosaic of oppositely charged regions on contacting materials attributed CE accompanied to material transfer. The observed mosaic charge patterns are verified by KPFM, confocal Raman, and XPS [51]. The research proposed that the non-equality of positive and negatively charged species from irregular mosaic structure results in a net charge on the surface, and this microscopic variation in surface composition explains the origin of charge formation upon contact between identical materials [52]. Moreover, a recent study has found that the charge is strongly associated with the materials' surface mechanical properties. Šutka *et. al* examined different thermoplastic polymers and found an inverse relationship between surface charge density and elastic modulus, suggesting that higher adhesion energy enhances material transfer and charge accumulation [53]. Based on a study on

PDMS polymer, the prepared PDMS film with a lower cross-linking degree thereby exhibits higher surface adhesion and higher surface charge, supporting the findings that polymers with strong surface adhesion and low cohesion energy in bulk enhance material transfer and higher surface charge. Later, Gong *et al.* utilised the strong surface adhesion properties of viscoelastic polymer adhesives (VPAs) to harvest high triboelectric charges when paired with PTFE [54]. The adhesive surface demonstrated a great performance enhancement effect compared to non-adhesive materials, highlighting the potential of adhesive materials for mechanical energy scavenging.

In summary, while each proposed charge transfer model contains certain limitations, CE likely arises from a combination of multiple mechanisms. The relative contributions of electron transfer, ion transfer, and material transfer depend on the material properties and environmental conditions. As a result, a comprehensive understanding of these mechanisms is essential for optimising CE in practical applications and systematically advancing the field of triboelectric energy harvesting.

2.1.3 Materials for TENG

Despite the rapid development of TENG in the past decade, the selection of materials remains a critical challenge that limits their practical application and commercialisation. Conventional selection process for a triboelectric pair depends heavily on empirical triboelectric series, which classifies materials based on their triboelectric ability to attract or repel electrons. For the tribo-positive materials, metals such as copper and aluminium normally serve as excellent electron donors [55]. Although the charge density of metal is not the highest among the triboelectric series, it offers the advantage of functioning as both a positive layer and an electrode, which significantly reduces the cost and the size of the assembled TENG device. On the other hand, fluorinated polymers have shown exceptional effectiveness for TENG applications, especially as the tribo-negative layers due to their strong tendencies to attract electrons [20]. Commonly used materials such as polyvinylidene fluoride (PVDF), polydimethylsiloxane (PDMS), and polytetrafluoroethylene (PTFE) exhibit excellent surface charge density, making them prevalent choices in TENG studies [55]. Through years of development, this series has been extended with more advanced materials of different classes [56]. Despite the effectiveness of these electronegative materials, the practicality of TENG is still limited by the relatively low power output, which fails to meet the energy requirements for consistently charging daily-use electronics, such as Li-ion batteries, without substantial storage or hybrid systems [57]. As a result, there is an urgent need to develop new triboelectric materials with higher triboelectric output to overcome the current bottleneck. Multiple material-related strategies have been proposed and explored to enhance the electrical performance of TENG. These include (1) surface modification for improved surface charge density, (2) incorporation of filler materials as charge traps, and (3) enhancement of material's dielectric constant for higher capacitance [20,58].

The surface property of the material is crucial to the output performance of TENG, primarily through its inherent tribo-electronegativity and the effective contact area with the friction layer. Therefore, many studies have focused on increasing the surface charge density and optimising the effective contact area by modifying the surface morphology and functionality of the material. Chen *et al.* fabricated a SiO_2/P(VDF-TrFE) composite film with a layered micro-nano structure by electrospinning technology for application in stretchable TENGs [59]. Compared to pristine polyvinylidene fluoride copolymer (P(VDF-TrFE)) film, the SiO_2 nanoparticles introduced a hierarchical structure of nanofibre network, which significantly improved the surface roughness, thereby increasing the effective contact area. The assembled TENG demonstrated a maximum instantaneous output voltage of 170 V, a current density of 12.5 μA cm^{-2}, and a charge transfer density of 24 nC cm^{-2}, three times higher than that of the pristine film.

Moreover, embedding fillers into the dielectric material has been demonstrated as an effective approach to enhance charge trapping, providing additional pathways for charge accumulation and improving surface charge density. Wen *et al.* fabricated a nanocomposite film based on PVDF and monolayer titania (TOML) filler [60]. With 1.5 wt% of TOML, the prepared TENG device exhibited a peak output performance of 52.8 V and 5.69 μA cm^{-2}, achieving a 50-fold increase in peak output power density. This enhancement was attributed to the abundant charge-trapping sites provided by TOML, which significantly reduces the dissipation of tribo-induced charges on the film surface.

According to the fundamental working principle of contact-separation mode TENG, increasing the dielectric constant of the friction layer material can effectively improve its surface charge density during operation. Thus, many researchers attempted the embedding of high-permittivity inorganic materials such as perovskites to improve the working performance of TENG. For example, Jie *et al.* modified the conventional PDMS by incorporating nanoparticles with a high dielectric constant, including SiO_2, TiO_2, $BaTiO_3$, and $SrTiO_3$ [12]. Notably, the results revealed a direct correlation between the dielectric constant and output performance, with $SrTiO_3$ embedded PDMS exhibiting the highest output of 305 V and 7.18 $\mu A\ cm^{-2}$, i.e. 1.8 and 2.4 times higher than that of pristine PDMS-TENG.

In addition to the above-mentioned strategies, novel approaches and materials are still under investigation to overcome the limitation of the output performance of TENG. The advancement of highly efficient TENG materials will be essential for the development of sustainable power sources for wearable electronics, blue energy harvesting, and self-powered sensing applications.

2.2 Metal-organic framework (MOF)-based TENGs

2.2.1 Metal-organic frameworks (MOFs)

Metal-organic frameworks are hybrid nanomaterials fabricated by the self-assembly of metal ions and organic linkers, resulting in highly structured nanopores with exceptional crystallinity, as illustrated in Figure 2.6. Since the popularisation of MOF by Yaghi in 1995 [61], following the pioneering research by Robson and Hoskins [62], over 20,000 different MOF structures have been developed and extensively researched for a range of chemical and physical functionalities [63].

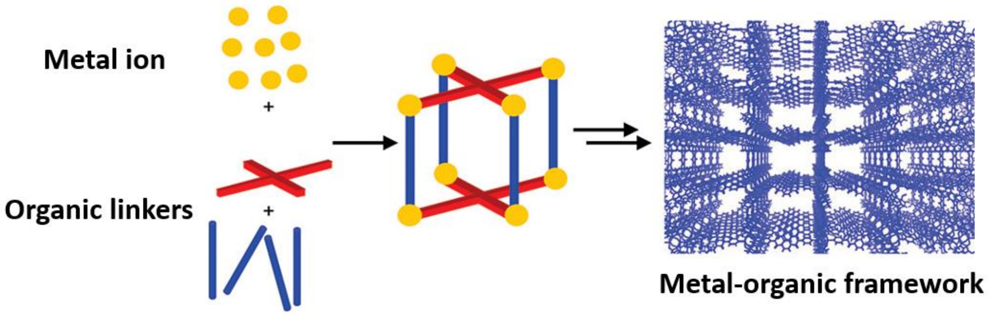

Figure 2.6. General scheme of MOF synthesis. Adapted from ref [64]. Copyright 2010, American Chemical Society.

MOF exhibits several outstanding properties, including ultra-high surface areas, high porosity, excellent flexibility, and tuneable chemical compositions. The building unit of MOFs can be customised by selecting various metal ions and ligands of different lengths and sizes to yield distinct coordination structures and framework topologies [65]. Therefore, by judicious molecular design and assembly of the building units, MOFs can be engineered to exhibit tailored geometries and properties suitable for applications in luminescence [66], dielectrics [67], catalysis [68], gas adsorption [69], charge transfer [70], drug delivery [71], sensing [72], and more. Although MOFs offer distinct advantages over traditional porous materials such as activated carbon and zeolites, one of the major challenges limiting their application is their chemical and physical stability. Due to the weak coordination bond within the MOF structure, many MOFs suffer from poor stability when exposed to solvents, acids, bases, or mechanical stress. As a result, the development of stable MOFs has become a critical research focus, and the assessment of MOF stability has become critical for engineering applications [73].

Since 2019, there has been a growing interest in exploring MOFs for TENG applications, driven by the need for novel materials with enhanced triboelectric output to meet practical operational demands [74]. Excellent physicochemical properties of MOFs, including their large surface-to-volume ratio and tuneable surface chemistry, enable their electronic structure to be precisely designed to optimise TENG output performance. Additionally, the potential reasons of using MOFs as triboelectric materials has been proposed by several researchers. For example, Mi *et al.* claimed that the metal ion centre of MOF provides a dense electron cloud, which facilitates electron excitation and transfer [75]. While these metal centres are evenly distributed within the MOF framework, they provide multiple pathways for charge transport and reduce the energy barrier for electron escape. On the other hand, the organic ligands of MOF with different spatial arrangements and abundant electrons contribute to charge separation. The variety of ligand selection provides an opportunity to establish a clear structure-property relationship, providing guidelines for novel material design [76]. Moreover, Wang *et al.* proposed that the assembled framework structure with high pore density accommodates and retains more charges with excellent triboelectric properties. Under external mechanical stress, the lattice of porous crystalline structure will deform under intermolecular forces, leading to overlap of the building unit, thereby increasing the contact area and charge density [77]. Together, these perspectives highlight the promising features of MOFs for triboelectric applications, yet further work is needed to directly link structural features to the observed triboelectric performance.

MOFs can be utilised in TENGs either as thin films or as fillers in polymer matrices, each offering distinct advantages. As thin films, MOFs provide a well-defined, uniform interface for charge transfer, ensuring efficient electron exchange during triboelectric contact. Their high surface area and tuneable electronic properties enable enhanced triboelectric charge generation. Alternatively, as fillers in polymer composites, MOFs improve triboelectric performance by modulating surface roughness, enhancing dielectric properties, and introducing additional charge-trapping sites. Both preparation methods make MOF-based TENGs promising for energy harvesting and sensing applications. The following sections will detail recent advancements in these two approaches toward MOF-based TENGs.

2.2.2 MOF thin films for TENGs

Utilising MOF thin films as triboelectric layers in TENG is a straightforward strategy for preparing MOF-based TENGs. The abundant electrons and high surface charge from the coordination between the metal ion and organic ligands at the MOF framework structure enabled the high triboelectric output. Generally, two methods are employed for preparing MOF thin films for triboelectric applications: *in situ* growth on metal electrodes and adhesive transfer using conductive tape to paste the pre-synthesised MOF powders.

In 2019, Khandelwal *et al.* first proposed the use of Zeolitic Imidazole Framework-8 (ZIF-8) as a tribo-positive material in a contact-separation mode TENG for tetracycline sensing. The ZIF-8 thin film was synthesised *via in situ* growth, with different growth cycles optimising its output. The result shows the highest power density output of 392 mW m^{-2} at 20 growth cycles, demonstrating the feasibility of using MOF thin films as charge-generating materials in TENG [13].

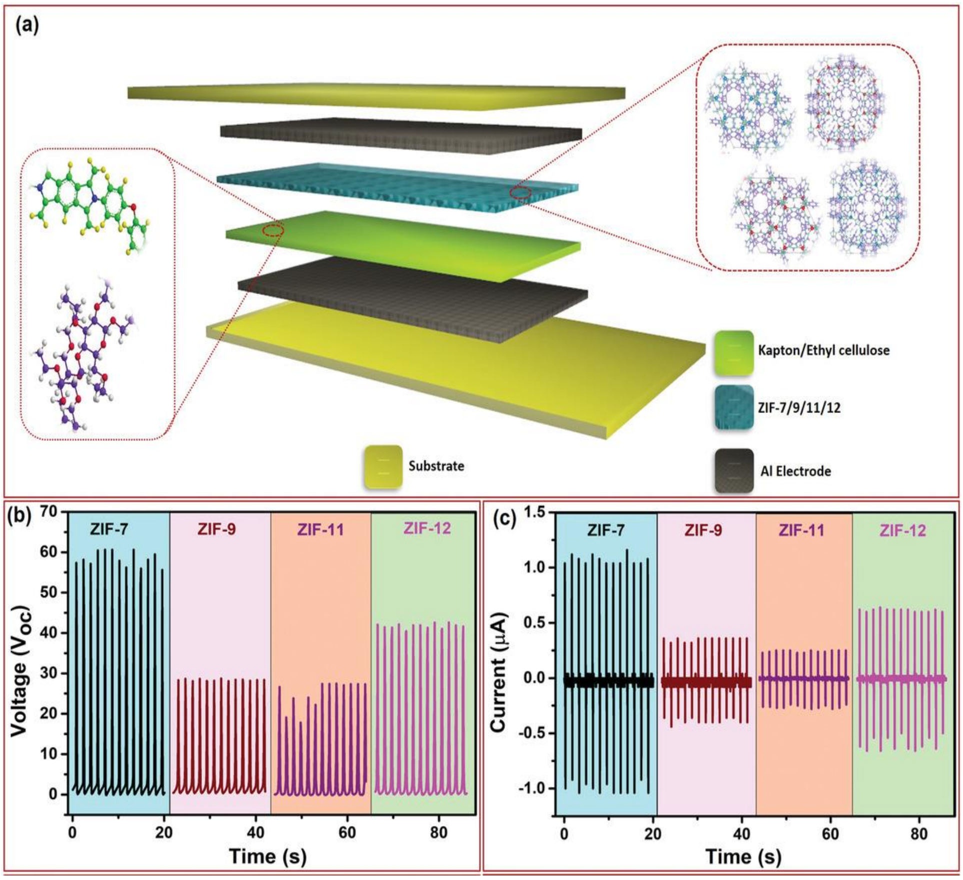

Figure 2.7. (a) Schematic depiction of ZIF-TENG. (b,c) The voltage versus time and current versus time graphs for different ZIF-TENG, respectively. Adapted from ref [78]. Copyright 2020 John Wiley and Sons.

Later, Khandelwal *et al.* further investigated the triboelectric performance of various ZIFs, including ZIF-7, ZIF-9, ZIF-11, and ZIF-12, as shown in Figure 2.7 [78]. The research indicated that the surface roughness, MOF morphology, and surface potential are crucial to the output performance of TENG. The prepared samples successfully charged up capacitors and low-power electronic devices, with ZIF-7 showing the highest open-circuit voltage of 60 V as a result of its high surface potential and good hydrophobicity.

Khandelwal *et al.* also reported ZIF-62 in combination with different negative layer materials for TENG applications [79]. The highest power output is generated when Kapton serves as the tribo-negative layer, yielding a voltage of 62 V. The prepared TENG was demonstrated to charge capacitors and harvest energy from human activities such as lifting and squatting, broadening its application scope to self-powered fitness monitoring and confirming the effectiveness of MOF materials in TENG.

Jayababu and Kim fabricated a bimetal organic framework (BMOF) containing both cobalt and zinc metal ions which proved to have enhanced TENG power output at an optimum Zn composition of 15 mol% [80]. The prepared Co/Zn BMOF nanosheets were coated on carbon fibre to ensure the flexibility and structural integrity of the device. Ascribed to the powerful sensing properties of MOF materials, the fabricated TENG was also tested to be employed as an ammonia sensor. The prepared device showed great selectivity and high durability towards ammonia sensing, offering a good prospect for practical applications.

An innovative method was introduced by Li *et al.* to coat MOF nanoparticles on the surface of the living leaf which can be used to sense the wind speed and other environmental changes [81]. The surface attached metal-organic frameworks (SURMOF) have controllable properties by introducing different ligands and functional groups, making them more biocompatible and stable. The prepared living leaf samples show good self-powered sensing properties where a current signal of 0.8 μA can be achieved under a high wind speed.

In 2022, Shaukat *et al.* [17] studied the potential of using MOF-5 as a tribo-positive material in both triboelectric and piezoelectric nanogenerators. Results show that the MOF-5-based TENG exhibits an excellent output performance of 484 V and 40 μA under contact-separation mode. Moreover, the prepared TENG was durable under extreme temperature and humidity environments, presenting a good robustness of electrical output under harsh conditions. Although the study reports piezoelectric behaviour in the prepared MOF-5/PDMS film, it remains uncertain whether this property originates intrinsically from the MOF. Further validation using Piezoresponse Force Microscopy (PFM) and mechanism studies is necessary to clarify the underlying origin of the observed piezoelectricity.

Table 2.1 summarises the reported MOF thin film-based TENG devices in recent literature. Although MOF thin films exhibit excellent triboelectric output, their mechanical stability remains a challenge. Many of the MOFs cannot be grown directly on the metal substrates, while adhesive-based techniques often result in inconsistencies in film thickness, impacting triboelectric performance evaluation. Furthermore, the brittleness of MOF films and particles can lead to material loss during repeated contact-separation cycles, reducing long-term stability. To overcome this challenge, alternative fabrication methods such as ink-jet printing and electrodeposition can help to improve the mechanical robustness and consistency of MOF films for TENG applications in future studies.

Table 2.1. Overview of MOF thin film-based triboelectric nanogenerators.

Preparation methods	Positive layer	Negative layer	Area	Voltage	Current	Force & Frequency	Power Density	Application	Ref.
In-situ growth	ZIF-8	Kapton	2.5 × 2.5 cm^2	164 V	7 μA	-	392 mW m^{-2}	UV counterfeit system and tetracycline sensing	**[13]**
Tape adhesion	ZIF-7	Kapton	2.5 × 2.5 cm^2	60 V	1.1 μA	2 Hz			**[78]**
	ZIF-9			29 V	0.3 μA				
	ZIF-11			28 V	0.25 μA				
	ZIF-12			40 V	0.55 μA				
Tape adhesion	ZIF-62	Teflon	2.5 × 2.5 cm^2	62 V	1.4 μA	1 Hz, 18 N	9.68 mW m^{-2}	Fitness monitoring	**[79]**
Tape adhesion	CD-MOF	Teflon	2 × 2 cm^2	152 V	1.2 μA	2 Hz	80 mW m^{-2}	Backpack and Yoga exercise monitoring	**[82]**
Tape adhesion	ZIF-67	Teflon		118 V	1.7 μA	2 Hz	150 mW m^{-2}	Object recognition on robot	**[83]**
Tape adhesion	MIL-88A	FEP	2.5 × 2.5 cm^2	80 V	2.2 μA	1.3 Hz	10.4 mW m^{-2}		**[84]**
In-situ growth	ZIF-8	PDMS	3.5 × 2 cm^2	24.3 V	0.32 μA	50 N		Smart electrochromic windows	**[85]**
Tape adhesion	ZUT-75 (Co)		5 × 5 cm^2	565.67 V	90.72 μA	8 Hz			**[86]**
	ZUT-75 (Zn)			389.03 V	54.75 μA				
	ZUT-75 (Cu)			339.28 V	48.82 μA				

Table 2.1 (cont'd). Overview of MOF thin films based triboelectric nanogenerators.

Preparation methods	Positive layer	Negative layer	Area	Voltage	Current	Force & Frequency	Power Density	Application	Ref.
	ZIF-8	Kapton		150 V	3.6 µA	2Hz		Robotic tilt table to identify balance	**[87]**
Tape adhesion	Zn/Co-MOF	PVDF	5 × 5 cm^2	611.78 V	59.19 µA	8 Hz, 3.49 N			**[88]**
	ZIF-8/MO-PPy@CelF	PTFE		129 V	6.8 µA	2 Hz, 50 N			**[89]**
Tape adhesion	MOF-5	PTFE	2.5 × 2.5 cm^2	484 V	40 µA	10 Hz, 58 N		Tribo/Piezo-electric generator	**[17]**
In-situ growth	Cu	UiO-66 (-H, NO2, NH2, Br)	1 × 1 cm^2	23.79 V	0.29 µA	-			**[90]**
In-situ growth	ZIF-67	FEP	4.5 × 4.5 cm^2	280 V	70 µA	4 Hz	2350 mW m^{-2}	Smart parking	**[91]**
Tape adhesion	ZUT-8	PVDF	5 × 5 cm^2	562.78 V	97.03 µA	5 Hz, 3.53 N	2217.18 mW m^{-2}	Self-powered anticorrosion	**[76]**
Tape adhesion	Cd-MOF	PVDF	5 × 5 cm^2	451.8V	55.47 µA	5 Hz, 3.5 N			**[92]**
In-situ growth	ZIF-8@ZnO	PVDF	3 × 3 cm^2	58 V	10 µA	3 Hz	250 mW m^{-2}	Methanol sensor	**[93]**
Tape adhesion	ZUT-iMOF-1(Cu)	PVDF	5 × 5 cm^2	536.78 V	73.79 µA	5 Hz, 3.53 N	3133.23 mW m^{-2}	Anti-corrosion	**[94]**
Blade coating	MIL-101 (Cr)	PTFE	2.5 × 2.5 cm^2	105 V	11 µA	2 Hz, 10 N	2503 mW m^{-2}	Catalytic degradation of methylene blue (MB) dye	**[95]**

2.2.3 MOF/Polymer composites for TENGs

Instead of using MOFs as standalone thin films, researchers have embedded these nanoparticles into conventional polymer matrices to enhance the electrical output of the triboelectric material while simultaneously improving the device's flexibility and durability. The enhancement of electrical output is attributed to the improved surface roughness and addition of electron trapping sites within the polymer matrix created by the high surface-to-volume ratio of MOF nanoparticles. With more trapping sites and higher electron affinity, more charges can be transferred and stored deep into the material surface to prevent charge recombination, thereby generating higher power output [96,97].

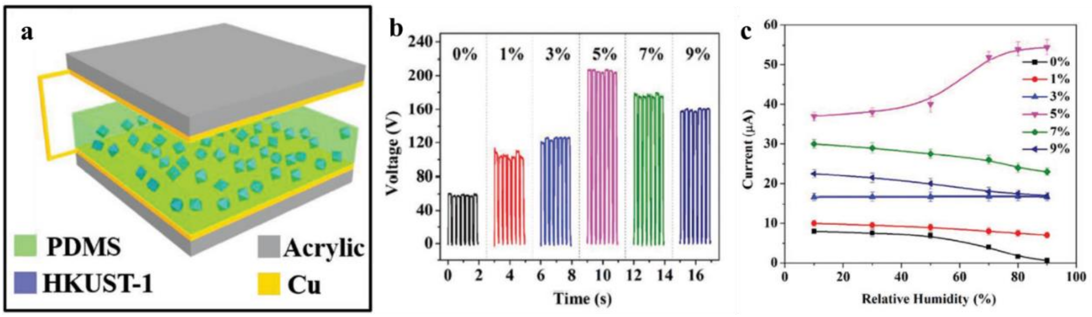

Figure 2.8. (a) Schematic description of using HKUST-1@PDMS as a tribo-negative layer in TENG. (b) voltage signals of TENG based on the PDMS/HKUST-1 nanocomposite films. (c) Humidity sensitivity of PDMS/HKUST-1 TENG output. Adapted from ref [98]. Copyright 2019 John Wiley and Sons.

In 2019, Wen *et al.* first developed a humidity-resistive TENG by incorporating HKUST-1 within the PDMS polymer matrix by solution mixing and blade casting procedures [98]. Due to the remarkable electron trapping capacity and dielectric constant of HKUST-1, the power output of prepared TENG increased by 13 times that of pristine polymer. In addition, the nanopores in HKUST-1 exhibited water absorption properties, thus enhancing the dielectric constant and increasing triboelectric output under high humidity conditions, as shown in Figure 2.8.

Moreover, Rana *et al.* carbonised ZIF-67 to form a cobalt nanoporous carbon (Co-NPC), which is used as a filler in the charge-generating layer in a non-contact mode TENG [99]. A filler loading of 3 wt% in the Ecoflex matrix doubled the power output caused by the high porosity and charge trapping capacity. The prepared TENG is also capable of sensing human motions and detecting obstacles within 20 cm range, making it feasible to be combined with AI, human-machine interface, or other progressive computational techniques. Wen *et al.* further reported the approach of using ZIF-8 as fillers in PDMS matrix instead of acting as a tribo-positive layer in Khandelwal's research [100]. The addition of ZIF-8 nanoparticles was found to increase the TENG output up to 176 V and 16.3 μA, over 2 times higher than that without ZIF-8. A list of MOF-based composites for TENG applications is summarised in Table 2.2.

Although different MOF materials have been tested to show promising performance of MOF-polymer composites in TENG, there is a lack of systematic study on the necessary screening criteria for MOF materials [101]. Moreover, the quantification of power output for MOF-based TENG devices is not standardised due to different experimental configurations, making it difficult to compare results across different studies. Other properties of MOF, such as dielectric constant, polarity, hydrophobicity, and particle size have been little studied in past literature. Therefore, there is a need for a better understanding of the structure-property correlations between MOF structures and TENG device output performance.

Table 2.2. Overview of MOF composites-based triboelectric nanogenerators.

Positive layer	**Negative layer**	**Area**	**Voltage**	**Current**	**Force & Frequency**	**Power Density**	**Application**	**Ref.**
Al	KAUST-8/PDMS	2 × 3 cm^2	530V (peak-to-peak)	3.2 μA	2 Hz, 40 N	0.52 W m^{-2}		**[15]**
Aligned ZIF-67/Silk fibroin	PDMS	2 × 2.5 cm^2	120 V	8 μA	2 Hz, 10 N			**[102]**
Cellulose aerogel/Ni-HITP	PVDF	5.5 cm circle	80 V	1.6 μA	2 Hz	0.0115 W m^{-2}	Self-powered air filter	**[103]**
Nylon-11	Co-NPC(ZIF-67)/PVDF		948 V (peak-to-peak)	248.66 mA /m^2	6 Hz, 10 N	9.24 W m^{-2}		**[22]**
glove	Co-NPC(MOF-525)@Mxene@Ecofloex		1452 V (peak-to-peak)	78 mA/m^2	4 Hz, 15 N	25.7 W m^{-2}	Tactile sensor array for gaming control	**[104]**
Ag-coated fabric	MXene/ZiF-67	2 × 2 cm^2	1340 V		4 Hz, 10 N	65 W m^{-2}	Object detection, wearable keyboard	**[105]**
Al	UiO-66/PDMS	3 × 3 cm^2	375 V	8 μA	2 Hz, 57 N	1.69 W m^{-2}		**[16]**
Cu	Cd-MOF/PDMS	2 × 3 cm^2	193.4 V	0.86 μA	-	0.124 W m^{-2}	Air mouse	**[106]**
ZIF-67/PVDF	FEP	5 × 5 cm^2	395 V	95 μA	4 Hz	3.1 W m^{-2}		**[107]**
Nylon-66	Ni-MOF/PVDF	2.5 × 2.5 cm^2	45 V	0.77 μA	16.2 N	0.01 W m^{-2}	Underwater pulse sensor	**[108]**
Cu	Ni-MOF-derived Ni/C@PVDF	4 × 4 cm^2	820 V	110 μA	5 Hz, 20 N	10.1 W m^{-2}	Wearable positioning system	**[109]**

Table 2.2 (cont'd). Overview of MOF composites-based triboelectric nanogenerators.

Positive layer	Negative layer	Area	Voltage	Current	Force & Frequency	Power Density	Application	Ref.
PAN@ZIF-8	PTFE	2 cm × 2 cm	260 V	24.5 µA	12 Hz, 13 N	1.91 W m^{-2}	Visible light communication (VLC) system	**[110]**
ZIF-8@ZnO	PMMA	5 × 5 cm^2	200.5 V	41.5 µA	4-5 Hz	0.8 W m^{-2}		**[111]**
	ZIF-8, LiCl, PAAm-co-HEA hydrogel	3.5 × 3.5 cm^2	232 V	56.3 mA m^{-2}	2 Hz, 20 N	3.47 W m^{-2}	Wearable keypad	**[112]**
skin	MOF-525@silicone@α-MoO3	3 × 3 cm^2	1760 V		4 Hz, 18 N	18.38 W m^{-2}	Electromyography signals sensing	**[113]**
ZIF-67@PAN	Mxene@PVDF	2.5 × 2.5 cm	305 V	10.6 µA	5 Hz, 4 N	10.91 W m^{-2}	Smart door	**[114]**
Al	MIL-53 (Ni) nanosheets/PVDF				5 Hz, 2.4 N	0.31 W m^{-2}		**[115]**
Al	MIL-101(Cr)/PVDF	2 × 2 cm^2	536 V	21.7 µA	3 Hz	8.712 W m^{-2}	Smart home control	**[116]**
	UiO-66–4F/PDMS	3 × 3 cm^2	937 V	30.6 µA	0.35 Hz	38.7 W m^{-2}		**[117]**
ZIF-67/silk fibroin	PDMS	2 × 2.5 cm^2	144 V	10 µA	2 Hz, 10 N	1.44 W m^{-2}		**[118]**
PVP/PAA/ MIL-88A	PTFE	2 × 2 cm^2	53.8 V	84.3 nA cm^{-2}	2 Hz, 10 N		Humidity-sensitive gripper	**[119]**
CNT/CS/PVP/PVA	PLA@ZIF-8	5 × 1 cm^2	30.8 V	53.6 nA	0.5 Hz, 10 N		PM0.3 filtration and bacterial inhibition	**[120]**

2.2.4 Applications of MOF-based TENGs

The remarkable improvements in triboelectric performance from MOF-based TENGs have broadened this technology's application. Moreover, the unique properties of MOF offer designs of functionalised TENG devices, which have opened new opportunities for TENG. The critical applications of MOF-based TENG can be categorised in the following fields: (1) micro-power energy harvesters [107,111,121], (2) smart sensors for intelligent control or monitoring systems [85,114,116,122,123]; (3) tactile sensors for robotics [83,87,119,124]; (4) gas or liquid molecule sensing [93,125-128]; and (5) air filtration [103,120,129-132].

Firstly, harvesting micropower mechanical energy is one of the most prominent applications of TENGs. Compared to traditional TENG devices, MOF-based TENGs have demonstrated significant improvement in energy harvesting efficiency and long-term output stability. Through years of research, the highest power density of MOF-based TENG can reach up to 20 W m^{-2} under contact-separation mode [104,113]. The high operating efficiency offers more opportunities for micropower harvesting. For example, Li *et al.* designed a novel multi-dimensional CoC@FeNiG-F composite derived from a bimetallic MOF. The prepared composite shows excellent environmental adaptability, specifically excellent mechanical stability, superamphiphobicity, and anticorrosion. The first MOF-based liquid-solid TENG has been designed to harvest energy from water waves, achieving a voltage and current output of 19.7 V and 1.68 μA against waterdrops, offering great potential in harvesting blue energy [133]. In addition, Sasmal *et al.* incorporated MIL-53 nanosheets within PVDF matrix to boost the total electroactive phase and dielectric property of PVDF composites [115]. Due to the high surface area of the 2D MOF structure, both piezoelectric and triboelectric energy harvesting performance have been enhanced, enabling a higher energy harvesting rate for applications such as power sources. Recent research of MOF-based TENGs focusing on improved environmental adaptability and operating efficiency will be the key to expand the scope to encompass energy scavenging.

Smart sensor for intelligent control is another key application of TENG devices as the demand for long-lasting, self-powered electronics surges in the era of Internet of Things. The electrical signal directly generated from TENG avoids redundant signal processing and identification for intelligent control and sensing. Different smart control systems have been developed based on MOF-TENGs, including a smart home control system for wireless device operation based on MIL-101(Cr) [116], a smart glove for paralysed patient care employing ZIF-67 [134], a smart fabric for thermal environment monitoring using ZIF-8 [135], and a Cd-MOF-based air mouse for remote pointer control [106]. These applications leverage the high-voltage, fast-response signal from the MOF-TENG devices triggered by soft contact, converting them into different control information based on the force, duration, and intervals of contact and separation. With the high sensitivity and long-term stability of MOF-based TENG, a reliable control and monitoring system can be designed to fit into a wider range of scenarios.

Moreover, as TENGs generate pressure-dependent electrical signals from random mechanical motions, the application of TENGs as tactile sensors in the field of robotics has become of great interest. From the amplitude and frequency information of the electrical signal, the operating states of the device can be analysed, and the specific external stimuli can be quantified. With the involvement of MOFs, the sensitivity and resolution of TENGs as tactile sensors can be improved. As a result, MOF-based TENGs are specifically favoured for robotic grippers for object detection. Kakim *et al*. designed a three-finger robotic gripper based on a flexible composite prepared by incorporating 0.25 wt% MIL-125 within Ecoflex substrate. The gripper collects 20,000 data points from each detection. Combined with machine learning algorithms and neural networks, the collected data from the TENG can be studied and processed to predict the shape of objects on the gripper, with the highest prediction accuracy of 86% [124]. Another novel robotic application of MOF-based TENG was introduced by Zhou *et al*., where the humidity-sensitive property of MIL-88A was leveraged to design a breathable gripper that can be actuated with moisture [119]. The opening and closing of abundant pores in MIL-125 under various humidities regulate the operating angle of the gripper. Meanwhile, different triboelectric responses can be obtained depending on the contacting object for perception.

The unique sensing properties of MOFs expand the border of TENG applications. The sensing properties of MOF originated from the interactions between the targeted gas or liquid analyte and the host MOF structure. The high designability of MOF, including its tuneable pore size, topology, and active sites, has enabled strong sensing potential of MOF [136]. By introducing gas-sensitive MOFs into TENG devices, the assembled devices are capable of detecting various molecules. A formaldehyde sensing device has been designed by Wang *et al.* made of ZIF-8/copper foam [125]. Due to the gas adsorption on the ZIF-8 nanopores, the resistance of device increases as formaldehyde concentration rises, thereby affecting the triboelectric output. The sensing device exhibits a low detection limit of 2 ppm and a rapid response/recovery time of 14/15 s, demonstrating excellent potential in practical applications. Another ammonia sensing device was prepared by Hu *et al.*, where an *in situ* grown $Ti_3C_2T_x$/ZIF-8 nanosheet was embedded in cellulose nanofibrous membranes, and then assembled with a negative PVDF layer to form a triboelectric device [127]. The introduction of ZIF-8 provides active adsorption sites for ammonia gas molecules, while the functional groups on $Ti_3C_2T_x$ react with ammonia, resulting in an increase in the electrical resistance of the device. The prepared sensing device shows a linear triboelectric response against ammonia concentration with excellent reusability. The integration of MOF-TENG with gas sensing properties has demonstrated great potential for dual-functional sensors as environmental monitors and is expected to develop more selective, stable, and scalable devices in future research.

The high internal surface area and rich functionality of MOFs are beneficial for capturing gaseous air pollutants. While incorporating MOFs in TENG, a dual-functional air filtration system can be designed to absorb outdoor particulate matter while monitoring air condition at the same time. For example, Fu *et al.* prepared a conductive cellulose aerogel/Ni-HITP composite for self-powered air filtration and real-time breath monitoring. Ni-HITP MOF with high surface area and amino functional groups provides a strong electron-donating effect which boosts the charge generating performance of prepared TENG devices, thereby providing more electrostatic charges on the surface of composite to facilitate capture of particulate matter with a diameter of $\leqslant 1.0$ μm ($PM_{0.1}$) [103]. Similarly, electrospun fibre of biodegradable polylactic acid (PLA) was combined with ZIF-8 nanoparticles to enhance the electrostatic adsorption property for air filtration applications by Zhu *et al*. [120]. The team prepared a self-charging air filter operated under airflow vibrations, demonstrating a high bacterial inhibition rate of 100% against Staphylococcus aureus. These studies open new avenues for MOF-TENG devices utilising the unique highly porous properties of MOF.

Other applications of MOF-based TENG have also evolved in more recent studies, such as anti-corrosion [76,94], catalytic degradation [95], and UV anti-counterfeiting system [137], where the introduction of MOF also plays a significant role in these applications. It can be expected that more advanced applications can be deployed by harnessing the multifunctional nature of MOFs.

3

Experimental Procedures and Methods

3.1 TENG test rig configurations

3.1.1 Contact-separation mode

A customised TENG test bench was designed and built to generate the mechanical loading required for contact-separation mode triboelectric measurements, as shown in Figure 3.1. The oscillatory impact was carried out by a Ling Dynamic Systems (LDS) model V201 electromagnetic shaker, powered by an arbitrary functional generator (Gwinstek AFG 2105) with a dual MOSFET driver to achieve its maximum capability. One of the two electrodes of TENG was attached to the head of the shaker, where the other electrode was attached to a sample holder in parallel to the first electrode to avoid misalignment between the contacting materials, with a <10 mm spacing. The force was measured by connecting the sample holder to a RS Pro stainless steel S beam tension cell (500 kg range) powered by a DC power supply PS-304 II. The electrical signal from the load cell was measured by the digital oscilloscope after being amplified by a signal amplifier (AD620). The load cell output was calibrated, resulting in the calibration curve shown in Figure 3.2.

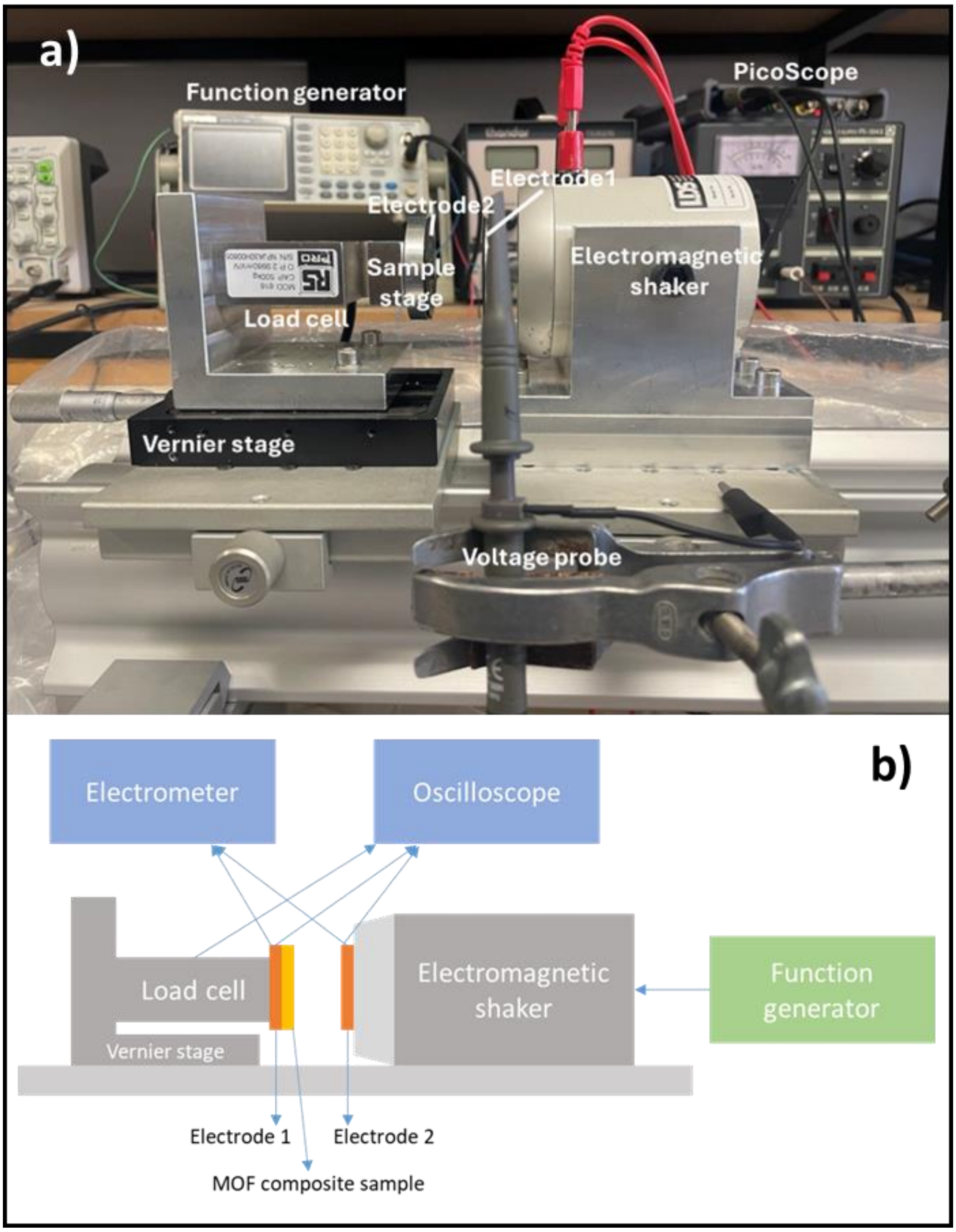

Figure 3.1. (a) Photograph and (b) schematic diagram of a customised test bench for contact-separation mode TENG electrical output performance tests.

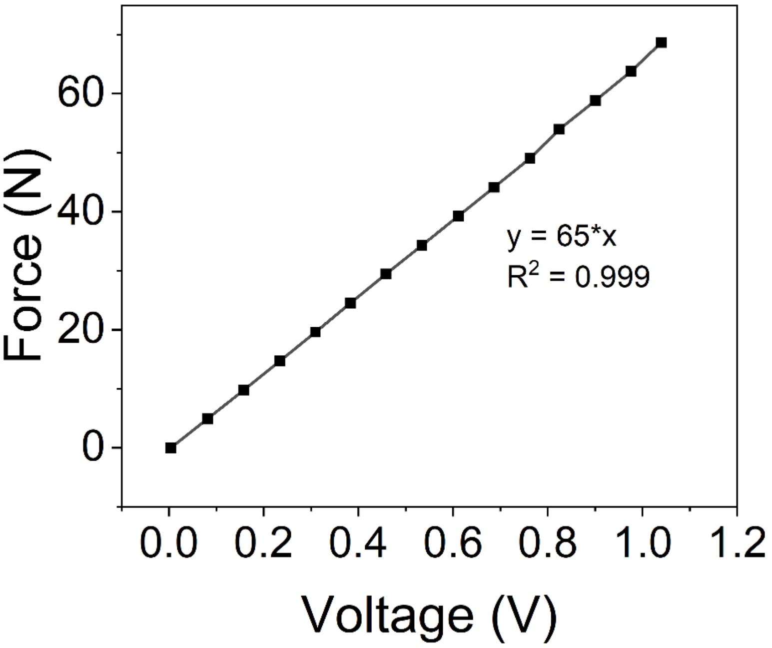

Figure 3.2. Calibration curve of RS Pro stainless steel S beam tension cell (500 kg range).

To ensure the robustness and consistency of the testing condition, all components, including the electromagnetic shaker, force sensor, and sample holder, were securely mounted on an optical rail (Newport). The space between the two electrodes can be finely controlled by a Vernier stage for replacing the sample and adjusting the displacement of the shaker. After assembling the cyclic impact system, the prepared TENG devices were tested by placing the as-fabricated materials onto one of the electrodes to study the electrical output at a range of impact forces and frequencies. Three key electrical properties were measured, including open-circuit voltage, closed-circuit current, and charge transfer.

3.1.2 Rotational free-standing mode

A rotational free-standing mode TENG was employed to expand the potential application of MOF-based TENG, as shown in Figure 3.3. This setup was built by a previous undergraduate research student in the group, Dylan Jubb, and subsequently modified by the author. The TENG comprises a stator unit and a rotor unit. The mounts for the rotor and stator components were 3D printed and attached separately on two carriages sitting on an optical rail (Newport). The stator comprised an inner and an outer interdigitated electrode arranged horizontally without contact, fabricated by an aluminium sheet to allow periodic switch of active material along the two electrodes while it rotates.

The rotor had a similar design to the inner electrode of the stator with 8 blades. It is driven by a motor powered by a DC voltage supply. A reflective tape was affixed to the shaft of the rotor to enable a tachometer to record the rotational frequency of the rotor. The rotational frequency of the rotor was controlled by the voltage supplied to the motor. To test the triboelectric output of a material, it is cut into the shape of rotor and adhered to the rotor. For testing under non-contacting free-standing mode, the rotor is subjected to prior triboelectrification by contacting with an aluminium sheet. The distance between the stator and rotor is controlled and recorded by the dial on the vernier stage supporting the stator.

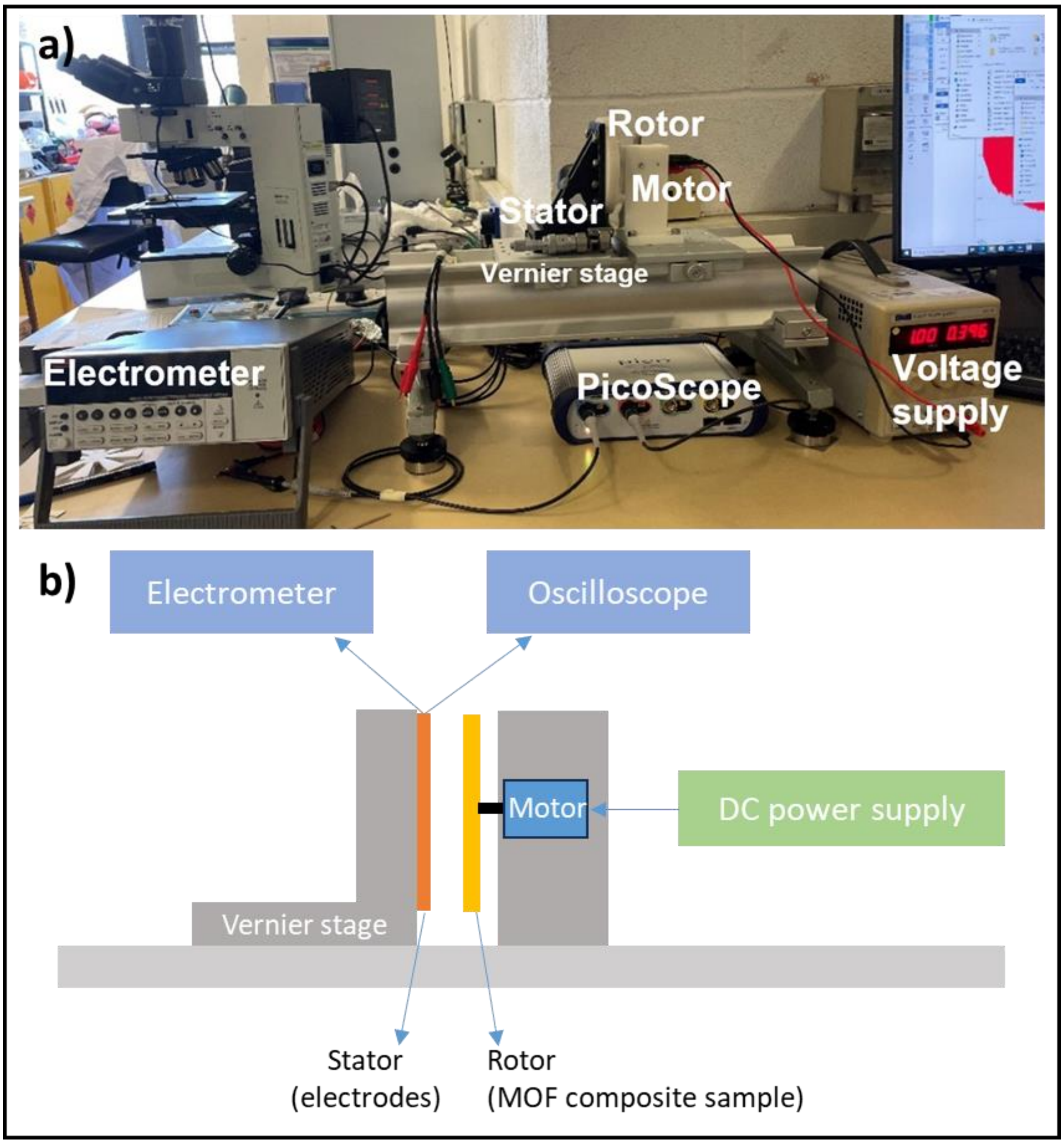

Figure 3.3. (a) Photograph and (b) schematic diagram of a customised test bench for free-standing mode TENG electrical output performance tests.

3.1.3 Energy harvesting performance test

To examine the triboelectric output performance, a digital oscilloscope (PicoScope 5444B) equipped with a 100 MΩ high voltage probe (Rigol RP1300H) was used to measure the voltage output on the PicoScope 7.1 software. An electrometer (Keithley 6517B) was used to measure current output and transferred charge. The measurements were recorded while the triboelectric output voltage was stabilised after 30 minutes.

For examining the maximum instantaneous power density, a series of resistors was used to build a closed circuit with TENG devices, ranging from 100 kΩ to 2 GΩ, while the output voltage was measured by connecting the oscilloscope in parallel with the load. The peak power density P_d under different resistance loadings was calculated by $P_d = V^2/(RA)$, where V is the measured voltage across the load resistor, R is the resistance of the resistor, and A is the area of TENG device.

For capacitor charging experiments, a rectifying circuit was used to convert the AC output from TENG into DC using a full bridge rectifier, with the circuit shown in Figure 3.4. The energy stored in capacitor E is calculated by $E = CV^2/2$, where C is the capacitance of the capacitor and V is the measured voltage across the capacitor.

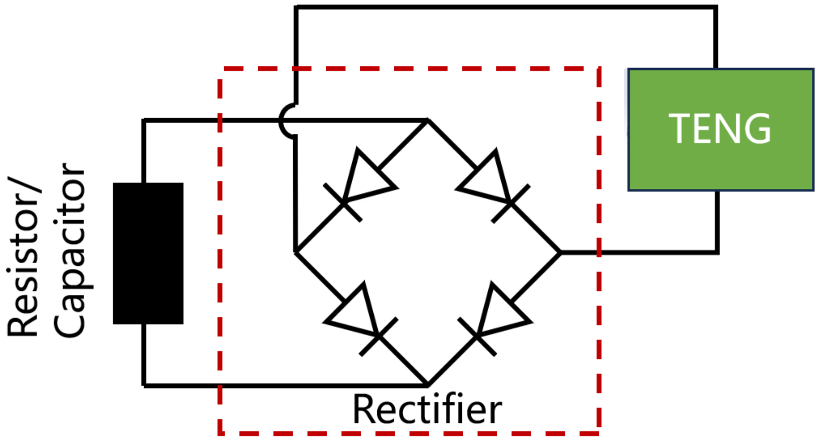

Figure 3.4. Full bridge rectifier circuit for energy harvesting.

To measure the triboelectric response of the TENG device under varying humidity, a transparent glove bag was used to enclose the entire test rig with a thermohydrometer sitting next to the sample to record the relative humidity (RH). The humidity was regulated by either purging dry nitrogen gas to reduce RH or by dosing humidified gas through a bubbler to increase RH.

3.2 Characterisation techniques

3.2.1 Scanning electron microscopy

Scanning electron microscopy (SEM) was used to visualise the surface microstructural morphology of prepared materials at high resolution. SEM operates by the emission of a beam of high-energy electrons from the electron source onto the specimen surface. The electron beam interacts with the specimen to produce a signal that contains information about the surface topography and texture of the material [138]. Two microscopes were used in this study, including a Hitachi TM3030Plus desktop scanning electron microscope and a LYRA$_3$ GM TESCAN field-emission scanning electron microscope (FESEM). For membrane and fibrous samples, Hitachi TM3030Plus was used under the secondary electron (SE) mode at 15 kV with a working distance of 6.5 mm. The morphological images were taken under 1000× to 5000× magnifications to generate an overview of the samples. For materials of smaller size requiring higher resolution, such as nanoparticles, the FESEM was employed at 10 keV with a working distance of 9 mm. The resolution can reach ~5 nm under optimised operating conditions.

During sample preparation stage, the specimens were mounted by carbon tape onto a cylindrical substrate with a diameter of 1.2 cm. To reduce the charging effect during SEM scans, the samples were sputter coated with Au/Pd using a sputter coater for 90 seconds.

3.2.2 X-ray diffraction

The crystalline structures of prepared nanoparticles and nanocomposites were characterised by X-ray diffraction (XRD) using a Rigaku MiniFlex diffractometer with a Cu Kα source (1.541 Å). From the information on peak position, peak intensity, and peak shape obtained from the XRD patterns, both qualitative and quantitative analysis of the crystal structure can be obtained [139]. During measurement, a step size of 0.01° in 2θ and a scan speed between 0.1°/min to 1°/min was used depending on the required level of resolution. The simulated XRD patterns were obtained from the Cambridge Crystallographic Data Centre (CCDC) database to compare with the experimentally determined pattern [140].

3.2.3 Attenuated total reflection Fourier-transform infrared spectroscopy

The attenuated total reflection Fourier-transform infrared spectroscopy (ATR-FTIR) was performed on a ThermoFisher Scientific Nicolet iS10 FTIR spectrometer equipped with an ATR module equipped with a diamond crystal. ATR-FTIR is a reliable technique to measure the vibrational modes of chemical compounds, MOFs, and polymers [141]. To obtain the molecular vibration information of the sample, an infrared beam was emitted onto a crystal with a high refractive index, and the incident beam was then modulated by an interferometer and interacted with the sample assembled on the crystal. This interaction is demodulated and Fourier transformed to obtain the FTIR spectrum [142]. The FTIR spectra in this study were obtained under the absorbance mode by taking the average of 64 scans with a resolution of *ca*. 0.4 cm^{-1} for a spectral range of 650 to 4000 cm^{-1}.

3.2.4 Synchrotron radiation infrared spectroscopy

The synchrotron radiation (SR) infrared spectroscopy was recorded at the multimode IR imaging and microspectroscopy (MIRIAM) Beamline B22 at the Diamond Light Source synchrotron. The mid-IR and far-IR spectra were recorded under vacuum by a Bruker Vertex 80v FTIR spectrometer equipped with an ATR accessory from Bruker Optics. Compared to conventional IR sources, SR FTIR has significantly higher brilliance and a broad range of wavelengths to overcome the low throughput of lab-based IR spectroscopy [143]. SR FTIR allows measurement in the terahertz region to obtain far infrared (far-IR) spectra under a wavenumber range below 700 cm^{-1}, and the signal was detected by a bolometer cooled by liquid helium. Measurements were conducted with a resolution of 4 cm^{-1} and an averaging of 256 scans to obtain high signal-to-noise ratio data. Post-measurement, the obtained data was processed using the OPUS 7.2 software to perform baseline correction, normalisation, peak fitting, and characteristic band analysis.

3.2.5 Atomic force microscopy

The surface topography of prepared specimens was characterised by atomic force microscopy (AFM) using a neaSNOM instrument (Neaspec GmbH). AFM operates by scanning a silicon cantilever under tapping mode over the surface of a sample. While tapping the surface at a small amplitude, the tip at the end of the cantilever will cause the cantilever to bend, deflecting the laser beam to the photodetector for the construction of a height topography map [144]. In this study, platinum-coated Arrow-NCPt probe with a tip radius of <25 nm and a resonance frequency of 285 kHz was used. The collected topographical data were analysed using Gwyddion 2.59 software [145].

To prepare the samples for AFM, the nanocrystals were first dispersed in a copious amount of methanol solution. The dilute dispersion was then drop cast on a cleaned silicon wafer. The wafer is then dried under vacuum at 60 °C for 2 hours to evaporate the solvent.

3.2.6 Fourier transform infrared nanospectroscopy (nano-FTIR)

The Fourier transform infrared nanospectroscopy (nano-FTIR) combines the chemical specificity of FTIR spectroscopy with the nanoscale resolution of AFM. By leveraging the near-field optical effect, a spatial resolution of < 20 nm can be achieved [146] at the tip of a platinum-coated AFM probe (Arrow-NCPt oscillating at 285 kHz). Unlike conventional FTIR, nano-FTIR focuses the incident IR light on the tip apex, creating a near-field interaction between the tip and the sample. The scattered IR light, carrying information about local vibrational properties, is then detected as an interferogram and demodulated at higher-order harmonics of the tip's tapping frequency to reduce background contributions. In this study, the nano-FTIR spectra of samples were determined using a scattering-type neaSNOM instrument (Neaspec GmbH) operating under the tapping-mode AFM equipped with mid-IR illumination optics. A broadband mid-IR beam was generated from a TOPTICA laser source to interact with samples to generate back-scattered near-field signals, which are then collected by a liquid-nitrogen-cooled mercury cadmium telluride (MCT) detector. For nano-FTIR absorption spectra, the collected signal was demodulated at the 2nd order harmonics to reduce the background effect. Each spectrum was obtained at a resolution of 8.3 to 14 cm^{-1}, an average of 12 individual measurements, and an integration time of 10.2 ms, using a silicon substrate as the reference spectrum. The collected interferogram and nano-FTIR spectra were processed and analysed using the neaPLOT software.

3.2.7 Tip force microscopy

Tip Force Microscopy (TFM) was carried out under the contact mode using the scattering-type neaSNOM instrument (Neaspec GmbH) equipped with Arrow-NCPt probes. As an extension of AFM technique, TFM enables the nanoscale characterisation of mechanical properties such as stiffness, adhesion, and elastic modulus [147,148]. The technique operates by bringing the silicon cantilever in contact with the sample surface while measuring the force exerted by the tip.

Prior to each measurement, calibration was conducted to ensure accurate quantification. The dimensionless stiffness value was first calibrated on a hard silicon substrate, which was assigned a reference value of 1. Then the Young's modulus calibration was performed using Brucker polystyrene (PS)/ low-density polyethylene (LDPE) sample to yield values of 2 GPa for the PS phase and 100 MPa for the LPDE matrix. The measurements were performed at a setpoint of 95%. The collected mechanical property data were analysed using Gwyddion 2.59 [145] software.

3.2.8 Kelvin probe force microscopy

The Kelvin probe force microscopy (KPFM) was carried out using the Asylum Research Cypher ES AFM equipped with the ASYELEC-01-R2 conductive probe coated with Ti and Ir. KPFM combines topographical imaging with nanoscale electrical characterisation, which measures the local surface potential and work function of sample surfaces compared to the contacting probe. During operation, an AC voltage is applied on the tip to induce oscillating electrostatic force between the tip and the sample surface.

During sample preparation, the bottom of the prepared sample is attached to the metal substrate by a conductive adhesive for better electrical contact. Moreover, the samples need to be stabilised overnight to prevent the accumulation of electrostatic charges prior to the experiment.

3.3 Materials synthesis and composite fabrication

3.3.1 ZIF synthesis

3.3.1.1 ZIF-71 family

ZIF-71 and ZIF-72 are MOFs with identical chemical compositions but distinct topologies. ZIF-71 was synthesised via a solvothermal method while ZIF-72 was prepared under a solvent-free and high-temperature condition to obtain the dense framework structure. The synthesis routes of ZIF-71 and ZIF-72 are as follows:

ZIF-71 (RHO): 2.4 mmol of zinc acetate ($Zn(OAc)_2{\cdot}2H_2O$) and 9.6 mmol of 4,5-dichloroimidazole (dcIm) were each dissolved in 15 mL of methanol. After 1 hour of sonication, the two solutions were combined at room temperature and stirred for 24 hours, forming a white suspension. The resulting product was then centrifuged at 8000 rpm for 10 minutes and washed three times with methanol to remove excess ligands. Finally, the purified ZIF-71 powder was obtained by drying at room temperature overnight.

ZIF-72 (LCS): 2 mmol of zinc oxide (ZnO) powder was physically mixed with 6 mmol of 4,5-dichloroimidazole (dcIm) in a 50 mL Schott bottle. The bottle was then sealed and heated at 150 °C for 24 hours of reaction. The resulting powder was washed with excess methanol to remove unreacted ligands, followed by centrifugation at 10,000 rpm for 10 minutes. After three washing cycles, the yellowish ZIF-72 powder was obtained by drying at room temperature overnight.

3.3.1.2 ZIF-8 family

ZIF-8 was functionalised with various electron-withdrawing groups for the study illustrated in Chapters 5 and 6. All synthesised ZIF-8-X demonstrate SOD topology with porous structure, despite the differences in the synthesis protocol:

ZIF-8-CH_3: 1.2 mmol of zinc nitrate ($Zn(NO_3)_2{\cdot}6H_2O$) was dissolved in 15 mL of dimethylformamide (DMF) and sonicated for 5 minutes. Then, 2.5 mmol of 2-methylimidazole (2-mIm) was added, and the solution was stirred for another 5 minutes to ensure complete dissolution. The mixture was then transferred to a 20 mL PTFE-lined stainless-steel autoclave and heated at 100 °C for 72 hours. After cooling to room temperature, the resulting white suspension was centrifuged and washed three times with methanol to remove excess linker and solvent. The purified ZIF-8-CH_3 powder was then collected and activated at 70 °C.

ZIF-8-Br: 0.4 mmol of zinc nitrate and 0.8 mmol of 2-bromo-1H-imidazole (2-Br-Im) were dissolved in 4 mL of ethanol. The solution was then transferred to a 20 mL PTFE-lined stainless-steel autoclave and heated at 100 °C for 72 h. After cooling, the resulting yellowish powder was collected by centrifugation, washed three times with ethanol, and dried at 70 °C overnight.

ZIF-8-Cl: 0.4 mmol of zinc nitrate and 0.8 mmol of 2-chloro-1H-imidazole (2-Cl-Im) were dissolved in 4 mL of ethanol. The synthesis and washing steps were identical to those used for ZIF-8-Br to obtain a yellowish powder of ZIF-8-Cl.

ZIF-8-CF_3: A mechanical grinding approach was utilised for the synthesis of ZIF-8-CF_3. 0.2 mmol of zinc carbonate basic ($Zn_5(CO_3)_2(OH)_6$) and 2 mmol of

2-trifluoromethyl-1H-imidazole (2-CF_3-Im) were physically mixed in a 20 mL glass vial. Then, 50 µL of DMF and three zirconium ball bearings were added to the solid mixture. The glass vial was placed on a vortex grinder under 1200 rpm for 60 minutes of reaction. The resulting mixture was washed with methanol and centrifuged three times to yield white ZIF-8-CF_3 powders.

3.3.2 Composite fabrication

3.3.2.1 Electrospinning of PVDF

Electrospinning technique was utilised to prepare porous PVDF-based composite fibres. The PVDF solution used for electrospinning was prepared by dissolving 13.7 wt% of HSV900 PVDF powder in DMF to form a polymer solution. The prepared MOF fillers were then combined with the PVDF solution via mechanical mixing. The homogenised solutions were stored in a glass syringe and gradually released by a syringe pump at a rate of 0.15 mL/h through a nozzle connected to a conductive blunt tip. During operation, the blunt tip was electrified at a voltage of 15 kV by a high-voltage generator, with an aluminum foil placed 16 cm underneath the nozzle, acting as the negative charge collector. The operating parameters were optimised to achieve a stable Taylor cone at the electrospinning nozzle. After 1 h of electrospinning, the electrospun fibres forming a porous membrane were then peeled off and dried.

3.3.2.2 Doctor blade

Doctor blade casting was utilised to prepare compact MOF/polymer composites. Polymer elastomer or solution was first mechanically mixed with MOF fillers. After being dispersed homogeneously by a motor-driven blender, the MOF/polymer mixture was dripped on a glass substrate and cast by a doctor blade with a defined gap size to obtain a film with uniform thickness. The cast film was heated for curation or evaporation of solvents. Then the films were peeled off from the glass substrate with the assistance of a scalpel.

3.3.2.3 PDMS surface functionalisation

The surface functionalisation of PDMS polymers was performed in collaboration with Prof. Adris Šutka from Riga Technical University. The prepared PDMS polymers were first treated with O_2 plasma for 5 min to develop hydroxyl groups on the surface. The polymers were then immersed in ethanol-based solutions of (3-aminopropyl)triethoxysilane (APTES), 3-(trimethoxysilyl)propyl methacrylate (TMSPMA), and vinyltrimethoxysilane (VTMS) at a concentration of 20 g L^{-1} for 1 hour. After the treatment, the samples were dried under ambient conditions for 30 minutes to obtain surface functionalised PDMS.

3.4 Simulations

3.4.1 Triboelectric performance simulation

To simulate the performance of triboelectric nanogenerators, a numerical model was developed using COMSOL Multiphysics with the Electrostatics Module. A two-dimensional (2D) model of the TENG structure was created, consisting of a triboelectric layer sandwiched between two conductive electrodes with predefined separation distances. The dimensions of the model were chosen based on experimental parameters to ensure realistic simulations. Then the dielectric layer was assigned the respective dielectric constants, surface charge densities, and mechanical properties. The electrodes were set as aluminium or copper metals to enable charge accumulation and transfer. The electrostatic potential distribution was computed using Gauss's Law, and the voltage output of TENG was modelled under open-circuit boundary conditions. The output parameters, including electrostatic potential, electric field distribution, and surface charge density, were extracted and analysed after computation. A parametric study was conducted to investigate the effects of key variables such as dielectric thickness and surface charge density on TENG performance.

3.4.2 Molecular simulations

Molecular Density Functional Theory (DFT) calculations on ligand molecules for ZIF-8-X in Chapter 5 and SAM molecules in Chapter 7 were performed using the Gaussian 09 software package [149]. The molecular structures were first geometrically optimised utilising the B3LYP functional combined with the 6-31G basis set [150,151]. The optimised structures were verified to be at a local minimum. Electrostatic potential maps (ESP) were then generated at the same level of theory to visualise the charge distribution across the molecules.

Periodic Density Functional Theory calculations on ZIF-8-CF_3 model in Chapter 6 were carried out in collaboration with Dr Lorenzo Donà from University of Turin. Calculations were performed with the CRYSTAL23 [152] code at PBEsol0-3c [153] level of theory. PBEsol0-3c is a composite method based on a hybrid Hartree–Fock/DFT Hamiltonian combined with a double-ζ quality basis set, augmented with a semiclassical dispersion term and a geometrical counterpoise correction. For the numerical integration of the exchange-correlation term, 75 radial points and 974 angular points (XLGRID) in a Lebedev scheme were adopted. The SCF convergence was set to 10^{-7} and 10^{-10} Hartrees during geometry optimisation and frequency calculation steps, respectively. The Pack-Monkhorst/Gilat shrinking factors for the diagonalisation of the Kohn-Sham matrix in reciprocal space were set to 2. The truncation criteria (TOLINTEG) for the bielectronic integrals (Coulomb and exchange series) were set to 7 7 7 7 25.

A full relaxation of both lattice parameters and atomic positions was performed. After geometry optimisation, vibrational frequencies at the Γ-point were computed using two-point numerical differentiation, and the CPHF/KS (Coupled-Perturbed Hartree-Fock/Kohn-Sham) approach was employed to calculate the infrared intensities. Subsequently, a Lorentzian peak broadening with a FWHM of 8 cm^{-1} was employed to simulate both the infrared and Raman spectra.

Electrostatic potential maps and the highest occupied and lowest unoccupied crystalline orbitals (HOCO and LUCO) were computed at the same level of theory to analyse the electronic structure of the investigated model system. Computed results were plotted using JMol [154].

4

Topological Effect on MOF/PDMS Composites as Tribo-negative Materials

4.1 Background and motivation

MOFs are promising candidates for triboelectric layers due to their unique combination of properties, including excellent mechanical stability, compatibility with polymer matrices, and customisable composition and surface functionality. Among these attributes, the topology of MOFs—a defining structural feature—is one of the critical factors influencing their chemical, physical, and mechanical properties. Specifically, the topology of a MOF determines the arrangement of metal ions and organic linkers, thereby directly affecting the material's porosity, density, and dielectric constant, which will impact the electrical output from a triboelectric nanogenerator.

While using identical constitutional linkers and metal nodes, different MOFs can be synthesised under different reaction conditions, resulting in structural isomers. These isomers share the same chemical formula and atomic ratios, yet differ in crystallographic arrangement [155]. The fundamental building units of MOFs are known as metal-organic polyhedra (MOPs), which exhibit diverse topological configurations depending on synthesis conditions. Even small variations in the reaction parameters will lead to distinct topological structures and properties [156,157]. Figure 4.1 demonstrates a variety of typical MOF topologies, showcasing the diversity of MOP geometries.

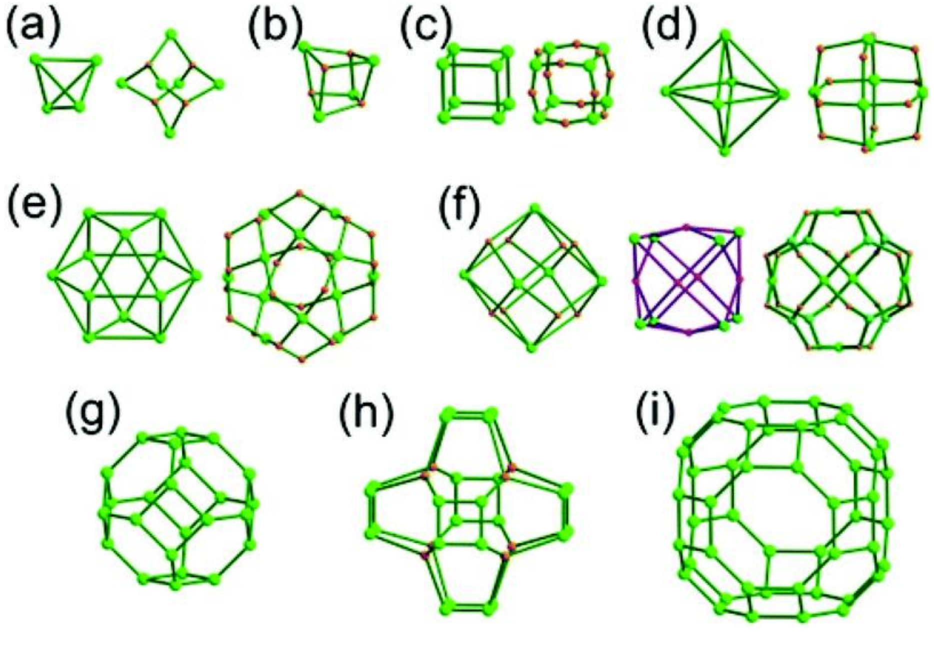

Figure 4.1. Topologies of MOPs. (a) Tetrahedral MOPs of a 3^4 face symbol and a 6^4 face symbol. (b) A heterocubic MOP of a 4^6 face symbol. (c) Cubic MOPs of a 4^6 face symbol and an 8^6 face symbol. (d) Octahedral MOPs of a 3^8 face symbol and a 6^8 face symbol. (e) Cuboctahedral MOPs of a $3^8 \cdot 4^6$ face symbol and a $6^8 \cdot 8^6$ face symbol. (f) Two rhombic dodecahedral MOPs of the same 4^{12} face symbol and the other rhombic dodecahedral MOP of an 8^{12} face symbol. (g) Truncated octahedral MOP (sodalite (SOD) cage) of a $4^6 \cdot 6^8$ face symbol. (h) Partially truncated rhombic dodecahedral MOP of a $4^6 \cdot 6^{12}$ face symbol. (i) Truncated cuboctahedral MOP (lta cage) of a $4^{12} \cdot 6^8 \cdot 8^6$ face symbol. Reproduced with permission from ref [156]. Copyright 2015 Royal Society of Chemistry.

The effect of MOF topology towards applications has been studied specifically in the field of adsorptive separation and gas storage [155,158-160]. The topology of a MOF can be regulated to optimise the pore structure and pore size for selective separation or capture of certain molecules. For example, Wang *et al.* reported a topologically guided design of Zirconium-based MOFs for selective separation of C6 alkane isomers. A MOF with FTW topology is capable of separating N-hexane with its branched isomers. Another MOF with SCU topology shows strong selectivity while separating mono- and di-branched C6 alkane isomers owing to the optimised pore aperture [161]. Moreover, Xue *et al.* further highlighted the effectiveness of topology control by developing two new MOFs with FTW topology through reticular chemistry. The prepared MOFs demonstrate remarkable performance in propylene/propane separation as a result of modulated rectangular pore apertures [162].

Despite the highlighted importance of MOF topology in separation, its effect on the triboelectric properties of MOF remains unexplored. The electrical performance of a triboelectric nanogenerator can be affected by multiple parameters, including hydrophobicity, dielectric constant, mechanical properties, and surface roughness. Modifying MOF topology inevitably alters these properties, potentially impacting triboelectric output. In 2018, Ryder *et al.* systematically investigated various MOF systems with different structural topologies, including IRMOF, UiO-66, MIL-140, and MOF-74 [163]. The findings revealed a strong correlation between porosity and dielectric constant, concluding that an interpenetrated MOF structure with small links exhibited enhanced dielectric responses. Another study utilising synchrotron-based infrared reflectivity experiments investigated the dielectric response of ZIF families [164]. Results demonstrated that the primary contributing factors to the dielectric constant are closely related to framework density driven by different topologies.

Moreover, the relationship between ZIF topology and mechanical properties was studied by Tan *et al.*, where the elastic modulus and hardness of ZIFs with five different network topologies were studied [165]. Their study established a structural-mechanical property relationship that the moduli scale nonlinearly with framework density, while the stiffness increases denser framework structure. These findings highlight the critical role of MOF topology in TENG applications, where dielectric properties influence triboelectric charge generation, and mechanical properties are essential for effective contact area during operation, along with long-term device stability.

However, current studies on MOF-based TENGs are predominantly limited to isolated materials, lacking comparative analyses across different MOFs. This has resulted in fragmented findings and an absence of universal design criteria for MOFs in TENG applications. Therefore, there is an urgent need for the comparison of various MOFs to devise a general guideline for a systematic design of MOF-based TENG. To close this knowledge gap, Paper I is the first study concerning the chemical and physical properties of two zeolitic MOFs with the same chemical composition but of significantly different topology and porosity. Moreover, nanoscale chemical and physical characterisations were applied for the in-depth analysis of topological effect on triboelectric output. This chapter aims to establish selection guidelines for MOFs in TENG devices, providing a foundation for future advancements in this field. Additionally, the study highlights potential applications of topologically modulated TENGs in diverse day-to-day scenarios, leveraging the flexible nature of these potential devices.

4.2 Summary of Paper I

4.2.1 Porous and non-porous MOF synthesis

Paper I introduces the fabrication of novel ZIF-71 and ZIF-72 based TENG devices to illustrate how modification of MOF topology influences triboelectric performance. During the material selection process, meticulous screening of potential MOFs has been conducted for TENG applications, considering factors such as ligand group electronegativity, mechanical and chemical stability, hydrophobicity, particle size, etc. The isostructural pair ZIF-71 and ZIF-72 was selected due to several reasons. Firstly, based on previous MOF-based TENG research, it has been found that ligands with highly electronegative groups can improve the triboelectric output as tribo-negative material. The chlorine atoms in ZIF-71 and ZIF-72 have their potential as charge-generating and trapping sites to facilitate electron transfer. In addition, ZIF-71 and ZIF-72, despite their identical chemical composition, are the two extremes of topologies, namely ZIF-71 with a highly porous RHO topology and ZIF-72 with a non-porous LCS topology. Furthermore, both MOFs exhibit good chemical and mechanical stabilities, which are critical for triboelectric applications requiring repetitive use and prolonged working lifetime. Although a few research have identified the formation of ZIF-72 through various methods, the chemical and mechanical behaviour of non-porous MOF (ZIF-72) is rarely studied. This study leverages ZIF-71 and ZIF-72 to evaluate their potential in TENG applications, providing insights into the relationship between MOF topology and triboelectric performance.

The topological structures of synthesised ZIF-71 and ZIF-72 were confirmed by comparison with the simulated X-ray diffraction patterns and FTIR absorption analysis, as described in detail in Paper I (Figure 2). Figure 4.2 demonstrates the FTIR spectra of synthesised ZIF-71 and ZIF-72 nanoparticles, both in their pristine form and embedded into PDMS matrices. The spectra of ZIF-71 and ZIF-72 exhibit similar vibrational bands on FTIR spectra, confirming their same chemical composition. Within the composites, the characteristic peak intensity of ZIFs increases along with higher loading percentages without shifting in vibrational frequency. This is clear evidence that these nanofillers are successfully incorporated into the matrix without chemical interaction.

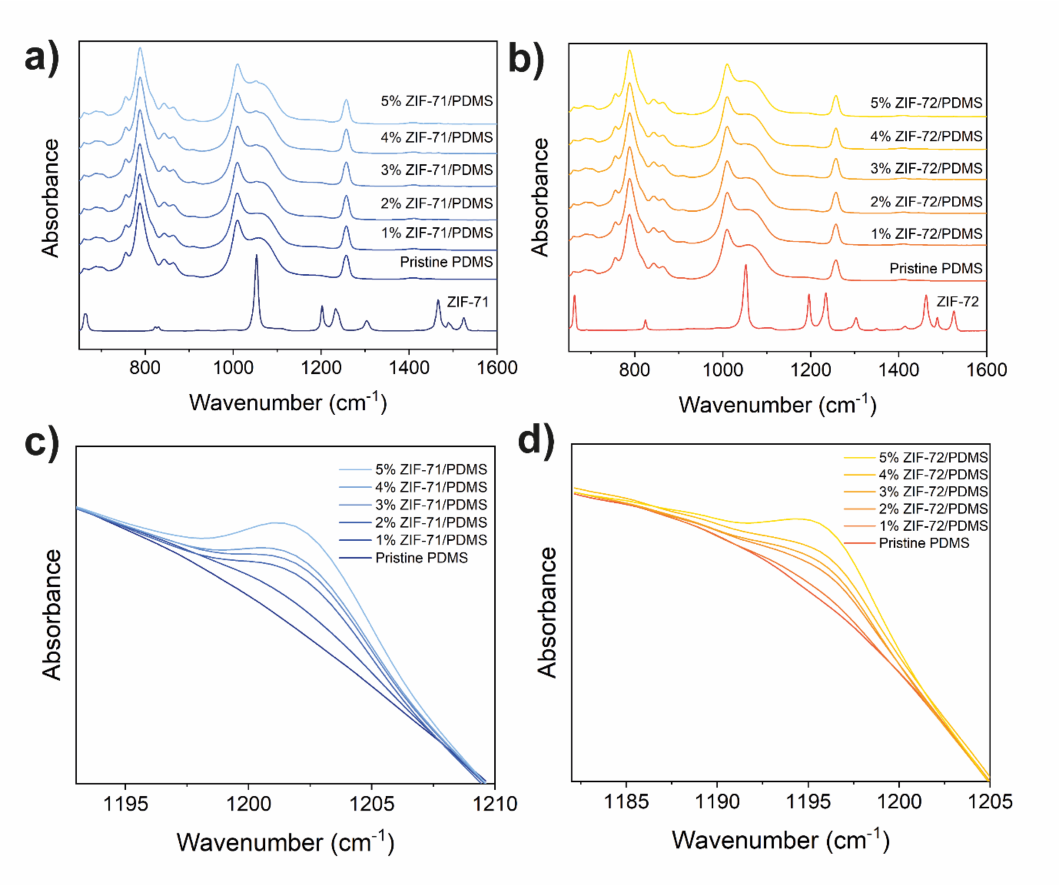

Figure 4.2. (a) FTIR spectra of ZIF-71 embedded PDMS films under different mass loadings (wt%), compared with the pristine ZIF-71 nanoparticles. (b) FTIR spectra of ZIF-72 embedded PDMS films under different mass loadings, compared with the pristine ZIF-72 nanoparticles. (c) Superimposed FTIR spectra of ZIF-71/PDMS composites between 1192 cm^{-1} and 1210 cm^{-1}. (d) FTIR spectra of ZIF-72/PDMS composites from 1182 cm^{-1} to 1205 cm^{-1}.

To examine the relative porosity of synthesised MOFs, Brunauer-Emmett-Teller (BET) analysis was conducted to measure the physical adsorption isotherms, with results shown in Figure 4.3. The BET result shows distinct porosity of the pair, with ZIF-71 having an exceptionally high BET surface area of 874 m^2/g, compared to 5.6 m^2/g for the non-porous ZIF-72. ZIF-71 exhibits a type I isotherm, with a rapid initial gas uptake at low relative pressure and no significant hysteresis loop, indicating micropore filling. On the other hand, ZIF-72 with type II isotherm demonstrates the non-porous nature with limited adsorption on the surface of the material.

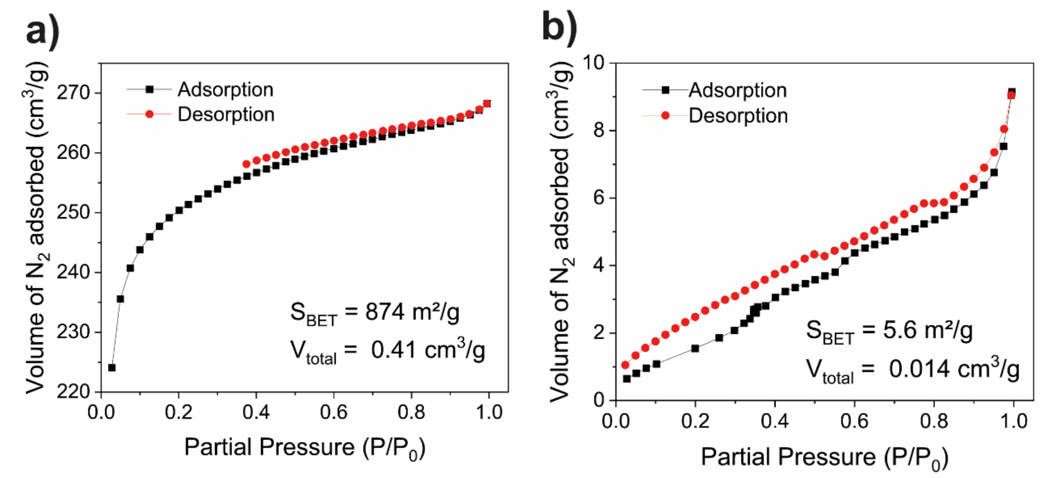

Figure 4.3. Nitrogen adsorption and desorption isotherms at 77 K for powder samples of (a) ZIF-71, and (b) ZIF-72.

The drastic difference in the porosity of ZIF-71 and ZIF-72 leads to changes in their dielectric constants. Due to the presence of air within the porous ZIF-71 framework, its dielectric constant is 3 at 1 MHz, while ZIF-72 shows a higher dielectric constant of 4.5. After encapsulation in PDMS matrix, both ZIF-71 and ZIF-72 exhibit an increase in the dielectric constant of composite, but ZIF-72/PDMS composite indicates a higher dielectric constant, which improved the dielectric constant of PDMS from 2 to 2.5, as shown in Figure 2e in Paper I. Since the dielectric property of a material has a significant effect on its triboelectric properties [12], the higher dielectric constant of the ZIF-72/PDMS composite enhances charge induction and storage within a TENG device.

4.2.2 Triboelectric performance of devices

The triboelectric performance of prepared ZIF-71 and ZIF-72 nanocomposites in actual devices was tested in Paper I (Figure 3). Figure 4.4 compares the open-circuit current and transferred charge from the ZIF-71 and ZIF-72-based TENGs under oscillatory motion testing under the same temperature and humidity conditions. Two independent sets of samples were prepared and tested on different dates to validate the reproducibility of the result. While some variation in the absolute output values of voltage and current was observed, the results exhibited consistent trends, indicating good repeatability of the measurement. It can be observed that both ZIF-71 and ZIF-72 improved the triboelectric output, with ZIF-72 almost tripling the current and charge output compared to the pristine PDMS. In addition, the prepared ZIF-72/PDMS TENG exhibits excellent sensitivity towards varying contacting forces, as shown in Figure 4.5. Both short-circuit current and transferred charge show improved output with increasing contact force. The voltage-force correlation shows a two-segmented response. In the low-force region, the devices maintained a high voltage with a strong voltage-force sensitivity of 63.4 V/N. While at higher forces, a lower sensitivity of 9.5 was observed due to the saturation of conformal contact between the composite and the electrode. Moreover, the prepared device exhibited remarkable durability, maintaining stable output over 50,000 cycles with fast response time, highlighting its great potential as a force sensor.

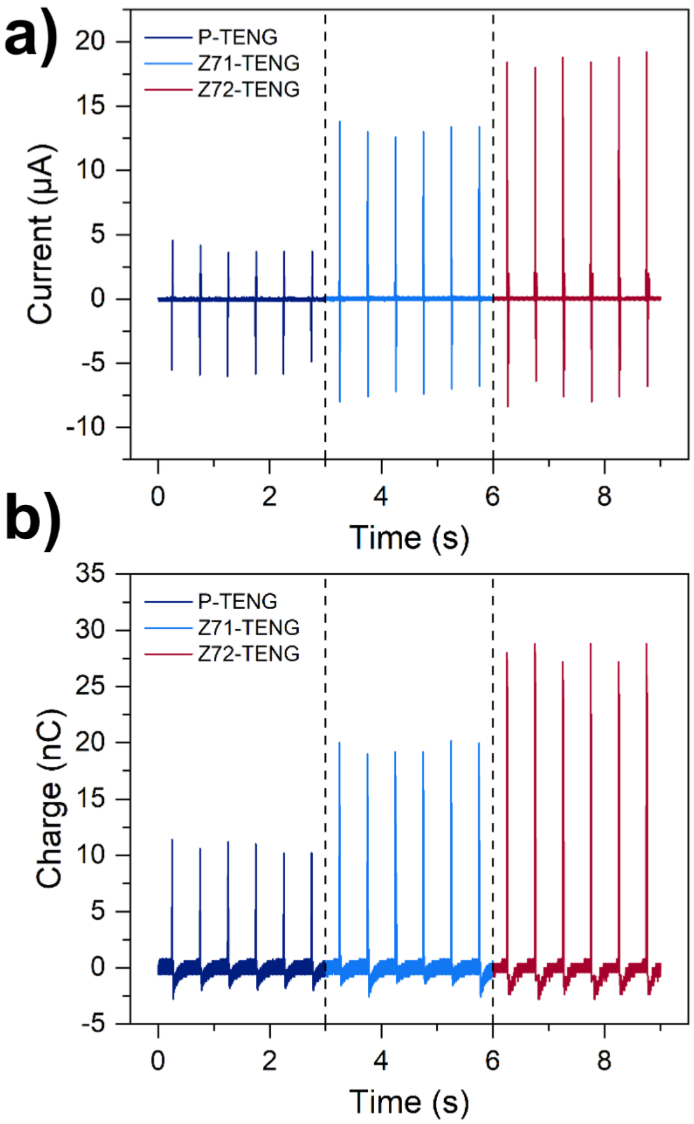

Figure 4.4. Comparison of (a) open-circuit current, and (b) transferred charge between ZIF-72/PDMS TENG (1 wt%), ZIF-71/PDMS TENG (2 wt%), and PDMS-based TENG under 2 Hz oscillatory motion with 16 N impact force.

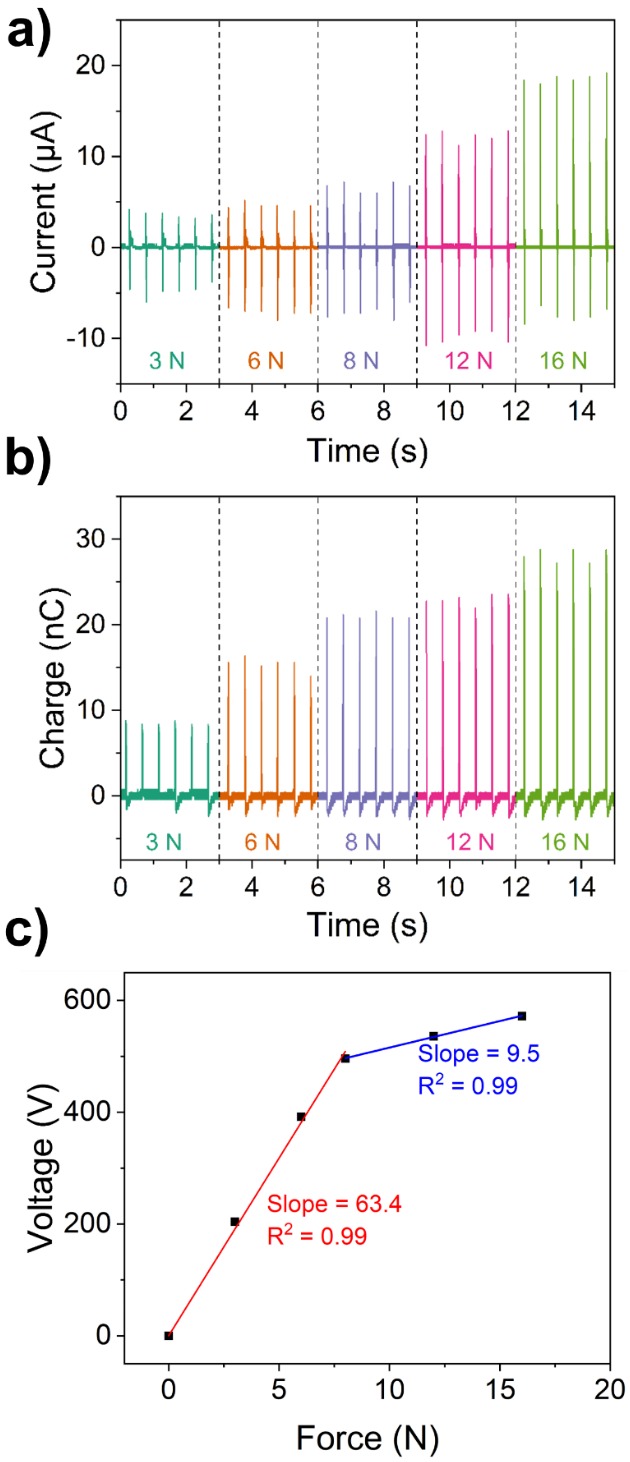

Figure 4.5. (a) Open-circuit current, and (b) transferred charge of ZIF-72/PDMS-TENG (1 wt%) at 2 Hz subject to a varying impact force. (c) Correlation between force and voltage for ZIF-72/PDMS TENG.

The superior electrical performance of prepared TENG arises from several factors. Firstly, the incorporation of MOFs, particularly the non-porous ZIF-72, improved the dielectric constant of the composite material from 2 to 2.5 at 1 MHz. As dielectric constant is fundamental to the charge generation of TENG, whereby a higher value of dielectric constant is considered an effective method to improve triboelectric output [166]. Secondly, surface chemical variation creates charge generating sites validated from nano-FTIR measurements in Paper I (Figure 4), facilitating surface charge transfer. The chlorinated chemical bonds on the composite surface improved the charge generating and trapping properties of the device by higher affinity to electrons and stronger charge retention. Thirdly, the incorporation of nanoparticles alters the local mechanical properties of the composite, as determined by TFM, as shown in Figure 4.6. Both the surface roughness and the effective contact area during charge generation have been greatly increased. Moreover, the measured Young's modulus and dimensionless stiffness were modified by the incorporation of nanoparticles, creating local heterogeneity in mechanical properties on the surface of the composite film. This heterogeneous stiffness can lead to non-uniform stress distribution and facilitate charge transfer [167]. Furthermore, the highest measured surface adhesion force from MOF-based TENG was significantly improved, increasing from 6.8 nN for pristine PDMS to 71 nN for ZIF-72 incorporated TENG. This improved adhesion leads to greater separation stress during the contact-separation process, further boosting the triboelectric output. It is important to acknowledge that the surface roughness effect of the prepared PDMS composites will also contribute to the difference in triboelectric performance. In the present study, the effect of surface roughness was considered negligible, as the incorporation of a relatively low concentration of fillers did not lead to significant changes in the surface morphology of the PDMS matrix. To summarize, the observed differences in output performance are primarily attributed to variations in dielectric properties and mechanical properties. Nonetheless, the potential contribution of morphological differences cannot be entirely excluded and may require further investigation in future studies.

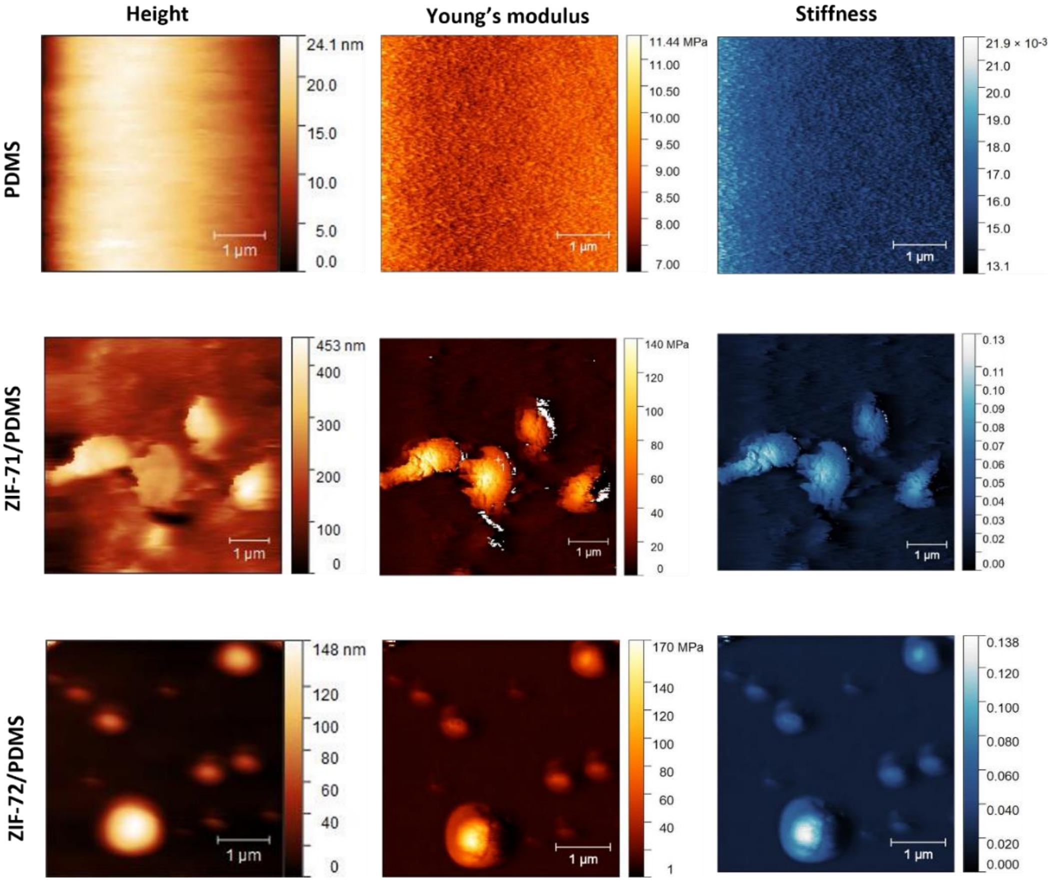

Figure 4.6. Nanoscale surface characterisation using TFM to determine the surface height topography, Young's modulus, and dimensionless stiffness of the neat PDMS, ZIF-71/PDMS, and ZIF-72/PDMS films.

4.2.3 Applications of MOF-TENG

The fabricated ZIF-72/PDMS TENG demonstrated its versatility in applications such as light-emitting diode (LED) illumination, microelectronics charging, remote body motion sensing, and Morse code generation, as illustrated in Paper I. Other than the above-mentioned applications, a prototype of a smart keyboard was also developed using ZIF-72/PDMS composites as the tribo-positive material. The keyboard keys were fabricated by sandwiching a ZIF-72/PDMS film between the two electrodes with a piece of sponge with 1 mm thickness as a spacer to ensure the recovery of TENG to its initial position after pressing. Four keys were prepared, named by different letters, including "A", "S", "E", and "T", as shown in Figure 4.7, which were used to constitute a number of words.

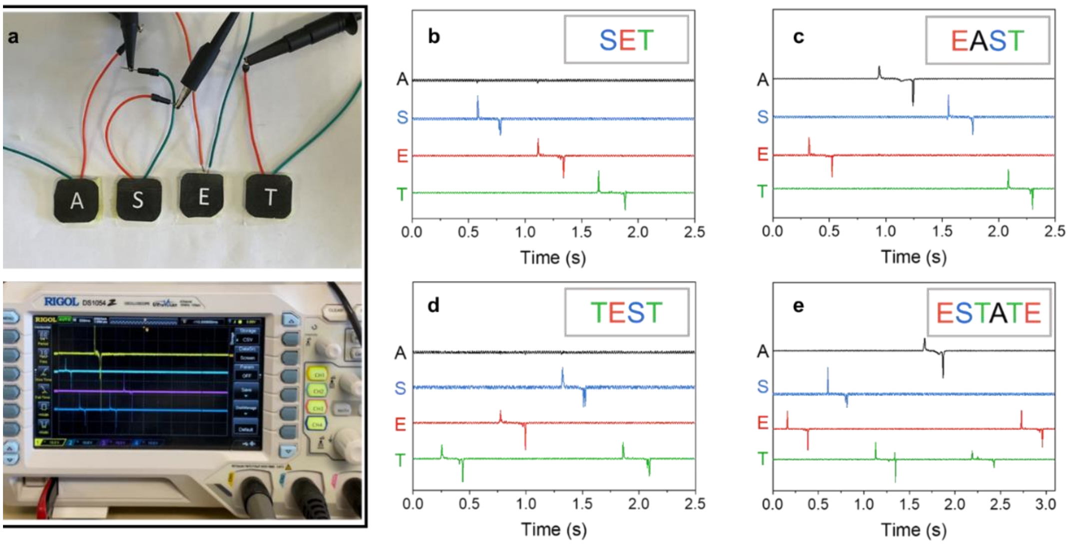

Figure 4.7. (a) Picture of a smart keyboard and the output electrical signal displayed on the four-channel oscilloscope. (b-e) Electrical signals collected by typing the corresponding words and translated based on the chronological order of the received signal.

Each of the keys had a contact area of 4 cm^2 using polyethylene terephthalate (PET) film as a substrate and was connected to an oscilloscope to collect the generated electrical signal. Here, the output of all four keys was recorded simultaneously by the four-channel oscilloscope shown in Figure 4.7a. When tapping on the keys, the corresponding channel will show a spike in output signal, representing a capturable voltage being generated. Despite the small contact area and low force when tapping the keys, the voltage output created by these small TENG devices can reach up to 20 V. To examine the performance of the keyboard, different words were typed on the keys to mimic the use of keyboard in real life, as shown in Figure 4.7b-e. By translating the output signal chronologically, words such as “set”, “east”, “test”, and “estate” can be attained. This prototype outlined the usage of MOF-TENG as a self-powered smart keyboard when fitting in all letters and controlling by a central processor. A communication module can also be implemented to transmit signals remotely.

4.3 Paper I: *High-Performance Triboelectric Nanogenerators Incorporating Chlorinated Zeolitic Imidazolate Frameworks with Topologically Tunable Dielectric and Surface Adhesion Properties*

Online version: https://doi.org/10.1016/j.nanoen.2023.108687

Nano Energy 114 (2023) 108687

Contents lists available at ScienceDirect

Nano Energy

journal homepage: www.elsevier.com/locate/nanoen

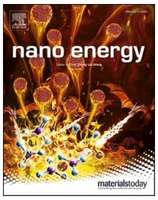

High-performance triboelectric nanogenerators incorporating chlorinated zeolitic imidazolate frameworks with topologically tunable dielectric and surface adhesion properties

Jiahao Ye, Jin-Chong Tan *

Multifunctional Materials & Composites (MMC) Laboratory, Department of Engineering Science, University of Oxford, Parks Road, Oxford OX1 3PJ, United Kingdom

ARTICLE INFO

Keywords:
Triboelectric nanogenerators
Metal-organic frameworks
Zeolitic imidazolate frameworks
Composite material
Energy harvesting

ABSTRACT

Triboelectric nanogenerator (TENG), a device that can convert mechanical energy into electricity based on the principle of triboelectrification, has gained tremendous attention since its first discovery in 2012. Although TENG has versatile applications in energy harvesting and self-powered sensing, its commercialization is still limited by the low power output. Recently, metal-organic frameworks (MOFs), with their large surface area and excellent tunability, have been explored to enhance the electrical performance of TENG. Herein, we synthesized nanoparticles of hydrophobic zeolitic imidazolate framework ZIF-71 (RHO topology) and its non-porous counterpart ZIF-72 (LCS topology), which were subsequently incorporated in a polydimethylsiloxane (PDMS) matrix as filler materials. By modifying the topology of ZIF nanofillers, we found the dielectric constant and surface adhesion of composites are both enhanced, thereby generating significantly higher triboelectric output. Moreover, we show the resultant ZIF/PDMS nanocomposite films exhibit enhanced triboelectric properties and long-term stability under cyclic mechanical loading. After integrating the prepared nanocomposite films into TENG devices, we accomplished the peak output voltage and current of 578 V and 19 μA for thin films (3×3 cm^2, thickness ~0.33 mm), respectively, by embedding 1 wt % of ZIF-72 nanoparticles into PDMS matrix, with an instantaneous maximum power density of ~5 W m^{-2}. In this study, the mechanism of improved TENG performance by incorporating MOF nanoparticles has, for the first time, been revealed through nanoscale-resolved mechanical and chemical studies. Furthermore, the practicality of MOF-based TENG was demonstrated by harvesting energy from oscillatory motions, for powering up commercial microelectronics, transmitting electrical signals remotely, and functioning as a self-powered Morse code generator.

1. Introduction

Triboelectric nanogenerator (TENG) is an evolving technology first proposed by the Wang group in 2012 [1]. As a simple and cost-effective energy generating device, TENG is capable of transforming mechanical motions into electric energy, which can be harvested for a variety of scenarios, including self-powered sensors [2–5] and energy harvesters [6,7]. These applications have essential roles in the development of emergent technologies such as the Internet of Things (IoT) [8], wearable electronics [9], and artificial intelligence (AI) [10]. Although the concept of TENG was first introduced in the 21st century, the triboelectric effect, a fundamental physical phenomenon, has been observed for thousands of years, and a number of research have investigated the theory behind it [11–13]. Currently, the selection of materials for triboelectric nanogenerators is commonly referred to the triboelectric series, ranked by the ability to attract or repel electrons through empirical results [14]. For the tribo-positive materials, metals like copper and aluminum are the conventional options attributed to their excellent electron-donating properties [15]. On the other hand, for tribo-negative materials, fluorinated polymers dominate the triboelectric series due to their high electronegativity and surface charge density [16]. Despite these materials having been present in the series for well over a decade, the practical applications of TENGs are still limited by the low power output. The challenge, therefore, is to develop new tribo-electric materials beyond the ones present on the conventional tribo-electric series with the aim for overcoming the current bottlenecks.

Through years of development, various strategies have been proposed to improve the electrical performance of TENG, including

---

* Corresponding author.
E-mail address: jin-chong.tan@eng.ox.ac.uk (J.-C. Tan).

https://doi.org/10.1016/j.nanoen.2023.108687
Received 14 April 2023; Received in revised form 26 June 2023; Accepted 9 July 2023

material surface modification [16]. incorporation of filler materials as charge traps [17], and amplification of material's dielectric constant [18]. Among all approaches, the addition of nanoparticles as a filler material into conventional triboelectric materials is considered as the most convenient and effective to improve the triboelectric properties of a material from all above aspects. A variety of materials have been studied to improve the operating performance and the robustness of TENG, such as perovskites [19], MXenes [20], graphenes [21], carbon nanotubes [22], etc. Recently, metal-organic framework (MOF) material has gained tremendous attention due to its organic-inorganic hybrid structure. MOF is a class of material fabricated by the self-assembly of metal ions and organic linkers with formation of well-structured nanopores and high surface areas. The high flexibility and tunability of MOF enable functionalization of its structure for different applications such as sensing [23], luminescence [24], catalysis [25], and gas adsorption [26]. Likewise, these excellent properties can be leveraged for improving the output performance of TENG by tuning the dielectric constants [27,28], improving the surface charge density or controlling the surface roughness. In 2019, Wen et al. first developed a humidity resistive TENG by incorporating HKUST-1 within the PDMS polymer matrix [29]. Due to the remarkable electron trapping capacity and high dielectric constant of HKUST-1, the power output of prepared TENG increased by 13 times compared to that of TENG without MOF. Moreover, Jayababu and Kim fabricated a bimetal organic framework (BMOF) containing both cobalt and zinc metal ions which showed an enhanced TENG power output [30]. Ascribed to the tunable sensing properties of MOF materials, the fabricated TENG was tested to be employed as an ammonia sensor with great selectivity and durability. Besides, Rana et al. carbonized ZIF-67 to form a cobalt-containing nanoporous carbon (Co-NPC) and used it as a filler material for the charge generating layer of a non-contact mode TENG [31]. A filler loading of 3 wt % in the Ecoflex matrix improved the power output by 2 times due to the high porosity and charge trapping capacity of MOF. Later in 2021, Wen et al. further reported the approach of using ZIF-8 as a filler in PDMS matrix [32]. The addition of ZIF-8 nanoparticles was reported to increase the TENG output up to 176 V and 16.3 μA, over 2 times higher than that without ZIF-8.

In this work, a chlorinated zeolitic imidazolate framework (a subclass of MOF), $Zn(4,5\text{-dichloroimidazole})_2$, commonly known as ZIF-71 with a RHO topology, is selected as the nanofiller for TENG applications. ZIF-71 has advantages such as ease of synthesis, moderate particle size, high resistance to humidity, and good compatibility with polymer matrices. Based on these excellent properties, we further modulated the topology of $Zn(4,5\text{-dichloroimidazole})_2$ to a non-porous form with an LCS topology, named ZIF-72. On the contrary, ZIF-72, due to its dense framework structure and unconventional synthesis condition, was rarely studied in literature, yet its unique properties such as higher dielectric constant (amongst MOF structures) and excellent environmental stability could be favorable for practical TENG applications. By incorporating an optimum quantity of the above-mentioned MOF nanoparticles into PDMS matrix, TENG devices with much enhanced electrical performance were fabricated. We herein report for the first time by taking the unique advantage of non-porous MOF materials for improved electrical performance of TENG. By comparing the output performance of TENG based on MOFs with the same composition but different topology, this work provides valuable insights into the judicious selection of MOF as triboelectric materials. Based on our findings, we propose that the high external surface area of MOF is more advantageous for TENG applications compared with its internal surface area, as a denser framework will improve the dielectric constant for a higher triboelectric output. The presence of chlorine atoms in the ligand of ZIF-71 and ZIF-72 induced high electronegativity, hence improving the charge generating capability of the prepared ZIF/PDMS composites. The high external surface of MOFs incorporated in polymer matrix created a larger effective contact area which behaves as charge traps to draw electrons deeper into the film, creating more opportunities for charge transfer.

The effects of physical properties such as porosity, dielectric constant, mechanical property, and surface adhesion on the output performance were revealed under various nano-microscopy techniques and analyzed to establish the general design criteria for the selection of MOF in TENG. As a result, the prepared TENG devices fabricated by ZIF-71/PDMS and ZIF-72/PDMS nanocomposites both showed improved electrical output performance compared with a neat polymer, with ZIF-72/PDMS TENG achieving a high open-circuit voltage and short-circuit current of 578 V and 19 μA, respectively, which are 2.8 times and 4.2 times higher than the pristine PDMS TENG. An instantaneous power density of 5 $W\,m^{-2}$ was achieved under an external load resistance of 20 MΩ. Additionally, a prototype for a pedometer that can transmit signals remotely via Bluetooth and a Morse code generator device were designed to demonstrate the future potential of using the ZIF-72/PDMS TENG as self-powered sensors.

2. Methods

2.1. Materials

All chemicals used in this work are commercially available. Zinc acetate ($Zn(OAc)_2{\cdot}2H_2O$), 4,5-dichloroimidazole (dcIm), zinc oxide (ZnO), and methanol were purchased from Sigma-Aldrich. Sylgard 184 (polydimethylsiloxane (PDMS) elastomer and curing agent) was obtained from Dow Corning.

2.2. Synthesis of MOF nanoparticles

(1) ZIF-71 nanoparticles were synthesized through a solution mixing method [33] performed under ambient conditions. 2.4 mmol of zinc acetate and 9.6 mmol of 4,5-dichloroimidazole were dissolved in 15 mL of methanol, respectively. After 1 h of homogenization, the two solutions were combined at ambient temperature and stirred for another 24 h to produce a white suspension product. The product was then centrifuged at 8000 rpm for 10 min and washed three times in methanol to remove excess ligands. After drying at room temperature overnight, the resulting ZIF-71 powder was obtained. (2) ZIF-72 nanoparticles were synthesized through a solvent-free, high-temperature method [34]. Initially, 2 mmol of zinc oxide powder was physically mixed with 6 mmol of 4,5-dichloroimidazole inside a 50 mL Schott bottle. Then the Schott bottle was capped and heated at 150 °C for 24 h. The as-synthesized powder product was then washed with excessive methanol to dissolve the unreacted ligands and then centrifuged at 10,000 rpm for 10 min. After three washing cycles, the yellowish ZIF-72 powder was dried overnight.

2.3. Preparation of ZIF/polymer nanocomposite

The ZIF/PDMS composite film was prepared by doctor blade casting. PDMS elastomer was first combined with the curing agent at a weight ratio of 10:1. The synthesized MOF particles (crystals of ZIF-71 and ZIF-72) were then added to the PDMS solution at different weight ratios of 0, 1, 2, 3, 4 and 5 wt %, respectively. After being dispersed homogeneously by a motor-driven blender overnight, the ZIF/polymer mixture was dripped on a glass substrate and casted by a doctor blade with a defined gap size to obtain a film with uniform thickness. The cast film was then cured at 100 °C for 30 min in a vacuum oven and peeled off from the substrate. The prepared ZIF/PDMS composites were cut into small pieces with a dimension of 3 cm × 3 cm for subsequent tests. The average thickness of the prepared nanocomposite films was determined to be ca. 330 ± 30 μm.

2.4. Fabrication of TENG devices

TENG devices were fabricated in the contact-separation mode. To ensure a flat contact surface, a pair of 3D-printed boards with a contact area of 3 cm × 3 cm was used as the substrate for fabricating a TENG device. The customized board was designed to have a uniform force distribution during oscillatory contact and maintain a low energy loss through jumper wires. A piece of aluminum (Al) foil was used as the negative electrode adhered to one of the boards by a double-sided adhesive. The prepared ZIF/PDMS nanocomposite film was then attached to the Al foil to form the tribo-negative layer. Another piece of Al foil was pasted on the other board to act as both the tribo-positive layer and the counter electrode. Three types of TENG devices were prepared by neat PDMS (P-TENG), ZIF-71/PDMS (Z71-TENG), and ZIF-72 PDMS (Z72-TENG). The periodic contact-separation movement of TENG was driven by a permanent magnet shaker (Brüel & Kjær LDS V201) powered by a voltage-amplified arbitrary function generator (GW Instek AFG-2105). In a standardized test, the operating parameters comprising frequency (2 Hz), maximum impact force (16 N), and amplitude of displacement (4 mm) for the magnetic shaker were applied. The optimum separation gap of 4 mm was selected to be a standard based on experimental results as it achieved the highest electrical output by balancing the effect of impact force and electrostatic potential between the TENG electrodes.

2.5. Materials characterization

The surface morphologies of the as-prepared MOF materials were characterized by a field-emission scanning electron microscope (FESEM LYRA$_3$ GM TESCAN). The crystalline structures of MOF and nanocomposites were analyzed by X-ray diffraction (XRD) using a Rigaku MiniFlex with a Cu Kα source (1.541 Å). The Brunauer-Emmett-Teller (BET) surface area of MOF was determined by the N2 physisorption measurements at 77 K (Autosorb iQ Station 2). The atomic force microscope (AFM) height topography and nano-FTIR spectra (at ~20 nm resolution [35]) of the nanoparticles and nanocomposites were determined from a scattering-type scanning nearfield optical microscope (Neaspec s-SNOM). A Nicolet iS10 FTIR spectrometer equipped with an attenuated total reflectance (ATR) module was used to record the Fourier-transform infrared (FTIR) spectrum. The far-IR spectroscopy was performed at the multimode IR imaging and microspectroscopy (MIRIAM) Beamline B22 at the Diamond Light Source synchrotron via a Bruker Vertex 80v FTIR spectrometer, equipped with an ATR accessory (Bruker Optics). The dielectric measurements were assessed by an LCR meter (Hioki IM3536) as a function of frequency sweeping from 4 Hz to 8 MHz. The output voltage was measured by an oscilloscope (Rigol DS1054Z) with a 100 MΩ high voltage probe (Rigol RP1300H). The output current and charge transfer of the device were measured by an electrometer (Keithley 6514) and a multifunctional impedance spectrometer (IviumStat.h).

2.6. Numerical modeling

The variation of electric potential was simulated using the finite element method (FEM) implemented in the COMSOL Multiphysics software. The simulation was performed by the electrostatics analysis model. The geometry of the simulated triboelectric nanogenerator device was created to match the dimensions of the actual experiment (an area of 3 cm × 3 cm for electrodes and composite material, with a maximum separation gap of 4 mm between the electrodes). Aluminum was selected as the material for the top and bottom electrodes, and the material properties of the ZIF/PDMS composite films were specified based on experimental measurements. The boundary conditions for the simulation were defined by employing the dielectric surface charge density measured on the composite surface and the electrode potential under open-circuit condition. Stationary studies were then performed with respect to the variation of displacement between the electrodes to predict the resultant electrical potentials across the triboelectric nanogenerator device.

3. Results and discussion

3.1. Composite films of ZIF/PDMS

ZIF-71 and ZIF-72 nanoparticles were constructed through the self-assembly of the Zn^{2+} cations and dcIm linkers, as illustrated in Fig. 1a. However, the variation of reaction conditions resulted in two distinctive framework topologies and physico-chemical properties. The SEM micrographs of the single nanoparticles of ZIF-71 and ZIF-72 are shown in Fig. 1b and c. Dissimilar crystal morphologies have been observed for ZIF-71 and ZIF-72. Specifically, ZIF-71 is a rhombic dodecahedron nanocrystal with well-defined facets, whereas ZIF-72 nanoparticles exhibit no specific morphology. Based on the AFM height topography shown in Fig. 1d-g, the lateral crystal size of ZIF-71 was found to be ~730 ± 130 nm with a height of ~250 ± 60 nm. In contrast, ZIF-72 has a relatively smaller particle size of ~150 ± 60 nm, and with a stronger tendency to form aggregates.

The FTIR spectra of prepared nanoparticles in both mid-IR and far-IR regions are shown in Fig. 2a and b, respectively. Due to the same constituting dcIm ligand and corresponding functional groups, ZIF-71 and ZIF-72 show similar vibrational modes. However, some minor differences are identifiable due to the difference in their coordination structure. The shifts of peaks are observed at 1466 cm^{-1} for N – CH bending, and 1202 cm^{-1} for CH bending. Some distinct peaks also exist for ZIF-72 at 1414 cm^{-1} and 1350 cm^{-1} which originate from the different topological arrangement of atoms within the framework structure. Within the far-IR region, similar results are identified with subtle differences detected in the terahertz (THz) collective modes due to the metal-ligand interactions. Moreover, by incorporating the ZIF-71 and ZIF-72 fillers into the PDMS matrix, there is no obvious band shifting observed from the FTIR spectra, which imply minimal chemical interactions between the fillers and the PDMS matrix, and thus no sign of decomposition of the MOF fillers. The superimposed FTIR result shows a clearer view of the relationship between the peak height at 1202 cm^{-1} and the amount of MOF loading (wt %), as shown in Fig. S1 of the Supplemental information (SI).

Fig. 2c shows the crystallinity of the as-synthesized ZIF-71 and ZIF-72 nanoparticles, characterized by powder XRD. Both diffraction patterns are consistent with the simulated pattern, indicating the successful fabrication of the MOF structures. It can be seen that ZIF-71 with an RHO topology shows Bragg peaks at 2θ angles of 4.4° and 7.6°, whereas ZIF-72 with an LCS topology exhibits salient peaks at 12.7° and 16.9°. Meanwhile, after the incorporation of MOF nanoparticles into PDMS matrix, the intensity of the main Bragg peaks increases with higher MOF loading which suggests a homogeneous dispersion of nanoparticles within the polymer matrix, and the crystallinity of ZIFs was retained, as shown in Fig. S2. The surface morphologies of the composite films of ZIF-71/PDMS and ZIF-72/PDMS are shown in Figs. S3 and S4.

3.2. Contact electrification and the effect of dielectric constant

Fig. 2d illustrates the structure of a conductor-to-dielectric contact-separation mode TENG, prepared using the ZIF/PDMS nanocomposites. The as-prepared composite film with a size of 3 cm × 3 cm was sandwiched between a pair of Al electrodes, the former acts as a tribo-negative layer for charge generation and charge storage. The working principle of a contact-separation mode TENG can be explained using the proposed electron transfer model [2,36]. At the initial stage (Fig. 2d(i)), the top electrode is not contacted with ZIF/PDMS nanocomposite film, and no charge transfer occurs between the electrodes. When the top electrode and ZIF/PDMS nanocomposite come into contact under the application of an external force (Fig. 2d(ii)), equal and opposite charges are induced on the contacting triboelectric surfaces due to tribo-electrification. The high electron affinity of the ZIF/PDMS nanocomposite attracts the electrons from the more electron-donating Al metal layer on its top. As a result, the nanocomposite layer becomes

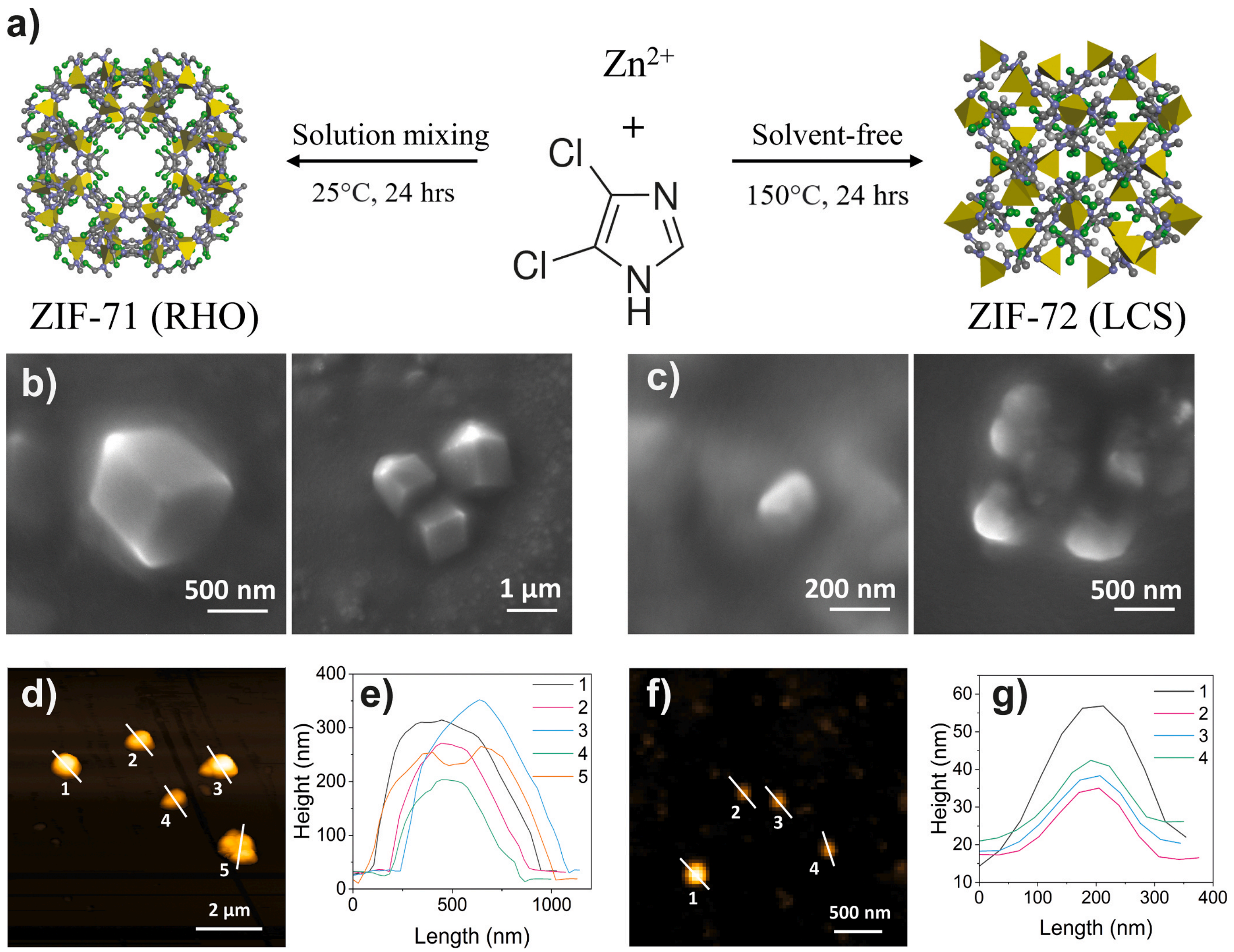

Fig. 1. (a) Schematics illustrating the synthesis routes of ZIF-71 (RHO topology) and ZIF-72 (LCS topology) nanoparticles (color scheme: ZnN_4 tetrahedron in yellow, nitrogen in purple, carbon in gray, hydrogen in white, and chlorine in green). (b) SEM micrographs of ZIF-71 nanocrystals. (c) SEM micrographs of ZIF-72 nanocrystals. (d,e) AFM height topography of ZIF-71 single crystals and the corresponding cross-sectional profiles. (f,g) AFM height topography of ZIF-72 single crystals and the corresponding cross-sectional profiles.

negatively charged, while the top metal electrode acquires a positive charge of equal magnitude. Subsequently, when the contacting force is released (Fig. 2d(iii)), the nanocomposite layer separates from the top electrode and a potential difference is induced, driving the electrons to flow from the bottom electrode to the top electrode through the external circuit. When the contact force is completely released and a fully separated state is reached (Fig. 2d(iv)), the electrons stop flowing. Subsequently, when the top metal electrode is brought into contact again (Fig. 2d(v)), it approaches the highly electronegative nanocomposite layer, causing the electrons to flow in the reverse direction. The flow of electrons stops when a fully contacted state is reached again (Fig. 2d(ii)). Through periodic contact and separation cycles, an alternating current (AC) output can be generated. For a conductor-to-dielectric contact-separation mode TENG, the potential difference between the triboelectric materials (ΔV) can be expressed as [37],

$$\Delta V = E_d d + E_{air} x(t) = -\frac{Q}{S\varepsilon_0}(d_0 + x(t)) + \frac{\sigma x(t)}{\varepsilon_0} \tag{1}$$

where E_d is the electrical field strength of dielectric material (in this case, the ZIF/PDMS nanocomposite), d is the thickness of the dielectric material, $x(t)$ is the distance between the plates as a function of time, and Q is the electrical charge transferred between the two electrodes. ε_0 and ε_d are the permittivity of vacuum and the relative permittivity of the dielectric material, respectively. d_0 represents the effective thickness constant ($d_0 = d/\varepsilon_d$), and σ is the surface charge density. Under open-circuit condition, where no electric charge is transferred between the two electrodes ($Q = 0$), the open-circuit voltage (V_{oc}) of TENG can be simplified as,

$$V_{oc} = \frac{\sigma x(t)}{\varepsilon_0} \tag{2}$$

From Eq. (2), it can be seen that the surface charge density of the dielectric material is a crucial parameter to determine the output voltage, and can be further expanded to [38],

$$\sigma = \frac{\varepsilon_0 \varepsilon_d V_{tri}}{d} \tag{3}$$

where V_{tri} is the triboelectric voltage that is dependent on the material itself. According to Eq. (3), the dielectric constant of material (ε_d) corresponds to one of the most important properties for TENG output. By modulating the topology of ZIF-71 to ZIF-72, the dielectric constant of the nanocrystal is improved from 3.0 to 4.5 at 1 MHz, as shown in Fig. 2e. The higher dielectric constant of ZIF-72 compared with ZIF-71 can be attributed to its non-porous structure. The porosity level was confirmed by N_2 adsorption–desorption isotherms at 77 K (Fig. S5),

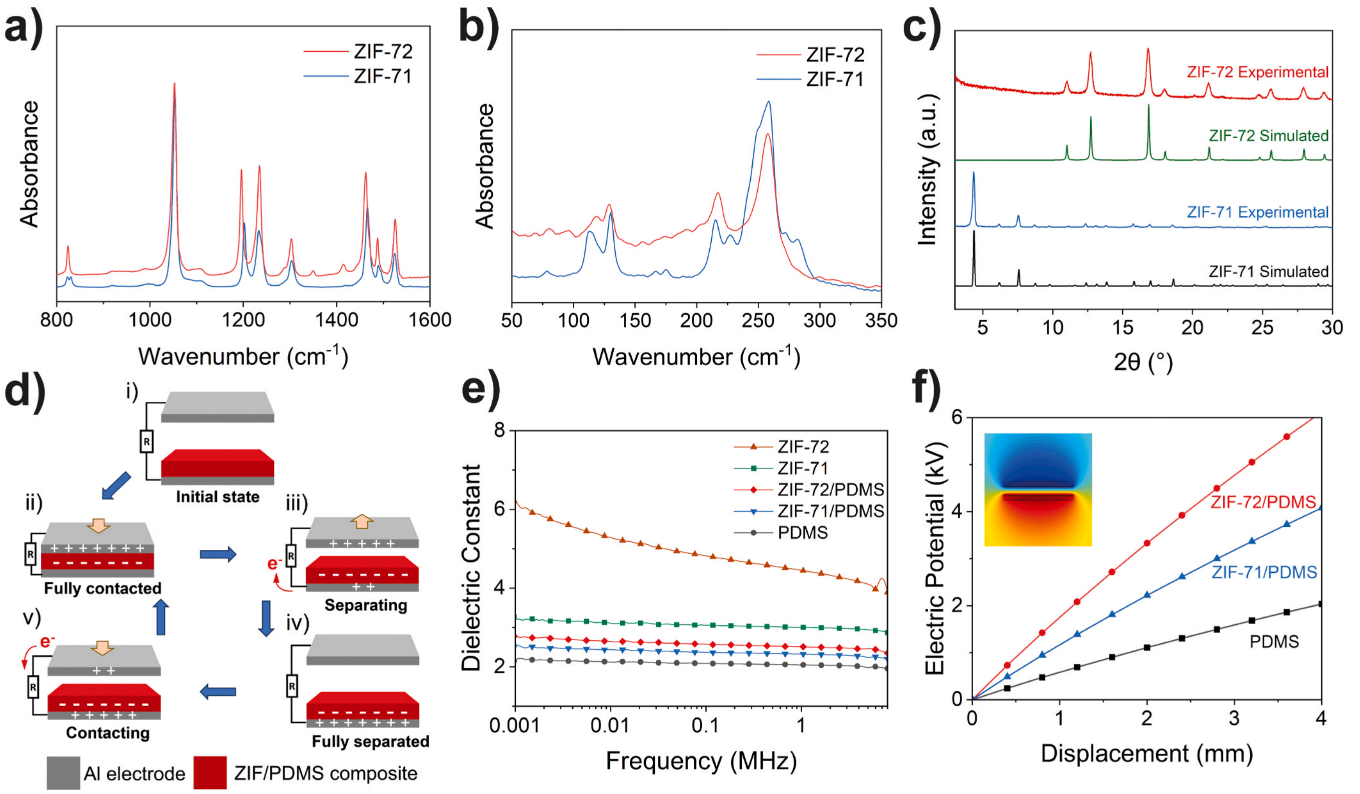

Fig. 2. FTIR spectra of the as-synthesized ZIF-71 (a) and ZIF-72 (b) nanoparticles in the mid-IR and far-IR regions, respectively. (c) XRD patterns of as-synthesized ZIF-71 and ZIF-72 nanoparticles compared with the simulated patterns (generated from crystallographic information file (CIF) in the Cambridge Structural Database (CCDC code: GITVIP and GIZJUV)). (d) Schematic diagram of the working mechanism (i-v) of a conductor-to-dielectric contact-separation mode TENG, based on ZIF/PDMS nanocomposite. (e) Dielectric constants of ZIF-72 pellet, ZIF-71 pellet, ZIF-72/PDMS (1 wt %), ZIF-71/PDMS (2 wt %), and pristine PDMS films, measured from 4 Hz to 8 MHz. (f) FEM predictions of electric potentials on the triboelectric material surfaces as a function of displacement between the pair of electrodes (as depicted in (d)).

where the BET surface areas of (porous) ZIF-71 and (dense) ZIF-72 were determined as 874 m^2/g and 5.6 m^2/g, respectively. Normally, a material with high volumetric density and highly polar molecular groups tends to have a higher dielectric constant [39]. Likewise, a porous MOF structure is known to exhibit a smaller value of dielectric constant due to the presence of air ($\varepsilon_d \sim 1$) in the pores [40,41]. Since ZIF-71 and ZIF-72 structures comprise the same dcIm linker with abundant and polar C−Cl bonds, the difference in their volumetric densities in consequence of their structural topology played a critical role to their dielectric constants. For ZIF-71, the existence of its nanopores hinders its polarizability and reduces the effective dielectric property. In contrast, the dense framework structure of ZIF-72 has a significantly lower porosity, thereby resulting in greater polarizability. The theoretical density of ZIF-72 determined from its crystal structure is 1.77 g cm^{-3}, whereas ZIF-71 has a relatively lower density of 1.15 g cm^{-3}. Therefore, the higher volumetric density of ZIF-72 leads to a larger dielectric constant. Fig. 2e also shows the measured dielectric properties of the pristine PDMS (neat), ZIF-71/PDMS and ZIF-72/PDMS thin films under a broad range of frequencies from 4 Hz to 8 MHz. With the incorporation of ZIF-71 nanoparticles into the neat PDMS (ε_d ~2.05), the dielectric constant was found to be improved, with the highest dielectric constant of 2.3 achieved at 2 wt % of ZIF-71 at a frequency of 1 MHz. On the other hand, incorporation of ZIF-72 further improved the dielectric constant up to 2.5 under a filler loading of 1 wt %. Both MOFs were found to improve the dielectric constants of the PDMS film with a similar trend. This increment of dielectric constant can be explained by the formation of micro-capacitors as MOF nanoparticles are incorporated into the polymer matrix. The nanoscale capacitor networks increase the polarizability of the MOF-based nanocomposite material, and as a result they enhance the dielectric properties. However, as the MOF loading increases beyond a threshold value (see Fig. S6) a decline in dielectric constant was observed, this could be attributed to the adverse effect of filler aggregation.

An FEM simulation was also performed using the COMSOL software to model the electric potential generated between the two electrodes of a TENG device, as shown in Fig. 2f. Experimental measurements of dielectric constant (at 1 MHz) and surface charge for different materials were applied as inputs for the FE simulation. The general trend of electrical potential during operation is inline with the proposed working principle, which increases with a larger separation distance between the pair of electrodes. ZIF-72/PDMS composite with higher dielectric constant also shows a much higher electrical potential compared with ZIF-71/PDMS and neat PDMS polymer, indicating the important role of dielectric constant. We note the overpredictions in the magnitude of the output voltages, which can be ascribed to the idealized model and lossless boundary conditions imposed in the model, compared with real materials with imperfections as observed in the experiments.

3.3. *Output performance of ZIF/PDMS TENGs*

The output performance of the assembled MOF-TENG was measured on a customized test bench to study the effect of nanoparticle embedment. The open-circuit voltage, closed-circuit current, and charge transfer between the electrodes of TENG were measured for both Z71-TENGs and Z72-TENGs at different wt % loadings. Fig. S7 shows the experimental setup for the electrical output performance of TENGs and the dimensions of the fabricated nanocomposite films. Fig. 3a and b show the relationship between the filler loading in polymer matrix and the electrical performance of the device. For Z71-TENG, it was established that a 2 wt % composite exhibits the most outstanding electrical

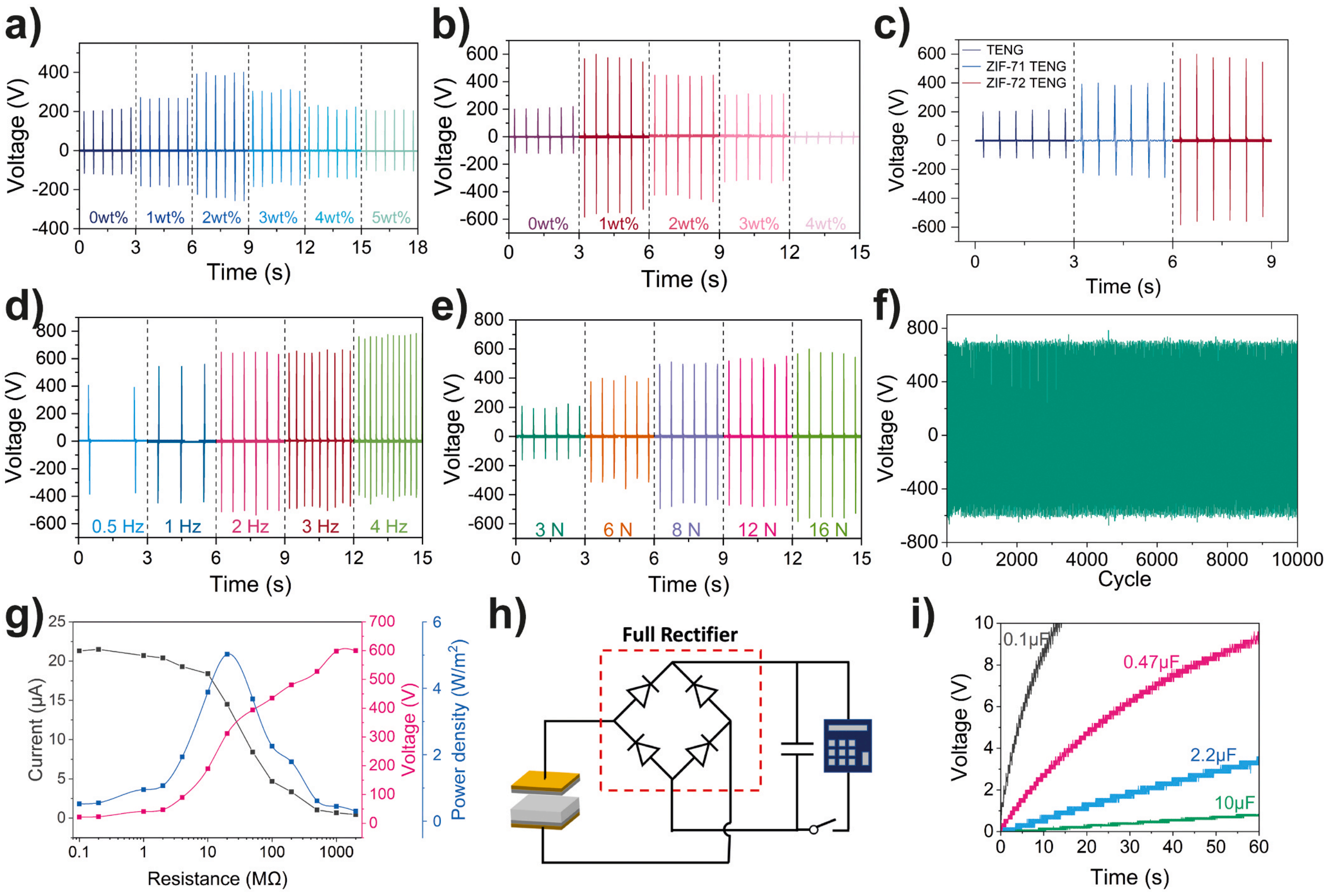

Fig. 3. (a) Open-circuit voltage of Z71-TENG at different mass loadings (wt %) under an oscillatory motion of 2 Hz. (b) Open-circuit voltage of Z72-TENG at different mass loadings under an oscillatory motion of 2 Hz. (c) Comparison of electrical output performance between Z72-TENG (1 wt %), Z71-TENG (2 wt %), and P-TENG under 2 Hz oscillatory motion with 16 N impact force. (d) Electrical output performance of Z72-TENG at 16 N under different frequencies. (e) Electrical output performance of Z72-TENG at 2 Hz with varying impact forces. (f) Durability test of the Z72-TENG subject to a continuous test of 10,000 impact cycles. (g) Peak voltage, current, and power density of Z72-TENG as a function of load resistance. (h) Schematic of an electrical circuit designed for the practical application studies of Z72-TENG. (i) Capacitor charging curves by operating Z72-TENG at 2 Hz for 0.1, 0.47, 2.2, and 10 μF capacitors.

performance with nearly doubled improvement of all electrical properties compared with the neat PDMS film, as shown in Fig. S8. Besides, the Z72-TENGs show a similar trend to Z71-TENGs, with the highest power output observed for the 1 wt % composite film. A remarkably high electrical output was obtained with an open-circuit voltage of 578 V, a peak-to-peak voltage of over 1139 V and a closed-circuit current of 19 μA, over 4 times higher than the neat PDMS film under identical test conditions. It is also worth noting that a reduction of output power was observed at higher MOF loadings. Such a decline can be attributed to the aggregation of nanoparticles at a higher mass concentration within the polymer matrix, which can also be observed in the SEM micrographs (see Fig. S3).

To have a closer look at the effect of embedding MOF nanoparticles into the matrix of a triboelectric composite material, the films of the highest electrical output were selected and compared with the pristine PDMS film, as shown in Figs. 3c and S10. The incorporation of MOFs shows a significant improvement in terms of the charge generating and charge trapping capacities of MOF nanoparticles. The presence of chlorine atoms in the ligand of ZIF-71 and ZIF-72 induces high electronegativity [42], hence improving the charge generating capability of the composite films. Moreover, more trapping sites are created by the uniform distribution of nanoparticles within the polymer matrix which can facilitate the charge transfer and charge storage within the composite. These trapping sites also hinder the charge recombination effect at the material surface during contact electrification, whereby drawing more charges to the inner structure of the material. On this basis, it can be reasoned that more induced charges can be collected at the chlorinated groups of ZIF-71 and ZIF-72 nanofillers, thereby enhancing the overall charge density of the material.

In addition to the study on the effect of mass loading, the frequency dependency of the electrical performance was also investigated under a range of frequencies from 0.5 Hz to 4 Hz generated by the magnetic shaker. Results in Fig. 3d reveal that the output voltage of the Z72-TENG showed an increasing trend with rising input frequency of the impactor. With an increase in the operating frequency, an unsymmetric voltage profile was observed due to the varying strain rates of the magnetic shaker [43]. We hypothesize that the higher frequency results in a faster contact speed, leading to a higher positive voltage. Meanwhile, the insufficient displacement during separation causes a lower absolute value of the negative voltage.

Moreover, the influence of the applied force on the output performance was investigated under varying forces from 3 N to 16 N at a 2 Hz input frequency. The force of the impact was controlled by the voltage supplied to the magnetic shaker and measured by a calibrated force transducer. Fig. 3e and Fig. S12 show the correlations between the impact force and output voltage, current, and charge. Specifically for the output voltage, a linear correlation can be found at the lower-force region (0–10 N), where the TENG device exhibits a higher sensitivity of 63.4 V/N with good linearity. Therefore, there is scope for deploying the Z72-TENG as a self-powered force sensor, and it is worthwhile to investigate this avenue in future. The durability of the Z72-TENG device was also tested, since a long working time and stable power output is crucial for practical implementations. To verify its robustness, the variation of its voltage output over continuous operation of 10,000 cycles under 2 Hz was recorded and shown in Fig. 3f. Moreover, the durability of prepared Z72-TENG and Z71-TENG over 50,000 cycles was tested under 5 Hz as shown in Fig. S14. At a longer run of 50,000 cycles, a relatively stable voltage was delivered throughout the cyclic tests, with an overall degradation of 10.6 % in peak voltage observed for Z72-TENG. During the cyclic impact, the prepared ZIF-72/PDMS nanocomposite showed good structural resilience and excellent attachment to the metal electrode. There was no significant change on the morphology of contacting surfaces, and structural integrity of electrode and nanocomposite was well-retained, as shown in Fig. S16.

The fabricated MOF-TENG devices were then connected into a closed circuit with varying load resistances, to examine the optimum operating conditions and to validate the practicability for real-world applications. Under a constant input frequency of 2 Hz and a compression load of 16 N, the closed-circuit voltage (V_{sc}) and closed-circuit current (I_{sc}) across the load resistor were measured, with power density P_d calculated using the equation $P_d = (V_{sc}I_{sc})/A$, where A is the nominal contact area. As shown in Fig. 3g, the Z72-TENG achieved a maximum power output of 5 W m^{-2} employing a load resistance of 20 MΩ, with measured voltage and current showing an inverse relationship due to ohmic loss. Notably, the optimum operating resistance of Z72-TENG is lower than pure PDMS-based TENG reported in other studies [44] due to the improved capacitance from the addition of ZIF-72. This optimum resistance corresponds to the internal resistance of the generator, where a low impedance can lead to a broader application in real life [45]. Furthermore, the improvement achieved in voltage, current, and output power density by Z72-TENG is compared with other reported works of PDMS-based TENG, as summarized in Table S1. For instance, in comparison to the study conducted by Guo *et. al* [46], where a fluorinated MOF, KAUST-8 was incorporated in PDMS as triboelectric material, although a similar maximum voltage was achieved, our Z72-TENG exhibited an order of magnitude higher current output and power density. Previous studies have also explored other MOF@PDMS composite materials, including ZIF-8 [32], UiO-66 [47], and its derivatives [48], and our Z72-TENG demonstrates 3.3, 2.8 and 3.0 times higher peak voltage output compared with these studies respectively. Although the experimental setup in each study is different in frequency, force, and exact configuration, broadly it can be seen that the electrical performance of Z72-TENG prepared in this study are positioned among the highest-performing works in the field.

3.4. *Charging and discharging of portable commercial electronics and LEDs*

To verify the effectiveness of TENG as an energy harvester, the alternating current produced by TENG was harvested and stored into capacitors through a full rectifier circuit, shown in Fig. 3h. After induced charges passing through the rectifying circuit, the alternating current was converted to direct current by a network of diodes, therefore reducing the energy loss during the charging process. The rectified current can be subsequently used to charge up capacitors and other small consumer electronics. As shown in Fig. 3i, several commercial capacitors with capacitances ranging from 0.1 μF to 10 μF were charged by a steady 2 Hz oscillation motion and 16 N compression load. A reasonably high charging voltage can be attained for all capacitors after a relatively short time of ~1 min, with less charging time required for smaller capacitors. More specifically, the result shows a charge voltage of 10 V for a 0.1 μF capacitor within 15 s, which suggests the feasibility to redistribute the stored electricity to other electronics. The difference in the charging speed to a 2.2 μF capacitor by Z72-TENG, Z71-TENG, and P-TENG is compared in Fig. S17. The prepared Z72-TENG shows significantly higher energy harvesting rate under the same testing conditions. For verification, a 47 μF capacitor was first charged to 3 V by the Z72-TENG and subsequently used to power up microelectronics, including a humidity thermometer, a digital timer, a calculator, and an array of LEDs. The charge-discharge curves for the different electronics are displayed in Fig. S18. Video S1 shows the charging of a commercial calculator. As the selected electronics have distinct operating voltage and power consumption rates, the operational time for each electronic was also recorded. We found that the charged capacitor can successfully power up all these electronics, with the calculator having the longest standby time among the four, where the number displayed on its screen remained visible after 30 s of operation. The illumination of 300 LEDs powered by the Z72-TENG was also demonstrated in Fig. S19 and Video S2.

Supplementary material related to this article can be found online at doi:10.1016/j.nanoen.2023.108687.

3.5. *Probing triboelectrification mechanism of ZIF/PDMS composites via nanoanalytics*

To further investigate the fundamental triboelectrification mechanism of ZIF/PDMS composites, we employed the near-field s-SNOM technique in combination with nano-FTIR and tip-force microscopy (TFM) technique to reveal the local chemical and mechanical information at a resolution of 20 nm. The nano-FTIR spectra of ZIF-71 and ZIF-72 single crystals shown in Fig. 4a-c are consistent with ATR-FTIR results (Fig. 2a), with the main characteristic peak at around 1050 cm^{-1} corresponding to the in-plane deformation of the imidazole ring [49]. After incorporating ZIF-72 nanoparticles into PDMS matrix, this main peak of nanofillers remains detectable from nano-FTIR taken across the composite, as shown in Fig. 4d-e. Although the characteristic peaks for PDMS at 1100 cm^{-1} and 1263 cm^{-1} still dominate at sampling points 1 and 3 as ZIF-72 particles are partially buried beneath the cross-linking of PDMS matrix, these nanoparticles are close enough to the material surface to alter the properties of the interface. Consequently, we propose that this nanoscale compositional variation at the near surface layer will lead to formation of charge traps by dissimilar functional groups with enhanced electron affinity, thereby generating higher triboelectric output.

The nanoscale mechanical properties at the composite surfaces were further investigated by TFM. As shown in Fig. 4f-i, the ZIF-71 and ZIF-72 nanoparticles present at the surface significantly have improved the surface adhesion of PDMS matrix to an order of magnitude higher. Previous research has found close relationship between adhesion energy and triboelectric output [43,50]. The nanostructure of ZIF-72 with high adhesion energy on PDMS surface improves the stress of contact and separation. As a result, the higher stress facilitates the energy conversion towards triboelectric energy and improves the amount of surface charge transfer [51]. The effect of adhesion force on the triboelectric output can also be revealed through the output voltage profile of TENG devices. As shown in Fig. 3b, Z72-TENG shows higher output voltage during separation with a more negative peak value compare with P-TENG. This finding can be explained by the higher acceleration during material detachment due to the greater adhesion force of ZIF-72/PDMS. The high separation acceleration resulted in strong electrostatic potential, thus more charge can be transferred. In addition, from the AFM height topography images shown in Fig. S20, the surface roughness of the composite material appeared to have increased at the nanoscale after the incorporation of ZIF-72 nanoparticles, thereby increasing the effective contact area during triboelectric charge transfer. Taken together, we conclude that such nanomechanical effects observed from nano-resolved investigations combined to result in the excellent triboelectrification property of ZIF-72/PDMS composites.

3.6. *Further prototypes of Z72-TENG devices*

Example real-world applications of prepared Z72-TENG devices were designed and tested outside a laboratory setting. To improve the compatibility of TENG in practical scenarios, the triboelectric material

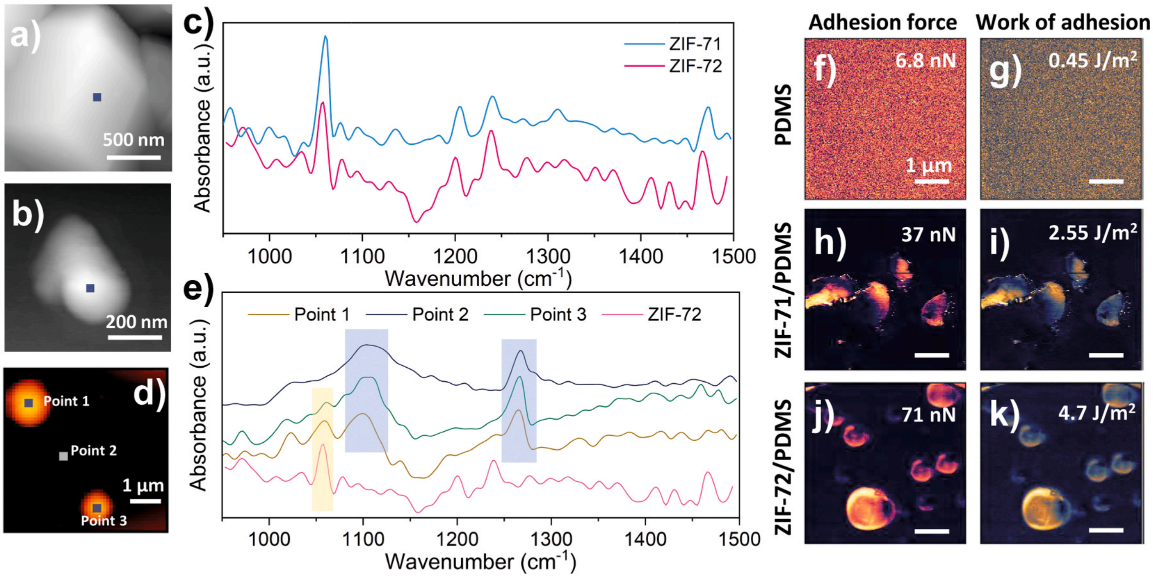

Fig. 4. AFM height topography of ZIF-71 single crystal (a), ZIF-72 single crystal (b), and corresponding nano-FTIR absorption spectra (c) measured on positions indicated in (a, b). (d) AFM height topography of the top surface of the ZIF-72/PDMS film. (e) Nano-FTIR absorption spectra measured at points 1–3 as marked in (d). Local distribution of adhesion forces and work of adhesion of PDMS (f,g), ZIF-71/PDMS (h,i), and ZIF-72/PDMS (j,k), highest measured values are indicated on the top-right corners.

was attached onto a flexible substrate instead of a hard 3D-printed board. In addition, by removing the top electrode of the contact-separation mode TENG, a single electrode mode Z72-TENG was fabricated for more versatile applications [52]. Fig. 5a illustrates the operation of TENG from daily human motions, such as touching, tapping, and smashing. The latex glove on the hand acted as a tribo-positive material, thereby transferring charges to the bottom electrode when it is in contact with the prepared ZIF-72/PDMS film. As the tested biomechanical motions were under different contact forces, different voltages were generated in proportion to force with a sensitive response. This demonstration proves the potential application of Z72-TENG to monitor different body motions as well as to harvest energy to enable the powering of portable electronics.

In addition to its application as an energy harvester, the Z72-TENG was also established to be an effective sensor to monitor the surrounding mechanical motions. Here, a prototype for a small TENG-based pedometer was designed to transmit output signal remotely via Bluetooth, as shown in Fig. 5b. The prototype constitutes of a ZIF-based TENG device, a capacitor, a Bluetooth module, and a central Arduino controller. During operation, a mechanical motion to the TENG device triggered a small electrical signal to charge the capacitor, where this small change in the voltage of capacitor was captured and processed by the central controller to generate a pulse signal. With a Bluetooth module integrated to the controller and connected to a mobile software, the stimuli signal was recorded and displayed on a remote device. As Video S3 shows, the operation of the pedometer by tapping the TENG device shows good sensitivity towards the frequency and the force of mechanical motion, demonstrating its excellent potential for self-powered sensors.

Finally, a Morse code generator was developed by leveraging the Z72-TENG. By matching the contact and separation motions of TENG device with “dots” and “dashes” signals in Morse coding, the electrical signal output can be used to represent different letters. Fig. 5c shows the original Morse signal created by Z72-TENG for short messages, with the output message decoded by the Python program. Our result confirms that the Morse code generated is easily recognizable by the computer program. The encoding and decoding of Morse code is also simple and timely to operate, showing an excellent potential of being used as a self-powered transmitter for sending emergency messages at remote places without any access to a power source. The operating principle of this application is explained further in Note S1.

4. Conclusions

In summary, this work demonstrated the effective incorporation of topologically modulated ZIF fillers into PDMS polymer matrix to fabricate mechanically durable TENG devices with outstanding power density. Owing to the high surface charge density, improved dielectric constant and surface adhesion of ZIF-72, the charge generating and charge trapping properties of its nanocomposites are both remarkably improved. We showed for the first time a systematic comparison between the TENG output of a porous versus non-porous MOF constructed from the same chemical building blocks, but with distinctively different framework architecture. Importantly, the triboelectrification mechanisms in ZIF/polymer composites are further investigated through various nanoscale analytical techniques, namely nano-FTIR and TFM, which have not been previously attempted. Among all fabricated MOF-TENG devices, an optimum mass loading of 1 wt % ZIF-72 in PDMS was found to generate the highest electrical output of 578 V and 19 μA, much higher than the pristine PDMS film. An instantaneous power density of ~5 W m^{-2} was also achieved under an external load of 20 MΩ. To illustrate the potential practical applications of the Z72-TENGs, capacitors with different capacitances, LED arrays, and commercial electronics were successfully powered. Lastly, a prototype for a Bluetooth-integrated pedometer and a Morse code generator were constructed which demonstrated a great potential for other innovative real-world applications.

CRediT authorship contribution statement

Jiahao Ye: Conceptualization, Methodology, Formal analysis, Investigation, Writing – Original draft preparation, Writing – review & editing. **Jin-Chong Tan:** Conceptualization, Supervision, Funding acquisition, Writing – review & editing.

Declaration of Competing Interest

The authors declare the following financial interests/personal

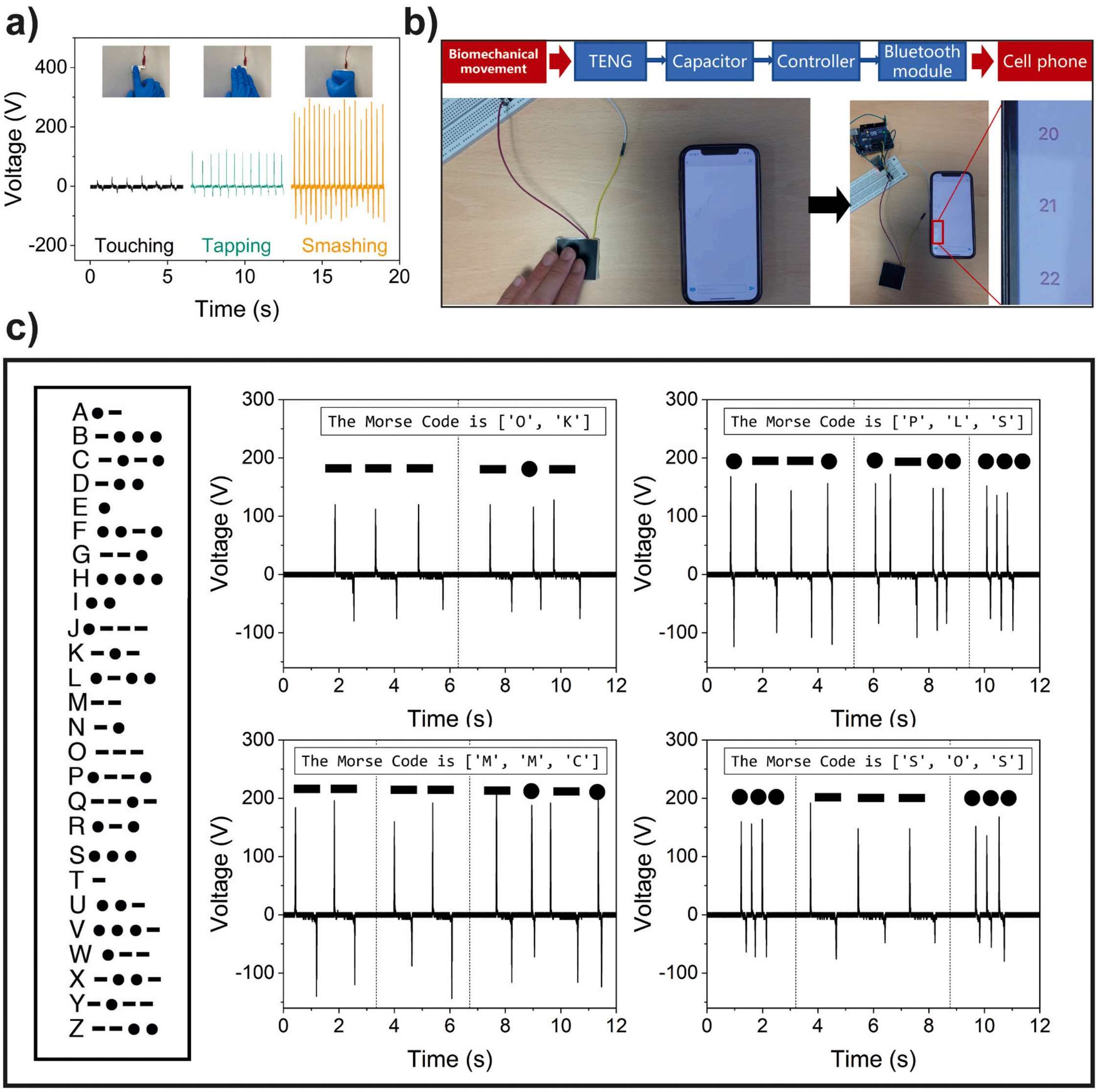

Fig. 5. (a) Harvesting biomechanical energy by touching, tapping, and smashing a single-electrode mode Z72-TENG. (b) Schematic of a Z72-TENG based pedometer with Bluetooth transmission; number of taps being detected remotely and displayed on the screen of a mobile phone. (c) International Morse code table for the alphabet (left panel) and the electrical signal output of a 2.25 cm^2 Z72-TENG device encoding short messages by hand tapping, translated by a Python program using the coding database. The long signal, represented by a "dash," corresponds to a prolonged contact, while the short signal, denoted as a "dot," is expressed a brief and rapid contact. A video recording is given as Video S4; further details can be found in Note S1 within SI.

relationships which may be considered as potential competing interests: J.Y. and J.C.T. are inventors on UK Patent application no. 2219095.3, which covers zeolitic metal-organic framework based nanocomposites for engineering high-performance triboelectric energy harvesters.

Data Availability

Data will be made available on request.

Acknowledgements

This work was supported by the European Research Council (ERC) Consolidator Grant (PROMOFS grant agreement 771575) and the Engineering & Physical Sciences Research Council (EPSRC) award (EP/R511742/1). We acknowledge the Diamond Light Source for the award of beamtime SM27504, and for the technical support kindly offered by Dr. Gianfelice Cinque during the experiments. We are grateful to Dr. Cyril Besnard and Prof. Alexander Korsunsky for access to the FESEM imaging facility in the MBLEM Lab at Oxford. We acknowledge Dr. James Taylor from the ISIS Neutron and Muon Source for the BET measurements.

Appendix A. Supporting information

Supplementary data associated with this article can be found in the online version at doi:10.1016/j.nanoen.2023.108687.

References

[1] F.-R. Fan, Z.-Q. Tian, Z. Lin Wang, Flexible triboelectric generator, Nano Energy 1 (2012) 328–334, https://doi.org/10.1016/j.nanoen.2012.01.004.

[2] Z. Li, Q. Zheng, Z.L. Wang, Z. Li, Nanogenerator-based self-powered sensors for wearable and implantable electronics, Research (Wash D C) 2020 (2020), 8710686, https://doi.org/10.34133/2020/8710686.

[3] Y. Su, J. Wang, B. Wang, T. Yang, B. Yang, G. Xie, Y. Zhou, S. Zhang, H. Tai, Z. Cai, G. Chen, Y. Jiang, L.Q. Chen, J. Chen, Alveolus-inspired active membrane sensors for self-powered wearable chemical sensing and breath analysis, ACS Nano 14 (2020) 6067–6075, https://doi.org/10.1021/acsnano.0c01804.

[4] D. Wang, D. Zhang, Y. Yang, Q. Mi, J. Zhang, L. Yu, Multifunctional latex/polytetrafluoroethylene-based triboelectric nanogenerator for self-powered organ-

like MXene/metal-organic framework-derived CuO nanohybrid ammonia sensor, ACS Nano 15 (2021) 2911–2919, https://doi.org/10.1021/acsnano.0c09015.

[5] S. Mishra, S. Potu, R.S. Puppala, R.K. Rajaboina, P. Kodali, H. Divi, A novel ZnS nanosheets-based triboelectric nanogenerator and its applications in sensing, self-powered electronics, and digital systems, Mater. Today Commun. 31 (2022), 103292, https://doi.org/10.1016/j.mtcomm.2022.103292.

[6] L. Long, W. Liu, Z. Wang, W. He, G. Li, Q. Tang, H. Guo, X. Pu, Y. Liu, C. Hu, High performance floating self-excited sliding triboelectric nanogenerator for micro mechanical energy harvesting, Nat. Commun. 12 (2021) 4689, https://doi.org/10.1038/s41467-021-25047-y.

[7] R. Walden, C. Kumar, D.M. Mulvihill, S.C. Pillai, Opportunities and challenges in triboelectric nanogenerator (TENG) based sustainable energy generation technologies: a mini-review, Chem. Eng. J. Adv. 9 (2022), 100237, https://doi.org/10.1016/j.ceja.2021.100237.

[8] T. Jin, Z. Sun, L. Li, Q. Zhang, M. Zhu, Z. Zhang, G. Yuan, T. Chen, Y. Tian, X. Hou, C. Lee, Triboelectric nanogenerator sensors for soft robotics aiming at digital twin applications, Nat. Commun. 11 (2020) 5381, https://doi.org/10.1038/s41467-020-19059-3.

[9] C.F. Hu, F. Wang, X.H. Cui, Y.T. Zhu, Recent progress in textile-based triboelectric force sensors for wearable electronics, Adv. Compos. HYBRID Mater. 6 (2023) 70, https://doi.org/10.1007/s42114-023-00650-3.

[10] K. Dong, X. Peng, Z.L. Wang, Fiber/fabric-based piezoelectric and triboelectric nanogenerators for flexible/stretchable and wearable electronics and artificial intelligence, Adv. Mater. 32 (2020), 1902549, https://doi.org/10.1002/adma.201902549.

[11] S. Pan, Z. Zhang, Fundamental theories and basic principles of triboelectric effect: a review, Friction 7 (2019) 2–17, https://doi.org/10.1007/s40544-018-0217-7.

[12] S. Pan, Z. Zhang, Triboelectric effect: a new perspective on electron transfer process, J. Appl. Phys. 122 (2017), 144302, https://doi.org/10.1063/1.5006634.

[13] D.J. Lacks, R.Mohan Sankaran, Contact electrification of insulating materials, J. Phys. D. - Appl. Phys. 44 (2011), 453001, https://doi.org/10.1088/0022-3727/44/45/453001.

[14] J. Chen, Z.L. Wang, Reviving vibration energy harvesting and self-powered sensing by a triboelectric nanogenerator, Joule 1 (2017) 480–521, https://doi.org/10.1016/j.joule.2017.09.004.

[15] R. Zhang, H. Olin, Material choices for triboelectric nanogenerators: a critical review, EcoMat 2 (2020) 12062, https://doi.org/10.1002/eom2.12062.

[16] Y.S. Choi, S.W. Kim, S. Kar-Narayan, Materials-related strategies for highly efficient triboelectric energy generators, Adv. Energy Mater. 11 (2021), 2003802, https://doi.org/10.1002/aenm.202003802.

[17] K. Shrestha, S. Sharma, G.B. Pradhan, T. Bhatta, P. Maharjan, S.S. Rana, S. Lee, S. Seonu, Y. Shin, J.Y. Park, A siloxene/ecoflex nanocomposite-based triboelectric nanogenerator with enhanced charge retention by MoS2/LIG for self-powered touchless sensor applications, Adv. Funct. Mater. 32 (2022), 2113005, https://doi.org/10.1002/adfm.202113005.

[18] J. Chen, H. Guo, X. He, G. Liu, Y. Xi, H. Shi, C. Hu, Enhancing performance of triboelectric nanogenerator by filling high dielectric nanoparticles into sponge PDMS film, ACS Appl. Mater. Interfaces 8 (2016) 736–744, https://doi.org/10.1021/acsami.5b09907.

[19] M. Sahu, S. Hajra, J. Bijelic, D. Oh, I. Djerdj, H.J. Kim, Triple perovskite-based triboelectric nanogenerator: a facile method of energy harvesting and self-powered information generator, Mater. Today Energy 20 (2021), 100639, https://doi.org/10.1016/j.mtener.2021.100639.

[20] M. Salauddin, S.M.S. Rana, M. Sharifuzzaman, M.T. Rahman, C. Park, H. Cho, P. Maharjan, T. Bhatta, J.Y. Park, A novel MXene/Ecoflex nanocomposite-coated fabric as a highly negative and stable friction layer for high-output triboelectric nanogenerators, Adv. Energy Mater. 11 (2021), 2002832, https://doi.org/10.1002/aenm.202002832.

[21] B.N. Chandrashekar, B. Deng, A.S. Smitha, Y. Chen, C. Tan, H. Zhang, H. Peng, Z. Liu, Roll-to-roll green transfer of CVD graphene onto plastic for a transparent and flexible triboelectric nanogenerator, Adv. Mater. 27 (2015) 5210–5216, https://doi.org/10.1002/adma.201502560.

[22] M. Su, B. Kim, Silk fibroin-carbon nanotube composites based fiber substrated wearable triboelectric nanogenerator, ACS Appl. Nano Mater. 3 (2020) 9759–9770, https://doi.org/10.1021/acsanm.0c01854.

[23] I. Stassen, N.C. Burtch, A.A. Talin, P. Falcaro, M.D. Allendorf, R. Ameloot, An updated roadmap for the integration of metal-organic frameworks with electronic devices and chemical sensors, Chem. Soc. Rev. 46 (2017) 3185–3241, https://doi.org/10.1039/c7cs00122c.

[24] M. Gutiérrez, Y. Zhang, J.-C. Tan, Confinement of luminescent guests in metal–organic frameworks: understanding pathways from synthesis and multimodal characterization to potential applications of LG@MOF systems, Chem. Rev. 122 (2022) 10438–10483, https://doi.org/10.1021/acs.chemrev.1c00980.

[25] J. Lee, O.K. Farha, J. Roberts, K.A. Scheidt, S.T. Nguyen, J.T. Hupp, Metal-organic framework materials as catalysts, Chem. Soc. Rev. 38 (2009) 1450–1459, https://doi.org/10.1039/b807080f.

[26] J.R. Li, R.J. Kuppler, H.C. Zhou, Selective gas adsorption and separation in metal-organic frameworks, Chem. Soc. Rev. 38 (2009) 1477–1504, https://doi.org/10.1039/b802426j.

[27] A.S. Babal, L. Donà, M.R. Ryder, K. Titov, A.K. Chaudhari, Z. Zeng, C.S. Kelley, M. D. Frogley, G. Cinque, B. Civalleri, J.-C. Tan, Impact of pressure and temperature on the broadband dielectric response of the HKUST-1 metal–organic framework, J. Phys. Chem. C. 123 (2019) 29427–29435, https://doi.org/10.1021/acs.jpcc.9b08125.

[28] K. Titov, Z. Zeng, M.R. Ryder, A.K. Chaudhari, B. Civalleri, C.S. Kelley, M. D. Frogley, G. Cinque, J.-C. Tan, Probing dielectric properties of metal–organic frameworks: MIL-53(Al) as a model system for theoretical predictions and experimental measurements via synchrotron far- and mid-infrared spectroscopy, J. Phys. Chem. Lett. 8 (2017) 5035–5040, https://doi.org/10.1021/acs.jpclett.7b02003.

[29] R. Wen, J. Guo, A. Yu, J. Zhai, Z. l Wang, Humidity-resistive triboelectric nanogenerator fabricated using metal organic framework composite, Adv. Funct. Mater. 29 (2019), 1807655, https://doi.org/10.1002/adfm.201807655.

[30] N. Jayababu, D. Kim, Co/Zn bimetal organic framework elliptical nanosheets on flexible conductive fabric for energy harvesting and environmental monitoring via triboelectricity, Nano Energy 89 (2021), 106355, https://doi.org/10.1016/j.nanoen.2021.106355.

[31] S.M.S. Rana, M.A. Zahed, M.T. Rahman, M. Salauddin, S.H. Lee, C. Park, P. Maharjan, T. Bhatta, K. Shrestha, J.Y. Park, Cobalt-nanoporous carbon functionalized nanocomposite-based triboelectric nanogenerator for contactless and sustainable self-powered sensor systems, Adv. Funct. Mater. 31 (2021), 2105110, https://doi.org/10.1002/adfm.202105110.

[32] R. Wen, L. Fan, Q. Li, J. Zhai, A composite triboelectric nanogenerator based on flexible and transparent film impregnated with ZIF-8 nanocrystals, Nanotechnology 32 (2021), 345401, https://doi.org/10.1088/1361-6528/ac020f.

[33] Y. Zhang, M. Gutiérrez, A.K. Chaudhari, J.-C. Tan, Dye-encapsulated zeolitic imidazolate framework (ZIF-71) for fluorochromic sensing of pressure, temperature, and volatile solvents, ACS Appl. Mater. Interfaces 12 (2020) 37477–37488, https://doi.org/10.1021/acsami.0c10257.

[34] M. Tu, D.E. Kravchenko, B. Xia, V. Rubio-Gimenez, N. Wauteraerts, R. Verbeke, I.F. J. Vankelecom, T. Stassin, W. Egger, M. Dickmann, H. Amenitsch, R. Ameloot, Template-mediated control over polymorphism in the vapor-assisted formation of zeolitic imidazolate framework powders and films, Angew. Chem. Int. Ed. 60 (2021) 7553–7558, https://doi.org/10.1002/anie.202014791.

[35] A.F. Möslein, M. Gutiérrez, B. Cohen, J.-C. Tan, Near-field infrared nanospectroscopy reveals guest confinement in metal–organic framework single crystals, Nano Lett. 20 (2020) 7446–7454, https://doi.org/10.1021/acs.nanolett.0c02839.

[36] S. Niu, S. Wang, L. Lin, Y. Liu, Y.S. Zhou, Y. Hu, Z.L. Wang, Theoretical study of contact-mode triboelectric nanogenerators as an effective power source, Energy Environ. Sci. 6 (2013) 3576–3583, https://doi.org/10.1039/C3EE42571A.

[37] B. Yang, W. Zeng, Z.H. Peng, S.R. Liu, K. Chen, X.M. Tao, A fully verified theoretical analysis of contact-mode triboelectric nanogenerators as a wearable power source, Adv. Energy Mater. 6 (2016), 1600505, https://doi.org/10.1002/aenm.201600505.

[38] Z. Chen, Y. Cao, W. Yang, L. An, H. Fan, Y. Guo, Embedding in-plane aligned MOF nanoflakes in silk fibroin for highly enhanced output performance of triboelectric nanogenerators, J. Mater. Chem. A 10 (2022) 799–807, https://doi.org/10.1039/d1ta08605g.

[39] Q. Chen, Y. Shen, S. Zhang, Q.M. Zhang, Polymer-based dielectrics with high energy storage density, Annu. Rev. Mater. Res. 45 (2015) 433–458, https://doi.org/10.1146/annurev-matsci-070214-021017.

[40] M.R. Ryder, Z. Zeng, K. Titov, Y. Sun, E.M. Mahdi, I. Flyagina, T.D. Bennett, B. Civalleri, C.S. Kelley, M.D. Frogley, G. Cinque, J.-C. Tan, Dielectric properties of zeolitic imidazolate frameworks in the broad-band infrared regime, J. Phys. Chem. Lett. 9 (2018) 2678–2684, https://doi.org/10.1021/acs.jpclett.8b00799.

[41] W.J. Li, J. Liu, Z.H. Sun, T.F. Liu, J. Lu, S.Y. Gao, C. He, R. Cao, J.H. Luo, Integration of metal-organic frameworks into an electrochemical dielectric thin film for electronic applications, Nat. Commun. 7 (2016) 11830, https://doi.org/10.1038/ncomms11830.

[42] J.E. Huheey, The electronegativity of groups, J. Phys. Chem. 69 (1965) 3284–3291, https://doi.org/10.1021/j100894a011.

[43] J.H. Lee, I. Yu, S. Hyun, J.K. Kim, U. Jeong, Remarkable increase in triboelectrification by enhancing the conformable contact and adhesion energy with a film-covered pillar structure, Nano Energy 34 (2017) 233–241, https://doi.org/10.1016/j.nanoen.2017.02.032.

[44] M.T. Rahman, S.M.S. Rana, M.A. Zahed, S. Lee, E.-S. Yoon, J.Y. Park, Metal-organic framework-derived nanoporous carbon incorporated nanofibers for high-performance triboelectric nanogenerators and self-powered sensors, Nano Energy 94 (2022), 106921, https://doi.org/10.1016/j.nanoen.2022.106921.

[45] T. Vijayakanth, A.K. Srivastava, F. Ram, P. Kulkarni, K. Shanmuganathan, B. Praveenkumar, R. Boomishankar, A flexible composite mechanical energy harvester from a ferroelectric organoamino phosphonium salt, Angew. Chem. Int. Ed. 57 (2018) 9054–9058, https://doi.org/10.1002/anie.201805479.

[46] Y. Guo, Y. Cao, Z. Chen, R. Li, W. Gong, W. Yang, Q. Zhang, H. Wang, Fluorinated metal-organic framework as bifunctional filler toward highly improving output performance of triboelectric nanogenerators, Nano Energy 70 (2020), 104517, https://doi.org/10.1016/j.nanoen.2020.104517.

[47] Y.M. Wang, X. Zhang, D. Yang, L. Wu, J. Zhang, T. Lei, R. Yang, Highly stable metal-organic framework UiO-66-NH2 for high-performance triboelectric nanogenerators, Nanotechnology 33 (2021), 065402, https://doi.org/10.1088/1361-6528/ac32f8.

[48] R. Wen, B. Zhao, L. Fan, J. Guo, J. Zhai, Controlling the output performance of triboelectric nanogenerator through filling isostructural metal–organic frameworks with varying functional groups, Adv. Mater. Technol. 8 (2023), 2201330, https://doi.org/10.1002/admt.202201330.

[49] A.F. Möslein, J.-C. Tan, Vibrational modes and terahertz phenomena of the large-cage zeolitic imidazolate framework-71, J. Phys. Chem. Lett. 13 (2022) 2838–2844, https://doi.org/10.1021/acs.jpclett.2c00081.

[50] L. Lapčinskis, K. Mālnieks, J. Blūms, M. Knite, S. Oras, T. Käämbre, S. Vlassov, M. Antsov, M. Timusk, A. Šutka, The adhesion-enhanced contact electrification and

efficiency of triboelectric nanogenerators, Macromol. Mater. Eng. 305 (2020), 1900638, https://doi.org/10.1002/mame.201900638.
[51] W. Yang, X. Wang, P. Chen, Y. Hu, L. Li, Z. Sun, On the controlled adhesive contact and electrical performance of vertical contact-separation mode triboelectric nanogenerators with micro-grooved surfaces, Nano Energy 85 (2021), 106037, https://doi.org/10.1016/j.nanoen.2021.106037.
[52] A. Manjari Padhan, S. Hajra, M. Sahu, S. Nayak, H. Joon Kim, P. Alagarsamy, Single-electrode mode TENG using ferromagnetic NiO-Ti based nanocomposite for effective energy harvesting, Mater. Lett. 312 (2022), 131644, https://doi.org/10.1016/j.matlet.2021.131644.

Jiahao Ye received his MEng degree in Chemical Engineering from Imperial College London in 2021. He is currently a DPhil student in the Department of Engineering Science at Oxford University. His current research focuses on metal-organic frameworks, polymers, nanocomposites, triboelectric nanogenerators, self-powered sensors, and energy harvesting devices.

Jin-Chong Tan is Professor of Nanoscale Engineering in the Department of Engineering Science at Oxford University. He received his BEng (UTM Malaysia, 1999) and MEng (NTU Singapore, 2001) in mechanical & materials engineering, and Ph.D. in materials science (2005) from Cambridge University. In 2012, he founded the MMC Lab at Oxford, focusing on the physical and functional properties of novel materials targeting real-world applications. Recent research interests include nanoengineering of composites for energy, structural, and sensing technologies.

5

Halogenated MOF Based TENGs for Improved Charge Generation Properties

5.1 Background and motivation

Improving the triboelectric output of MOF-based TENG devices has always been the most urgent and challenging objective for industrial applications. In Chapter 3, we utilised a different synthetic approach to yield MOFs with distinct topological structures. However, there are many other factors that determine the overall physicochemical properties of MOF and thereby its performance within a triboelectric nanogenerator device. Previous research has been focusing on modifying the two constitutional parts of MOF, namely the metal ion centre and ligand, for property regulation of MOF-based TENG applications.

The effect of metal centre of MOF on TENG has been evaluated in a few studies. Chen *et al.* examined the triboelectric output performance of ZUT-75 composed of different metal centres, including Co, Zn, Cu, and Mn. The ZUT-75

(Mn) was first synthesised, and the rest were prepared by central-metal-ion exchange reactions to yield isomorphic frameworks. By evaluating the triboelectric output performance of prepared TENG devices, ZUT-75 with Co centre demonstrated the highest power density of 3280.5 mW m^{-2} due to the low ion coupling. The reduced binding effect of metal ions to electrons leads to higher electron mobility and enhanced triboelectric output [86]. Moreover, Shao *et al.* switched the metal centre of ZUT-9 with different metal ion centres, including Zn, Ni, and Co, to improve the triboelectric output signal. By changing the type of metal centre to Co, the electron delocalisation effect was enhanced; therefore, the magnetism behaviour and triboelectric property can be regulated [168].

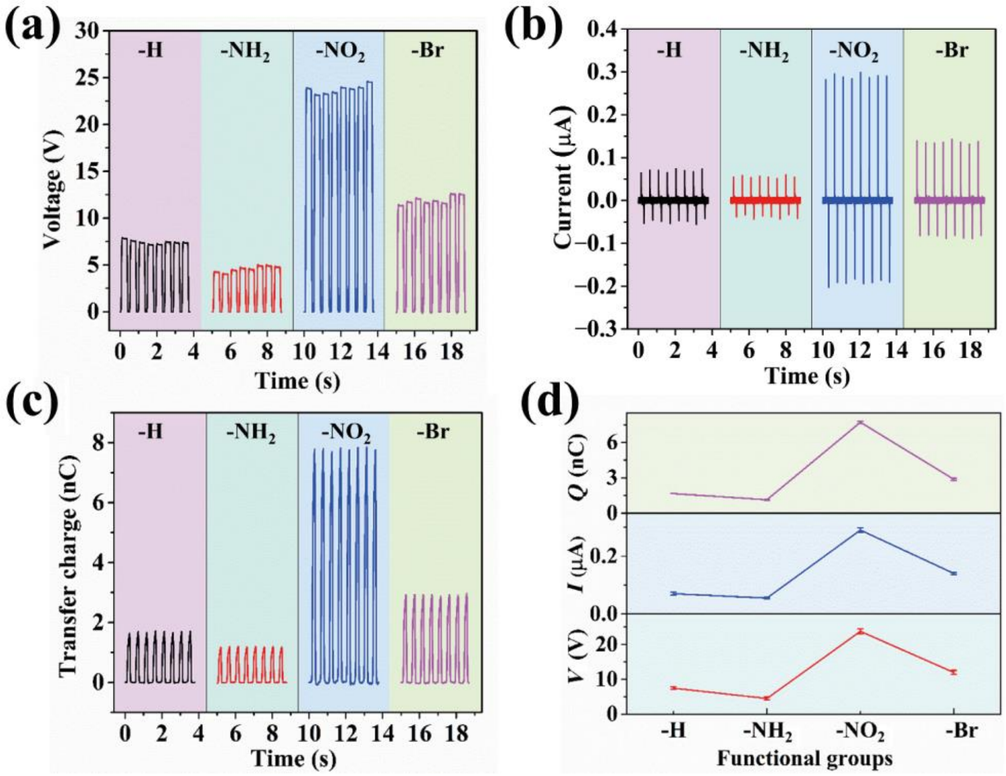

Figure 5.1. (a) Output voltage, (b) output current, and (c) charge transfer signals of the UiO-66-X TENG as a function of time. (d) The output current, voltage, and transfer charge of TENG as a function of functional groups. Reproduced with permission from ref [169]. Copyright 2022 Springer Nature.

Changing the ligand of MOF is considered another effective approach to controlling the output of triboelectric nanogenerators. In 2022, Wen *et al.* prepared UiO-66 thin films with different functional groups on ligands and deposited them on tin oxide electrode to act as a tribo-negative layer [169]. The triboelectric output performance of the UiO-66-X (X = H, NH_2, NO_2, Br) films are ranked in the order of $NO_2 > Br > H > NH_2$, as shown in Figure 5.1. The reason behind the improvement is explained by the highly electron-withdrawing nature of NO_2 group. Through DFT simulation, it has been confirmed that the LUMO energy has decreased the most by NO_2 group, thereby promoting electron transfer from the contacting metal to MOF. As a result, the functional group of MOFs may play a vital role in tuning its triboelectric behaviour.

In addition, More *et al.* explored the isoreticular subfamily of the UiO-66(Zr) MOFs by incorporating -H and -Br functional groups within the MOF structure [170]. The prepared MOFs were embedded within a PVDF matrix to amplify the electrical output of TENG devices, as illustrated in Figure 5.2. During triboelectric performance testing, a peak-to-peak voltage of 110.4 V was achieved with UiO-66-Br/PVDF composite film, demonstrating a 14-fold increase compared to the pristine PVDF film. This significant improvement was attributed to the high electron density provided by the Br atoms, which facilitated charge transfer by creating electron-rich regions within the MOF framework. Moreover, functionalisation of the linker significantly improved the surface potential of the MOF/polymer composite while also increasing surface roughness, further enhancing charge generation due to the alteration of the surface mechanical behaviour. In line with our previous study described in Chapter 3, which employed a chlorinated ligand (dcIm), this earlier research also suggested that halogenated ligands can be the key to improving the triboelectric performance in MOFs.

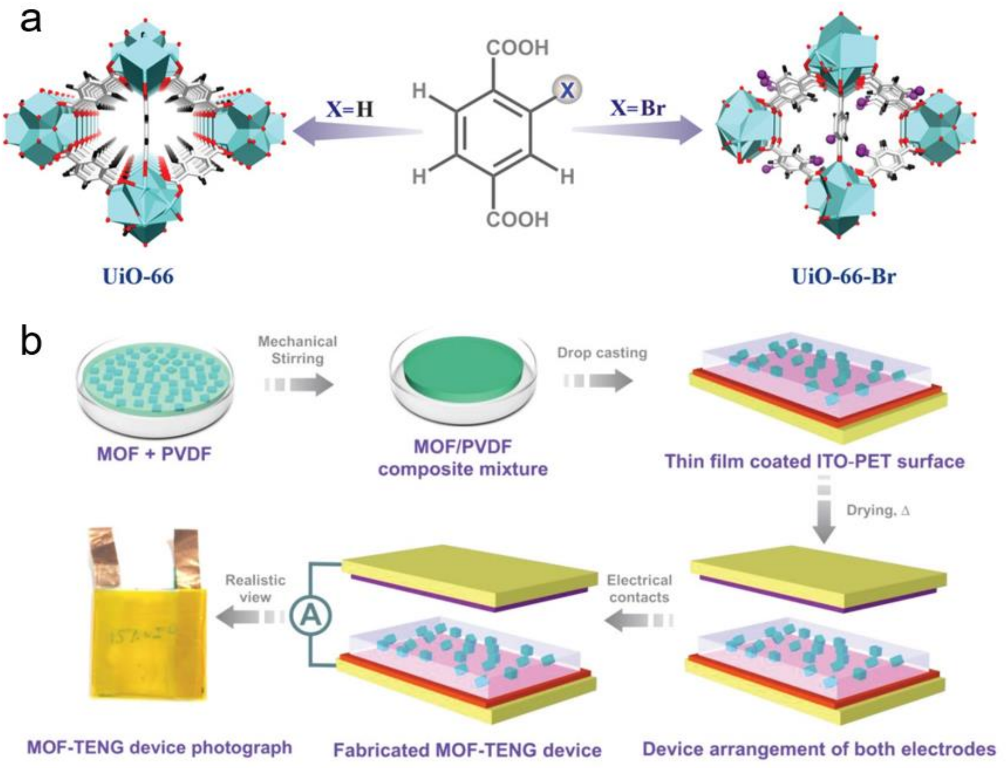

Figure 5.2. (a) Schematic illustration of the synthesis of compounds 1 (UiO-66) and 2 (UiO-66-Br) by ligand functionalisation. (b) Stepwise fabrication procedure adopted for UiO-66/PVDF and UiO-66-Br/PVDF composite-based mechanical energy harvesting devices. Reproduced with permission from ref [170]. Copyright 2022 John Wiley and Sons.

Despite several research papers having explored the functionalisation of MOFs in TENG applications, they have primarily focused on the UiO-66 system as the base material. This narrow focus means that the broader applicability of the functionalisation approach across different families of MOF structures has remained largely unexplored. To bridge this knowledge gap, this chapter explores further the functionalisation approach on a different MOF system, namely ZIF-8, which has distinctive chemical, topological, and structural properties compared with UiO-66. ZIF-8 is known for its ease of synthesis, good mechanical and chemical stability, and great versatility. With these great advantages, ZIF-8 can be functionalised with various halogenated groups to modify its electrical properties [171-173]. Although a few papers have reported improved triboelectric performance using ZIF-8 as either tribo-positive or tribo-negative material [100,111,174], the performance of the assembled ZIF-8 based TENG devices is not exceptionally high compared with other MOF-based TENGs, and its potential as triboelectric material has not been fully explored. The work described in Chapter 5 thus aims to address how other halogenated groups, particularly -Br and -Cl, affect the triboelectric output of ZIF-8.

5.2 Summary of Paper II

5.2.1 Halogenation of ZIF-8

In Paper II, isostructural ZIF-8-X (X = CH_3, Br, Cl) with different functional groups have been synthesised through the solvothermal approach (see Section 3.3.1.2). Three ligands were used, namely 2-methylimidazole, 2-bromo-1H-imidazole, and 2-chloro-1H-imidazole, with their only structural difference at the 2-position of the imidazolate ring to prepare the ZIF-8-CH_3, ZIF-8-Br, and ZIF-8-Cl, respectively. The linkers were selected based on their relative electronegativity. Specifically, the electrostatic potential (ESP) of the ligands of ZIF-8-X was simulated by DFT calculations to predict the relative electron distribution, as shown in Figure 5.3. As the functional group of ligand changes from -CH_3 to -Br and -Cl, the polarity of the molecule increases due to the more asymmetrical distribution of electrons. The stronger electron-withdrawing effect of halogen atoms has led to a stronger negative potential shown at the location of the functional group, as denoted in Figure 5.3. However, the simulation of the ligand molecule does not represent the actual electron distribution of the periodic framework structure being synthesised. While the organic ligand interacts with the metal ion centre through coordination bonds within the framework, the hydrogen atom bonded to oxygen undergoes deprotonation, leaving the lone pair of electrons on the oxygen atom coordinated to the metal centre. As a result, the overall electrostatic potential distribution will be different within the extended framework. However, it is still evident that the introduction of halogenated functional groups into the ligand structure enhances the overall polarity of the ligand molecules, which can influence the electronic environment within the framework.

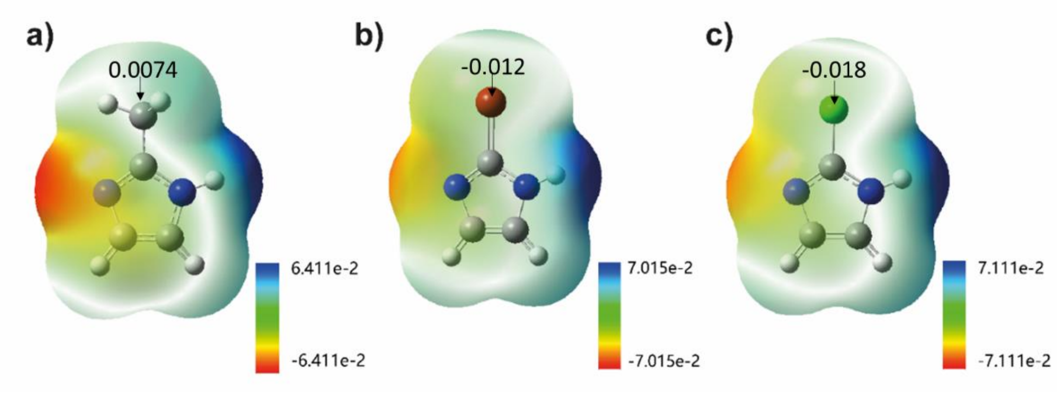

Figure 5.3. Electrostatic potential maps of (a) 2-methylimidazole, (b) 2-bromo-1H-imidazole, and (c) 2-chloro-1H-imidazole calculated by the DFT code Gaussian 09W (unit = kcal/mol).

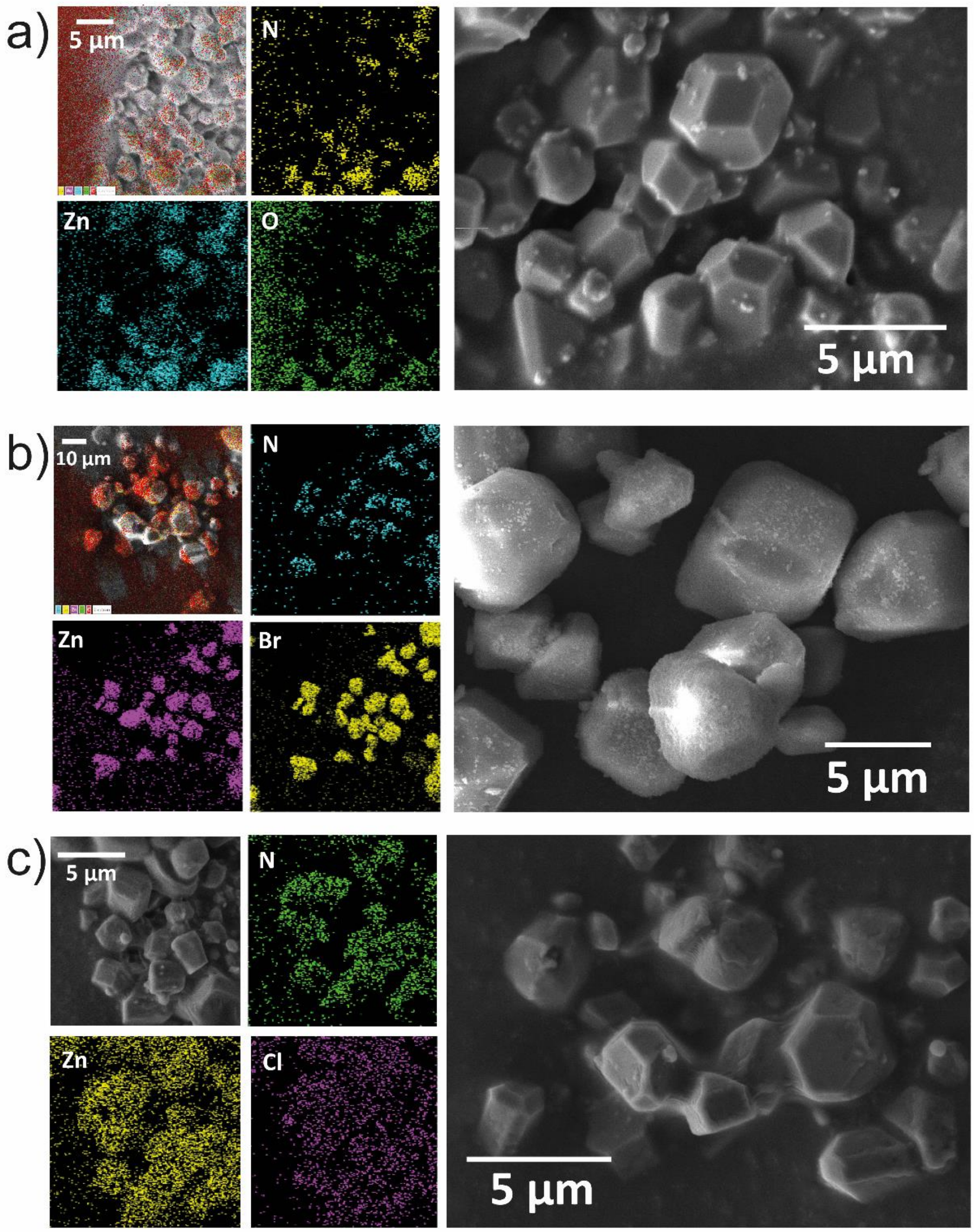

Figure 5.4. EDS elemental mapping analysis and FESEM image of (a) ZIF-8-CH_3, (b) ZIF-8-Br, and (c) ZIF-8-Cl crystals.

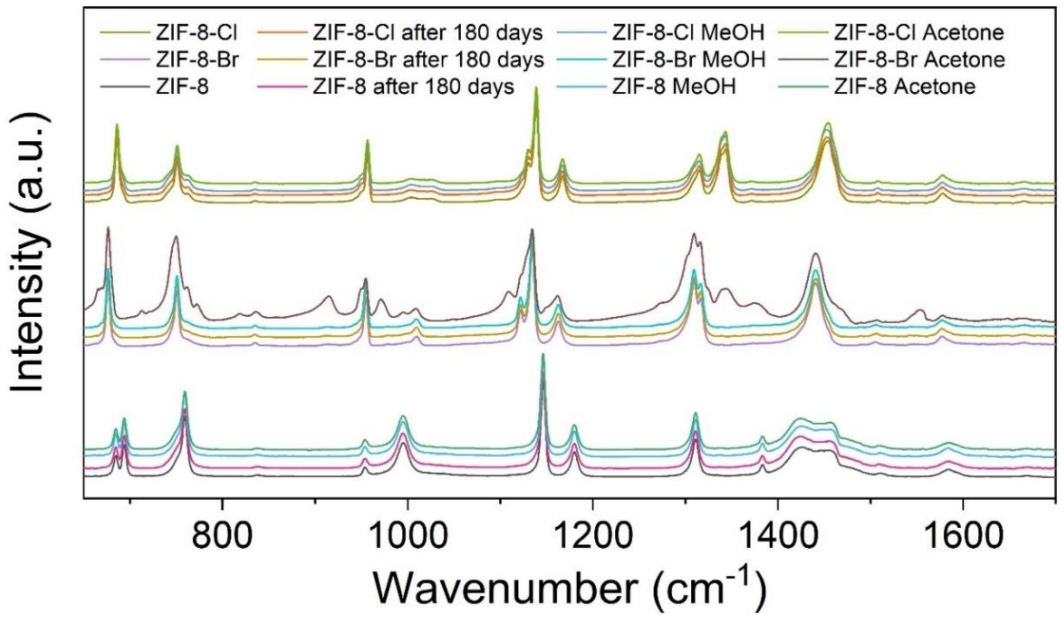

Figure 5.5. ATR-FTIR spectra of ZIF-8-X particles after an extended exposure to ambient conditions for 180 days, and after being immersed in methanol or acetone solvents for 3 days.

Figure 5.4 shows the FESEM images of the synthesised ZIF-8-X materials. The crystalline particles are around 5 μm in size, with energy-dispersive X-ray spectroscopy (EDS) analysis showing the successful incorporation of halogenated linkers within the framework structure. Based on the XRD and FTIR results, we determined that the ZIF-8-Xs demonstrate similar crystalline structures and chemical compositions. In addition, the prepared ZIF-8-X samples show good structural stability within different organic solvents, despite ZIF-8-Br showing some degradation in crystallinity after being immersed in acetone solution, as shown by IR bands broadening in Figure 5.5. Compared with ZIF-8-Cl, ZIF-8-Br is less stable in polar aprotic solvents such as acetone due to the higher steric strain attributed to the larger size of Br atom. Moreover, the electronegativity of Br is weaker than Cl, resulting in a weaker chemical bond with the ZIF framework, making the structure less stable.

Subsequently, the ZIF-8-Xs were blended with PVDF solutions for electrospinning (see Section 3.3.2.1). These filler particles are uniformly attached to the PVDF fibres, thus increasing the surface roughness and effective contact area when the porous fibre mat is compressed. The electrospinning technique is useful for increasing the internal surface area of material to achieve a larger effective contact area. Moreover, more filler materials can be embedded into a fibre morphology without the formation of obvious aggregation, thereby leveraging more advantages of filler material. The nano-FTIR spectra shown in Figure 5.6 and Figure 5.7 demonstrated examples of the incorporation of ZIF-8-CH_3 and ZIF-8-Br on a single PVDF fibre. Based on AFM topography image, it can be seen that the incorporated particles are larger than the thickness of the fibre, therefore increasing the overall surface area of the fibre. While scanning along the composite fibre, it is observed that the characteristic peaks of the ZIF-8-X fillers gradually evolve towards the centre of the scan, creating a variation of chemical bonds. We propose that these chemical variations alter the work function on the fibre surface, and present as charge traps while contacting with materials of different triboelectric properties. In contrast to a homogeneous PVDF fibre, the introduction of fillers creates more opportunities for material contact to occur between different materials, hence conferring a higher difference in relative work function and larger amount of charge transfer.

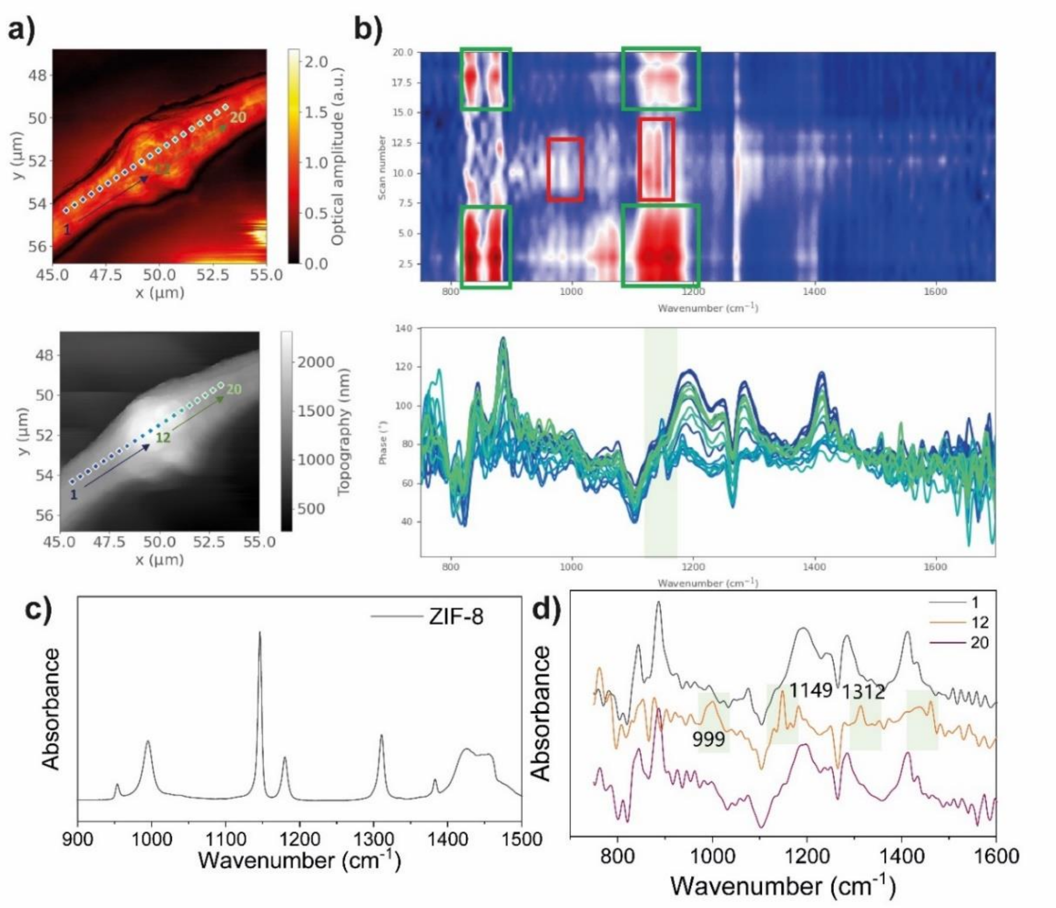

Figure 5.6. (a) Nearfield infrared O2A signal and AFM height topography of the as-synthesised ZIF-8-CH_3/PVDF composite fibre. (b) Contour plot and line-scan nano-FTIR spectra of ZIF-8-CH_3/PVDF composite measured point-by-point along the fibre. The green box highlights the characteristic peaks of the PVDF matrix, and the red box denotes the peaks for the embedded ZIF-8-CH_3 particles. The FTIR peaks for the filler at 1000 cm^{-1} and 1150 cm^{-1} evolve as the scan progresses toward the centre of the AFM scan. (c) ATR-FTIR spectrum of ZIF-8-CH_3 particles. (d) Nano-FTIR spectra of points 1, 12, and 20 along the line-scan. The peaks for ZIF-8-CH_3 at 999 cm^{-1}, 1149 cm^{-1} and 1312 cm^{-1} are distinctly observed at position 12 but not evident on the smoother part of the fibre.

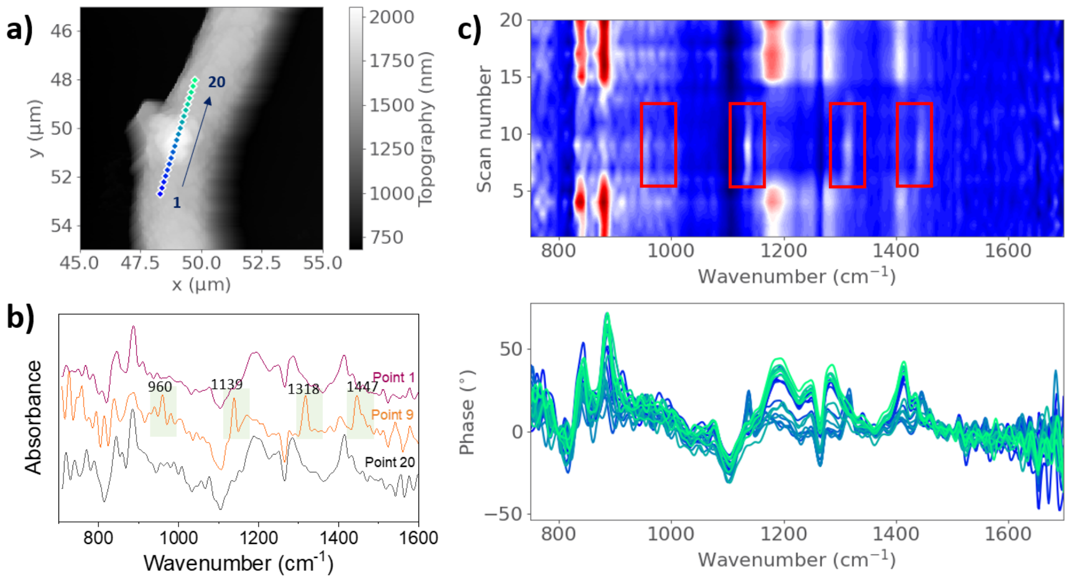

Figure 5.7. (a) AFM topography of the as-synthesised ZIF-8-Br/PVDF composite fibre. (b) Nano-FTIR spectra of points 1, 9, and 20 along the line-scan. The peaks for ZIF-8-Br at 960 cm^{-1}, 1139 cm^{-1}, 1318 cm^{-1}, and 1447 cm^{-1} are distinctly observable at point 9. (c) Contour plot and line-scan nano-FTIR spectrum of ZIF-8-Br/PVDF composite along the fibre. The red box highlights the characteristic peaks of the embedded ZIF-8-Br particles as the scan progresses towards the centre of the AFM scan.

5.2.2 Comparison of triboelectric output

The performance of ZIF-8-X/PVDF fibres was characterised through periodic contact-separation tests employing the assembled TENG devices. Two batches of devices were fabricated and tested on separate dates, exhibiting consistent performance due to the stable device architecture with sponge and substrate encapsulation. All electrical output, including voltage, current, and charge, shows an identical trend, with all composite fibres showing improved performance compared to the neat polymer. Notably, the ZIF-8-Cl/PVDF device exhibits the highest output of 312.4 ± 2.0 V, as shown in Figure 5.8d. While comparing the peak-to-peak voltage output, ZIF-8-Cl/PVDF demonstrates the highest value of 448 V, which is three times higher than that of the pristine PVDF fibre, as summarised in Figure 5.9.

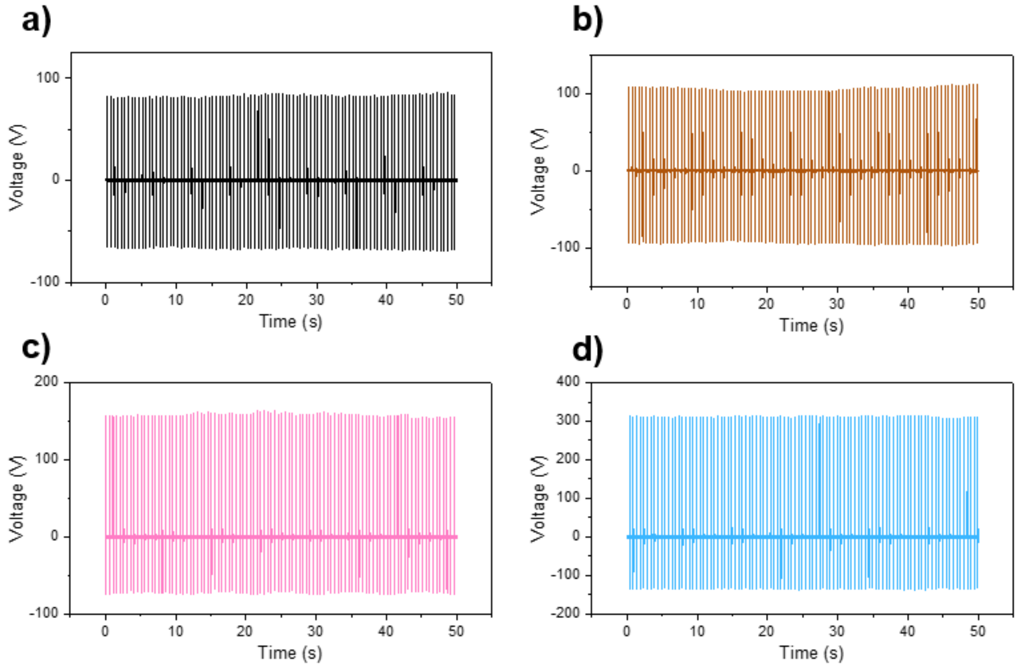

Figure 5.8. The voltage output over 100 contact-separation cycles generated by (a) PVDF-based TENG (control), (b) ZIF-8-CH_3/PVDF-based TENG, (c) ZIF-8-Br/PVDF-based TENG, and (d) ZIF-8-Cl/PVDF-based TENG.

The practical use of the prepared composite fibre-based TENGs is further explored by testing under various resistance loads. By measuring the voltage across different resistances, the power output can be calculated and compared across the ZIF-8-X/PVDF devices. The internal resistance of each device was obtained from the load resistance at the highest power density, as given by V^2/R. All devices show similar internal resistance in the range of 10 MΩ, as shown in Figure 5.10. For practical applications, higher internal resistance is normally suitable for high-voltage applications to prevent energy loss. However, due to the low current output in high impedance TENG devices, the power delivery efficiency will be low, and applications in current-intensive scenarios will be limited. Therefore, the design of power efficient electrical circuit is essential for future research [175,176].

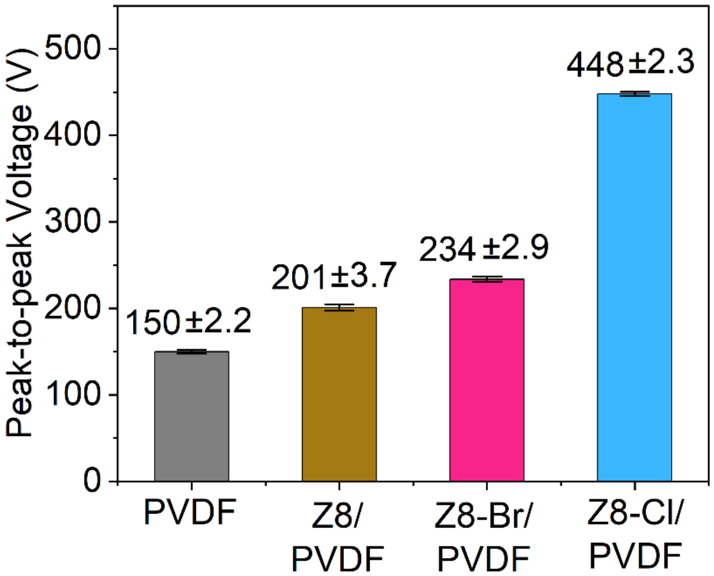

Figure 5.9. The average peak-to-peak voltage output generated by the ZIF-8-X/PVDF-based TENG. The mean and standard deviation values were determined from a total of 100 contact-separation cycles.

Another set of ZIF-8-Cl/PVDF composites was prepared by doctor blade technique instead of electrospinning, as shown in Paper II (Figure 6). Based on the surface potential analysis of the composite surfaces *via* KPFM (Figure 5.11), it was identified that the incorporation of the ZIF-8-X fillers had resulted in a more negative potential, visualised as dark regions in the map. In accordance with the trend determined from the relative electronegativity of ligand functional groups (-Cl > -Br > -CH_3), the ZIF-8-Cl/PVDF demonstrates the most negative potential, followed by ZIF-8-Br and ZIF-8-CH_3. The surface potential measured by KPFM was correlated to the work function of the sample (see Figure 5 in Paper II), whereby the surface potential map reveals a difference in the work function and ability to donate or withdraw electrons during contact. We reasoned that the difference in work function creates local heterogeneities to facilitate localised electron transfer, hence enhancing the charge storage on the material surface and promoting triboelectric performance.

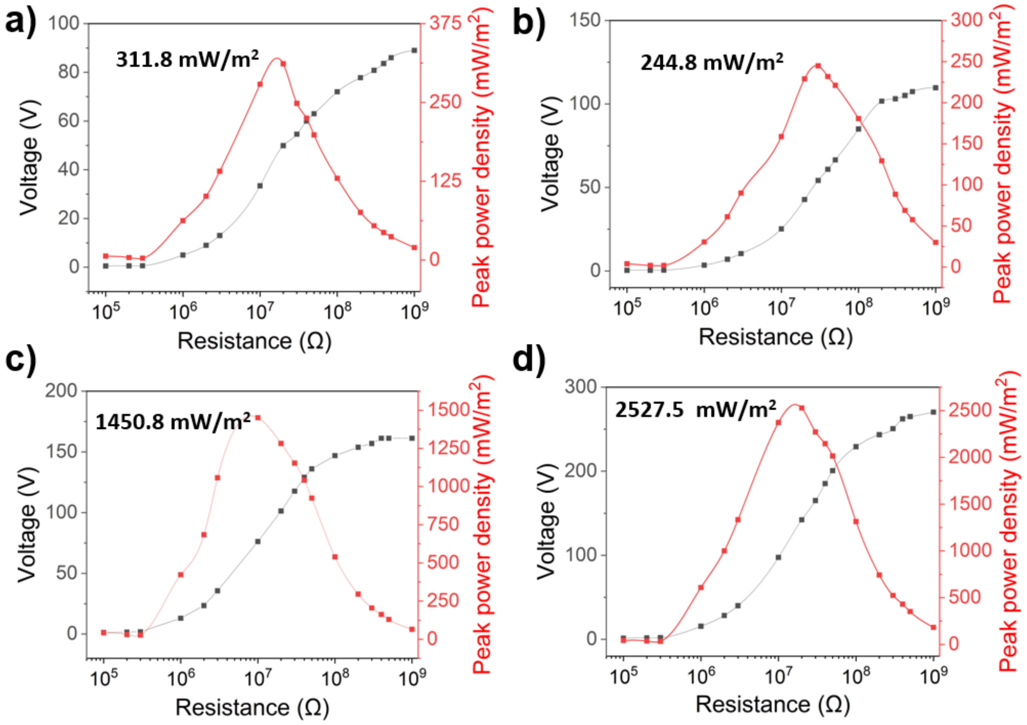

Figure 5.10. Peak voltage and power density as a function of load resistance for (a) PVDF-based TENG, (b) ZIF-8-CH_3/PVDF-based TENG, (c) ZIF-8-Br/PVDF-based TENG, and (d) ZIF-8-Cl/PVDF-based TENG, with the highest power density labelled.

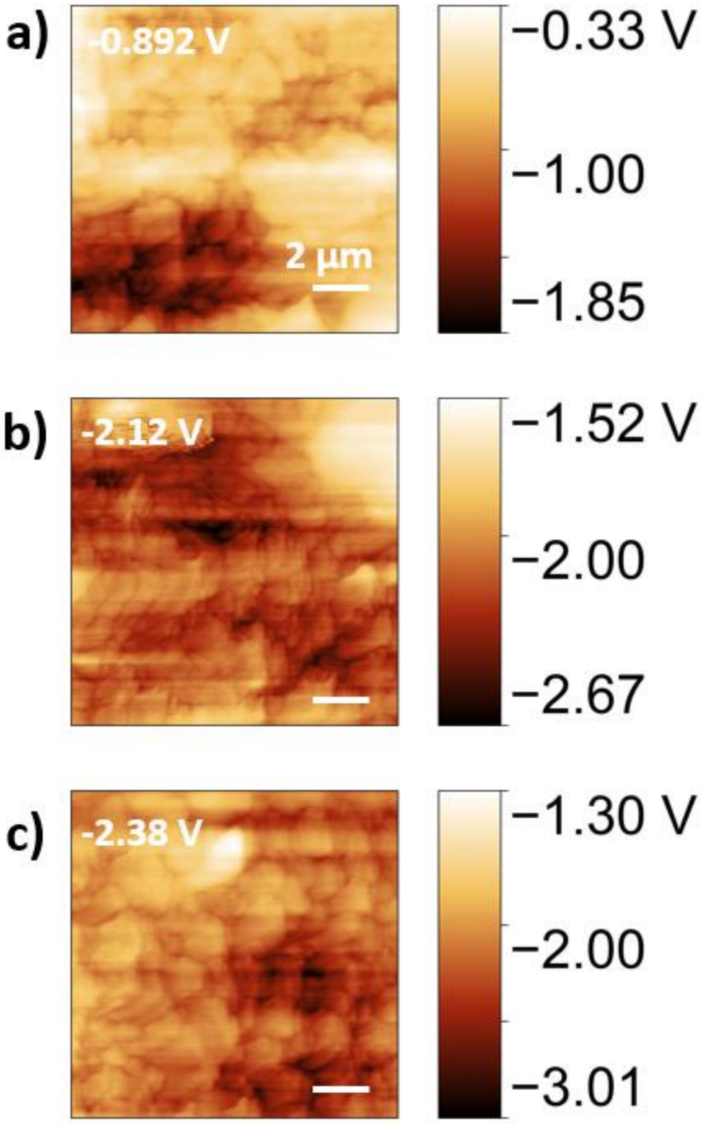

Figure 5.11. Surface potential of (a) ZIF-8-CH_3/PVDF, (b) ZIF-8-Br/PVDF, and (c) ZIF-8-Cl/PVDF measured by Kelvin Probe Force Microscopy (KPFM), with average surface potential denoted at the top left corner.

5.3 Paper II: *Triboelectric Nanogenerators Based on Composites of Zeolitic Imidazolate Frameworks Functionalised with Halogenated Ligands for Contact and Rotational Mechanical Energy Harvesting*

Online version: https://doi.org/10.1021/acsanm.4c06732

ACS APPLIED NANO MATERIALS

www.acsanm.org

Article

Triboelectric Nanogenerators Based on Composites of Zeolitic Imidazolate Frameworks Functionalized with Halogenated Ligands for Contact and Rotational Mechanical Energy Harvesting

Jiahao Ye, Tianhuai Xu, and Jin-Chong Tan*

Cite This: *ACS Appl. Nano Mater.* 2025, 8, 3942−3953

Read Online

ACCESS | Metrics & More | Article Recommendations | SI Supporting Information

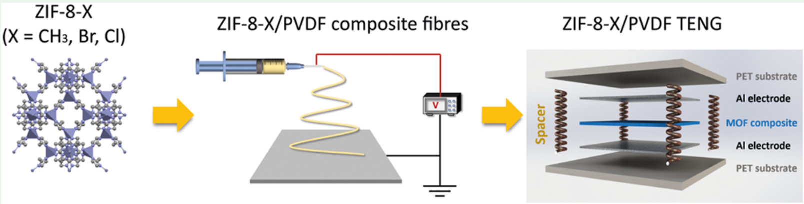

ABSTRACT: Triboelectric nanogenerator (TENG) based on the coupling effect of triboelectrification and electrostatic induction can convert mechanical motions into electric energy. Recent studies have found that metal−organic framework materials are promising triboelectric materials due to their large surface area and excellent tunability. In this study, we incorporated isostructural zeolitic imidazolate frameworks, ZIF-8-X (X = CH_3, Br, Cl), into poly(vinylidene fluoride) (PVDF) electrospun fibers and assembled them in TENG devices to investigate the underlying relationship between functional group electronegativity (via varied imidazolate linkers) and triboelectric output performance. Results show that ZIF-8-Cl/PVDF composite fiber demonstrated the highest average voltage and current output of 312.4 ± 2.0 V and 4.90 ± 0.07 μA, respectively, which are 3.8 and 5.5 times higher than that of the pristine PVDF. The practicality of ZIF-8-X-based TENG was tested for harvesting energy from oscillatory motions to power up LEDs and capacitors. A freestanding mode TENG based on ZIF-8-Cl was also designed to harvest rotational energy without physical contact for wider applications. The working mechanism of ZIF-8-X-based TENG was also revealed through nanoscale-resolved chemical studies, providing valuable insights into the design of MOF materials for improved performance of TENGs.

KEYWORDS: *triboelectric nanogenerators, metal−organic frameworks, composite material, functionalization, electrospinning*

1. INTRODUCTION

In the era of the Internet of Things (IoT), there has been an increasing demand for small-scale, mobile sensors. By 2030, more than 100 billion sensors are projected to be connected to the IoT with the electronics industry expected to grow into a USD 301 billion market in 2028.[1,2] However, the energy supply for this enormous number of sensors could be a big challenge. Current technologies for energy transfer and storage will inevitably raise serious environmental concerns and maintenance difficulties.[3,4] Therefore, triboelectric nanogenerator (TENG), an evolving energy harvesting technology, has drawn tremendous attention from researchers for its outstanding ability to convert mechanical motions into electrical energy under a variety of scenarios.[5−12]

Metal−organic framework (MOF), a class of porous materials that are fabricated by the coordination bond between organic ligands and inorganic metal ions, has diverse applications in gas absorption,[13] drug delivery,[14] catalysis,[15] and sensing.[16] Recently, various studies have explored the potential of using MOF for triboelectric nanogenerators.[17−23] Attributed to their highly tunable structure and functional properties, MOFs have shown significantly improved TENG performance by enhancing charge generation capabilities and retaining device stability across diverse environmental conditions and applications.[24,25] In 2019, Wen et al. introduced a copper-based MOF, HKUST-1, to improve the humidity resistance of the fabricated TENG devices due to the absorption of water molecules by HKUST-1 filler and subsequently higher dielectric constant.[26] Following this, a fluorinated MOF was prepared by Guo et al. as a bifunctional filler to enhance the triboelectric performance of the device.[27] Despite these promising advancements, a deeper understanding of the basic mechanisms and design principles of MOF-TENG systems is crucial for further development of this field.[28]

Received: November 30, 2024
Revised: February 3, 2025
Accepted: February 8, 2025
Published: February 18, 2025

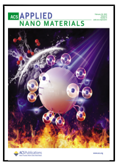

https://doi.org/10.1021/acsanm.4c06732

Recent studies have explored several strategies to enhance the triboelectric output of MOF-based TENGs, with three primary approaches being investigated: by modifying the framework topology,[29] exchanging the metal ion center,[30] and functionalizing the organic ligand.[31−33] Among these strategies, ligand functionalization has emerged as a relatively simple and highly effective method. In 2022, Wen et al. modulated UiO-66 by introducing various functional groups onto the ligands and deposited them onto tin oxide electrodes. The triboelectric output performance of the UiO-66-X (X = H, NH_2, NO_2, Br) films are ranked in the order of NO_2 > Br > H > NH_2, which correlates to the electron-withdrawing nature of the functional group.[32] In addition, Wang et al. reported a high-performance TENG device based on UiO-66-4F, where the enhanced charge generation property was attributed to the strong electron-withdrawing effect of the fluorinated group.[31] While several studies have been conducted on the ligand functionalization approach, most of them have primarily focused on the UiO-66 system, which means that the universal applicability of this approach across different MOF structures remains unexplored. Given the critical role of functional groups in contact electrification,[34] it is essential to develop a clearer understanding of the relationship between the end-group electronegativity and triboelectric output. In this research, we henceforth investigated the broader applicability of the functionalization approach by focusing on a well-studied zeolitic imidazolate framework (ZIF), ZIF-8. Recently, ZIF-8 has been characterized as a tribo-positive material with promising applications in energy harvesting.[35−40] For example, Khandelwal et al. developed the first ZIF-8-based TENG device in 2019, demonstrating a sustainable triboelectric output of 164 V and 7 μA when contacting against Kapton. Moreover, Ma et al. prepared a TENG based on ZIF-8@ZnO as a self-powered methanol sensor. When paired with a tribo-negative PVDF film, the prepared TENG yields a triboelectric output of 58 V and 10 μA, representing 2.4 and 3.3 times enhancement compared to the ZnO-based TENGs, respectively. Despite extensive research on ZIF-8-based TENGs, their triboelectric output remains relatively low compared to other MOF-based devices,[24] and its potential of being a tribo-negative material has yet to be demonstrated.

In this study, we report a general strategy for tailoring and boosting the triboelectric effect of ZIF-8-based TENGs through the ligand functionalization approach. Conventional ZIF-8 (herein designated as ZIF-8-CH_3) has been functionalized with various halogenated groups, including bromine and chlorine groups to yield the ZIF-8-Br and ZIF-8-Cl structures with similar morphology and crystallinity as tribo-negative materials. By incorporating these filler materials into PVDF electrospun fiber, we successfully prepared high-performance nanogenerators with the average electric output of 312.4 ± 2.0 V and 4.90 ± 0.07 μA over 100 cycles achieved by ZIF-8-Cl-based TENG due to the strong electron-withdrawing ability of the chlorinated group. The triboelectric performance of prepared devices shows a consistent trend with the electronegativity of the functional groups, supported by nanoscale-resolved Kelvin probe force microscopy (KPFM) and nanoscale Fourier transform infrared spectroscopy (nano-FTIR) studies. The ZIF-8-Cl-based TENG shows high durability over 40,000 cycles and demonstrates excellent practicability for real-world applications. The high-performance ZIF-8-Cl was further doped into PVDF membranes to build a freestanding mode TENG which further expands the applications of the MOF-based TENG, allowing energy harvesting of rotational energy without physical contact.

2. METHODOLOGY

2.1. Materials. All chemicals used in this study are commercially available. Zinc nitrate hexahydrate ($Zn(NO_3)_2\cdot 6H_2O$), 2-methylimidazole (2-mIm), dimethylformamide (DMF), ethanol, and methanol were purchased from Sigma-Aldrich. 2-Bromo-1H-imidazole (2-Br-Im) and 2-chloro-1H-imidazole (2-Cl-Im) were purchased from Doug Discovery. HSV900 poly(vinylidene fluoride) (PVDF) was obtained from Arkema.

2.2. Synthesis of ZIF-8 and Its Halogenated Derivatives. The synthesis of the ZIF-8-X particles is adapted and modified based on previous reports.[41,42]

(1) For the synthesis of the ZIF-8, herein termed ZIF-8-CH_3, 350 mg of $Zn(NO_3)_2\cdot 6H_2O$ (1.2 mmol) was first dissolved in 15 mL of DMF. After sonication for 5 min, 200 mg of 2-methylimidazole (2.5 mmol) was added to the solution and stirred for another 5 min for complete dissolution. Afterward, the solution was transferred to a 20 mL PTFE-lined stainless-steel autoclave and heated at 100 °C for 72 h. After cooling to room temperature, the resulting white suspension was centrifuged and washed three times with methanol to remove excessive linker and solvent. 70 mg of white ZIF-8-CH_3 powder was harvested and activated at 70 °C.

(2) For the synthesis of ZIF-8-Br, 121 mg of $Zn(NO_3)_2\cdot 6H_2O$ (0.4 mmol) and 2-bromo-1H-imidazole (120 mg, 0.8 mmol) were dissolved in 4 mL of ethanol.[43] Then, the solution was transferred to a 20 mL PTFE-lined stainless-steel autoclave and heated at 100 °C for 72 h. Then, the same reaction protocol and washing process were followed to yield 60 mg of a yellowish powder.

(3) A similar procedure was followed to prepare ZIF-8-Cl. 121 mg of $Zn(NO_3)_2\cdot 6H_2O$ (0.4 mmol) and 2-chloro-1H-imidazole (120 mg, 0.8 mmol) were dissolved in 4 mL ethanol by stirring for 10 min. The synthesis and washing procedures were the same as previously followed by ZIF-8-Br. 50 mg of yellowish powder was obtained after drying.

2.3. Fabrication of MOF/PVDF Composites. The MOF/PVDF composites were prepared by an electrospinning technique. The PVDF solution used for electrospinning was prepared by dissolving 13.7 wt % of HSV900 PVDF powder in DMF to form a polymer solution. The prepared ZIF-8-X (X = $-CH_3$, $-Cl$, $-Br$) were then combined with the PVDF solution via mechanical mixing to yield a mass ratio of 1:19 between ZIF-8-X and HSV900 PVDF powder. The homogenized solutions were stored in a glass syringe and gradually released by a syringe pump at a rate of 0.15 mL/h through a nozzle (conductive blunt tip). During operation, the blunt tip was electrified at a voltage of 15 kV by a high-voltage generator, with an aluminum foil placed 16 cm underneath the nozzle, acting as the negative charge collector. These parameters were optimized based on our previous studies to achieve a stable Taylor cone at the electrospinning nozzle.[44,45] After 1 h of electrospinning, the electrospun fibers forming a porous membrane were then peeled off and dried to obtain approximately a nominal thickness of 120 ± 8 μm. The nanofibers produced by the high voltage formed uniform composite fibers without obvious MOF aggregation.

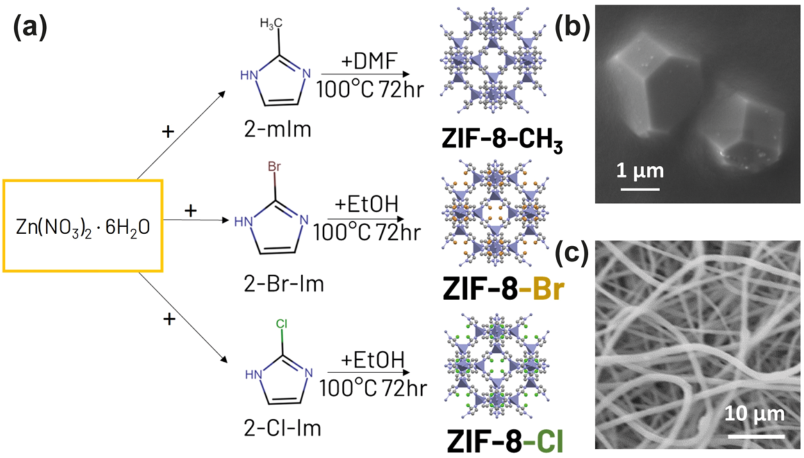

Figure 1. (a) Schematics illustrating the synthesis routes of ZIF-8-X and its halogenated derivatives, where X = $-CH_3$, $-Cl$, $-Br$. (b) SEM micrograph of synthesized ZIF-8-Cl comprising micrometer-sized single crystals. (c) SEM micrograph of ZIF-8-Cl/PVDF fibers fabricated by electrospinning.

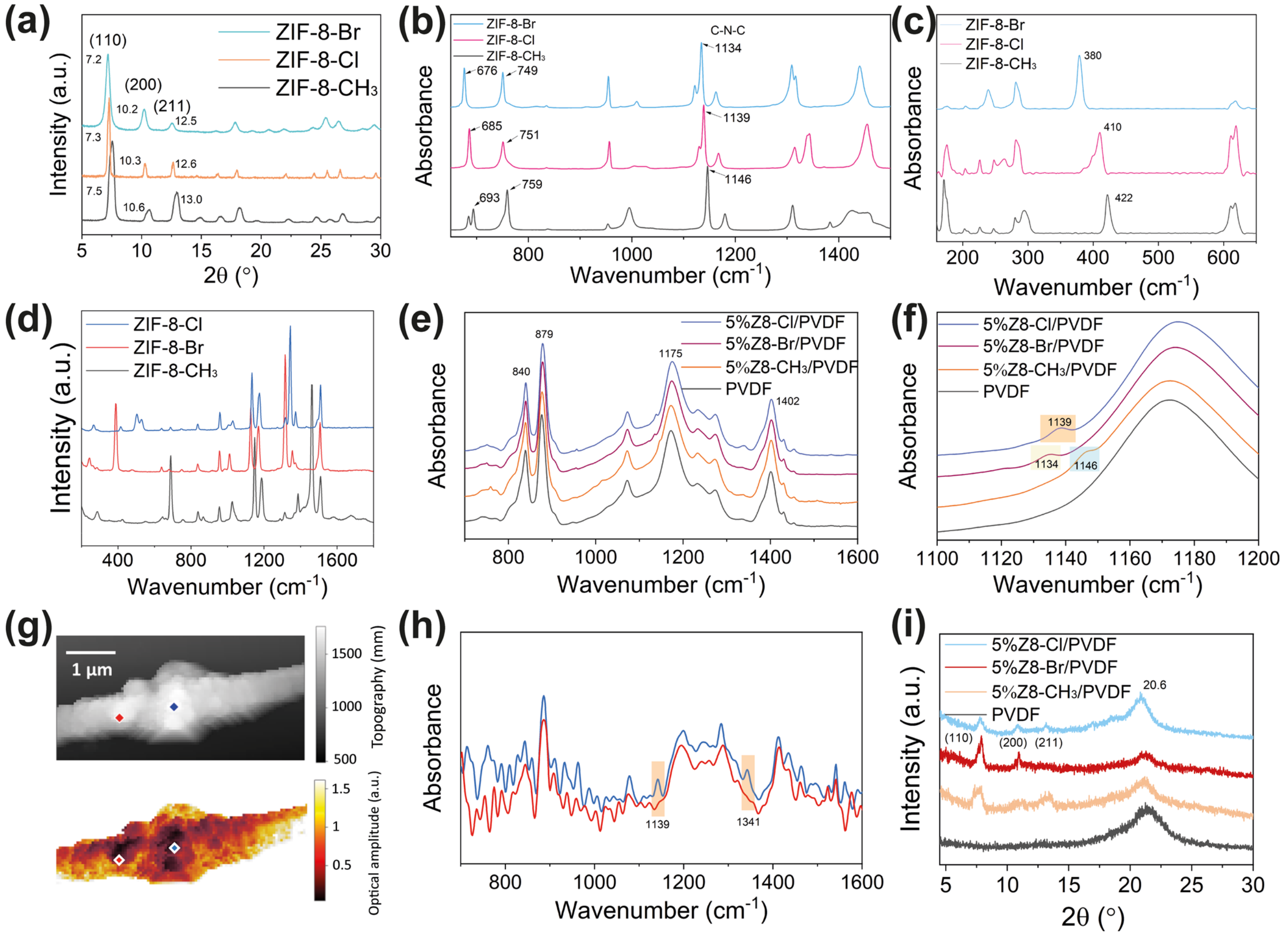

Figure 2. (a) XRD patterns of ZIF-8-X, where X = $-CH_3$, $-Cl$, and $-Br$. (b) ATR-FTIR and (c) synchrotron far-IR spectra of ZIF-8-X nanoparticles. (d) Raman spectra of as-synthesized ZIF-8-X. (e) FTIR spectra of ZIF-8-X/PVDF composites, simplified as Z8-X/PVDF for all figures thereafter. (f) Superimposed FTIR spectra of ZIF-8-X/PVDF composites between 1100 and 1200 cm^{-1}. (g) AFM topography of ZIF-8-Cl composite fiber (top) and its corresponding near-field IR absorption image (bottom). (h) Nano-FTIR spectra correspond to the red and blue points marked on the AFM image. (i) XRD patterns of the ZIF-8-X/PVDF composite fibers.

The fibers are subsequently cut into dimensions of 2 cm × 2 cm for the fabrication of TENG devices.

2.4. Testing of Contact-Separation Mode TENG. Aluminum foils of 2 cm × 2 cm in size were attached to the center of PET substrates with dimensions of 3 cm × 3 cm. Then, the electrospun membrane comprising MOF/PVDF composite fibers was sandwiched between a pair of Aluminum foils. Four TENG devices were prepared by PVDF, ZIF-8-CH_3/PVDF, ZIF-8-Br/PVDF, and ZIF-8-Cl/PVDF. For a standard test, a prepared TENG device was vertically attached to the sample holder connected to a load cell (RS PRO). A permanent magnet shaker (Brüel & Kjær LDS V201) powered by a voltage-amplified arbitrary function generator (GW Instek AFG-2105) was operated on the other side of the TENG device to generate the contact-separation motion. To examine the triboelectric response of the prepared TENG under varying humidities, the setup was encapsulated in an enclosed glovebag. Humidified air was first introduced through a bubbler filled with water to increase the relative humidity (RH) up to 60%, ensuring no potential damage on the equipment. Subsequently, pure dry nitrogen gas was purged into the glovebag to gradually reduce the RH down to 10% while recording the triboelectric output of the TENG devices under contact-separation mode.

2.5. Testing of Freestanding Mode TENG. MOF/PVDF composites comprising ZIF-8-Cl for the freestanding mode TENG were prepared by the doctor blade coating method. The ZIF/polymer solution mixture was dripped onto a glass substrate, which had a sharp doctor blade at a fixed distance above the surface. The blade is then moved in line with the surface to obtain a film with a uniform thickness of 100 μm. The freestanding mode was designed to study the energy harvesting ability of TENG devices under rotational motions. The setup comprises a stator and a rotor. The rotor was a 3D-printed fan blade-shaped substrate coated with the ZIF-8-Cl/PVDF membrane. A motor was connected to the substrate to generate and control the rotational motion of the rotor. The stator was designed with noncontacting inner and outer electrodes which allows the periodic displacement of active material along the two electrodes while it rotates. The rotational speed of the sample was measured with a tachometer (RS AT-8).

2.6. Characterization. A field-emission scanning electron microscope (FESEM LYRA3 GM TESCAN) was used to examine the surface morphologies of the prepared MOF and the MOF/PVDF composite materials. Energy-dispersive X-ray spectroscopy (EDS) was conducted on a microscope to evaluate the element composition of prepared samples. X-ray diffraction (XRD) was performed on a Rigaku MiniFlex with a Cu Kα source (1.541 Å) to determine the crystallinity of the samples. Atomic force microscopy (AFM) height topography and nano-FTIR spectra of ZIF-8-X and composite fibers were characterized by a scattering-type scanning near-field optical microscope (Neaspec s-SNOM). Fourier transform infrared (FTIR) spectroscopy was performed with a Nicolet iS10 FTIR spectrometer equipped with an attenuated total reflectance (ATR) module. The far-IR spectrum was recorded at the multimode IR imaging and microspectroscopy (MIRIAM) Beamline B22 at the Diamond Light Source synchrotron. A Bruker Vertex 80v FTIR spectrometer equipped with an ATR accessory (Bruker Optics) was used to perform the measurement. The surface potential image was obtained in Kelvin probe force microscopy (KPFM) mode by using an Asylum Research Cypher AFM. The confocal Raman spectra were obtained by an Oxford Instruments WITec Raman microscope. The electrical outputs, including voltage and current, were measured by a digital oscilloscope (PicoScope 5444B) with a 100 MΩ high-voltage probe (Rigol RP1300H) and an electrometer (Keithley 6514).

3. RESULTS AND DISCUSSION

A group of functionalized ZIF-8-X materials was synthesized by a solvothermal method under the same reaction time and temperature but with different functional groups, namely, 2-mIm, 2-Br-Im, and 2-Cl-Im, as illustrated in Figure 1a. Figure 1b shows a representative SEM image of ZIF-8-Cl crystals, which displays an average particle size of ca. 2.1 ± 0.5 μm, with a similar morphology to those of other ZIF-8-X materials. The EDS elemental mapping analysis and additional SEM images for ZIF-8-CH_3, ZIF-8-Br, and ZIF-8-Cl (Figures S1−S3, respectively) confirm the successful incorporation of halogenated groups. For TENG device fabrication and triboelectric performance testing, the prepared materials were then embedded into PVDF fiber by electrospinning, with the SEM image shown in Figure 1c. The photographic images of synthesized ZIF-8-X particles and the corresponding composites are shown in Figure S4.

3.1. Material Characterization of ZIF-8-X. Figure 2a shows the XRD patterns of the synthesized ZIF-8-X samples, confirming their good crystallinity. All synthesized MOF crystals exhibit the (110), (200), and (211) facets, which indicate the formation of the sodalite (SOD) topology consistent with the simulated results, as shown in Figure S5. It was observed that the diffraction peaks of the (110) facet for ZIF-8-CH_3, ZIF-8-Cl, and ZIF-8-Br are detected at 2θ of 7.54, 7.29, and 7.17°, respectively. This shift to the smaller diffraction angle means a larger porosity and lattice cell volume of the framework is formed due to the expansion of the unit cell structure by the bulkier end groups of the constituting ligand.[46,47] Moreover, the XRD patterns of ZIF-8-X differ by the relative intensities at (110), (200), and (211) facets, as shown in Figure S5, which is due to the change in preferred orientation induced by the linker substitution.[48] The synthesized ZIF-8-Xs also show good structural stability under ambient conditions and immersion in organic solvents, as illustrated in Figure S6.

In Figure 2b, the ATR-FTIR spectra of ZIF-8-X are similar despite some red shifts of vibrational modes as the linker gets bulkier and with weaker interactions.[49] The shifts of peaks were observed at around 1140, 750, and 680 cm^{-1}, where these IR bands are attributed to the imidazole ring vibrations due to different interactions between the end group and the imidazole ring. As the functional group of the framework gets heavier from CH_3 to Cl and subsequently to Br, the vibrational frequency decreases and thus lowers the wavenumbers. The far-IR spectra shown in Figure 2c reveal the metal−ligand interactions in the terahertz region below ∼20 THz. Similar to ATR-FTIR, it can be seen that the collective mode attributed to the 12 THz peak (∼400 cm^{-1}) systematically shifts toward a smaller wavenumber due to the larger framework. Figure 2d shows the Raman spectra of the ZIF-8-X particles. The spectrum for ZIF-8-CH_3 matches well with previous reports,[50,51] and the spectra for ZIF-8-X are similar in the range of 800−1800 cm^{-1} region, though a minor difference was detected due to the halogenation of the MOF. For ZIF-8-CH_3, the characteristic peak at 686 and 1462 cm^{-1} was observed for C−H bond stretching and in-plane bending modes, respectively. For ZIF-8-Br, C−Br stretching occurs at 390 cm^{-1}, and C−Cl stretching in ZIF-8-Cl takes place at 503 cm^{-1}. The chemical bond vibrations of synthesized ZIF-8-X were also characterized by the near-field nano-FTIR technique, as shown in Figure S7. The height topography images of ZIF-8-X demonstrate the particle morphologies and nano-FTIR was taken on the MOF crystals with a 20 nm spatial resolution.[52] The nano-FTIR spectra show broader peaks compared with ATR-FTIR due to the local measurements performed on isolated single-crystal MOFs, though the same redshift pattern is observed at ∼1150 cm^{-1} for the imidazolate ring stretching due to the bulkier functional group.

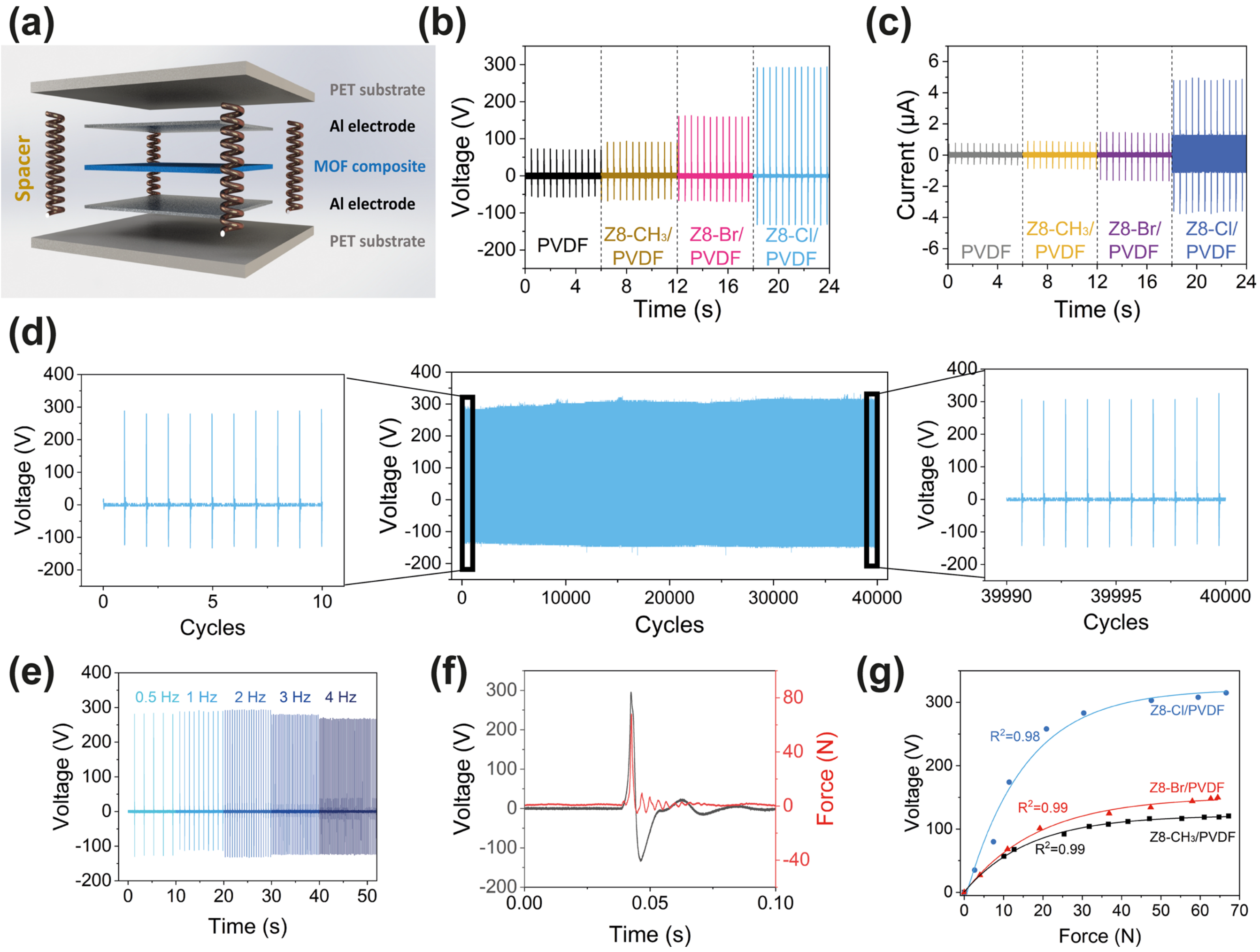

Figure 3. (a) Exploded view illustrating the stacked assembly of the prepared ZIF-8-X/PVDF TENG devices. (b) Open-circuit voltage output of the TENG devices. (c) Closed-circuit current output of the TENG devices. (d) Long-term durability of ZIF-8-Cl/PVDF-based TENG over a continuous running test of 40,000 contact-separation cycles. (e) Voltage output of ZIF-8-Cl/PVDF-based TENG under varying frequencies. (f) Relationship between the force experienced by the TENG device in a contact-separation cycle and the corresponding output current over the same time scale. (g) Voltage output of ZIF-8-X/PVDF-based TENGs under varying forces.

3.2. Material Characterization of ZIF-8-X/PVDF Composites. The synthesized ZIF-8-X are then incorporated into PVDF fiber by electrospinning technique as described in Section 2.3 with a schematic shown in Figure S8. The fiber form PVDF is preferred for the triboelectric nanogenerator application over the casted type PVDF due to a higher effective surface area between the fiber layers. Moreover, higher loading of MOF fillers can be embedded into the fiber without the formation of obvious aggregates due to the larger active surface area. The surface roughness of fiber also provides a higher contact area during the contact-separation process for triboelectric energy generation.[53] The ATR-FTIR spectra of the prepared composite show the evolution of peaks from ZIF-8-X at ∼1140 cm^{-1}, as displayed in Figure 2e,f, demonstrating the successful incorporation of ZIF crystals as a filler into the electrospun fiber matrix. The prepared composite fibers were further characterized by the nano-FTIR technique. The AFM topography of a ZIF-8-Cl embedded fiber in Figure 2g shows the successful incorporation of MOF. As denoted in Figure 2h, the nano-FTIR spectrum on the filler (blue) shows characteristic peaks at 1142 and 1342 cm^{-1} in addition to the neat PVDF matrix (red), which corresponds to the imidazolate ring stretching and aromatic C—N stretching in ZIF-8-Cl.[54] The nano-FTIR characterizations for ZIF-8-CH_3/PVDF and ZIF-8-Br/PVDF fibers are also shown and explained in Figures S9 and S10, respectively. The XRD pattern of the composite fiber shown in Figure 2i indicates the retained crystallinity of ZIF-8-X, showing minimal chemical interactions during the composite fabrication process. The dielectric properties of the prepared composite fibers were measured, and the results are shown in Figure S11. The dielectric constant of the fibers incorporating different MOF fillers exhibits only slight variations in the lower-frequency regime tested, which can be attributed to the low filler concentration and the high porosity inherent to the fibrous material. Although the dielectric constant is considered a crucial factor influencing triboelectric output, its impact has been controlled to isolate the effects of ligand modifications of MOF, ensuring the observed difference in triboelectric performance can be primarily attributed to the ligand modification.

3.3. Electrical Performance. The prepared ZIF-8-X/PVDF composite fibers were cut and assembled into contact-separation type TENG devices for electrical performance testing. The fibers were sandwiched between aluminum electrodes and PET substrates, separated by sponge as spacer, as illustrated in

Figure 3a. Photographs of the assembled device of the ZIF-8-X/PVDF-based TENG and the electrical performance testing rig are shown in Figure S12. The proposed working principle of the designed contact-separation type TENG for the ZIF-8-X-based composite fiber is summarized in Figure S13. In short, triboelectrification happens when ZIF-8-X/PVDF composite fiber contacts the Al electrode, causing electron transfer at the interface. During separation, electrostatic induction due to the potential difference drives electrons back to their original state. An AC output is generated through periodic contact and separation processes.

The electrical outputs of fabricated ZIF-8-X/PVDF fibers including open-circuit voltage and short-circuit current are measured and presented in Figure 3b,c, respectively. With the same MOF loading of 5 wt % into PVDF, ZIF-8-Cl/PVDF generates the highest average output of 312.4 ± 2.0 V and 4.90 ± 0.07 μA calculated from 100 cycles, which is 3.8 and 5.5 times higher than the neat PVDF fiber, followed by ZIF-8-Br and ZIF-8-CH_3. For peak-to-peak voltage, each sample was tested for 100 cycles (as shown in Figure S14) and the average output and standard deviation were calculated and are displayed in Figure S15. The optimum loading of 5 wt % was selected based on the measured voltage output at various mass ratios of MOF fillers in the composites, as shown in Figure S16. This filler concentration was also supported by previous studies on PVDF-based composites,[55,56] serving as a standard to evaluate the effect of ligand modification under consistent parameters. Based on the triboelectric output measurement of prepared ZIF-8-X/PVDF fibers, there is an obvious trend that their performance is markedly different according to the distinctive functional group of ZIF-8-X. To evaluate the effect of those halogen groups, the electrostatic potential maps of functionalized imidazole ligands are simulated using the density functional theory (DFT) by Gaussian 09W software,[57] as displayed in Figure S17. Although the ligands will behave differently within a framework structure, as the nitrogen atoms are coordinated with the zinc ions, the simulation could provide insight into the electron-donating or -withdrawing effects of the functional groups. The methyl group of the 2-mIm linker demonstrates the only positive electrostatic potential on its surface, indicating its electron-donating nature, while 2-Br-Im and 2-Cl-Im exhibit strong electron-withdrawing effects due to the halogen substituents. As a result, the assembled conventional ZIF-8-CH_3 with the methyl group linker has a partial positive charge with low electronegativity, making it less compatible with the high electron-withdrawing ability of PVDF by the presented fluorine groups. As a result, ZIF-8 is normally considered a tribo-positive material in recent studies.[39,40] The minor improvement in the electrical output of ZIF-8-CH_3/PVDF is attributed to the improved surface roughness through the introduction of MOF fillers. As the functional groups become more electronegative from $-CH_3$ to $-$Br and to $-$Cl, both voltage and current output become higher due to the improved triboelectric charge generation property of the resultant material. For each TENG device, the collected voltage and current are relatively stable, with insignificant fluctuation of output. The triboelectric output of the prepared ZIF-8-Cl/PVDF fiber was evaluated against various materials, including copper, PDMS, Kapton, and poly(tetrafluoroethylene) (PTFE), with the corresponding voltage outputs presented in Figure S18. In general, the triboelectric output against aluminum and copper does not show significant differences due to the high electron-donating properties and high conductivity of metals. In contrast, as expected, the triboelectric output is lowered while pairing with other tribo-negative materials such as PDMS, Kapton, and PTFE. This trend aligns with the triboelectric series where materials with similar electron affinity exhibit lower charge generation when paired together. These findings further confirm the highly tribo-negative nature of the ZIF-8-Cl/PVDF composite.

To test the extended stability of the prepared samples, the same sample was tested under ambient temperature and humidity conditions, each with a 12-h interval. The result also shows good voltage output stability as shown in Figure S19. Moreover, the long-term durability of ZIF-8-Cl/PVDF-based TENG was also tested for over 40,000 cycles as demonstrated in Figure 3d. The prepared device maintained an excellent output voltage during long testing cycles, showing great potential for real-world applications. The SEM images of the fibers obtained before and after the durability test are demonstrated in Figure S20, showing minor changes in surface morphology. The sensitivity of prepared composites under various relative humidity (RH) conditions was also tested, as shown in Figure S21. The ZIF-8-Cl/PVDF composite fiber exhibited a relatively stable triboelectric output under low-humidity conditions, indicating its potential for applications in environments with controlled moisture. However, as the humidity increases, a 26% drop in the triboelectric output between 10% RH and 60% RH was observed. This reduction can be attributed to the increase in water adsorption onto the composite surface, which dissipates charge and reduces triboelectric charge generation. However, this 26% reduction of triboelectric output is not higher than that of the pristine PVDF (28%), suggesting that the incorporation of ZIF-8-Cl does not compromise the device performance under humid conditions.

The frequency dependency of the prepared TENG devices is also tested. From a testing frequency of 1−4 Hz, there is no significant change in the output voltage as the frequency varies for each type of TENG device, as shown in Figures 3e and S22. This is due to the same force applied to the material, and the same displacement has been achieved, such that each individual impact can be considered as discrete, independent of frequency. Small reductions of output voltage were observed at higher frequencies, which we attribute to the insufficient displacement during contact and separation. Previous research studied the relationship between the electrical output of TENG and stabilized force instead of the instantaneous peak force. In this case, we were able to measure the applied force and output voltage transiently and simultaneously using an integrated force sensor at one side of the TENG device during the contact-separation cycle. Figure 3f shows the corresponding relationship between current and force for the operation of a ZIF-8-Cl-based TENG recorded on the same time scale. It has been found that for all materials, each contact and separation process only happens within 0.05 s. The positive and negative currents from the current profile demonstrate the signal created during contact and separation, respectively. It is worth noticing that the appearance of current happens slightly before the force is applied, which is at the point when two materials are still approaching, and no physical contact has occurred yet. This finding supported the transfer of electrons as the mechanism during the contacting step. When the two triboelectric materials are approaching, the contact electrification process happens. However, the peak force and peak current occur at almost the same instance which implies that the current output has a strong correlation to the maximum force we applied. Once the applied force is retracted, the negative current shows due to electrostatic

https://doi.org/10.1021/acsanm.4c06732
ACS Appl. Nano Mater. 2025, 8, 3942−3953

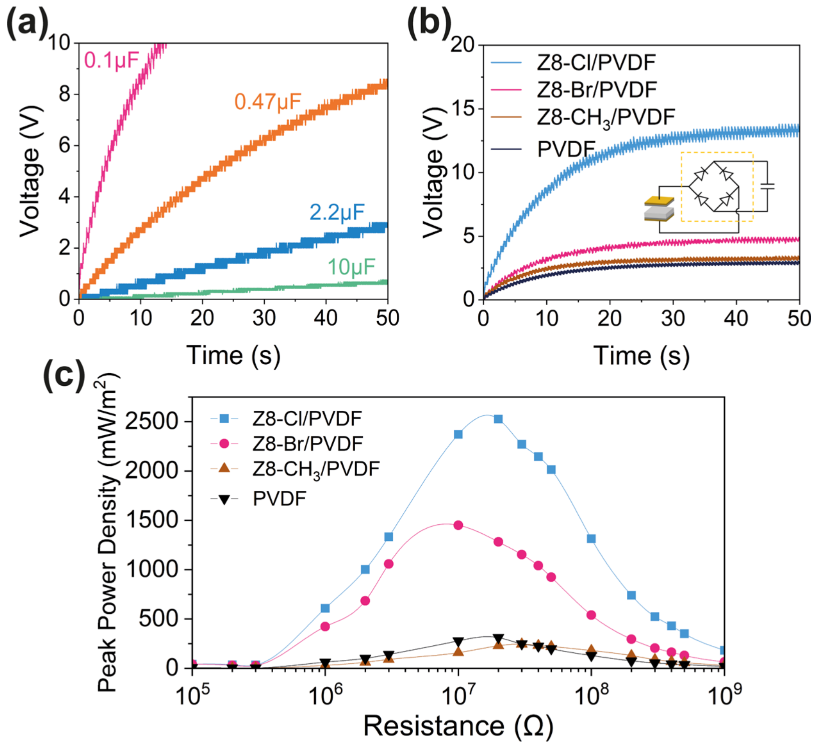

Figure 4. (a) Voltage profiles measured over different capacitors charged by the 2 Hz operation of the ZIF-8-Cl/PVDF-based TENG. (b) Comparison between charging speeds on a 0.1 μF capacitor by different ZIF-8-X-based TENGs. (c) Comparison between the peak power densities of prepared ZIF-8-X/PVDF TENG over a range of load resistances.

induction. The most negative current occurs slightly after the force is completely unloaded, as the triboelectric layers are recovered to their fully separated state. Similar results have been found in the other ZIF-8-X-based TENG devices that we studied, as shown in Figure S23. The relationship between the maximum instantaneous force and output voltage was then recorded by varying the voltage input to our electromagnetic shaker. The result reveals a nonlinear correlation between force and voltage, which can be characterized as an exponential relationship in that the sensitivity of measurement varies between the high- and low-pressure ranges. Figure 3g displays the voltage−force relationships for each of the TENG devices that we prepared under logarithmic fittings. The devices demonstrate a clear and predictable trend between output voltage and force, with R^2 values of over 0.98, suggesting their potential use as highly sensitive pressure or force sensors. This nonlinear relationship originates from the presence of surface roughness on the surfaces of contacting materials.[58] The real contact area between two materials will increase monotonically with the higher applied contact load due to more deformed material surface, until reaching a saturation at full contact based on Persson's contact theory.[59] As a result, the relationship between load and real contact area leads to the nonlinear, logarithmic load dependency observed in the triboelectric output.

3.4. Applications. The alternating current produced by a TENG is harvested and stored in capacitors through a full rectifier circuit to convert it into direct current. Then, the rectified current can be used to charge small commercial electronics, such as calculators, LEDs, and capacitors. Here, several capacitors with capacitances ranging from 0.1 to 10 μF were charged by a steady 2 Hz oscillation motion on the ZIF-8-Cl/PVDF-based TENG, as shown in Figure 4a. The capacitors can be easily charged up to a reasonably high voltage for powering small electronics. The same experiment is done on other prepared TENG devices, and the results are shown in Figure S24. In addition, Figure 4b compares the capabilities of different TENG devices for charging a 0.1 μF capacitor. It is clear that the ZIF-8-Cl/PVDF-based TENG has exceptionally high charging ability compared with other materials, demonstrating excellent potential for energy harvesting. By calculation using the formula $E = 1/2CV^2$, where E is the energy stored in a capacitor, C is the capacitance, and V is the voltage, we found that 22 times more energy is harvested in a 0.1 μF capacitor within 50 s compared with the pristine PVDF. The energy harvested through triboelectric displacement can be rectified to directly power LEDs.

The prepared TENG devices are then connected to an external resistor to form a closed circuit. Here, the closed-circuit voltage of each TENG is measured under different varying resistances from 100 kΩ to 2 GΩ. The power output P was calculated using the equation $P = V^2/R$, where V is the closed-circuit voltage and R is the load resistance. Figure S25 summarizes the detailed correlation between the load resistance and power output for each of the prepared TENG devices. Similar to the capacitor charging correlation, the peak power of the ZIF-8-Cl/PVDF-based TENG is exterior to other devices, with an instantaneous power density of 2.54 W/m^2, 8.2 times higher than PVDF, as shown in Figure 4c. The triboelectric output of the ZIF-8-Cl/PVDF-based TENG is on par with those of other PVDF-based TENG devices incorporating MOF or other filler materials under the contact-separation mode, as summarized in Table S1. Despite variations in the specific experimental configurations across different studies, the voltage, current, and power output of ZIF-8-Cl/PVDF-based TENG in

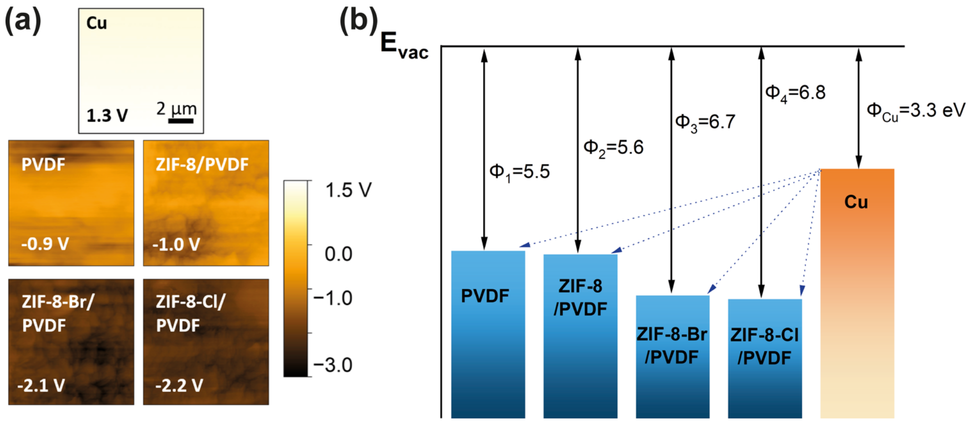

Figure 5. (a) Surface potentials of ZIF-8-X/PVDF composites and Cu electrode from KPFM measurements, presented under the same color scale. (b) Surface state model of ZIF-8-X/PVDF-based TENG. The work functions Φ were calculated based on the measured V_{CPD} value, using a Pt/Ir-coated AFM tip with a reported work function value of 4.6 eV.[63]

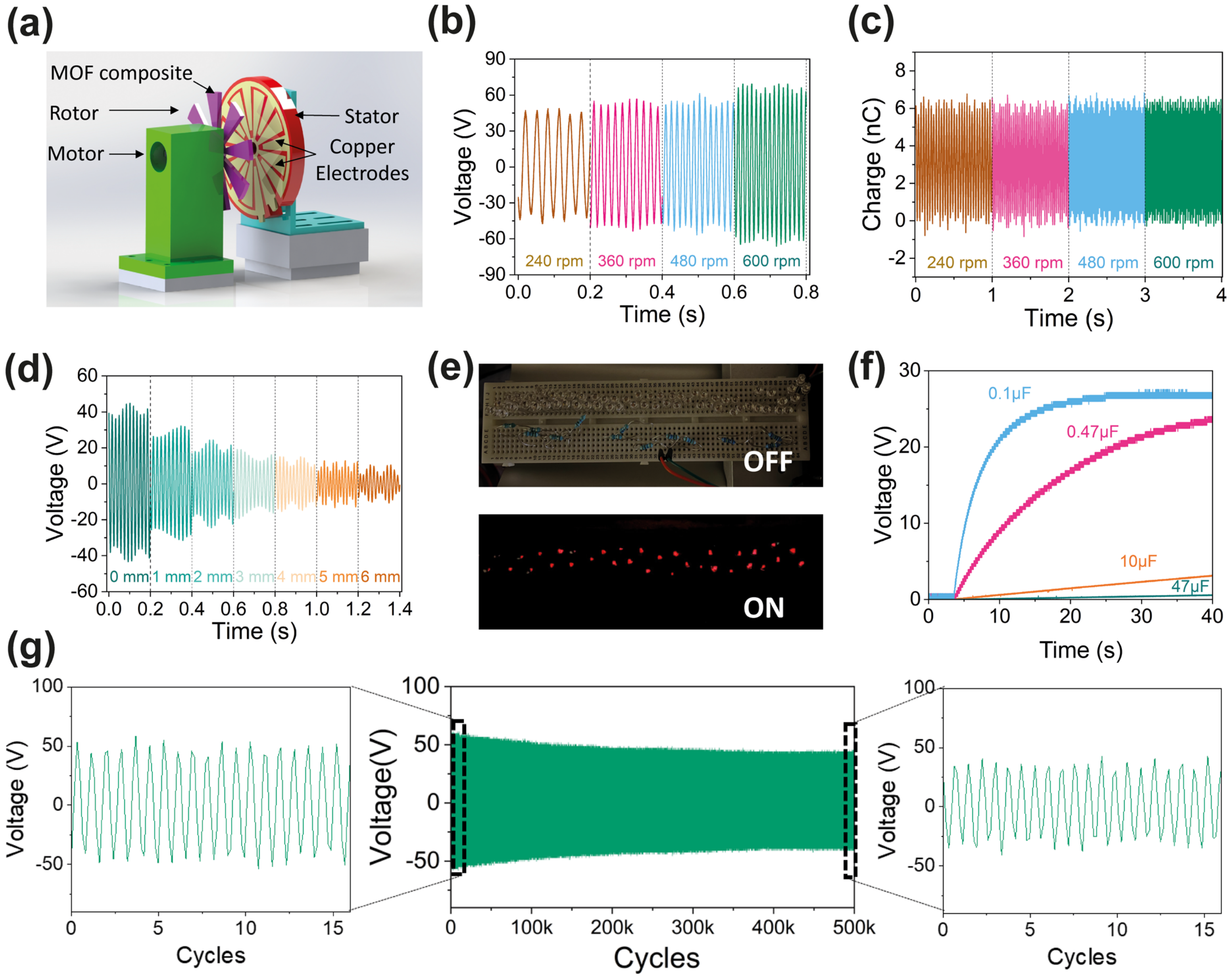

Figure 6. (a) Schematic diagram of noncontacting freestanding TENG setup. (b) Voltage output of ZIF-8-Cl/PVDF-based noncontacting TENG at varying rotational speeds. (c) Charge output of ZIF-8-Cl/PVDF-based noncontacting TENG at varying rotational speeds. (d) Voltage output of ZIF-8-Cl/PVDF-based noncontacting TENG with the same rotational speed but varying gap distance between the rotor and stator. (e) Continuous illumination of 40 LEDs by a ZIF-8-Cl/PVDF-based TENG. (f) Capacitor charging curves by operating ZIF-8-Cl/PVDF-based TENG at 600 rpm for charging the 0.1, 0.47, 10, and 47 μF capacitors. (g) Long-term durability of ZIF-8-Cl/PVDF-based noncontacting mode TENG measured over a continuous test comprising 50,000 cycles.

this work demonstrate comparable performance to other high-performance TENG devices reported in the field.

3.5. Rotational Mechanical Energy Harvesting. To demonstrate more practical applications of the prepared ZIF-8-Cl/PVDF composites, the membranes were also packed in a freestanding mode TENG, as described in Section 2.5, to examine the energy harvesting performance for rotational mechanical motions. Copper plates were used as electrodes in this configuration for their structural rigidity, processability, long-term stability under ambient conditions, and similar triboelectric output compared with aluminum electrodes. Under the designed freestanding mode, the rotor and stator operate without physical contact to minimize material wear. Therefore, the membrane needs to undergo prior tribo-electrification by contacting a copper sheet before assembling into TENG, as the operation of the noncontact TENG relies on the residual charge on the material surface in the absence of contact triboelectrification. The KPFM results denoted an average surface potential of −2.2 V for ZIF-8-Cl-based PVDF film after prior contact, more negative than that of ZIF-8-CH_3 and ZIF-8-Br, as presented in Figure 5a. The KPFM technique measures the contact potential difference (V_{CPD}) of the tested materials, which provides insight into their relative work functions according to the following equation:

$$\Phi_{sample} = \Phi_{tip} - e\cdot V_{CPD} \tag{1}$$

where Φ_{sample} is the work function of the measured ZIF-8-X/PVDF composite, Φ_{tip} is the work function of the KPFM tip, and e is the elementary charge. The work function of a material represents the minimum energy required for the removal of an electron from a solid surface, which has been projected to play a critical role in the output performance of TENG devices.[60,61] According to the electron transfer model, electrons transfer from a material with a lower work function to a higher one to maintain the Fermi level balance.[62] Figure 5b illustrates the surface state model according to the measured work functions. The energy levels of the functionalized composites are positioned according to the calculated work functions based on the measured V_{CPD} determined by KPFM. It is observed that as the functional group of ZIF-8-X changes to more electronegative halogens, the work function of the composites gets higher from 5.5 eV for the neat PVDF to 6.8 eV for the ZIF-8-Cl/PVDF. This increment enlarges the energy gap between the composite and copper. In order to balance the energy, the large energy gap facilitates the hopping of electrons upon contact, thereby generating more charge transfer during contact electrification.

The working principle of the noncontact TENG is illustrated and explained in Figure S26. For the freestanding mode TENG, two electrodes are positioned parallel to each other with an adjustable gap spacing between them and the freestanding dielectric layer (ZIF-8-Cl/PVDF composite membrane) is placed above the electrodes. Triboelectric charges will be induced on the surfaces of electrodes when the composite membrane is moving between the two electrodes, resulting in the flow of charges across the two electrodes through the external circuit.[64,65] As a result, a freestanding mode TENG is a more flexible operating mode that does not require actual contact between the electrode and the dielectric material.

For the more efficient conversion of energy, we designed the inner and outer electrodes with an alternating pattern, as depicted in Figure 6a to enhance the electrical output. During operation, the rotation of active triboelectric material generates a consistent and sinusoidal voltage output, as shown in Figure S27. The design of 8 fan blades on the rotor and stator enables more frequent charge transfer, therefore increasing the AC output frequency. Figure 6b presents the open-circuit voltage of the noncontacting TENG at various rotational speeds, where the increase in rotational speed will improve the voltage output. The same trend is identified for the short-circuit current, as shown in Figure S28. However, it is worth noticing that the charge generated by the noncontacting TENG for each cycle remains constant regardless of the rotational speed as shown in Figure 6c. This is because no triboelectrification happens in noncontacting operational mode and a similar amount of charge is transferred at each cycle. The higher rotational speed increases only the frequency, not the quantity of charge transfer.

Furthermore, the current and voltage produced by a noncontact mode TENG can also be tuned by adjusting the distance between the MOF composite rotor and the electrode. In particular, the current and voltage reduce as the gap increases. By controlling the gap using the vernier stage, it has been observed that both voltage and current will experience exponential decay according to the distance between tribo-electric layers, as shown in Figures 6d and S29. A similar degradation rate was found for the voltage and current after normalization (Figure S30). Since an AC output was generated by the rotational motion, harnessing this energy for practical applications like illuminating LED arrays or charging capacitors requires an additional step of rectification. This process was achieved through the circuit illustrated in Figure S31. Subsequently, the noncontacting TENG was employed to continuously illuminate LEDs due to its relatively high rotation speed (80 Hz), demonstrated in Figure 6e and Video S1, offering distinct advantages over contact-separation mode.[66] In addition, the voltage across various capacitors when included in a circuit connected to the rotary device described is also measured in Figure 6f. The high operating frequency of the noncontacting rotary mode enables faster charging speed compared with the contact-separation mode, thereby offering great opportunities for efficient energy harvesting. The long-term output stability of the composite used in this mode was also tested, as depicted in Figure 6g, demonstrating a relatively high voltage production after 500,000 cycles. Although the absence of physical contact will lead to diminished surface charge over time and therefore a slight degradation of voltage output, the composite exhibits robust retention of triboelectric charges under ambient conditions.

4. CONCLUSIONS

In this work, we demonstrated an effective approach to enhance the triboelectric output of MOF-based materials by modifying their functional groups with higher electron-withdrawing capabilities. Through successful functionalization of ZIF-8 with halogenated groups to yield ZIF-8-Br and ZIF-8-Cl, we established a significant correlation between the electron-withdrawing ability of the functional group and the resulting output performance. Notably, our ZIF-8-Cl/PVDF composite fiber achieved remarkable voltage and current outputs of 312.4 ± 2.0 V and 4.90 ± 0.07 μA, respectively, which are 3.8 and 5.5 times higher than that of the pristine PVDF of the same nominal surface area. Moreover, the prepared ZIF-8-Cl-based device showed 8.2 times higher peak power density and demonstrated stability after 40,000 cycles. The origin of its high triboelectric performance has been revealed through molecular simulation and various nanoresolved characterization techniques including nano-FTIR and KPFM. In addition, practical applications of prepared TENG devices were tested by charging small electronics such as LEDs and capacitors. A rotational free-standing TENG device employing a ZIF-8-Cl/PVDF membrane further extends the practical use of the device, with promising applications in rotational energy harvesting. The proposed ligand halogenation approach, which introduces stronger electronegativity to the MOF, can significantly improve the charge-generating and trapping capability of the material and can be applicable to other tunable MOF structures. We believe this work not only provides valuable insights into the judicious design of MOF materials for improved performance of TENGs but also opens new possibilities for the application of MOFs in sustainable energy solutions.

■ ASSOCIATED CONTENT

Data Availability Statement

Data will be made available upon request.

Supporting Information

The Supporting Information is available free of charge at https://pubs.acs.org/doi/10.1021/acsanm.4c06732.

> X-ray diffraction, ATR-FTIR, nano-FTIR, AFM, and KPFM characterization data; voltage, current, and power output data; schematic diagrams of experimental setups; and device working mechanisms (PDF)
>
> Demonstration of a noncontacting freestanding mode TENG based on ZIF-8-Cl/PVDF composite continuously powering an LED array (Video S1) (MP4)

■ AUTHOR INFORMATION

Corresponding Author

Jin-Chong Tan − *Multifunctional Materials & Composites (MMC) Laboratory, Department of Engineering Science, University of Oxford, Oxford OX1 3PJ, United Kingdom*; orcid.org/0000-0002-5770-408X; Email: jin-chong.tan@eng.ox.ac.uk

Authors

Jiahao Ye − *Multifunctional Materials & Composites (MMC) Laboratory, Department of Engineering Science, University of Oxford, Oxford OX1 3PJ, United Kingdom*; orcid.org/0000-0001-8421-5786

Tianhuai Xu − *Multifunctional Materials & Composites (MMC) Laboratory, Department of Engineering Science, University of Oxford, Oxford OX1 3PJ, United Kingdom*

Complete contact information is available at: https://pubs.acs.org/10.1021/acsanm.4c06732

Author Contributions

J.Y.: Conceptualization, methodology, investigation, formal analysis, writing—original draft preparation, writing—review and editing. T.X.: Methodology, formal analysis, writing—review and editing. J.-C.T.: Conceptualization, supervision, funding acquisition, writing—review and editing.

Notes

The authors declare no competing financial interest.

■ ACKNOWLEDGMENTS

This work was supported by the ERC Consolidator Grant (PROMOFS Grant Agreement 771575) and the EPSRC Award (TEGMOF EP/Z534146/1). We acknowledge the Diamond Light Source for the award of beamtime SM30369 and for the technical support kindly offered by Dr. Gianfelice Cinque during the far-IR measurements on Beamline B22 MIRIAM. We thank Dylan Jubb for his assistance in the design, construction, and testing of the noncontact TENG rig. We are grateful to Dr. Yang Zhang for scientific discussions.

■ REFERENCES

(1) Qiu, C.; Wu, F.; Lee, C.; Yuce, M. R. Self-powered control interface based on Gray code with hybrid triboelectric and photovoltaics energy harvesting for IoT smart home and access control applications. *Nano Energy* **2020**, *70*, No. 104456.

(2) Lu, L.; Hu, G.; Liu, J.; Yang, B. 5G NB-IoT System Integrated with High-Performance Fiber Sensor Inspired by Cirrus and Spider Structures. *Adv. Sci.* **2024**, *11* (18), No. 2309894.

(3) Zhou, Y.; Shen, M.; Cui, X.; Shao, Y.; Li, L.; Zhang, Y. Triboelectric nanogenerator based self-powered sensor for artificial intelligence. *Nano Energy* **2021**, *84*, No. 105887.

(4) Kim, W. G.; Kim, D. W.; Tcho, I. W.; Kim, J. K.; Kim, M. S.; Choi, Y. K. Triboelectric Nanogenerator: Structure, Mechanism, and Applications. *ACS Nano* **2021**, *15* (1), 258−287.

(5) Khandelwal, G.; Maria Joseph Raj, N. P.; Kim, S.-J. Triboelectric nanogenerator for healthcare and biomedical applications. *Nano Today* **2020**, *33*, No. 100882.

(6) Shi, Q.; Sun, Z.; Zhang, Z.; Lee, C. Triboelectric Nanogenerators and Hybridized Systems for Enabling Next-Generation IoT Applications. *Research* **2021**, *2021*, No. 6849171.

(7) Wen, J.; Chen, B.; Tang, W.; Jiang, T.; Zhu, L.; Xu, L.; Chen, J.; Shao, J.; Han, K.; Ma, W.; Wang, Z. L. Harsh-Environmental-Resistant Triboelectric Nanogenerator and Its Applications in Autodrive Safety Warning. *Adv. Energy Mater.* **2018**, *8* (29), No. 1801898.

(8) Jin, T.; Sun, Z.; Li, L.; Zhang, Q.; Zhu, M.; Zhang, Z.; Yuan, G.; Chen, T.; Tian, Y.; Hou, X.; Lee, C. Triboelectric nanogenerator sensors for soft robotics aiming at digital twin applications. *Nat. Commun.* **2020**, *11* (1), No. 5381.

(9) Xu, T.; Ye, J.; Tan, J.-C. Unravelling the Ageing Effects of PDMS-Based Triboelectric Nanogenerators. *Adv. Mater. Interfaces* **2024**, *11*, No. 2400094.

(10) Lin, L.; Wang, S.; Xie, Y.; Jing, Q.; Niu, S.; Hu, Y.; Wang, Z. L. Segmentally Structured Disk Triboelectric Nanogenerator for Harvesting Rotational Mechanical Energy. *Nano Lett.* **2013**, *13* (6), 2916−2923.

(11) Zhang, C.; Liu, Y.; Zhang, B.; Yang, O.; Yuan, W.; He, L.; Wei, X.; Wang, J.; Wang, Z. L. Harvesting Wind Energy by a Triboelectric Nanogenerator for an Intelligent High-Speed Train System. *ACS Energy Lett.* **2021**, *6* (4), 1490−1499.

(12) Feng, T.; Ling, D.; Li, C.; Zheng, W.; Zhang, S.; Li, C.; Emel'yanov, A.; Pozdnyakov, A. S.; Lu, L.; Mao, Y. Stretchable on-skin touchless screen sensor enabled by ionic hydrogel. *Nano Res.* **2024**, *17* (5), 4462−4470.

(13) Qian, Q.; Asinger, P. A.; Lee, M. J.; Han, G.; Mizrahi Rodriguez, K.; Lin, S.; Benedetti, F. M.; Wu, A. X.; Chi, W. S.; Smith, Z. P. MOF-Based Membranes for Gas Separations. *Chem. Rev.* **2020**, *120* (16), 8161−8266.

(14) Gandara-Loe, J.; Souza, B. E.; Missyul, A.; Giraldo, G.; Tan, J. C.; Silvestre-Albero, J. MOF-Based Polymeric Nanocomposite Films as Potential Materials for Drug Delivery Devices in Ocular Therapeutics. *ACS Appl. Mater. Interfaces* **2020**, *12* (27), 30189−30197.

(15) Wang, Q.; Astruc, D. State of the Art and Prospects in Metal−Organic Framework (MOF)-Based and MOF-Derived Nanocatalysis. *Chem. Rev.* **2020**, *120* (2), 1438−1511.

(16) Gutiérrez, M.; Zhang, Y.; Tan, J.-C. Confinement of Luminescent Guests in Metal−Organic Frameworks: Understanding Pathways from Synthesis and Multimodal Characterization to Potential Applications of LG@MOF Systems. *Chem. Rev.* **2022**, *122* (11), 10438−10483.

(17) Rahman, M. T.; Rana, S. M. S.; Zahed, M. A.; Lee, S.; Yoon, E.-S.; Park, J. Y. Metal-organic framework-derived nanoporous carbon incorporated nanofibers for high-performance triboelectric nanogenerators and self-powered sensors. *Nano Energy* **2022**, *94*, No. 106921.

(18) Shaukat, R. A.; Saqib, Q. M.; Kim, J.; Song, H.; Khan, M. U.; Chougale, M. Y.; Bae, J.; Choi, M. J. Ultra-robust tribo- and piezo-electric nanogenerator based on metal organic frameworks (MOF-5) with high environmental stability. *Nano Energy* **2022**, *96*, No. 107128.

(19) Khandelwal, G.; Chandrasekhar, A.; Maria Joseph Raj, N. P.; Kim, S. J. Metal−Organic Framework: A Novel Material for Triboelectric Nanogenerator−Based Self-Powered Sensors and Systems. *Adv. Energy Mater.* **2019**, *9* (14), No. 1803581.

(20) Chen, Z.; Cao, Y.; Yang, W.; An, L.; Fan, H.; Guo, Y. Embedding in-plane aligned MOF nanoflakes in silk fibroin for highly enhanced output performance of triboelectric nanogenerators. *J. Mater. Chem. A* **2022**, *10* (2), 799−807.

(21) Wang, Y. M.; Zhang, X.; Yang, D.; Wu, L.; Zhang, J.; Lei, T.; Yang, R. Highly stable metal-organic framework UiO-66-NH2for high-performance triboelectric nanogenerators. *Nanotechnology* **2022**, *33* (6), No. 065402.

(22) Jayababu, N.; Kim, D. Co/Zn bimetal organic framework elliptical nanosheets on flexible conductive fabric for energy harvesting and environmental monitoring via triboelectricity. *Nano Energy* **2021**, *89*, No. 106355.

(23) Khandelwal, G.; Maria Joseph Raj, N. P.; Vivekananthan, V.; Kim, S. J. Biodegradable metal-organic framework MIL-88A for triboelectric nanogenerator. *iScience* **2021**, *24* (2), No. 102064.

(24) Rajaboina, R. K.; Khanapuram, U. K.; Vivekananthan, V.; Khandelwal, G.; Potu, S.; Babu, A.; Madathil, N.; Velpula, M.; Kodali, P. Crystalline Porous Material-Based Nanogenerators: Recent Progress, Applications, Challenges, and Opportunities. *Small* **2024**, *20* (1), No. 2306209.

(25) Nitha, P. K.; Chandrasekhar, A. Marriage between metal-organic frameworks/covalent-organic frameworks and triboelectric nanogenerator for energy harvesting − A review. *Mater. Today Energy* **2023**, *37*, No. 101393.

(26) Wen, R.; Guo, J.; Yu, A.; Zhai, J.; Wang, Zl. Humidity-Resistive Triboelectric Nanogenerator Fabricated Using Metal Organic Framework Composite. *Adv. Funct. Mater.* **2019**, *29* (20), No. 1807655.

(27) Guo, Y.; Cao, Y.; Chen, Z.; Li, R.; Gong, W.; Yang, W.; Zhang, Q.; Wang, H. Fluorinated metal-organic framework as bifunctional filler toward highly improving output performance of triboelectric nanogenerators. *Nano Energy* **2020**, *70*, No. 104517.

(28) Shao, Z. C.; Chen, J. S.; Xie, Q.; Mi, L. W. Functional metal/covalent organic framework materials for triboelectric nanogenerator. *Coord. Chem. Rev.* **2023**, *486*, 23.

(29) Ye, J.; Tan, J.-C. High-performance triboelectric nanogenerators incorporating chlorinated zeolitic imidazolate frameworks with topologically tunable dielectric and surface adhesion properties. *Nano Energy* **2023**, *114*, No. 108687.

(30) Chen, J.; Shao, Z.; Zhao, Y.; Xue, X.; Song, H.; Wu, Z.; Cui, S.; Zhang, L.; Huang, C.; Mi, L.; Hou, H. Metal-Ion Coupling in Metal-Organic Framework Materials Regulating the Output Performance of a Triboelectric Nanogenerator. *Inorg. Chem.* **2022**, *61* (5), 2490−2498.

(31) Wang, Y. M.; Zhang, X. X.; Liu, C. S.; Wu, L. T.; Zhang, J. J.; Lei, T. M.; Wang, Y.; Yin, X. B.; Yang, R. S. Remarkable improvement of MOF-based triboelectric nanogenerators with strong electron-withdrawing groups. *Nano Energy* **2023**, *107*, No. 108149.

(32) Wen, R. M.; Feng, R.; Zhao, B.; Song, J. F.; Fan, L. M.; Zhai, J. Y. Controllable design of high-efficiency triboelectric materials by functionalized metal-organic frameworks with a large electron-withdrawing functional group. *Nano Res.* **2022**, *15* (10), 9386−9391.

(33) More, Y. D.; Saurabh, S.; Mollick, S.; Singh, S. K.; Dutta, S.; Fajal, S.; Prathamshetti, A.; Shirolkar, M. M.; Panchal, S.; Wable, M.; Ogale, S.; Ghosh, S. K. Highly Stable and End-group Tuneable Metal−Organic Framework/Polymer Composite for Superior Triboelectric Nanogenerator Application. *Adv. Mater. Interfaces* **2022**, *9* (34), No. 2201713.

(34) Li, S.; Nie, J.; Shi, Y.; Tao, X.; Wang, F.; Tian, J.; Lin, S.; Chen, X.; Wang, Z. L. Contributions of Different Functional Groups to Contact Electrification of Polymers. *Adv. Mater.* **2020**, *32* (25), No. 2001307.

(35) Khandelwal, G.; Chandrasekhar, A.; Raj, N.; Kim, S. J. Metal-Organic Framework: A Novel Material for Triboelectric Nanogenerator-Based Self-Powered Sensors and Systems. *Adv. Energy Mater.* **2019**, *9* (14), No. 1803581.

(36) Ma, H. Z.; Luo, C.; Zhao, J. N.; Shao, Y.; Zhang, Y. H.; Liu, X.; Li, S.; Yin, B.; Zhang, K.; Ke, K.; Zhou, L.; Yang, M. B. Metal-Organic Framework Based Triboelectric Nanogenerator for a Self-Powered Methanol Sensor with High Sensitivity and Selectivity. *ACS Appl. Mater. Interfaces* **2023**, *15* (31), 37563−37570.

(37) Li, Q.; An, X. H.; Qian, X. R. Methyl Orange-Doped Polypyrrole Promoting Growth of ZIF-8 on Cellulose Fiber with Tunable Tribopolarity for Triboelectric Nanogenerator. *Polymers* **2022**, *14* (2), 332.

(38) Hajra, S.; Sahu, M.; Sahu, R.; Padhan, A. M.; Alagarsamy, P.; Kim, H. G.; Lee, H.; Oh, S.; Yamauchi, Y.; Kim, H. J. Significant effect of synthesis methodologies of metal-organic frameworks upon the additively manufactured dual-mode triboelectric nanogenerator towards self-powered applications. *Nano Energy* **2022**, *98*, No. 107253.

(39) Liu, M. N.; Chen, T.; Yin, F.; Song, W. Z.; Wu, L. X.; Zhang, J.; Ramakrishna, S.; Long, Y. Z. Smart Bandage Based on a ZIF-8 Triboelectric Nanogenerator for In Situ Real-Time Monitoring of Drug Concentration. *ACS Appl. Mater. Interfaces* **2024**, *16* (30), 39079−39089.

(40) Pandey, P.; Thapa, K.; Ojha, G. P.; Seo, M.-K.; Shin, K. H.; Kim, S.-W.; Sohn, J. I. Metal-organic frameworks-based triboelectric nanogenerator powered visible light communication system for wireless human-machine interactions. *Chem. Eng. J.* **2023**, *452*, No. 139209, DOI: 10.1016/j.cej.2022.139209.

(41) Chaplais, G.; Fraux, G.; Paillaud, J.-L.; Marichal, C.; Nouali, H.; Fuchs, A. H.; Coudert, F.-X.; Patarin, J. Impacts of the Imidazolate Linker Substitution (CH3, Cl, or Br) on the Structural and Adsorptive Properties of ZIF-8. *J. Phys. Chem. C* **2018**, *122* (47), 26945−26955.

(42) Tu, M.; Xia, B.; Kravchenko, D. E.; Tietze, M. L.; Cruz, A. J.; Stassen, I.; Hauffman, T.; Teyssandier, J.; De Feyter, S.; Wang, Z.; Fischer, R. A.; Marmiroli, B.; Amenitsch, H.; Torvisco, A.; Velasquez-Hernandez, M. J.; Falcaro, P.; Ameloot, R. Direct X-ray and electron-beam lithography of halogenated zeolitic imidazolate frameworks. *Nat. Mater.* **2021**, *20* (1), 93−99.

(43) Abraha, Y. W.; Tsai, C.-W.; Niemantsverdriet, J. W. H.; Langner, E. H. G. Optimized CO2 Capture of the Zeolitic Imidazolate Framework ZIF-8 Modified by Solvent-Assisted Ligand Exchange. *ACS Omega* **2021**, *6* (34), 21850−21860.

(44) Zhang, Y.; Tan, J.-C. Electrospun rhodamine@MOF/polymer luminescent fibers with a quantum yield of over 90%. *iScience* **2021**, *24* (9), No. 103035.

(45) Kachwal, V.; Mollick, S.; Tan, J.-C. Tailored Broad-Spectrum Emission in Hybrid Aggregation Induced Emission (AIE)-MOFs: Boosting White Light Efficiency in Electrospun Janus Microfibers. *Adv. Funct. Mater.* **2024**, *34* (6), No. 2308062.

(46) Yagi, R.; Ueda, T. Substitution (CH3, Cl, or Br) effects of the imidazolate linker on benzene adsorption kinetics for the zeolitic imidazolate framework (ZIF)-8. *Phys. Chem. Chem. Phys.* **2023**, *25* (30), 20585−20596.

(47) Abid, H. R.; Azhar, M. R.; Iglauer, S.; Rada, Z. H.; Al-Yaseri, A.; Keshavarz, A. Physicochemical characterization of metal organic framework materials: A mini review. *Heliyon* **2024**, *10* (1), No. e23840.

(48) Grassi, G.; Scala, A.; Piperno, A.; Iannazzo, D.; Lanza, M.; Milone, C.; Pistone, A.; Galvagno, S. A facile and ecofriendly functionalization of multiwalled carbon nanotubes by an old mesoionic compound. *Chem. Commun.* **2012**, *48* (54), 6836−6838.

(49) Andreeva, A. B.; Le, K. N.; Chen, L.; Kellman, M. E.; Hendon, C. H.; Brozek, C. K. Soft Mode Metal-Linker Dynamics in Carboxylate MOFs Evidenced by Variable-Temperature Infrared Spectroscopy. *J. Am. Chem. Soc.* **2020**, *142* (45), 19291−19299.

(50) Tanaka, S.; Fujita, K.; Miyake, Y.; Miyamoto, M.; Hasegawa, Y.; Makino, T.; Van der Perre, S.; Cousin Saint Remi, J.; Van Assche, T.; Baron, G. V.; Denayer, J. F. M. Adsorption and Diffusion Phenomena in Crystal Size Engineered ZIF-8 MOF. *J. Phys. Chem. C* **2015**, *119* (51), 28430−28439.

(51) Luanwuthi, S.; Krittayavathananon, A.; Srimuk, P.; Sawangphruk, M. In situ synthesis of permselective zeolitic imidazolate framework-8/

graphene oxide composites: rotating disk electrode and Langmuir adsorption isotherm. *RSC Adv.* **2015**, *5* (58), 46617−46623.

(52) Möslein, A. F.; Gutiérrez, M.; Cohen, B.; Tan, J.-C. Near-Field Infrared Nanospectroscopy Reveals Guest Confinement in Metal−Organic Framework Single Crystals. *Nano Lett.* **2020**, *20* (10), 7446−7454.

(53) Kim, D. W.; Lee, J. H.; Kim, J. K.; Jeong, U. Material aspects of triboelectric energy generation and sensors. *NPG Asia Mater.* **2020**, *12* (1), No. 6.

(54) Zhang, Y.; Jia, Y.; Hou, La. Synthesis of zeolitic imidazolate framework-8 on polyester fiber for PM2.5 removal. *RSC Adv.* **2018**, *8* (55), 31471−31477.

(55) Mondal, S.; Maiti, S.; Paul, T.; Poddar, S.; Das, B. K.; Chattopadhyay, K. K. CsPbI3−PVDF Composite-Based Multimode Hybrid Piezo-Triboelectric Nanogenerator: Self-Powered Moisture Monitoring System. *ACS Appl. Mater. Interfaces* **2024**, *16* (7), 9231−9246.

(56) Bhatta, T.; Sharma, S.; Shrestha, K.; Shin, Y.; Seonu, S.; Lee, S.; Kim, D.; Sharifuzzaman, M.; Rana, S. M. S.; Park, J. Y. Siloxene/PVDF Composite Nanofibrous Membrane for High-Performance Triboelectric Nanogenerator and Self-Powered Static and Dynamic Pressure Sensing Applications. *Adv. Funct. Mater.* **2022**, *32* (25), No. 2202145.

(57) Frisch, M.et al. *Gaussian 09*, Revision D.01; Gaussian, Inc.: Wallingford, CT, 2009.

(58) Xu, Y.; Min, G.; Gadegaard, N.; Dahiya, R.; Mulvihill, D. M. A unified contact force-dependent model for triboelectric nanogenerators accounting for surface roughness. *Nano Energy* **2020**, *76*, No. 105067.

(59) Persson, B. N. J. Theory of rubber friction and contact mechanics. *J. Chem. Phys.* **2001**, *115* (8), 3840−3861.

(60) Zhou, J.; Zhang, J.; Deng, Y.; Zhao, H.; Zhang, P.; Fu, S.; Xu, X.; Li, H. Defect-mediated work function regulation in graphene film for high-performing triboelectric nanogenerators. *Nano Energy* **2022**, *99*, No. 107411.

(61) Seung, W.; Yoon, H.-J.; Kim, T. Y.; Ryu, H.; Kim, J.; Lee, J.-H.; Lee, J. H.; Kim, S.; Park, Y. K.; Park, Y. J.; Kim, S.-W. Boosting Power-Generating Performance of Triboelectric Nanogenerators via Artificial Control of Ferroelectric Polarization and Dielectric Properties. *Adv. Energy Mater.* **2017**, *7* (2), No. 1600988.

(62) Xu, C.; Zi, Y.; Wang, A. C.; Zou, H.; Dai, Y.; He, X.; Wang, P.; Wang, Y.-C.; Feng, P.; Li, D.; Wang, Z. L. On the Electron-Transfer Mechanism in the Contact-Electrification Effect. *Adv. Mater.* **2018**, *30* (15), No. 1706790.

(63) Reddy, B. N.; Kumar, P. N.; Deepa, M. A Poly(3,4-ethylenedioxypyrrole)−Au@WO3-Based Electrochromic Pseudocapacitor. *ChemPhysChem* **2015**, *16* (2), 377−389.

(64) Lin, L.; Wang, S.; Niu, S.; Liu, C.; Xie, Y.; Wang, Z. L. Noncontact Free-Rotating Disk Triboelectric Nanogenerator as a Sustainable Energy Harvester and Self-Powered Mechanical Sensor. *ACS Appl. Mater. Interfaces* **2014**, *6* (4), 3031−3038.

(65) Niu, S.; Liu, Y.; Chen, X.; Wang, S.; Zhou, Y. S.; Lin, L.; Xie, Y.; Wang, Z. L. Theory of freestanding triboelectric-layer-based nanogenerators. *Nano Energy* **2015**, *12*, 760−774.

(66) Tcho, I.-W.; Jeon, S.-B.; Park, S.-J.; Kim, W.-G.; Jin, I. K.; Han, J.-K.; Kim, D.; Choi, Y.-K. Disk-based triboelectric nanogenerator operated by rotational force converted from linear force by a gear system. *Nano Energy* **2018**, *50*, 489−496.

https://doi.org/10.1021/acsanm.4c06732
ACS Appl. Nano Mater. 2025, 8, 3942−3953

6

Noncontact TENGs with Fluorinated MOFs for Rotational Energy Harvesting

6.1 Background and motivation

Contact-separation mode TENGs often suffer from material abrasion and degradation due to repetitive frictional forces during operation. Despite the higher triboelectric output from contact-separation mode TENGs, their shorter device lifespan and output stability have limited the potential application of TENG in many areas [177]. This issue is also significant with MOF-based TENG devices, as MOF films are usually considered brittle and easy to crack under high impact forces [178], thereby affecting output stability subject to fatigue loading. To overcome this issue, noncontact TENGs have been developed under freestanding mode to mitigate material wear and tear while maintaining efficient energy harvesting for long-term performance. The noncontact TENGs exhibit improved durability and flexibility, making them suitable for applications in intelligent human-machine interfaces, gesture recognition systems, and wireless sensors [179]. Four distinct structures for noncontact TENGs have been developed, including approach-separation structure [180,181], turnable structure [182,183], spring-assisted structure [184,185], and magnetic-assisted structure [186,187]. Among the four designs, turnable structures have demonstrated excellent potential in the fields of energy collection in complex environments and automatic force sensing due to the continuous triboelectric output and relatively high power density compared to other designs [188].

For example, a rotary TENG was developed by Zhou *et al.* which collects kinetic energy from riding and braking of bicycles under either contact or non-contact mode, as shown in Figure 6.1 [189]. In this work, the movement of steel plate rotator induces charge displacement on the copper stator, generating a peak current output of 10 μA that can illuminate 156 LEDs simultaneously. The performance of the device was maintained after 10.3 km of cycling, demonstrating durable and stable electrical output. Moreover, several other noncontact rotational TENGs with varied structural designs demonstrated excellent potential in practical applications [190,191]. Based on the preliminary development of rotational TENGs conducted in Paper II, this chapter focuses on improving the device configuration and understanding the working mechanism of noncontact TENG. The aim of this study is to design a MOF-based TENG under noncontact mode to overcome the mechanical stability issue with brittleness of MOF while exploring a wider range of applications.

In Chapter 5, halogenated ligands with strong electron-withdrawing effects were shown to significantly improve the triboelectric output of MOF-based TENG devices. This principle can be further applied to noncontact TENG devices to improve their energy harvesting capabilities. Fluorine, the most electronegative element in nature, has been incorporated into several MOF structures to enhance charge transfer efficiency, making them ideal candidates for high-performance MOF-based TENGs. For example, in 2020, Guo *et al.* produced a highly effective TENG by using fluorinated KAUST-8 as a filler material in PDMS matrix [15]. The assembled TENG showed an 11-fold increase in output power compared to pristine PDMS film, attributed to the high electron affinity of fluorinated functional groups and the large surface area of porous MOF materials.

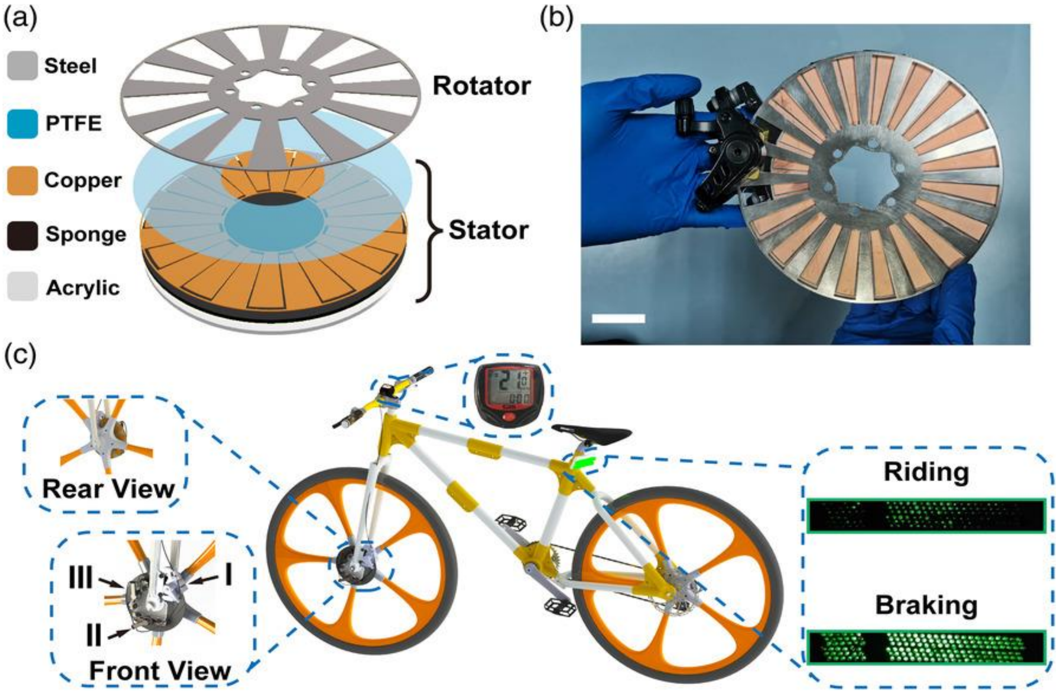

Figure 6.1. The overview of dual mode rotary triboelectric nanogenerator (DMR-TENG). (a) The 3D schematic of rotator and stator of the DMR-TENG. (b) Photograph of the DMR-TENG assembled into a bicycle brake. (Scale bar, 3 cm.) (c) The DMR-TENG is assembled into bicycle brake to drive a speedometer and 156 serial LEDs by collecting rotational kinetic energy as a power source. Inset figures show the front view and rear view of the DMR-TENG. Adapted from ref [189]. Copyright 2021 John Wiley and Sons.

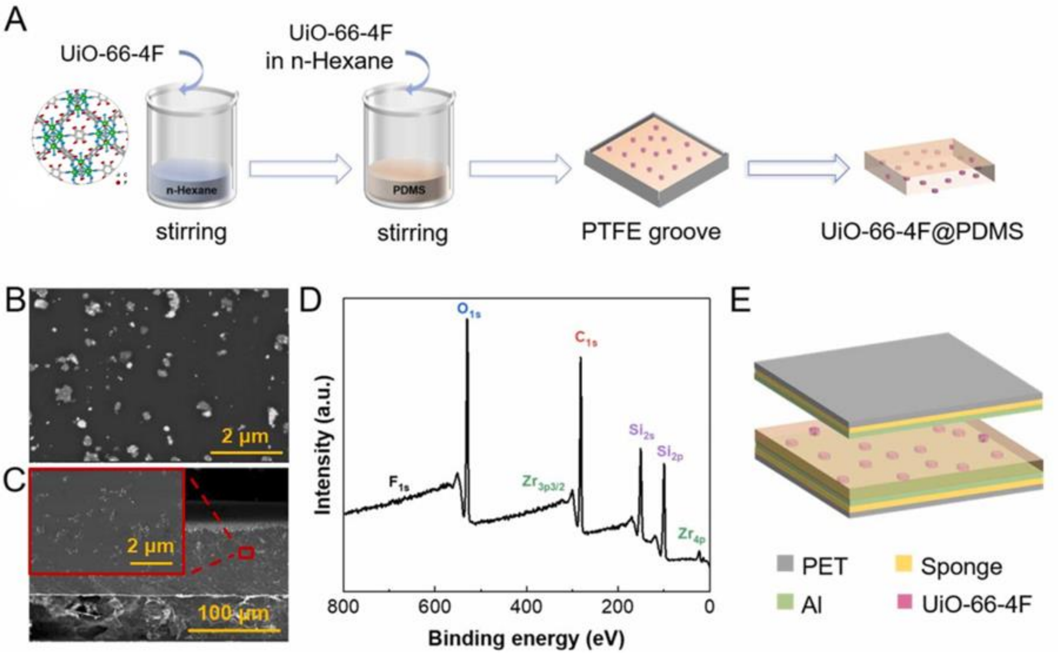

Figure 6.2. (a) Preparation procedure of UiO-66–4 F@PDMS composite films. (b) Top view and (c) side view SEM images of an UiO-66–4 F@PDMS composite film (9 wt.%). (d) XPS spectra of the UiO-66–4 F@PDMS composite film. (e) The schematic diagram of the UiO-66–4 F@PDMS TENG device. Adapted from ref [192]. Copyright 2023 Elsevier.

Moving forward, Wang *et al.* introduced a strongly tribo-negative UiO-66 material through functionalisation by doping high electron-withdrawing fluorine atoms, yielding UiO-66-4F [192]. The synthesised MOF was then embedded into PDMS matrix to prepare TENG devices, as shown in Figure 6.2. The prepared UiO-66–4F@PDMS composite film demonstrated an exceptionally high voltage and current output of 937 V and 30.6 μA, respectively, with 77.5 times higher power density compared to that of TENG without MOF inclusion. This research further emphasised the importance of having strong electron-withdrawing groups within the MOF structure. Given the recent progress in fluorinated MOF on improved performance of TENG devices, this chapter combines the concepts of fluorinated

MOFs and noncontact TENGs to develop an energy harvesting device that achieves both high triboelectric output and long-term durability.

6.2 Summary of Paper III

6.2.1 Preparation of ZIF-8-CF_3 and its composite

ZIF-8-CF_3 was selected as a study candidate due to its high fluorine content and its potential to enhance triboelectric property in prior works [193]. In Chapter 5, a series of ZIF-8-X materials were synthesised through solvothermal reactions (see Section 3.3.1.2). However, the same approach did not yield trifluoromethyl-functionalised ZIF-8 with SOD topology, instead forming QTZ topology due to unfavourable reaction kinetics. To overcome this limitation, ZIF-8-CF_3 in SOD topology was prepared through a mechanical grinding approach with a different metal salt precursor. The reactants were subjected to vortex grinding using three zirconium milling balls. The prepared ZIF-8-CF_3 particles were then embedded in PVDF matrices for enhanced flexibility in noncontact TENG. The SEM image and EDS mapping of the prepared composites are presented in Figure 6.3, confirming the successful incorporation of MOFs with zinc metal ion centres and fluorinated ligands within the PVDF matrix. Additionally, the XRD pattern and FTIR spectra of synthesised ZIF-8-CF_3 demonstrated strong agreement with molecular simulation results, as shown in Paper III (Figure 2).

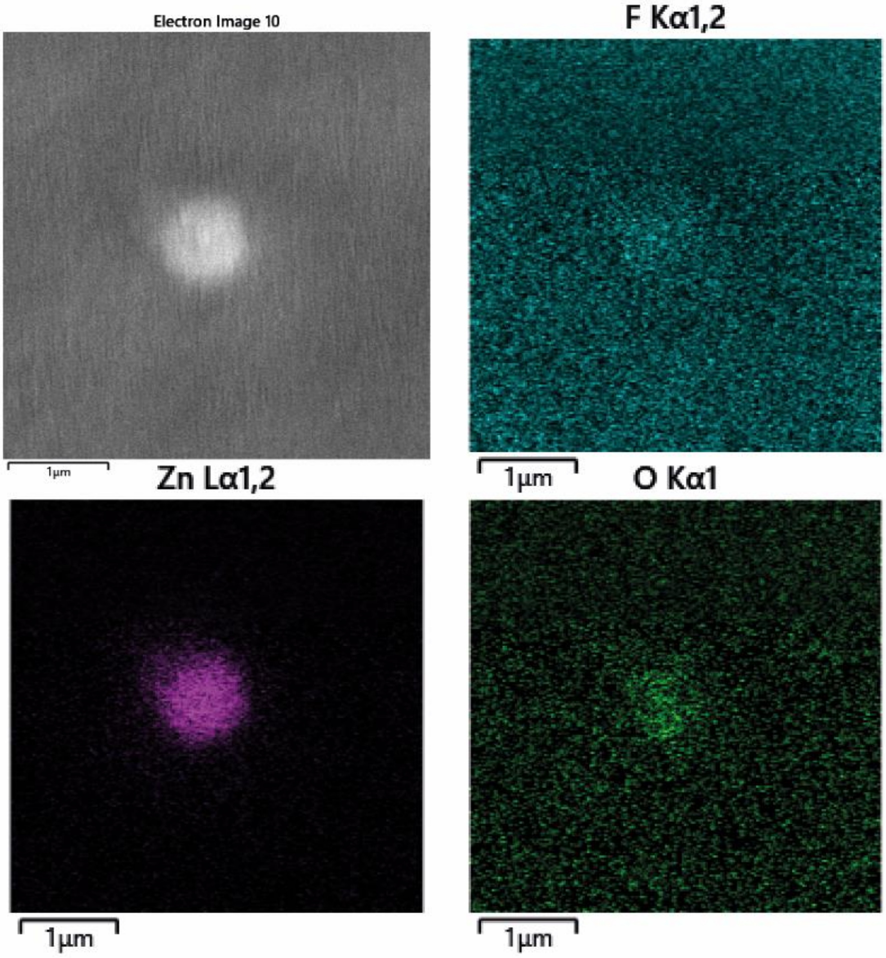

Figure 6.3. SEM image and EDS mapping analysis of ZIF-8-CF_3/PVDF composite film.

The physicochemical properties of synthesised ZIF-8-CF_3 were further characterised using multimodal analytical techniques, including nano-FTIR, synchrotron far-IR microspectroscopy, and confocal Raman imaging, as discussed in Paper III. Figure 6.4 and Figure 6.5 present the far-IR microscopic images and point-by-point spectra of the ZIF-8-CF_3 nanoparticles and ZIF-8-CF_3/PVDF composite films. The far-IR spectrum of MOF reveals the metal-ligand interactions with characteristic vibrational peaks primarily at 276 cm^{-1} and 591 cm^{-1}. The PVDF matrix presented distinctive peaks at 484 cm^{-1} and 510 cm^{-1} in the far-IR region, corresponding to the α-phase and β-phase crystalline interactions, respectively [194]. Within the composite, the band of ZIF-8-CF_3 evolved upon detection of the filler material, demonstrating successful incorporation of filler materials within polymer matrix without significant chemical interactions.

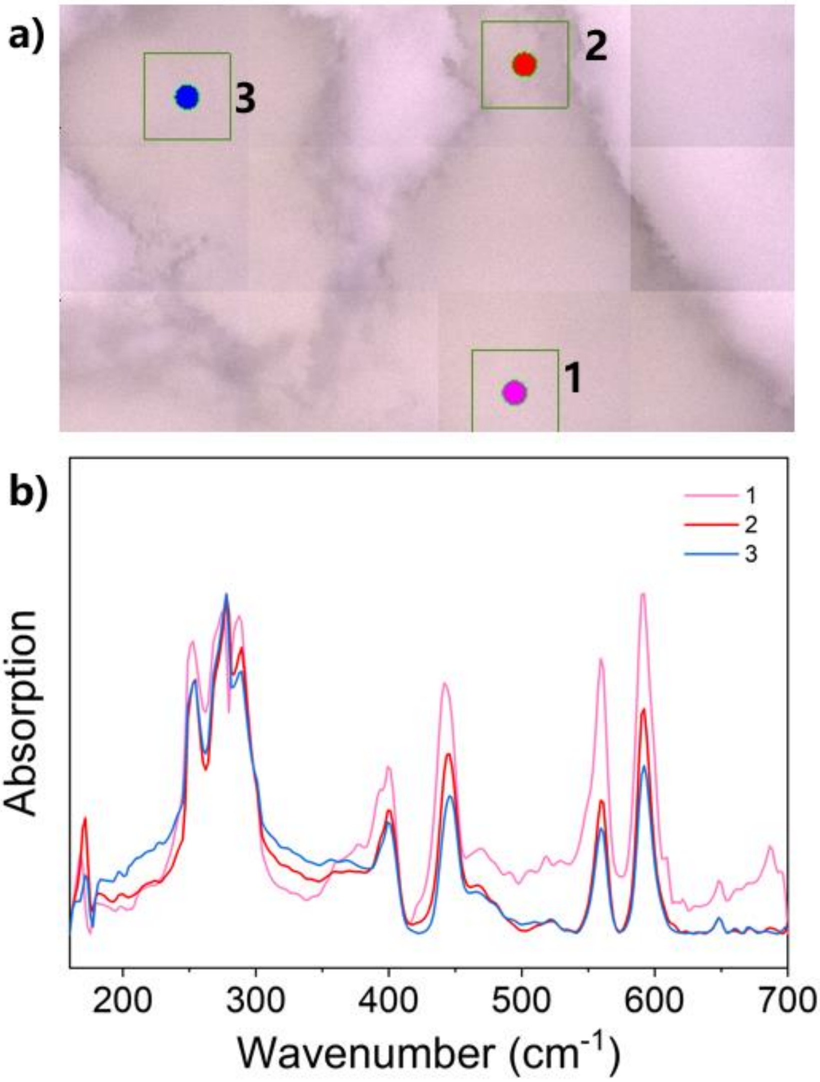

Figure 6.4. (a) Synchrotron far-IR microspectroscopic image and (b) point spectra of ZIF-8-CF_3 at the marked locations.

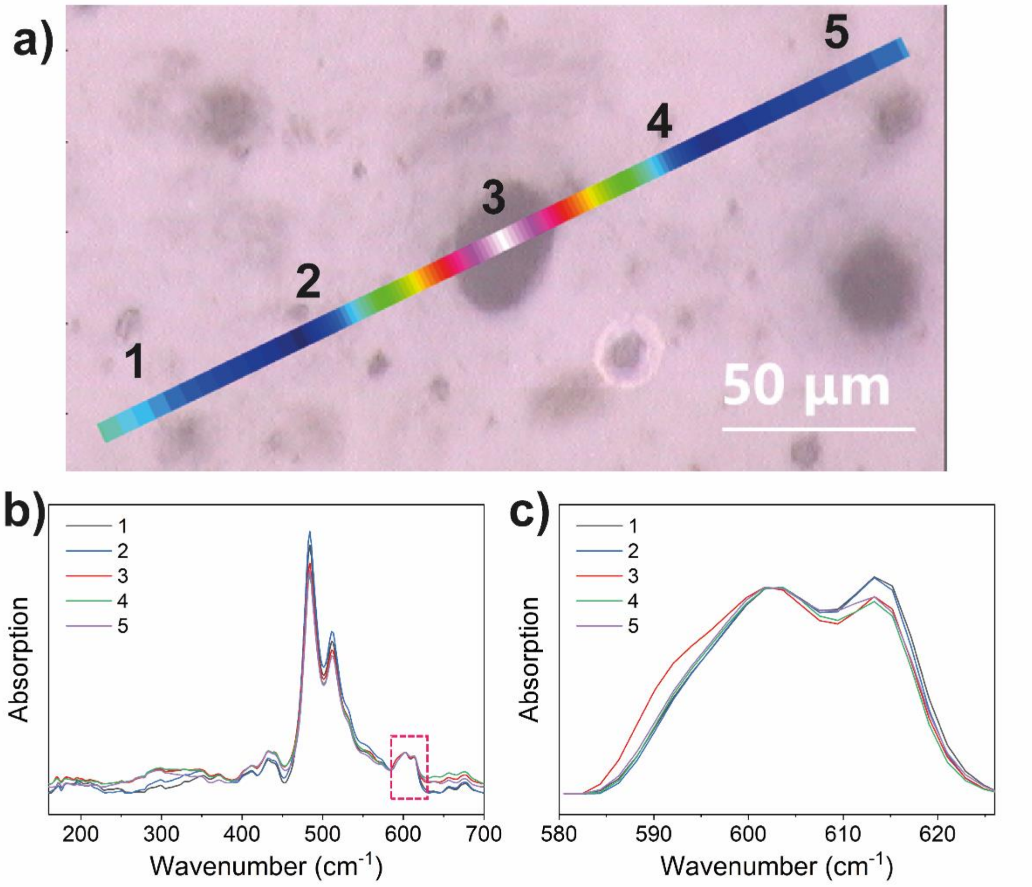

Figure 6.5. (a) Microscopic image of ZIF-8-CF_3/PVDF composite film, and (b, c) synchrotron far-IR spectra of ZIF-8-CF_3/PVDF composite film measured at positions marked in (a).

6.2.2 Design of noncontact TENG

The design of noncontact TENG was developed based on the customised experimental setup described in Chapter 3 (Section 3.1.2). The setup consists of a stator unit with alternatively arranged aluminium electrodes and a rotor unit embedded with prepared ZIF-8-CF_3/PVDF composite. The separation gap between the rotor and stator is maintained at 0.5 mm, allowing charge induction without direct physical contact. The design of the stator unit is illustrated in Figure 6.6, while the rotor has a similar configuration to the inner electrode (electrode 2). The rotor features eight blades that correspond to the alternatively arranged electrodes, increasing the output frequency by 8 times, ensuring the excellent continuity and stability of electrical output.

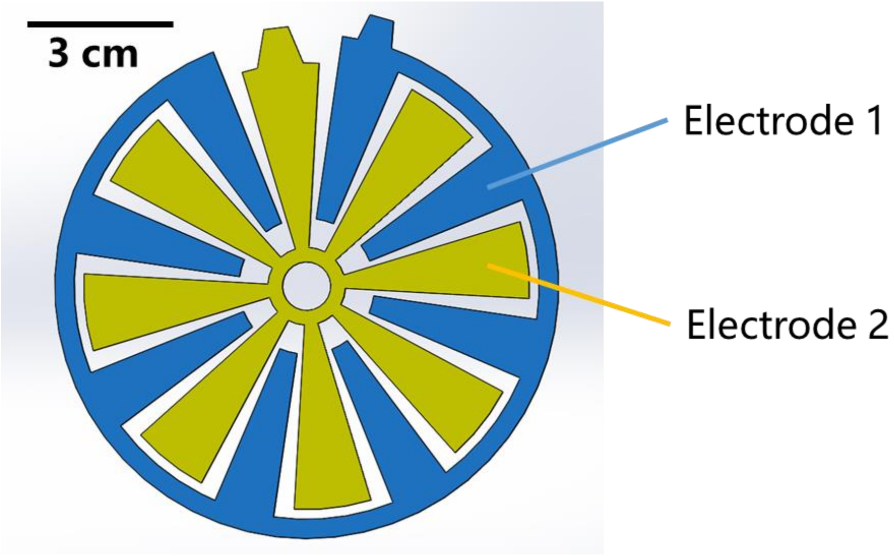

Figure 6.6. Design of stator unit with alternatively arranged electrodes.

The operating mechanism of the designed noncontact TENG is illustrated in detail in Paper III (Figure 3b) and involves two key stages: initially, the prepared tribo-active material on the rotor was contacted with metal to accumulate surface charges. Then, as the rotor rotated, unbalanced surface charges were induced between the alternating electrodes, leading to cyclic electrical output collected between the electrodes. A representative output voltage profile is shown in Figure 6.7, demonstrating a sinusoidal waveform at 80 Hz under an operating frequency of 10 Hz. Compared to conventional contact-separation mode, the noncontact TENG offers several advantages. Firstly, the operating frequency of contact-separation mode TENG is normally limited to 5 Hz, while rotational TENGs enable tuneable output frequencies for a wider range of applications. Moreover, in actual applications, the abrupt mechanical collisions during contact-separation mode usually introduce fluctuations in output, but a smoother waveform can be generated in a noncontact TENG compared to contact-separation mode. Furthermore, the mechanical vibration and noise of operation are kept minimum in noncontact TENG, making it suitable for wearable electronics and biomedical applications. Overall, the designed noncontact rotational mode TENG is a more durable, stable, and efficient alternative to the contact-separation mode, especially for high-speed, long-duration energy harvesting applications.

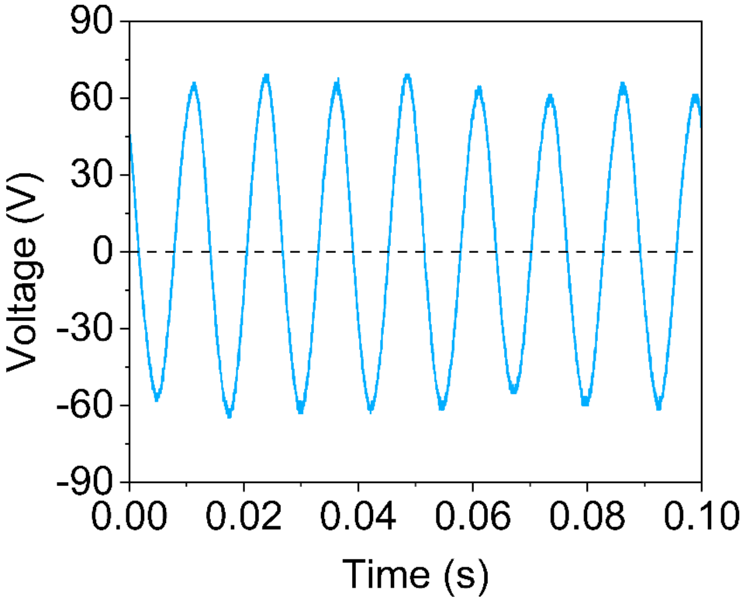

Figure 6.7. An example of voltage output profile from the noncontact TENG with an operating frequency of 10 Hz.

6.2.3 Triboelectric output evaluation

The triboelectric output of ZIF-8-CF_3-based composite under noncontact mode was subsequently evaluated using the customised setup described above. The triboelectric voltage and current output of ZIF-8-CF_3/PVDF-based noncontact TENG were measured and presented in Figure 6.8. The highest voltage and current output of 280 ± 8 V and 19 ± 0.4 μA were achieved under an operating frequency of 30 Hz with a separation gap of 0.5 mm. The voltage output remained relatively stable across different operating frequencies, while the current output showed a linear scaling with rotational speed due to direct proportionality to the charge transfer rate. The reduced voltage with lower frequency was also observed in a few studies related to noncontact TENG, which can be attributed to the increased approaching-separating rate with faster induced charge transfer and the change in gap between the electrodes due to the tremble of rotor during rotation [190,195,196]. Compared to pristine PVDF material, fluorinated ZIF-8-CF_3 significantly improved the triboelectric output under noncontact mode TENG by 1.5 times, as shown in Paper III (Figure 3c). Subsequently, combining the results from theoretical DFT calculations, electrical performance characterisation, and KPFM measurements, the mechanism of enhanced performance by ZIF-8-CF_3-based noncontact TENG was proposed and discussed in Paper III. Firstly, the simulated ESP distribution map of ZIF-8-CF_3 framework demonstrated a heterogeneous distribution of positive and negative charges across the framework structure, with the presence of the highest occupied crystal orbital (HOCO) and lowest unoccupied crystal orbital (LUCO) on the ligands. While charge transfer between materials normally takes place at LUCO, this indicates that the ligands with trifluoromethyl groups have a critical role during the contact electrification process. Moreover, the KPFM measurement on the sample surface detected a lower surface potential value near the area with the filler materials, demonstrating a strong electron-withdrawing ability to increase triboelectric charge generation. Both molecular simulations and experimental results confirmed the excellent performance of ZIF-8-CF_3 based TENG device.

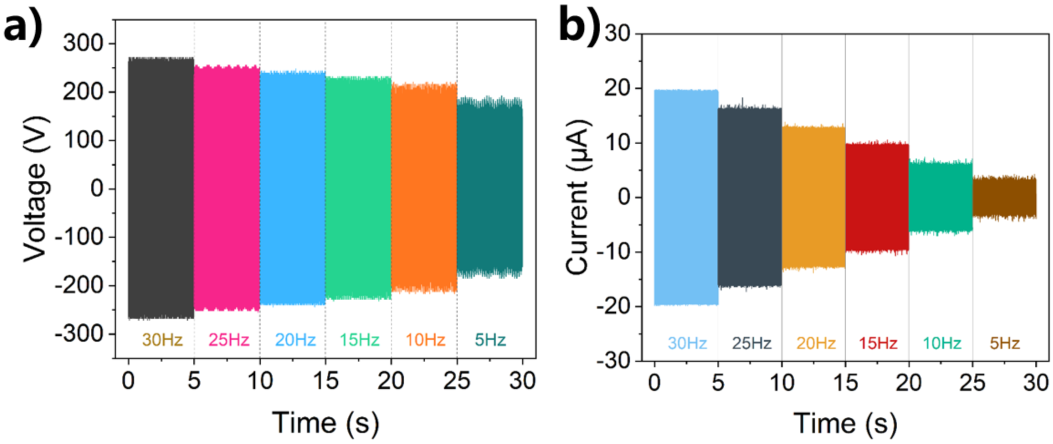

Figure 6.8. (a) The open-circuit voltage output and (b) short-circuit current output of 0.5 wt% ZIF-8-CF_3-based noncontact freestanding TENG under operating frequencies between 5 and 30 Hz.

Moreover, the practical applications of prepared noncontact TENG were verified by harvesting the rotational energy and storing it in capacitors through a rectifier circuit. Notably, the charging rate of capacitors under noncontact rotational mode was significantly higher than that of contact-separation mode TENGs. Here, a 0.1 μF capacitor was charged to 200 V within just 3 seconds owing to the high-frequency output, whereas the contact-separation mode TENG discussed in Chapter 4 reached only 5 V in the same duration. In addition, the noncontact TENG was capable of illuminating an array of over 180 LEDs continuously due to its high electric potential and output frequency. Figure 6.9 demonstrates the charging-discharging curves determined across the capacitor during operation of a timer. As the timer requires a sustained voltage of 1.3 V to operate, the non-contact TENG enables continuous operation of the timer. The noncontact operation mode further expands the boundary of real-life application for MOF-based TENG due to excellent triboelectric output and demonstrates potential in practical applications.

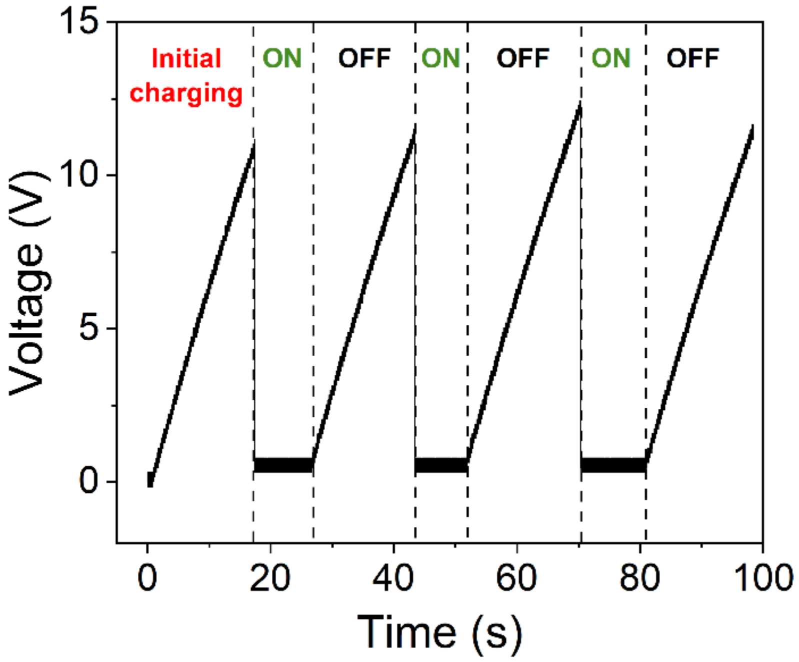

Figure 6.9. Voltage measured across a 10 μF capacitor while charging a timer.

6.3 ***Paper III:*** *Noncontact Triboelectric Nanogenerators Based on Fluorinated Metal-Organic Frameworks for Rotational Energy Harvesting and Sensing*

Online version: https://doi.org/10.1063/5.0273138

APL Electronic Devices

RESEARCH ARTICLE | JULY 15 2025

Noncontact triboelectric nanogenerators based on fluorinated metal–organic frameworks for rotational energy harvesting and sensing

Jiahao Ye ; Gianfelice Cinque ; Lorenzo Donà ; Jin-Chong Tan

Check for updates

APL Electronic Devices 1, 036109 (2025)
https://doi.org/10.1063/5.0273138

View Online

Export Citation

Articles You May Be Interested In

Advancements in triboelectric nanogenerator applications for health monitoring

AIP Advances (October 2024)

Coupling mechanism between photogenerated carriers and triboelectric charges and photoinduced reinforcement of a triboelectric nanogenerator

Appl. Phys. Lett. (August 2021)

Magnetic lifting triboelectric nanogenerators (ml-TENG) for energy harvesting and active sensing

APL Mater. (September 2021)

AIP Publishing

APL Electronic Devices ARTICLE pubs.aip.org/aip/aed

Noncontact triboelectric nanogenerators based on fluorinated metal–organic frameworks for rotational energy harvesting and sensing

Cite as: APL Electron. Devices 1, 036109 (2025); doi: 10.1063/5.0273138
Submitted: 28 March 2025 • Accepted: 25 June 2025 •
Published Online: 15 July 2025

Jiahao Ye,[1] Gianfelice Cinque,[2] Lorenzo Donà,[3] and Jin-Chong Tan[1,a)]

AFFILIATIONS

[1] Multifunctional Materials and Composites (MMC) Laboratory, Department of Engineering Science, University of Oxford, Parks Road, Oxford OX1 3PJ, United Kingdom
[2] Diamond Light Source, Harwell Campus, Chilton, Oxford OX11 0DE, United Kingdom
[3] Department of Chemistry, NIS and INSTM Reference Centre, University of Turin, Torino 10125, Italy

[a)] **Author to whom correspondence should be addressed:** jin-chong.tan@eng.ox.ac.uk

ABSTRACT

Metal–organic framework (MOF) materials have demonstrated promising potential as triboelectric nanogenerators (TENGs) in recent studies due to their unique advantages, such as high surface area and vast tunability in physicochemical response. However, the poor mechanical stability and durability of MOF-based TENGs may limit their practical applications. In this study, a MOF-based, noncontact rotational TENG has been designed using a highly fluorinated MOF, namely, ZIF-8-CF_3, incorporated into a poly(vinylidene fluoride) (PVDF) polymer matrix to enhance triboelectric output and mitigate material abrasion during operation. The noncontact TENG demonstrated excellent voltage and current output of 280 ± 8 V and 19.0 ± 0.4 μA, respectively. The power density of the prepared noncontact TENG based on the composite is ~66 $\mu W/cm^2$, about 2 times higher than that of the neat PVDF-based TENG. The noncontact TENG exhibits excellent mechanical stability, sustaining high triboelectric output over a test comprising half a million cycles. The potential application of the ZIF-8-CF_3/PVDF-based TENG was tested by powering various microelectronics under rotational operations. The prepared rotational device also shows strong potential for use in force and humidity sensing. The basic mechanism of the ZIF-8-CF_3/PVDF-based TENG was revealed by *ab initio* quantum mechanical modeling and nanoscale surface potential analysis.

I. INTRODUCTION

Triboelectric nanogenerators (TENGs), which operate based on contact electrification and electrostatic induction, have attracted significant research interest as an emerging technology for mechanical energy harvesting and self-powered sensors.[1,2] Over the past decade, TENGs have been explored for use in a range of scenarios, including harvesting energy from biomechanical motions,[3] wind,[4] ocean waves,[5] and mechanical vibrations.[6] Although TENGs have many advantages, such as simple fabrication, versatility in design, and excellent device flexibility, the power output of TENGs remains limited by the selection of counter-material pairs for optimal charge transfer. The tribo-positive component of a TENG, which donates electrons, is typically a cost-effective metal such as copper or aluminum, while the tribo-negative counterpart, which has a higher electron affinity, is largely restricted to fluorinated polymers such as polytetrafluoroethylene (PTFE) and poly(vinylidene fluoride) (PVDF). To further expand the choice of high-performance tribo-negative materials, researchers are exploring the potential use of metal–organic framework (MOF) materials for this purpose.

MOFs are a class of nanoporous hybrid materials with high tunability and large internal surface area. Taking their unique structure and physicochemical properties into account, MOFs have been developed for various applications, including gas separation and storage,[7,8] catalysis,[9,10] sensing,[11,12] and drug delivery.[13,14] Recently, MOFs have emerged as a promising candidate for TENG applications, with reports showing that the physicochemical properties of MOFs may significantly improve the performance of TENGs.[15–19]

Research has focused on tuning the MOF structure by functionalizing the organic ligand to enhance triboelectric properties.[20–23] In 2020, Guo *et al.* prepared a fluorinated MOF, KAUST-8, as both a charge-inducing and charge-trapping filler material in a PDMS matrix to yield TENG devices with enhanced triboelectric output.[24] The introduction of fluorine atoms, improved surface roughness, and higher capacitance together led to improved triboelectric performance. Moreover, Wang *et al.* embedded a hydrophobic MOF, UiO-66-4F, within a PDMS polymer to achieve a remarkably high triboelectric output of 937 V.[25] The fluorinated MOF demonstrated great electron-withdrawing ability in both molecular simulation and experimental results. These studies demonstrated that fluorinated MOFs can serve as effective filler materials for triboelectric applications.

Although MOF-based TENGs have been extensively studied in recent years, most research has focused on the contact-separation mode.[26] Despite their high triboelectric output, the structural robustness of MOF-based TENGs under high-frequency and high mechanical impact loads remains a challenge, and it is a major hindrance to commercialization.[15,27] Recently, noncontact triboelectric nanogenerators, which operate based on electrostatic induction, have drawn more attention as they avoid damage and wear on functioning materials due to the absence of direct physical interaction.[28,29] The first tunable-structure noncontact TENG was designed by Lin *et al.*, using fluoroethylene propylene copolymer (FEP) films as the rotary unit and aluminum foil as stationary electrodes.[30] Subsequent research has focused on the optimization of the device structure and exploration of novel applications.[31] Compared to other TENG structures, noncontact triboelectric nanogenerators offer advantages such as high efficiency and enhanced electrical performance.[32] More importantly, abrasion is avoided, enabling a longer device lifespan and better structural robustness. Currently, four distinct structures for noncontact TENGs have been developed, namely, the approach-separation structure,[33,34] rotational structure,[30,32] spring-assisted structure,[35,36] and magnetic-assisted structure.[37,38] Among the four designs, rotational structures have demonstrated excellent potential in the field of energy collection under complex environments and automatic force sensing due to their continuous triboelectric output and relatively high power density compared to other designs.[39]

Herein, to leverage the tunability of MOF and improve the structural robustness of MOF-based TENGs, we reported the development of a highly fluorinated MOF, Zn(2-(trifluoromethyl)-1H-imidazole)$_2$, denoted as ZIF-8-CF$_3$, as a promising filler material for a noncontact rotational triboelectric nanogenerator to harvest rotational mechanical energy. The high fluorine content in the periodic framework of ZIF-8-CF$_3$ provides a strong surface electron-withdrawing ability, creating stable and abundant charge-trapping sites during the initial contact electrification stage. Introducing these crystalline nanoparticles within the conventional PVDF matrix significantly improves the triboelectric performance of TENGs. An optimum filler loading of 0.5 wt. % was found to yield the highest output voltage and current output of 280 ± 8 V and 19.0 ± 0.4 μA, respectively. The highest power density output of 66.2 μW/cm^2 was achieved by the composite, which is about twice as high as that of the pristine PVDF-based TENG. The reason behind this improvement was further investigated through molecular simulation and surface potential analysis. The prepared device demonstrated its potential for applications in rotational energy harvesting and humidity sensing.

II. METHODOLOGY

A. Materials

Zinc basic carbonate [$Zn_5(CO_3)_2(OH)_6$] was purchased from Thermo Fisher. The 2-(trifluoromethyl)-1H-imidazole (CF$_3$Im) ligand was obtained from BLD Pharma. Dimethylformamide (DMF), dimethylacetamide (DMA), and methanol (MeOH) were purchased from Sigma-Aldrich. HSV900 poly(vinylidene fluoride) was supplied by Arkema. All chemicals were used as received.

B. Synthesis of ZIF-8-CF$_3$ and ZIF-8-CF$_3$/PVDF composite films

ZIF-8-CF$_3$ with sodalite topology was synthesized through a mechanical grinding approach.[40] Zinc basic carbonate (111 mg) and CF$_3$Im (280 mg) were physically mixed in a 20 ml glass vial. Then, 50 μL of DMF and three zirconium ball bearings were added to the solid mixture. The glass vial was placed on a vortex grinder at 1200 rpm for 60 min of reaction. The resulting mixture was washed with methanol and centrifuged three times to yield 160 mg of white ZIF-8-CF$_3$ powder.

To prepare the composite membrane, the synthesized powders were mixed with 13.7 wt. % PVDF/DMA solution to achieve a target filler weight loading of 0.2, 0.5, 2, and 5 wt. % in the polymer matrix composite. The solution was homogenized and then cast onto a PET substrate using a doctor blade. The PVDF composites were heated at 50 °C to evaporate the solvents. The resulting films had an average thickness of 100 ± 20 μm.

C. Fabrication of freestanding mode TENG

The freestanding mode triboelectric nanogenerator test rig comprises a stator unit of interdigitated electrodes and a rotor unit incorporating the prepared ZIF-8-CF$_3$/PVDF nanocomposite. Both units were supported by 3D-printed assemblies and securely mounted on a linear rail. The stator unit features a complementary pattern of two separate aluminum plates to ensure alternating electron transfer. The rotor unit was designed as a fan-blade-shaped substrate coated with the nanocomposite film. To ensure consistent testing conditions, the rotor unit was driven by a motor powered by a controlled power supply for different rotational frequencies. The gap between the stator and the rotor on the rail was adjusted by a Vernier stage. A tachometer (RS AT-8) was utilized to measure the rotational speed of the rotor. The TENG voltage output was measured by a Picoscope 5444B oscilloscope with a Rigol RP1300H 100 MΩ high-voltage probe. The output current and charge were measured by a Keithley 6517 electrometer. The surface potential profile at the macroscale was characterized by employing a surface direct current (DC) voltmeter (AlphaLab USSVM2) to measure the rate of surface charge decay. The triboelectric performance under various relative humidities (RH) was evaluated in a controlled environment by placing the TENG setup within a sealed glove bag. After a stable triboelectric output was achieved, the glove bag was purged with dry nitrogen gas until the RH reached 10%. Then, humidified air was gradually introduced to increase RH up to 85%, while continuously recording the generated triboelectric voltage.

D. Materials characterization

A field-emission scanning electron microscope (FESEM LYRA3 GM TESCAN) was used to examine the surface morphologies of the prepared MOF and the MOF/PVDF composite materials. Energy-dispersive x-ray spectroscopy (EDS) was performed with FESEM to evaluate the elemental composition of the prepared samples. The X-ray diffraction (XRD) patterns of MOF powders were measured by a Rigaku Miniflex diffractometer. Fourier-transform infrared spectra (FTIR) were recorded by a Nicolet iS10 FTIR spectrometer equipped with an attenuated total reflectance (ATR) module. Atomic force microscopic (AFM) height topography images and nano-FTIR spectra were measured by a scattering-type scanning near-field optical microscope (Neaspec s-SNOM). Confocal Raman microspectra were obtained by an Oxford Instruments WITec Raman microscope equipped with a 532 nm excitation laser. Far-IR microspectroscopy was performed at the multimode IR imaging and microspectroscopy (MIRIAM) Beamline B22 at the Diamond Light Source synchrotron via a Bruker Hyperion 3000 microscope coupled to a Vertex 80v interferometer.[41] Kelvin probe force microscopy (KPFM) was carried out using an Asylum Research Cypher ES atomic force microscope equipped with an ASYELEC-01-R2 conductive tip under the scanning Kelvin probe microscopy (SKPM) mode.

E. *Ab initio* quantum mechanical computational details

Periodic density functional theory (DFT) calculations on the ZIF-8-CF_3 model were carried out with the CRYSTAL23 [42] code at the PBEsol0-3c level of theory.[43] PBEsol0-3c is a composite method based on a hybrid Hartree–Fock/DFT Hamiltonian combined with a double-zeta quality basis set, augmented with a semiclassical dispersion term and a geometrical counterpoise correction. For the numerical integration of the exchange-correlation term, 75 radial points and 974 angular points (XLGRID) in a Lebedev scheme were adopted. The SCF convergence was set to 10^{-7} and 10^{-10} Hartrees during geometry optimization and frequency calculation steps, respectively. The Pack–Monkhorst/Gilat shrinking factors for the diagonalization of the Kohn–Sham matrix in reciprocal space were set to 2. The truncation criteria (TOLINTEG) for the bielectronic integrals (Coulomb and exchange series) were set to 7 7 7 7 25. A full relaxation of both lattice parameters and atomic positions was performed. After geometry optimization, vibrational frequencies at the Γ-point were computed using two-point numerical differentiation, and the CPHF/KS (Coupled-Perturbed Hartree–Fock/Kohn–Sham) approach was employed to calculate the infrared intensities. Subsequently, a Lorentzian peak broadening with a FWHM of 8 cm^{-1} was employed to simulate the infrared spectra. Electrostatic potential maps (ESP) and the highest occupied and lowest unoccupied crystalline orbitals (HOCO and LUCO) were computed at the same level of theory to analyze the electronic structure of the investigated model system. The computed results were plotted using JMol.[44]

III. RESULTS AND DISCUSSION

The functionalized ZIF-8-CF_3 nanoparticles were synthesized through a mechanical grinding approach, utilizing a mixture of zinc basic carbonate and 2-(trifluoromethyl)-1H-imidazole, as illustrated in Fig. 1(a). The prepared materials were then dispersed into a PVDF solution and fabricated into a composite film through doctor blade casting. The SEM image and EDS mapping images in Fig. 1(b) reveal homogeneously distributed fluorine atoms within the MOF crystals, confirming the successful formation of ZIF-8-CF_3. The as-synthesized ZIF-8-CF_3 crystals (average particle size of 400 nm) were then incorporated into PVDF membranes for triboelectric performance evaluation. These submicron-sized MOFs, with a high surface-to-volume ratio, are capable of improving charge-generating properties while avoiding agglomerations within the composite.[25] The SEM image of the composite film surface is shown in Fig. 1(c). A uniform dispersion of the nanoparticles within the polymer matrix was observed at a low filler wt. % concentration. The AFM height topography shown in Fig. 1(c) also confirms the homogeneous distribution of fillers within the polymer. Figures S2 and S3 present the

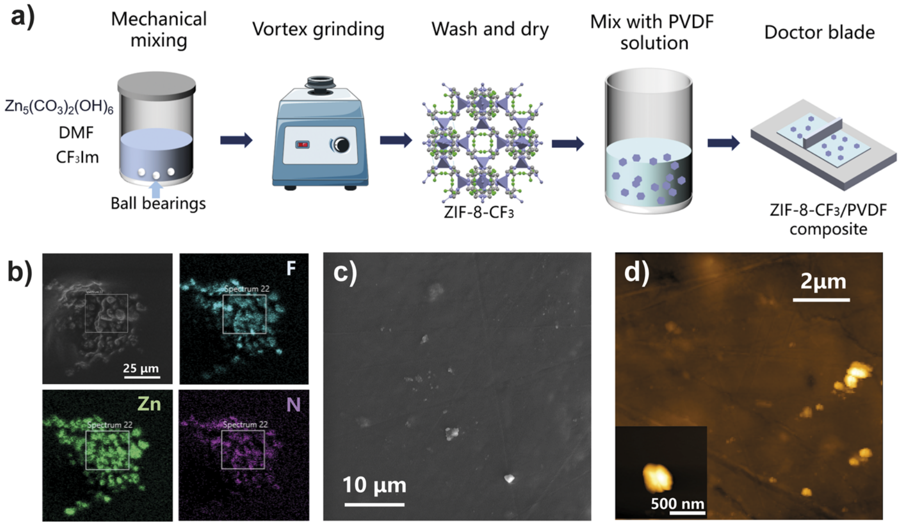

FIG. 1. (a) Schematic diagram of the preparation procedures for ZIF-8-CF_3 and ZIF-8-CF_3/PVDF composite film. (b) SEM image and EDS mapping analysis of ZIF-8-CF_3. The EDS spectrum of the framed area is presented in Fig. S1. (c) SEM image of a 0.5 wt. % ZIF-8-CF_3/PVDF film. (d) AFM height topography image of a 0.5 wt. % ZIF-8-CF_3/PVDF film. The inset shows the AFM image of a single ZIF-8-CF_3 particle.

EDS mapping images and spectrum of a ZIF-8-CF_3/PVDF composite film, showing evidence of ZIF-8-CF_3 particles embedded within the matrix. The larger-scale surface morphology of the 0.5 wt. % ZIF-8-CF_3/PVDF composite was examined by SEM, as shown in Fig. S4, demonstrating the uniformity of the prepared polymer matrix. Figure S5 shows the SEM images of PVDF composites doped with different amounts of MOF fillers. While MOF particles are evenly distributed within the matrix at low concentrations, some larger aggregates are observed as the filler loading increases to 2 wt. %, suggesting a reduction in the filler dispersion quality.

The powder XRD pattern of the as-synthesized ZIF-8-CF_3 is shown in Fig. 2(a). The experimental measurement aligns with

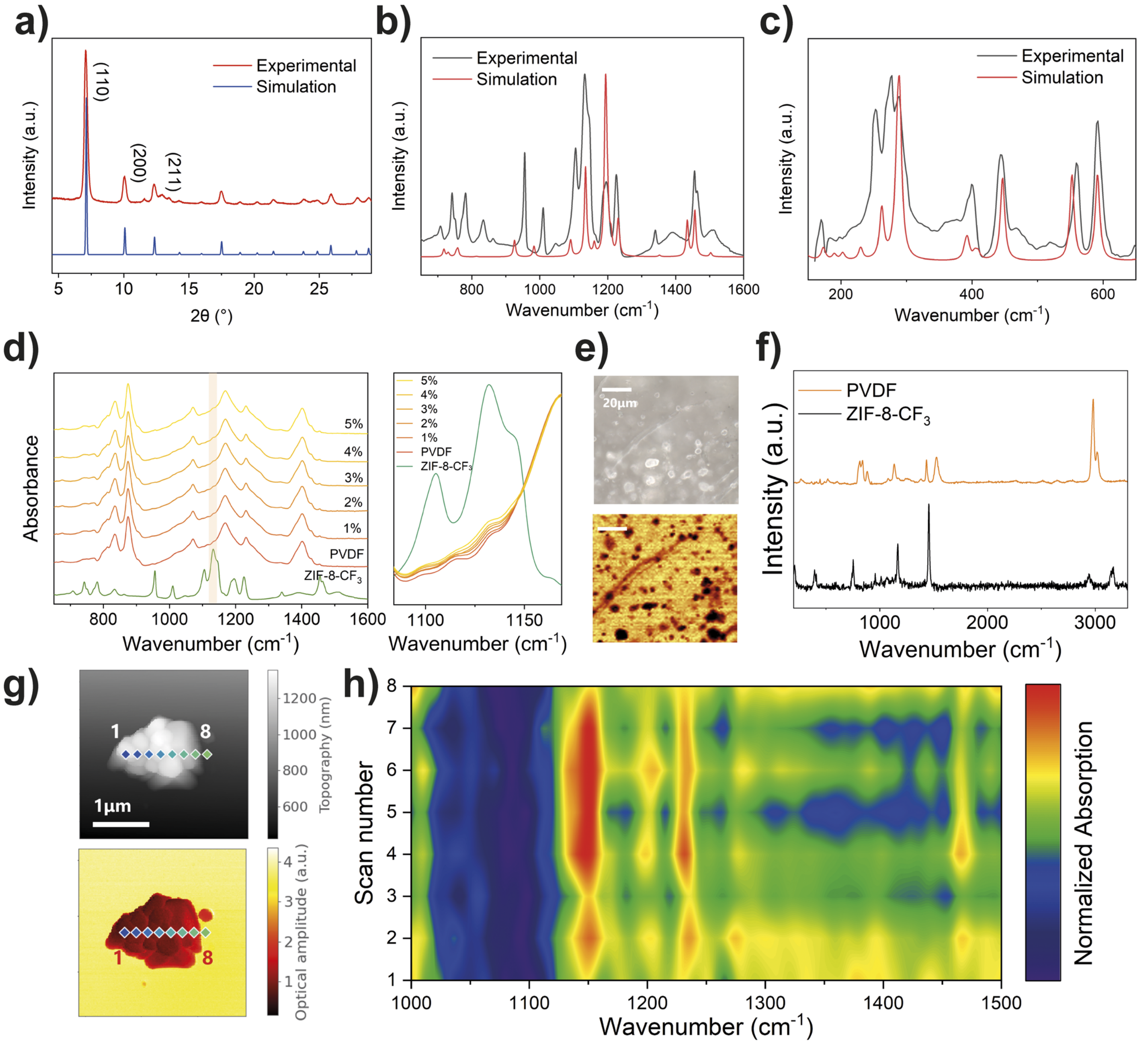

FIG. 2. (a) XRD patterns of the crystalline ZIF-8-CF_3 compound compared with the simulated pattern (CCDC 1859152). (b) ATR-FTIR spectra of ZIF-8-CF_3 compared with the simulated results by DFT. (c) Far-IR spectrum of ZIF-8-CF_3 compared with simulated results by DFT. (d) ATR-FTIR absorbance of ZIF-8-CF_3/PVDF composites between 1085 and 1170 cm^{-1}. (e) Optical microscope (top panel) and Raman mapping images of the ZIF-8-CF_3/PVDF composite. (f) Component analysis of the ZIF-8-CF_3/PVDF composite showing the confocal Raman spectra of the ZIF-8-CF_3 and PVDF constituents measured under 532 nm excitation, corresponding to the color in (e), bottom panel. (g) AFM height topography and near-field infrared second-harmonic optical amplitude (O2A) signal of ZIF-8-CF_3. (h) Contour plot of nano-FTIR spectra across the as-synthesized ZIF-8-CF_3, determined by a line scan from position 1–8 as indicated in (g).

the simulation results, with diffraction peaks at 7.1° (110), 10.1° (200), and 12.3° (211), confirming the sodalite (SOD) topology of the MOF crystals. This highly symmetrical and porous topology contributes to an increased effective surface area during contact. Figure 2(b) shows the ATR-FTIR spectra of ZIF-8-CF_3 compared with the DFT-simulated results. The characteristic bands at 1194 and 1224 cm^{-1} can be assigned to the C–F bond vibrations,[45] while the peaks at 1132 and 1105 cm^{-1} correspond to vibrations of the imidazole rings. The C–F groups with high electronegativity act as charge-trapping sites, thus enhancing charge transfer during contact electrification. The synthesized ZIF-8-CF_3 also shows excellent chemical stability, with minimal variations in its chemical constitution observed after immersion in different solvents, as shown in Fig. S6. The excellent chemical stability of ZIF-8-CF_3 makes it a promising candidate for real-world applications, especially under varying environmental conditions and long-term operations pertinent to practical TENG devices. Synchrotron far-IR or TeraHertz (THz) spectra and microspectroscopic image of a thin film of ZIF-8-CF_3 are presented in Figs. 2(c) and S7, respectively. Within the THz region, ZIF-8-CF_3 exhibits vibrational bands at 276, 400, 444, 560, and 591 cm^{-1}, corresponding to the interactions between the metal ion and the CF_3Im ligand. Figure S8 shows a large aggregate of ZIF-8-CF_3 embedded under the PVDF matrix, while the main characteristic peak of ZIF-8-CF_3 at 591 cm^{-1} remains detectable from the spectrum of the composite material. This demonstrated the successful incorporation of filler materials into the polymer matrix without significant chemical interactions.

Figure 2(d) shows the ATR-FTIR spectra of the ZIF-8-CF_3/PVDF composite film at different mass loadings (wt. %). No obvious band shift was observed, indicating the absence of strong chemical interactions between the MOF and the PVDF matrix due to the relatively low filler loading. In the 1085–1170 cm^{-1} region, an increase in the peak intensity at 1132 cm^{-1} for the composite film is observed as the concentration of ZIF-8-CF_3 increases, confirming the successful incorporation of fillers within the polymer matrix without strong chemical interactions. In addition, the observation of C–F bonds on the composite surface demonstrates the improved electronegativity of the material, contributing to a higher charge density. Figures 2(e) and 2(f) show the confocal Raman map analysis and component spectra of the ZIF-8-CF_3/PVDF composite film. The color difference in Fig. 2(e) distinguishes the filler materials (black) from the polymer matrix (orange), with their corresponding Raman spectra shown in Fig. 2(f). For ZIF-8-CF_3, the characteristic peaks at 753 and 1462 cm^{-1} were observed for the C–F bond deformation and the in-plane bending of the C–H bond, respectively.[46] For PVDF, the Raman band at 2970 cm^{-1} is assigned to CH_2 symmetric stretching, the band at 1429 cm^{-1} is assigned to the CH_2 scissoring and wagging, and the 1138 cm^{-1} peak is assigned to CF_2 symmetric stretching.[47] Figure S9 shows the confocal Raman analysis on the cross-section of a ZIF-8-CF_3/PVDF membrane, demonstrating a 3D distribution of particles within the matrix throughout both the planar [Fig. 2(e)] and thickness directions. These embedded fillers increase the contact area at the MOF–polymer interface, which acts as microcapacitors to trap more charges during contact electrification, thereby improving the triboelectric performance.[48] Figure 2(g) shows the s-SNOM infrared images and absorption spectra of an aggregate of ZIF-8-CF_3 particles. By scanning through the aggregate, the spectra show homogeneity across the line scan, with strong IR absorption peaks at 1150 and 1240 cm^{-1}. The near-field nano-FTIR averaged spectra of ZIF-8-CF_3 shown in Fig. S10 exhibit similar characteristic peaks compared to the far-field ATR-FTIR results, further confirming the successful synthesis and structural integrity of the MOF material.

The prepared nanocomposites were cut into circular sectors and pasted onto the 3D-printed rotor unit to yield an assembly of a noncontact freestanding mode TENG. A schematic of the overall design is shown in Fig. 3(a), and a photograph of the electrical performance testing rig is shown in Fig. S11. The energy generation mechanism consists of two steps: an initial contact electrification of the active triboelectric layer followed by electrostatic induction through cyclic rotational motion. First, the ZIF-8-CF_3/PVDF composite on the rotor undergoes prior contact electrification by contacting the aluminum electrodes on the stator to accumulate surface charges. Due to the high electron affinities of the composite surface and the strong electron-donating nature of aluminum, electrons transfer from the metal to the surface of the ZIF-8-CF_3/PVDF film, resulting in a net negative charge on the composite film. Then the layers were separated by a 0.5 mm gap. The rotor containing the prepared composite film rotates parallel to the aluminum electrodes to induce electrical output, with the operating principle of the designed noncontact TENG illustrated in Fig. 3(b). During rotation, the active triboelectric material on the rotor continuously passes over the interlaced electrodes on the stator. At the initial state (step i), the rotor is aligned with electrode 1. As it moves from step i to step ii, a potential difference is generated due to the imbalance of surface charges induced by the negative charges on the composite material, which drives the electrons to flow from electrode 2 to electrode 1. While the rotor continues to rotate and align with the position of electrode 2, the majority of electrons accumulate on electrode 1, leaving electrode 2 induced with positive charges. As the composite film continues to rotate along the stator, it moves to the next segment of electrode 1, as shown in step iv. Since the electrodes are alternatively arranged (illustrated in Fig. S12), the electrons flow backward from electrode 1 to electrode 2. The cycle then proceeds back to step i due to the periodic design of the rotation TENG. Therefore, the cyclic process facilitates a continuous back-and-forth flow of electrons, thereby generating an alternating current (AC) output.

The voltage output of the ZIF-8-CF_3/PVDF composites under the noncontact freestanding mode was measured at different mass loadings under a rotational frequency of 30 Hz, as shown in Fig. 3(c). The highest voltage was achieved by the 0.5 wt. % ZIF-8-CF_3/PVDF composite with 1.5 times higher output compared with the neat PVDF film. In noncontact mode, the surface roughness caused by the incorporation of filler materials may not enhance triboelectric performance through increased effective contact area, as observed in the contact-separation mode. Instead, a smooth surface contributes to a more stable and consistent electrical output. The enhanced performance at 0.5 wt. % can be attributed to a balance between surface charge enhancement and particle dispersion. At low concentrations (below 0.5 wt. %), the introduction of MOF dopants introduces additional charge-generating and trapping sites at the polymer–filler interface, which enhances the surface charge density and retention after prior contact. The MOF fillers introduce surface heterogeneity of chemical bonds, which facilitates the formation of local dipoles.[19]

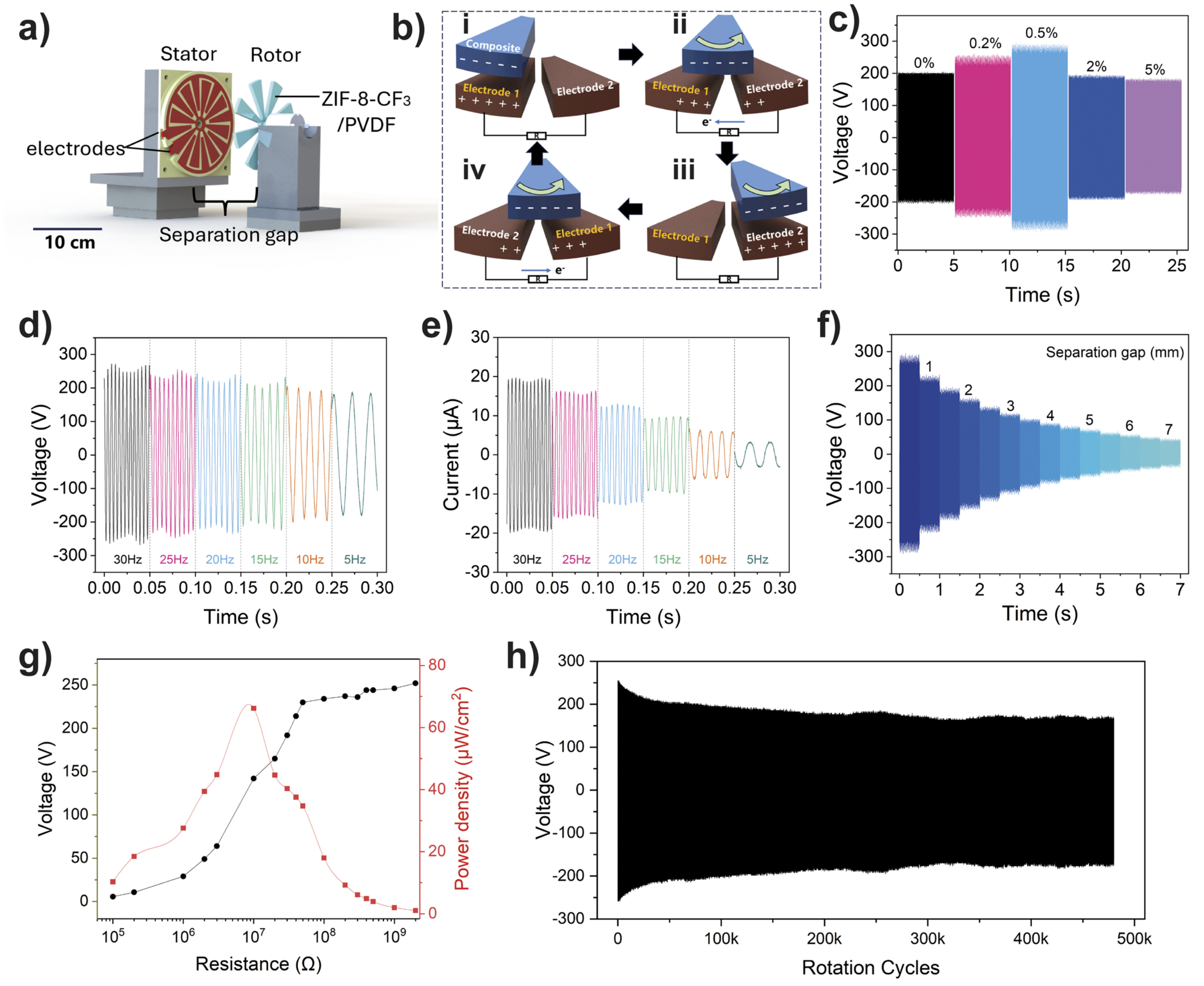

FIG. 3. (a) Schematic diagram of a noncontact rotational TENG comprising a stator unit and a rotor unit. (b) Operating mechanism of the ZIF-8-CF_3/PVDF-based noncontact rotational TENG. (c) Open-circuit voltage output of TENGs at different wt. % loadings of ZIF-8-CF_3 fillers. (d) Open-circuit voltage output and (e) short-circuit current output of a 0.5 wt. % ZIF-8-CF_3/PVDF TENG tested under various operating frequencies. (f) Open-circuit voltage of a 0.5 wt. % ZIF-8-CF_3/PVDF TENG at different separation gaps. (g) Peak voltage and power density as a function of load resistance for the 0.5 wt. % ZIF-8-CF_3/PVDF TENG. (h) Voltage stability of a 0.5 wt. % ZIF-8-CF_3/PVDF TENG over a durability test of up to 500 000 cycles.

However, as the filler content increases, a significant reduction in output performance was observed due to particle agglomeration, as shown in Fig. S5c, leading to a reduction in charge transport pathways and a decline in charge transfer efficiency.

The open-circuit voltage and short-circuit current of the 0.5 wt. % PVDF composite were measured at different rotational frequencies ranging from 5 to 30 Hz. For the voltage output, the prepared device could generate up to 280 ± 8 V and 19 ± 0.4 μA under an operating frequency of 30 Hz, as illustrated in Figs. 3(d) and 3(e). The voltage and current outputs at different frequencies on a larger time scale are shown in Figs. S13 and S14. The output signal does not show a significant reduction while the frequency changes. This is attributed to the origin of the potential difference induced by the difference in surface potential between the two materials. However, the minor reduction in voltage is likely due to variations in the approach and separation speeds of the tribo-active materials, which can induce faster charge transfer.[49] On the other hand, the current output exhibited a linear relationship with the operating frequency of the TENG. Since the electrical current is a measure of the charge flow rate, and the charge transferred through each cycle remains constant, the current is inversely proportional to time and thus directly proportional to the operating frequency.

The relationship between the electrical output of the TENG and the gap distance between the rotor and stator was also studied. By controlling the gap size between the electrode and the active nanocomposite material with a Vernier stage, it was observed that both the voltage and current outputs exhibited a significant decay as the triboelectric layers became further apart, as illustrated in Figs. 3(f) and S15. According to the theoretical modeling conducted by Niu *et al.*, both the open-circuit voltage and short-circuit transferred charge reduce as the separation distance increases, thereby decreasing the maximum harvested energy.[50]

The voltage output of the fabricated noncontact TENG was evaluated under closed-circuit conditions with various load resistances. The instantaneous power density P_d is calculated using the equation $P_d = V^2/(R \times A)$, where V is the measured closed-circuit voltage, R is the external load resistance, and A is the surface area of the rotor unit ($A = 30.46$ cm^2). As shown in Fig. 3(g), the 0.5 wt. % ZIF-8-CF$_3$/PVDF-based TENG exhibited an instantaneous power density of 66.2 μW/cm^2. In comparison, the neat PVDF-based TENG achieved a power density of 33.6 μW/cm^2, as shown in Fig. S16, indicating a 1.97-fold improvement in power density due to the incorporation of the ZIF-8-CF$_3$ filler. Furthermore, the long-term output stability of the prepared device was tested over 500 000 continuous cycles, as shown in Fig. 3(h). An initial decline was observed due to the dissipation of accumulated charges on the composite surface through air. However, the device maintained a considerably high and stable output thereafter, which we attributed to the excellent charge retention capability of the composite film. The noncontact design offers the unique advantage of eliminating mechanical wear and abrasion, thereby enhancing both the operational durability and mechanical resilience of the material. Small fluctuations in voltage observed during the test are likely caused by variations in humidity, which will be discussed below.

The underlying reason behind the electrical output improvement of the ZIF-8-CF$_3$/PVDF-based TENG was further investigated through *ab initio* periodic DFT calculations and nanoscale surface potential characterization. The electrostatic potential (ESP) map of the periodic structure of ZIF-8-CF$_3$ was first simulated using CRYSTAL23, as shown in Fig. 4(a). The trifluoromethyl (-CF$_3$) group, with its strong electron-withdrawing ability, induces a localized dipole within the framework, enhancing charge transfer and retention. The ESP map reveals a heterogeneous charge distribution with alternating positive (blue) and negative (red) regions, indicating the formation of abundant charge traps that facilitate electron capture and retention. Furthermore, the highest occupied crystalline orbital (HOCO) and the lowest unoccupied crystalline orbital (LUCO) of the ZIF-8-CF$_3$ structure, presented in Fig. 4(b), provide deeper insights into its electronic properties. The presence of HOCO and LUCO around the ligand of ZIF-8-CF$_3$ suggests that electron density is concentrated on the fluorine-rich ligands, influenced by the trifluoromethyl group. Since the charge acceptance of the ZIF-8-CF$_3$ structure occurs at LUCO, this indicates that the CF$_3$Im ligands dominate the charge transfer process, making them critical in enhancing the tribo-negative behavior of ZIF-8-CF$_3$.

Figures 4(c)–4(e) show the AFM height topography, KPFM surface potential map, and 3D mapping of the ZIF-8-CF$_3$/PVDF composite film. Compared to the neat PVDF film, ZIF-8-CF$_3$/PVDF exhibits a more negative contact potential difference (V_{CPD}) measured by KPFM, indicating a higher work function. According to electron transfer theory, electrons flow from materials with lower work functions to those with higher work functions.[51] Therefore, the lower V_{CPD} of ZIF-8-CF$_3$/PVDF represents a higher electron-withdrawing ability, making it an effective tribo-negative material in a triboelectric pair. In addition, the incorporation of ZIF-8-CF$_3$ particles ontp the polymer surface introduces surface potential heterogeneity, which further enhances charge retention at the nanoscale. Both simulation and experimental results confirm the critical role of the fluorinated MOF in enhancing the triboelectric properties of the composite structure. Figure S17 further demonstrates the charge retention performance of the prepared composites. Macroscale surface potential measurements were conducted using a surface DC voltmeter. The decay of surface potential over time was fitted to an exponential decay model to extract the time constant (τ), which reflects the material's ability to retain surface charges. The 0.5 wt. % composite exhibited a time constant of 349 s, significantly higher

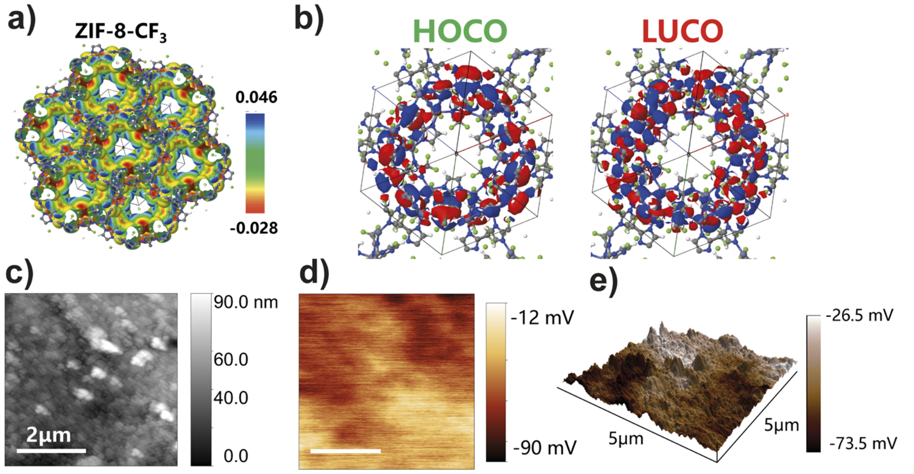

FIG. 4. (a) Electrostatic potential mapped on a charge density isosurface of 0.003 electron charge per Bohr^3 for the ZIF-8-CF$_3$ framework obtained from DFT. (b) Highest occupied crystalline orbital (HOCO) and lowest unoccupied crystalline orbital (LUCO) of the periodic structure of ZIF-8-CF$_3$. (c) AFM height topography image and (d) corresponding KPFM surface potential of a ZIF-8-CF$_3$/PVDF composite film. (e) 3D map of height topography superimposed with the corresponding surface potential shown in (d).

than the ~50 s measured for the pristine PVDF polymer, demonstrating improved charge retention. This enhancement is attributed to the incorporation of highly electronegative MOF fillers, which act as charge-trapping sites within the polymer matrix, thereby slowing charge dissipation.

To assess the practical application of the prepared TENG devices, the generated AC output was harvested and stored in capacitors through a full rectifier circuit, as shown in Fig. 5(a). After rectification, the alternating current (AC) generated from the rotational motion was converted into direct current (DC), doubling its frequency without significant energy loss, as shown in Fig. 5(b) and its inset. Compared with the conventional contact-separation mode, the noncontact mode TENG offers several advantages. First, its ability to operate at high rotational speeds results in electrical output with higher frequency and orders of magnitude greater energy output, significantly expanding its potential applications. Furthermore, the noncontact mode substantially extends the material's durability by mitigating wear and mechanical degradation. Although rotational energy harvesting is completed without physical contact, the energy stored in capacitors is relatively faster than the contact-separation mode. For instance, a 0.1 μF capacitor can be easily charged to its maximum operating voltage of 200 V within only 3 s, as illustrated in Fig. 5(c).

The capacitor charging curves for a 10 μF capacitor at different operating frequencies are demonstrated in Fig. 5(d). Following the same trend as the current output at various frequencies, the higher current output at a faster rotational speed improves the energy harvesting efficiency. In addition, the rectified electrical output was used for continuous LED illumination. Figure 5(e) shows the LED brightness variations with an increasing number of LEDs connected in series, reaching a maximum of 180 LEDs. Since the output current operates at 240 Hz, which is well above the flicker fusion

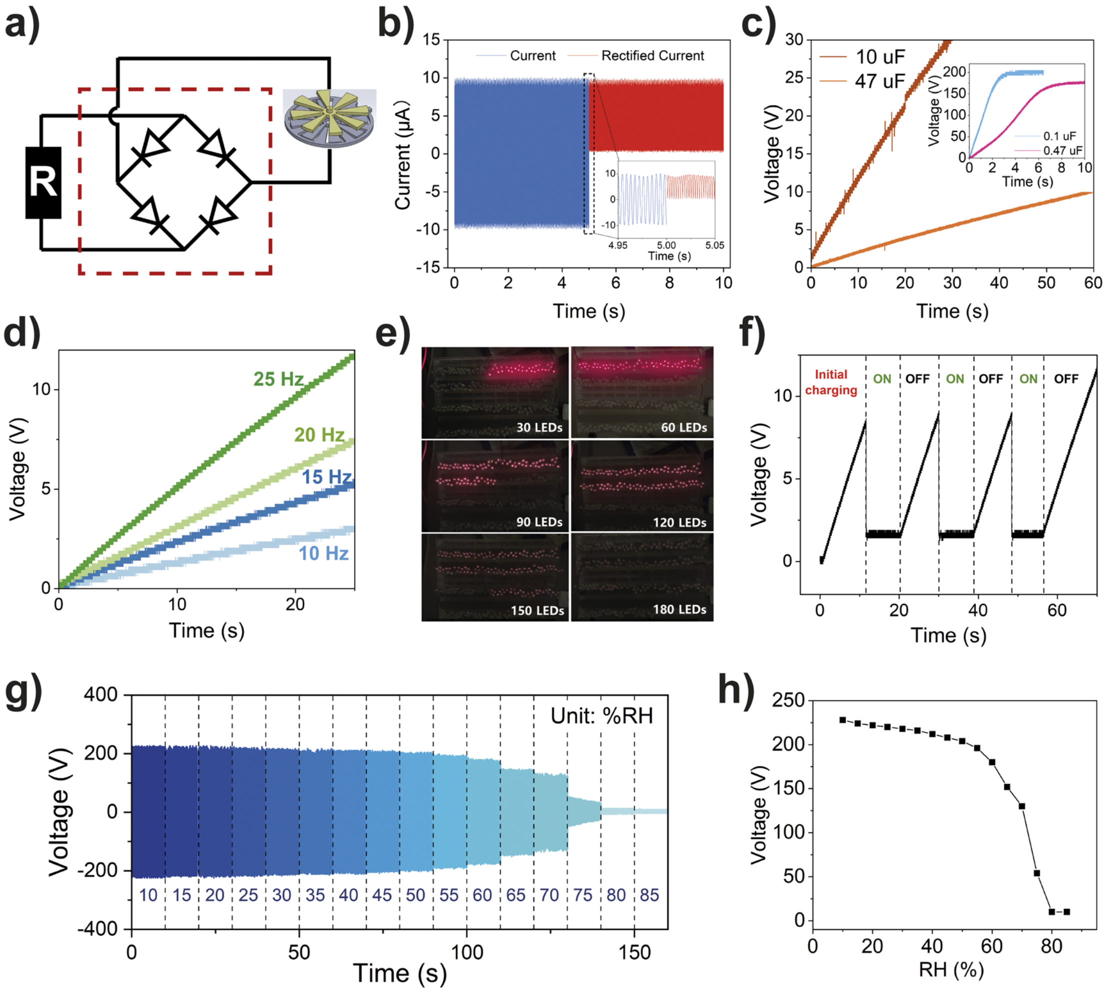

FIG. 5. (a) Schematic diagram of a full rectifier circuit. (b) Short-circuit current before and after rectification. (c) Charging speed of capacitors with different capacitances using the 0.5 wt. % ZIF-8-CF$_3$/PVDF TENG. (d) Charging speed of a 10 μF capacitor under different operating frequencies. (e) Continuous illumination of a large number of LEDs in series powered by the noncontact TENG. (f) Voltage across a 10 μF capacitor while charging a calculator. (g) Voltage output of the 0.5 wt. % ZIF-8-CF$_3$/PVDF TENG under different humidity levels. (h) Relationship between voltage output and relative humidity for the 0.5 wt. % ZIF-8-CF$_3$/PVDF TENG.

threshold of the human eye, the LEDs appear to emit a steady light. Video S1 (see supplementary material) shows the illumination of 60 LEDs under an operating frequency of 30 Hz. Beyond LED illumination, we show that other small electronics such as a calculator and a timer could be powered continuously during the operation of the noncontact TENG, with their charge and discharge curves demonstrated in Figs. 5(f) and S18, showing a reproducible cycling performance. The full demonstrations for charging these electronics are presented in Videos S2 and S3 (see supplementary material), demonstrating excellent potential in practical applications. The prepared noncontact TENG also demonstrates its potential as a humidity sensor, and its voltage response over a range of relative humidity levels is shown in Figs. 5(g) and 5(h). At low humidity levels (<50% RH), the device exhibits low sensitivity in output voltage toward variation in humidity. However, at higher humidity levels, a rapid decline in voltage was observed. This reduction is attributed to the increased water content in the air, which hinders charge accumulation and facilitates surface charge dissipation on the material surface. The strong dependence of output voltage on different RH conditions highlights the potential of noncontact TENG devices for environmental monitoring applications.

IV. CONCLUDING REMARKS

In conclusion, this work demonstrated a design for deploying a noncontact TENG based on a fluorinated metal–organic framework material, ZIF-8-CF_3, incorporated into a PVDF matrix. The device was rationally designed to operate at high frequencies while maintaining excellent mechanical and chemical stability. The incorporation of ZIF-8-CF_3 nanofillers significantly improved the overall electrical performance of the TENG device, achieving a voltage and current output of 280 ± 8 V and 19.0 ± 0.4 μA, respectively, under an optimum MOF filler loading of 0.5 wt. %. The observed performance enhancement is attributed to the excellent electron-trapping ability of the fluorine-rich microporous structure and the uniform distribution of charge sites on the MOF–polymer composite. The findings have been confirmed through *ab initio* DFT calculations and nanoscale KPFM characterization. Potential applications of this device have been demonstrated through capacitor charging, LED illumination, and the powering of small electronic devices. Its potential as a humidity and rotational speed sensor was also explored, showcasing the prospect for broader applications and opening new design strategies in MOF-based TENG development.

SUPPLEMENTARY MATERIAL

ATR-FTIR, nanoFTIR, far-IR microspectroscopy, and confocal Raman characterization data. Voltage and current data. Schematic diagrams of the experimental setups. Supplementary material videos: see Videos S1–S3 for demonstrations of applications.

ACKNOWLEDGMENTS

This work was supported by the UKRI Engineering and Physical Sciences Research Council (EPSRC) award (Grant No. TEGMOF EP/Z534146/1). We acknowledge the Diamond Light Source for the award of beamtime SM30369 on MIRIAM beamline B22. We thank Dylan Jubb for his assistance in the design, construction, and testing of the noncontact freestanding TENG rig. We are grateful to Professor Bartolomeo Civalleri from the University of Turin for his support on DFT calculations using the CRYSTAL code. L.D. acknowledges the Gauss Center for Supercomputing e.V. (https://www.gauss-centre.eu/) for providing computing time on the GCS Supercomputer SuperMUC-NG at Leibniz Super Computing Center (https://www.lrz.de/) and the support from Project CH4.0 under the MUR program "Dipartimenti di Eccellenza 2023–2027" (Grant No. CUP: D13C22003520001). We thank Oxford Instruments for the use of the WITec Raman microscope.

AUTHOR DECLARATIONS

Conflict of Interest

The authors have no conflicts to disclose.

Author Contributions

Jiahao Ye: Conceptualization (equal); Formal analysis (equal); Investigation (equal); Methodology (equal); Writing – original draft (equal); Writing – review & editing (equal). **Gianfelice Cinque**: Formal analysis (equal); Investigation (equal); Methodology (equal). **Lorenzo Donà**: Formal analysis (equal); Methodology (equal); Software (equal). **Jin-Chong Tan**: Conceptualization (equal); Funding acquisition (lead); Methodology (equal); Supervision (lead); Writing – review & editing (equal).

DATA AVAILABILITY

The data that support the findings of this study are available from the corresponding author upon reasonable request.

REFERENCES

[1] F.-R. Fan, Z.-Q. Tian, and Z. Lin Wang, "Flexible triboelectric generator," Nano Energy **1**(2), 328–334 (2012).

[2] J. Zhu, M. Zhu, Q. Shi, F. Wen, L. Liu, B. Dong, A. Haroun, Y. Yang, P. Vachon, X. Guo, T. He, and C. Lee, "Progress in TENG technology—A journey from energy harvesting to nanoenergy and nanosystem," EcoMat **2**(4), e12058 (2020).

[3] X. Pu, M. Liu, X. Chen, J. Sun, C. Du, Y. Zhang, J. Zhai, W. Hu, and Z. L. Wang, "Ultrastretchable, transparent triboelectric nanogenerator as electronic skin for biomechanical energy harvesting and tactile sensing," Sci. Adv. **3**(5), e1700015 (2017).

[4] Y. Xi, H. Guo, Y. Zi, X. Li, J. Wang, J. Deng, S. Li, C. Hu, X. Cao, and Z. L. Wang, "Multifunctional TENG for blue energy scavenging and self-powered wind-speed sensor," Adv. Energy Mater. **7**(12), 1602397 (2017).

[5] D. Zhang, J. Shi, Y. Si, and T. Li, "Multi-grating triboelectric nanogenerator for harvesting low-frequency ocean wave energy," Nano Energy **61**, 132–140 (2019).

[6] H. Wu, Z. Wang, B. Zhu, H. Wang, C. Lu, M. Kang, S. Kang, W. Ding, L. Yang, R. Liao, J. Wang, and Z. L. Wang, "All-in-one sensing system for online vibration monitoring via IR wireless communication as driven by high-power TENG," Adv. Energy Mater. **13**(16), 2300051 (2023).

[7] Q. Qian, P. A. Asinger, M. J. Lee, G. Han, K. Mizrahi Rodriguez, S. Lin, F. M. Benedetti, A. X. Wu, W. S. Chi, and Z. P. Smith, "MOF-based membranes for gas separations," Chem. Rev. **120**(16), 8161–8266 (2020).

[8] D. Alezi, Y. Belmabkhout, M. Suyetin, P. M. Bhatt, Ł. J. Weseliński, V. Solovyeva, K. Adil, I. Spanopoulos, P. N. Trikalitis, A.-H. Emwas, and M. Eddaoudi, "MOF crystal chemistry paving the way to gas storage needs: Aluminum-based soc-MOF for CH_4, O_2, and CO_2 storage," J. Am. Chem. Soc. **137**(41), 13308–13318 (2015).

[9] Q. Wang and D. Astruc, "State of the art and prospects in metal–organic framework (MOF)-based and MOF-derived nanocatalysis," Chem. Rev. **120**(2), 1438–1511 (2020).

[10] K. Shen, X. Chen, J. Chen, and Y. Li, "Development of MOF-derived carbon-based nanomaterials for efficient catalysis," ACS Catal. **6**(9), 5887–5903 (2016).

[11] Y. Zhang, S. Mollick, M. Tricarico, J. Ye, D. A. Sherman, and J.-C. Tan, "Turn-On fluorescence chemical sensing through transformation of self-trapped exciton states at room temperature," ACS Sens. **7**(8), 2338–2344 (2022).

[12] E. A. Dolgopolova, A. M. Rice, C. R. Martin, and N. B. Shustova, "Photochemistry and photophysics of MOFs: Steps towards MOF-based sensing enhancements," Chem. Soc. Rev. **47**(13), 4710–4728 (2018).

[13] M.-X. Wu and Y.-W. Yang, "Metal–organic framework (MOF)-based drug/cargo delivery and cancer Thecapy," Adv. Mater. **29**(23), 1606134 (2017).

[14] K. Suresh and A. J. Matzger, "Enhanced drug delivery by dissolution of amorphous drug encapsulated in a water unstable metal–organic framework (MOF)," Angew. Chem., Int. Ed. **58**(47), 16790–16794 (2019).

[15] P. K. Nitha and A. Chandrasekhar, "Marriage between metal-organic frameworks/covalent-organic frameworks and triboelectric nanogenerator for energy harvesting—A review," Mater. Today Energy **37**, 101393 (2023).

[16] Y. M. Wang, X. Zhang, Y. Ran, C. Liu, D. Wang, G. Mao, X. Jiang, S. Wang, X. B. Yin, and R. Yang, "Advances in metal–organic framework-based triboelectric nanogenerators," ACS Mater. Lett. **6**(8), 3883–3898 (2024).

[17] S. M. S. Rana, O. Faruk, M. R. Islam, T. Yasmin, K. Zaman, and Z. L. Wang, "Recent advances in metal-organic framework-based self-powered sensors: A promising energy harvesting technology," Coord. Chem. Rev. **507**, 215741 (2024).

[18] R. K. Rajaboina, U. K. Khanapuram, V. Vivekananthan, G. Khandelwal, S. Potu, A. Babu, N. Madathil, M. Velpula, and P. Kodali, "Crystalline porous material-based nanogenerators: Recent progress, applications, challenges, and opportunities," Small **20**(1), 2306209 (2024).

[19] J. Ye and J. C. Tan, "High-performance triboelectric nanogenerators incorporating chlorinated zeolitic imidazolate frameworks with topologically tunable dielectric and surface adhesion properties," Nano Energy **114**, 108687 (2023).

[20] Z. Abbas, A. P. S. Prasanna, M. Anithkumar, T. S. Bincy, N. Hussain, S.-J. Kim, and S. M. Mobin, "Development of new amine-functionalized metal-organic framework for enhanced triboelectrification using first-principle theory of nanogenerator," Nano Energy **132**, 110344 (2024).

[21] R. Wen, R. Feng, B. Zhao, J. Song, L. Fan, and J. Zhai, "Controllable design of high-efficiency triboelectric materials by functionalized metal–organic frameworks with a large electron-withdrawing functional group," Nano Res. **15**(10), 9386–9391 (2022).

[22] Y. D. More, S. Saurabh, S. Mollick, S. K. Singh, S. Dutta, S. Fajal, A. Prathamshetti, M. M. Shirolkar, S. Panchal, M. Wable, S. Ogale, and S. K. Ghosh, "Highly stable and end-group tuneable metal–organic framework/polymer composite for superior triboelectric nanogenerator application," Adv. Mater. Interfaces **9**(34), 2201713 (2022).

[23] J. Ye, T. Xu, and J.-C. Tan, "Triboelectric nanogenerators based on composites of zeolitic imidazolate frameworks functionalized with halogenated ligands for contact and rotational mechanical energy harvesting," ACS Appl. Nano Mater. **8**, 3942 (2025).

[24] Y. Guo, Y. Cao, Z. Chen, R. Li, W. Gong, W. Yang, Q. Zhang, and H. Wang, "Fluorinated metal-organic framework as bifunctional filler toward highly improving output performance of triboelectric nanogenerators," Nano Energy **70**, 104517 (2020).

[25] Y.-M. Wang, X. Zhang, C. Liu, L. Wu, J. Zhang, T. Lei, Y. Wang, X.-B. Yin, and R. Yang, "Remarkable improvement of MOF-based triboelectric nanogenerators with strong electron-withdrawing groups," Nano Energy **107**, 108149 (2023).

[26] A. Priyadarshini, S. Divya, J. Swain, N. Das, S. Swain, S. Hajra, S. Panda, R. Samantaray, M. Belal, K. R. Kaja, N. Kumar, H. J. Kim, T. H. Oh, V. Vivekananthan, and R. Sahu, "Advancements in framework materials for enhanced energy harvesting," Nanoscale **17**(4), 1790–1811 (2025).

[27] R. Walden, C. Kumar, D. M. Mulvihill, and S. C. Pillai, "Opportunities and challenges in triboelectric nanogenerator (TENG) based sustainable energy generation technologies: A mini-review," Chem. Eng. J. Adv. **9**, 100237 (2022).

[28] Y. Xi, J. Hua, and Y. Shi, "Noncontact triboelectric nanogenerator for human motion monitoring and energy harvesting," Nano Energy **69**, 104390 (2020).

[29] Z. Qu, M. Huang, R. Dai, Y. An, C. Chen, G. Nie, X. Wang, Y. Zhang, and W. Yin, "Using non-contact eccentric nanogenerator to collect energy continuously under periodic vibration," Nano Energy **87**, 106159 (2021).

[30] L. Lin, S. Wang, S. Niu, C. Liu, Y. Xie, and Z. L. Wang, "Noncontact free-rotating disk triboelectric nanogenerator as a sustainable energy harvester and self-powered mechanical sensor," ACS Appl. Mater. Interfaces **6**(4), 3031–3038 (2014).

[31] X. Fu, X. Pan, Y. Liu, J. Li, Z. Zhang, H. Liu, and M. Gao, "Non-contact triboelectric nanogenerator," Adv. Funct. Mater. **33**(52), 2306749 (2023).

[32] Q. Li, W. Liu, H. Yang, W. He, L. Long, M. Wu, X. Zhang, Y. Xi, C. Hu, and Z. L. Wang, "Ultra-stability high-voltage triboelectric nanogenerator designed by ternary dielectric triboelectrification with partial soft-contact and non-contact mode," Nano Energy **90**, 106585 (2021).

[33] S. A. Han, W. Seung, J. H. Kim, and S.-W. Kim, "Ultrathin noncontact-mode triboelectric nanogenerator triggered by giant dielectric material adaption," ACS Energy Lett. **6**(4), 1189–1197 (2021).

[34] H. Guo, X. Jia, L. Liu, X. Cao, N. Wang, and Z. L. Wang, "Freestanding triboelectric nanogenerator enables noncontact motion-tracking and positioning," ACS Nano **12**(4), 3461–3467 (2018).

[35] Z. Lin, B. Zhang, Y. Xie, Z. Wu, J. Yang, and Z. L. Wang, "Elastic-connection and soft-contact triboelectric nanogenerator with superior durability and efficiency," Adv. Funct. Mater. **31**(40), 2105237 (2021).

[36] T. Jiang, H. Pang, J. An, P. Lu, Y. Feng, X. Liang, W. Zhong, and Z. L. Wang, "Robust swing-structured triboelectric nanogenerator for efficient blue energy harvesting," Adv. Energy Mater. **10**(23), 2000064 (2020).

[37] X. Ren, H. Fan, C. Wang, J. Ma, S. Lei, Y. Zhao, H. Li, and N. Zhao, "Magnetic force driven noncontact electromagnetic-triboelectric hybrid nanogenerator for scavenging biomechanical energy," Nano Energy **35**, 233–241 (2017).

[38] L.-B. Huang, G. Bai, M.-C. Wong, Z. Yang, W. Xu, and J. Hao, "Magnetic-assisted noncontact triboelectric nanogenerator converting mechanical energy into electricity and light emissions," Adv. Mater. **28**(14), 2744–2751 (2016).

[39] G. Zhu, J. Chen, T. Zhang, Q. Jing, and Z. L. Wang, "Radial-arrayed rotary electrification for high performance triboelectric generator," Nat. Commun. **5**(1), 3426 (2014).

[40] B. Slater and J.-C. Tan, "Triboelectric behaviour of selected zeolitic-imidazolate frameworks: exploring chemical, morphological and topological influences," Chem. Sci. **15**(26), 10056–10064 (2024).

[41] A. Greenaway, B. Gonzalez-Santiago, P. M. Donaldson, M. D. Frogley, G. Cinque, J. Sotelo, S. Moggach, E. Shiko, S. Brandani, R. F. Howe, and P. A. Wright, "In situ synchrotron IR microspectroscopy of CO_2 adsorption on single crystals of the functionalized MOF $Sc_2(BDC\text{-}NH_2)_3$," Angew. Chem., Int. Ed. **53**(49), 13483–13487 (2014).

[42] A. Erba, J. K. Desmarais, S. Casassa, B. Civalleri, L. Donà, I. J. Bush, B. Searle, L. Maschio, L. Edith-Daga, A. Cossard, C. Ribaldone, E. Ascrizzi, N. L. Marana, J.-P. Flament, and B. Kirtman, "CRYSTAL23: A program for computational solid state physics and chemistry," J. Chem. Theory Comput. **19**(20), 6891–6932 (2023).

[43] L. Doná, J. G. Brandenburg, and B. Civalleri, "Extending and assessing composite electronic structure methods to the solid state," J. Chem. Phys. **151**(12), 121101 (2019).

[44] R. M. Hanson and X.-J. Lu, "DSSR-enhanced visualization of nucleic acid structures in Jmol," Nucleic Acids Res. **45**(W1), W528–W533 (2017).

[45] X. Wang, W. Wang, Y. Liu, M. Ren, H. Xiao, and X. Liu, "Characterization of conformation and locations of C–F bonds in graphene derivative by polarized ATR-FTIR," Anal. Chem. **88**(7), 3926–3934 (2016).

[46] H. A. Carter, C. Shiow-Chyn Wang, and J. n. M. Shreeve, "The Raman spectra of CF_3SCF_3, $CF_3S(O)CF_3$ and CF_3SSCF_3," Spectrochim. Acta, Part A **29**(7), 1479–1491 (1973).

[47]C. J. L. Constantino, A. E. Job, R. D. Simões, J. A. Giacometti, V. Zucolotto, O. N. Oliveira, G. Gozzi, and D. L. Chinaglia, "Phase Transition in poly(vinylidene fluoride) investigated with micro-Raman spectroscopy," Appl. Spectrosc. **59**(3), 275–279 (2005).

[48]S. M. S. Rana, M. T. Rahman, M. A. Zahed, S. H. Lee, Y. D. Shin, S. Seonu, D. Kim, M. Salauddin, T. Bhatta, K. Sharstha, and J. Y. Park, "Zirconium metal-organic framework and hybridized Co-NPC@MXene nanocomposite-coated fabric for stretchable, humidity-resistant triboelectric nanogenerators and self-powered tactile sensors," Nano Energy **104**, 107931 (2022).

[49]N. Zhang, C. Qin, T. Feng, J. Li, Z. Yang, X. Sun, E. Liang, Y. Mao, and X. Wang, "Non-contact cylindrical rotating triboelectric nanogenerator for harvesting kinetic energy from hydraulics," Nano Res. **13**(7), 1903–1907 (2020).

[50]S. Niu, Y. Liu, X. Chen, S. Wang, Y. S. Zhou, L. Lin, Y. Xie, and Z. L. Wang, "Theory of freestanding triboelectric-layer-based nanogenerators," Nano Energy **12**, 760–774 (2015).

[51]C. Xu, Y. Zi, A. C. Wang, H. Zou, Y. Dai, X. He, P. Wang, Y.-C. Wang, P. Feng, D. Li, and Z. L. Wang, "On the electron-transfer mechanism in the contact-electrification effect," Adv. Mater. **30**(15), 1706790 (2018).

7

Unravelling the Mechanism of Polymer/Metal Charge Transfer

7.1 Background and motivation

The underlying mechanism of contact triboelectrification (CE) has been a subject of controversy since its initial discovery thousands of years ago [39]. Despite centuries of research, the exact nature of charge transfer during CE remains unclear due to its complexity in nature and the lack of advanced characterisation techniques [3]. With the recent advancement of triboelectric nanogenerators since 2012, this topic has attracted new attention, leading to advancements in both theoretical and experimental approaches to better understand it.

Currently, the electron transfer model is the most widely accepted theory in CE. However, limitation of this model exists, leaving certain phenomena unable to be fully explained. Recent studies suggest that the energy barrier for atoms to approach sufficiently close in the repulsive region may be too high, making electron cloud overlap unlikely to occur as previously theorised [197]. This has raised questions about the validity of a purely electron-based transfer mechanism. Instead, research into material's mechanical properties suggests that the transfer of charged species, such as ions or small material fragments, may also contribute to CE [51,53]. While the mechanism of CE remains complex and multifaceted, understanding it is critical for precise control of the performance of TENGs. As a result, this chapter aims to unravel the underlying mechanism of charge transfer in CE, specifically focusing on the polymer/metal interfaces. Through various proposed models, the roles of chemical, mechanical, and surface electronic properties in influencing charge transfer are investigated.

To explore the mechanism of CE, A judicious selection of material was conducted. As demonstrated in Chapter 4, the approach of applying functionalised groups in MOF ligands has demonstrated its effectiveness in enhancing charge transfer and triboelectric outputs. This principle can be extended to pristine polymers by modifying the functional group on the surface, allowing for a deeper understanding of the mechanisms that might affect CE.

PDMS was selected as the polymer for this study due to its well-documented tribo-negative behaviour, high transparency, elasticity, and flexibility, making it a staple in TENG applications [28,59,198-201]. Although the functionalisation of PDMS is a well-established technique in biomedical applications, including cell culture [202], anticorrosion [203], antifouling [204], and molecule sensing [205], the effect of surface functionalisation of PDMS on triboelectric output remains largely unexplored in the field of triboelectric nanogenerators.

A well-known approach for functionalising PDMS surfaces is the formation of self-assembled monolayers (SAMs) [206]. SAMs are prepared by immersing a plasma-treated substrate into a solution. These molecules contain a head group capable of binding to the substrate and a tail group that determines the substrate's surface properties. In 2020, Wang *et al*. used highly fluorinated molecules as surface modification layers to improve the triboelectric property of PDMS, as shown in Figure 7.1. A SAM based on the highly fluorinated molecule, 1*H*,1*H*,2*H*,2*H*-perfluorododecyl (F_{21}) significantly improved the triboelectric output, increasing it from 200 V and 20 μA for pristine PDMS to 873 V and 78 μA. The improvement is attributed to the effective transfer of surface electrons from the aluminium counter electrode [207]. Additionally, SAM functionalisation on aluminium electrodes using 3-aminopropyl triethoxysilane (APTES) further enhanced the triboelectric performance. Later, the same group reported another cationic thiol-based SAM using cationic (11-mercaptoundecyl)-*N*,*N*,*N*-trimethylammonium bromide on PDMS, achieving record-breaking voltage and current output of 1008 V and 124.9 μA [208]. In general, these studies demonstrate the tuneability of triboelectric properties through SAM modifications, offering a valuable opportunity to investigate the chemical, mechanical, and surface potential factors contributing to CE.

As a result, this chapter aims to utilise SAM-functionalised PDMS as a platform to study the underlying mechanism of charge transfer at polymer/metal interfaces. The focus of this chapter lies in understanding how different functional groups influence surface properties and the triboelectric performance of TENGs.

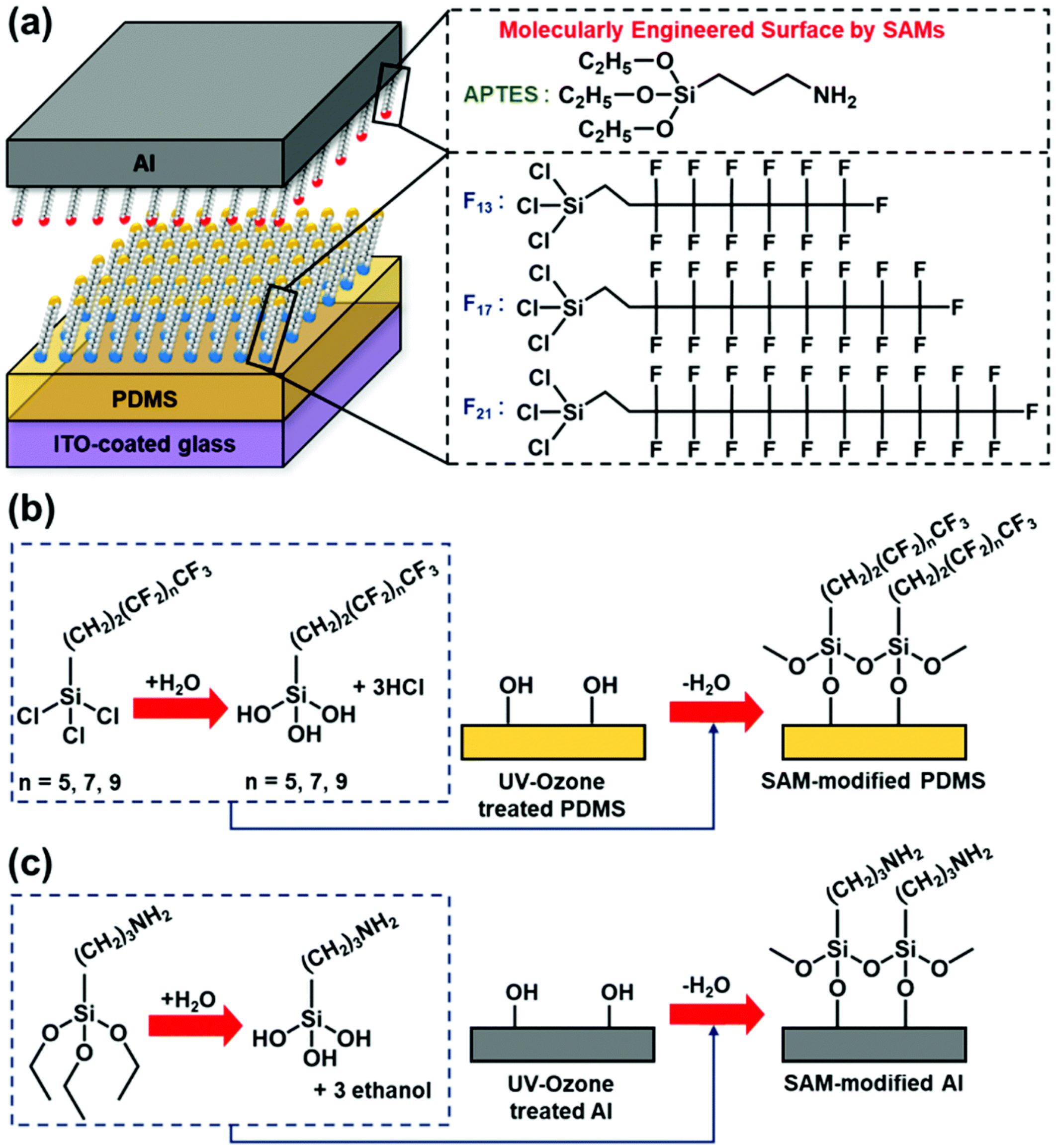

Figure 7.1. (a) Schematic illustration of the device architecture used in this study and chemical structures of silane-based SAM molecules. (b and c) Mechanism of silane-based SAM formation on a hydrated PDMS and aluminium (Al) surface. Adapted with permission from ref [207]. Copyright 2020 Royal Society of Chemistry.

7.2 Summary of Paper IV

7.2.1 Surface functionalisation of PDMS

The PDMS substrates are surface functionalised through SAMs of three siloxane molecules: (3-aminopropyl)triethoxysilane (APTES), 3-(trimethoxysilyl)propyl methacrylate (TMSPMA), and vinyltrimethoxysilane (VTMS). The chemical properties of SAMs were analysed through molecular simulations and FTIR characterisations, as shown in Paper IV (Figures 2 and 3). These siloxane molecules were selected based on variations in their head, tail, and spacer chemical groups, providing a range of electronegativity at the functional group's end (amine, vinyl, and methacrylate groups, respectively).

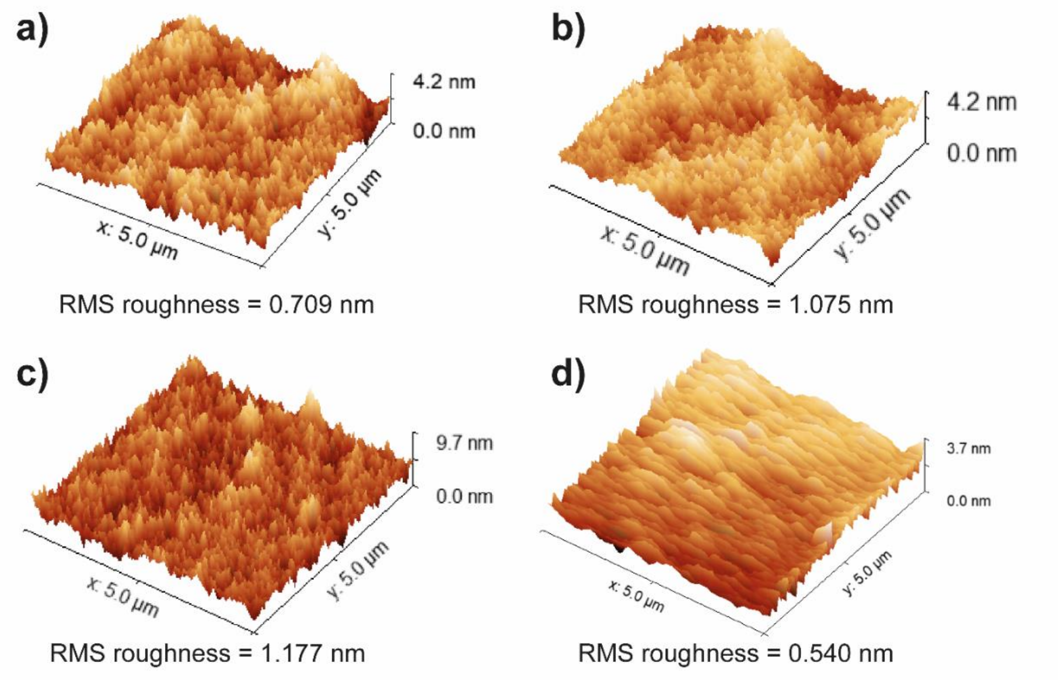

Figure 7.2. AFM 3D height topography of the (a) PDMS, (b) VTMS-PDMS, (c) APTES-PDMS, and (d) TMSPMA-PDMS surfaces.

The functionalised PDMS samples were prepared by immersing a spin-coated PDMS substrate into solutions of SAM molecules. The AFM image of the functionalised PDMS surfaces revealed minimal changes in the surface topography with comparable surface roughness across samples, as shown in Figure 7.2.

7.2.2 Electrical performance

The electrical performance of the functionalised PDMS samples was evaluated after being assembled into TENG devices, with indium tin oxide (ITO) electrodes as the counter material. Among the tested samples, TMSPMA-functionalised PDMS exhibited the highest triboelectric output, achieving voltage and current outputs of 189 V and 6.75 µA, respectively, as shown in Paper IV (Figure 4). Conversely, APTES-functionalised PDMS demonstrated the lowest performance when paired with ITO; the reason behind this outcome will be discussed below.

Figure 7.3. Triboelectric series summarising the relative triboelectric properties of the functionalised PDMS and ITO electrode.

A triboelectric series has been presented in Figure 7.3 to visualise the relative tendency of the material to gain or lose electrons through contact electrification. ITO, normally considered a highly tribo-positive material due to its high conductivity and electron-donating nature, has been widely used for TENGs [55]. Despite its relatively more positive position on the triboelectric series, the functionalisation of a highly electron-accepting PDMS membrane with APTES can lead to even more electron-donating properties over ITO. On the other hand, the incorporation of methyl acrylate groups enhanced the triboelectric output against ITO, placing it in the most negative region in the triboelectric series amongst the materials studied. All these observations supported that the variation of surface functional groups leads to significant changes in its triboelectric properties, demonstrating that the contact electrification process is an interfacial phenomenon and that the surface properties of a material have a more dominant effect on its triboelectric properties. Therefore, the variation in surface properties of the material can be an effective and universal approach for boosting the triboelectric performance of bulk materials.

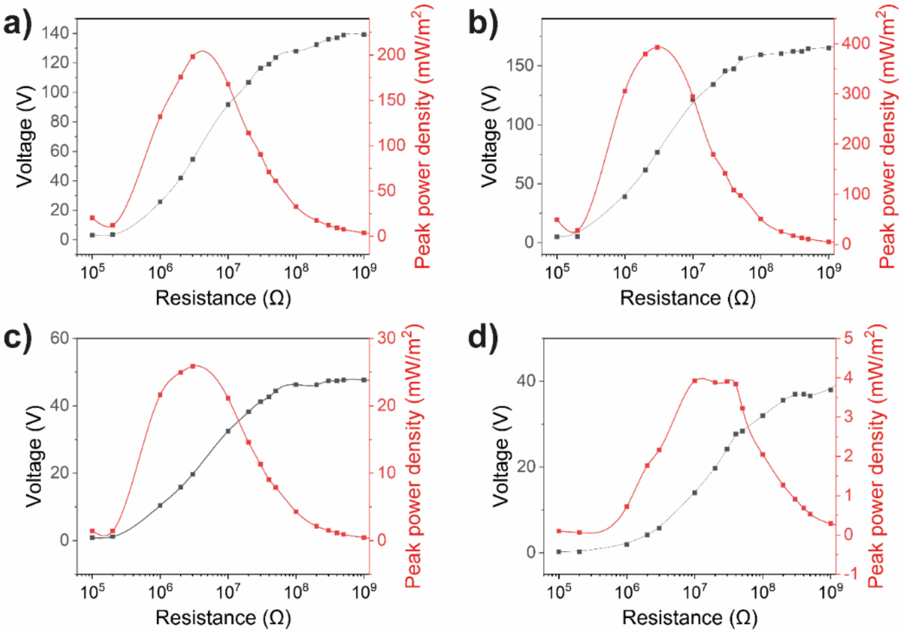

Figure 7.4. Variation of peak power output density and voltage output relative to different load resistances for the (a) PDMS, (b) TMSPMA-PDMS, (c) VTMS-PDMS, and (d) ATPES-PDMS based TENG devices.

The power densities of functionalised PDMS under various resistances were measured and presented in Figure 7.4. The power density output follows a similar trend to the triboelectric voltage and current output. When connected to an external resistive load, TMSPMA-PDMS exhibited the highest power density output of 393 mW m^{-2}, which is twice that of pristine PDMS. On the other hand, other functionalized PDMS samples demonstrated reduced power density due to the incorporation of electron-donating functional groups on the polymer surface. This effect was particularly pronounced in APTES-PDMS, where the triboelectric nature of PDMS shifted from electron-withdrawing to electron-donating, as shown in Figure 7.3, making the charge transfer with electrode less favourable. Furthermore, all PDMS samples exhibited their highest power density around 3 MΩ, except for APTES-PDMS, which reached its maximum at over 10 MΩ. The load resistance at the highest power density corresponds to the internal resistance of the prepared TENG device. As there is a high resistance for electrons to transfer in APTES-PDMS sample, the output density is significantly lower compared to other samples.

7.2.3 Nano-FTIR spectroscopy

To elucidate the charge transfer mechanism between functionalised PDMS and the ITO electrode, nearfield infrared nano-FTIR spectroscopy combined with AFM was employed, allowing for high-resolution analysis of surface chemical and physical properties. When contacting the PDMS membrane against a pristine ITO-PET sheet, fragments of PDMS were observed to transfer onto the ITO surface, forming lumps of various sizes detected under the AFM. For example, Figure 7.5

displays a large transferred particle with a size of over 10 μm. The chemical composition of the observed lump was characterised by nano-FTIR with a spatial resolution of 20 nm. Strong characteristic peaks have been identified at 1100 cm^{-1} and 1264 cm^{-1}, corresponding to the Si-O-Si and Si-CH$_3$ bending modes of PDMS, respectively.

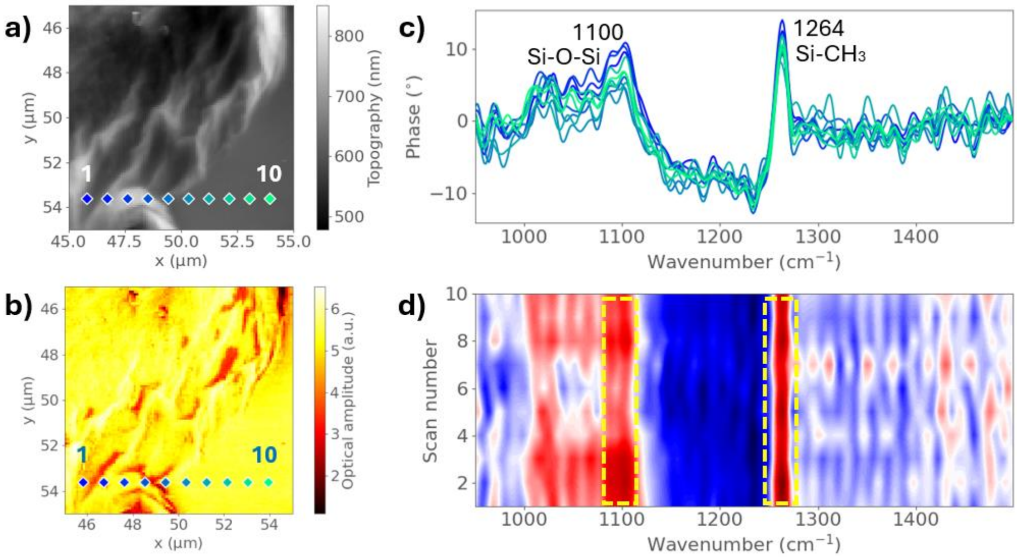

Figure 7.5. (a) AFM height topography and (b) its corresponding nano-FTIR absorption of a large-size PDMS residue (>10 μm) transferred to the ITO surface. (c) Nano-FTIR spectra that correspond to the points on a line marked in the AFM image. (d) The contour plot of nano-FTIR spectra of the line scan depicted in panel (b).

Similarly, residues of functionalised PDMS at smaller sizes were observed in Figure 7.6. Here, the characteristic IR absorption peaks at 1100 cm^{-1} and 1264 cm^{-1} were detected not only on the transferred particles, but also on the smooth ITO surface, although with a significantly weaker signal. This indicates that chemical bond breakage occurs in the contact region, leading to detectable residues. Moreover, while comparing the relative peak intensity of 1100 cm^{-1} and 1264 cm^{-1}, the Si-O-Si peak on the bulk ITO surface shows a lower intensity compared to TMSPMA-PDMS, indicating the potential of PDMS backbone breakage due to the contact-separation process. These findings provide additional evidence of material transfer during contact electrification, which is further discussed in Paper IV (Section 3.3).

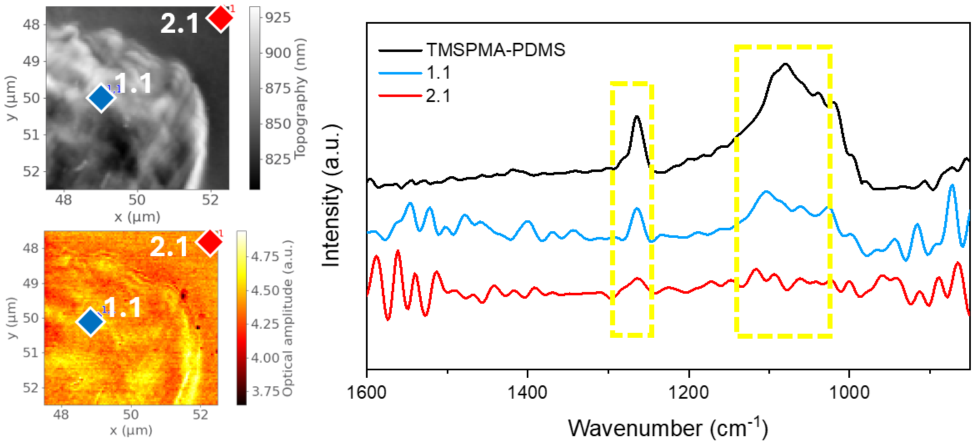

Figure 7.6. (a) AFM height topography and (b) its corresponding nano-FTIR absorption of a medium-size TMSPMA-PDMS residue (<10 μm) transferred to the ITO surface. (c) Comparison of nano-FTIR spectra that corresponds to the points marked on the AFM image and the neat TMSPMA-PDMS.

7.2.4 Surface mechanical behaviour

The mechanical property also has a significant contribution to the triboelectric properties of material based on previous studies [53,209]. The pull-off test was performed on functionalised PDMS membranes to examine the surface mechanical properties. To perform the test, a nanoindenter was used with a cylindrical flat punch at a radius of 26 μm. A standard load-depth correlation from the pull-off test is shown in Figure 7.7. The flat punch was initially positioned 2 μm above the sample surface. The tip was then lowered towards the surface at a speed of 100 nm s^{-1}, with surface detection facilitated by monitoring the phase signal. Upon contact, the punch applied a load at a rate of 0.01 mN s^{-1} to reach a maximum load of 0.1 mN. The tip remained at this peak load for 2 seconds before being unloaded at the same rate and retracted 5 μm from the surface. The pull-off force is the highest force required to separate the tip from the bonded surface, and the pull-off stress was calculated by dividing the measured pull-off force by the nominal contact area. The work of adhesion measures the energy required to separate the tip and sample surface, calculated by the integration of the area under the load-depth curve. Table 7.1 and Figure 7.8 represent the experimental results of the pull-off test conducted on PDMS samples. Among all tested samples, TMAPMS-PDMS exhibited the highest pull-off stress of 0.1 MPa and work of adhesion of 373.4 pJ. The results reveal a strong correlation between the material's adhesion property and triboelectric output, where a high work of adhesion enhances bond cleavage and material transfer during the contact-separation process, thereby facilitating greater charge transfer. The exception of VTMS-PDMS is attributed to the functional group effect compared to pristine PDMS. Through mechanical properties analysis, it was identified that the functionalisation process also modifies the surface mechanical properties of PDMS, further contributing to enhanced triboelectric output. The contributions of material transfer and electron transfer mechanisms in contact electrification of functionalised PDMS were discussed in detail in Paper IV (Section 3.3).

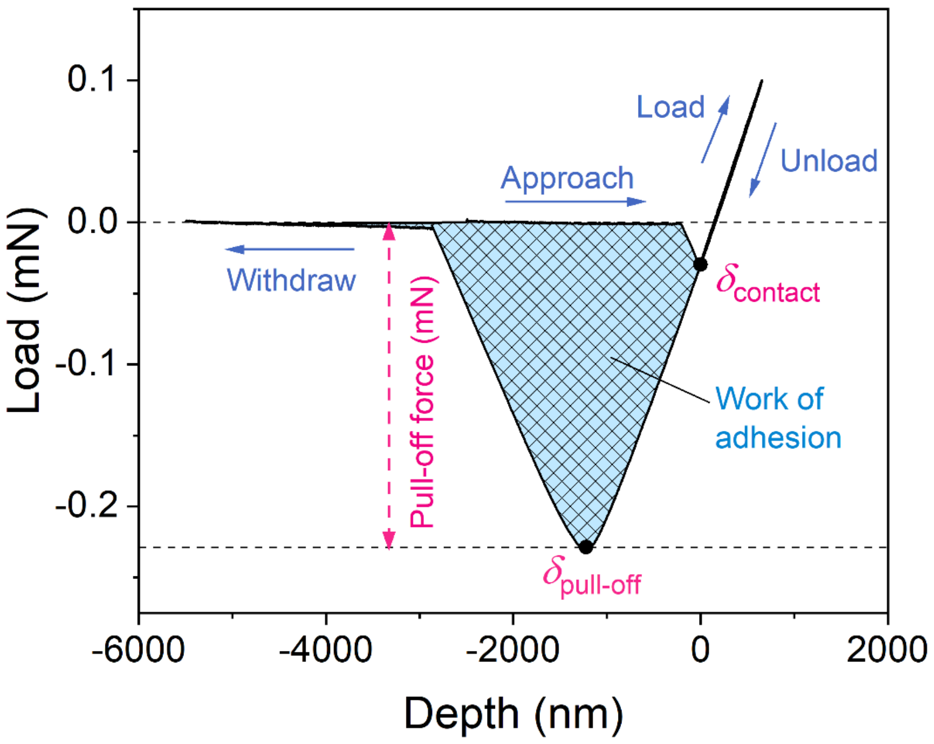

Figure 7.7. An example of load-depth curve obtained by a pull-off test. $\delta_{contact}$ is the depth of indentation at the jump-to-contact point, and $\delta_{pull\text{-}off}$ is the indentation depth at the maximum adhesive force. For each sample, a total of 12 tests were performed on a 5 × 5 mm^2 sample area.

Table 7.1. Comparison of the pull-off force, work of adhesion, peak voltage, and peak power density of pristine and surface functionalised PDMS samples.

Sample	Pull-off stress [MPa]	Work of adhesion [pJ]	Peak voltage [V]	Peak power density [mW/m^2]
APTES-PDMS	0.0618 ± 0.004	129.2 ±9.6	25.4	3.90
VTMS-PDMS	0.0805 ± 0.0024	229.0 ± 4.9	31.7	25.87
PDMS	0.0787 ± 0.0027	225.4 ± 4.4	136.1	198.02
TMSPMA-PDMS	0.1072 ± 0.0026	373.4 ± 11.3	198.7	393.22

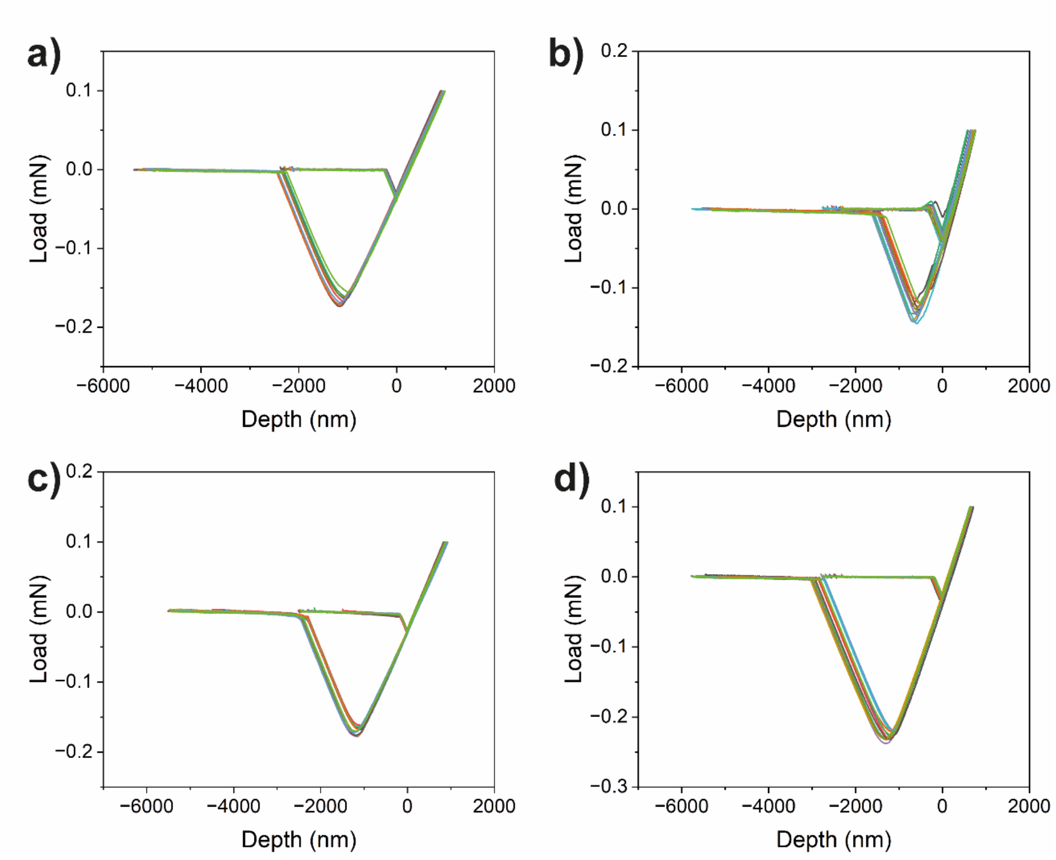

Figure 7.8. Load-depth curves of the PDMS samples obtained from the pull-off surface adhesion tests, for the (a) pristine PDMS, (b) APTES-PDMS, (c) VTMS-PDMS, and (d) TMAPMS-PDMS samples, respectively. Each sample was tested at 12 distinctive positions.

In conclusion, this study demonstrates that surface functionalisation of PDMS with SAMs significantly affects the triboelectric properties of the same starting material, as shown by marked differences observed in the electrical performance, mechanical adhesion, and interfacial charge transfer. Functional groups such as methacrylate and vinyl enhance tribo-negativity and significantly boost the triboelectric output, while the amine groups degrade performance due to their electron-donating nature. These findings underscore the importance of surface modifications in optimising TENG performance and provide a comprehensive understanding of the interfacial phenomena governing charge transfer. To further elucidate these effects, advanced nanoanalytical techniques, including nano-FTIR, KPFM, and mechanical studies, were employed to investigate both electron transfer and material transfer mechanisms between functionalised PDMS and an ITO counter electrode. This analysis offers valuable insights for the future design and development of high-performance triboelectric materials.

7.3 ***Paper IV:*** *Functionalized PDMS for regulating the triboelectric output of nanogenerators: a study of charge transfer mechanisms*

Online version: https://doi.org/10.1039/D4TC05325G

Journal of
Materials Chemistry C

ROYAL SOCIETY
OF CHEMISTRY

PAPER

View Article Online
View Journal | View Issue

Check for updates

Cite this: *J. Mater. Chem. C*, 2025, 13, 7654

Functionalized PDMS for regulating the triboelectric output of nanogenerators: a study of charge transfer mechanisms†

Jiahao Ye,[a] Tianhuai Xu,[a] Liva Germane,[b] Linards Lapcinskis,[b] Andris Šutka[b] and Jin-Chong Tan *[a]

Polydimethylsiloxane (PDMS) is one of the most widely used materials in triboelectric nanogenerators (TENGs) due to its remarkable flexibility and robustness, yet its triboelectric output often limits practical applications. In this study, we present a method for tuning the triboelectric properties of PDMS through surface functionalization using self-assembled monolayers of siloxane-based molecules. Our results demonstrate that the functionalized PDMS films exhibit distinct charge donating or withdrawing behaviours, confirmed by molecular simulations and experimental characterization. Notably, trimethylsiloxyphenylmethacrylate (TMSPMA) functionalized PDMS achieved the highest voltage of 189 ± 6 V and current output of 6.75 ± 0.26 μA, leading to a 2-fold increase in peak power density compared with the standard PDMS. Moreover, to elucidate the charge transfer mechanisms between the functionalized PDMS and indium tin oxide (ITO) electrode, nanoanalytical techniques such as nano-Fourier transform infrared spectroscopy (nano-FTIR) and Kelvin probe force microscopy (KPFM) were employed to evaluate the surface chemical and electrical properties at the local scale. This research not only enhances the understanding of polymer/metal contact electrification, but also opens avenues for optimizing TENG efficiency through targeted surface functionalization strategies.

Received 17th December 2024,
Accepted 25th February 2025

DOI: 10.1039/d4tc05325g

rsc.li/materials-c

1. Introduction

Triboelectric nanogenerators (TENGs) are an emerging technology that converts mechanical energy into electrical energy based on contact triboelectrification and electrostatic induction. With its great advantages of scalability, simple fabrication, and flexibility, extensive research has been conducted towards commercial applications.[1,2] Polydimethylsiloxane (PDMS), a silicone polymer with excellent mechanical resilience and electron-withdrawing ability, has become one of the most widely used polymer materials in research pertaining to TENG devices.[3] As a soft elastomer material, PDMS exhibits several advantages during TENG device manufacturing, including ease of processing, low cost, good transparency, and potential for surface functionalization.[4,5] Various applications of PDMS-based TENGs have been developed in biomechanical energy harvesting,[6,7] vital sign monitoring,[8,9] robotic sensors,[10,11] and Internet of Things (IoT).[12] However, the energy conversion efficiency of the prepared TENG devices is still limiting real-world applications. For example, a PDMS film generates a triboelectric output of 232 V and 6 μA while contacting with a copper electrode, as reported by Xu *et al.*[4] To overcome the current bottleneck in the triboelectric output of TENG devices, many approaches have been made to improve the triboelectric performance of PDMS-based TENG devices including ion injection,[13,14] surface micro-patterning design,[15,16] and incorporating high dielectric constant fillers.[17,18] For example, by the combination of using ion injection through an antistatic gun and surface microstructure using cilia, Seo *et al.* significantly improved the triboelectric performance of a single electrode PDMS-based TENG.[13] In 2017, Rasel and Park fabricated microstructured PDMS using sandpaper to enlarge the contact area during triboelectrification, producing a peak-to-peak open-circuit voltage of up to 103 V against human skin.[19] Moreover, Shi *et al.* modulated a PDMS-TENG by incorporating $BaTiO_3$ and Ag nanoparticles, and improved the dielectric constant and the charge-trapping ability of the nanocomposites, yielding a maximum output voltage and current of 88 V and 8.3 μA.[20] While these approaches contribute to performance improvements, a comprehensive understanding of the underlying charge transfer

---

[a] *Multifunctional Materials & Composites (MMC) Laboratory, Department of Engineering Science, University of Oxford, Parks Road, Oxford, OX1 3PJ, UK. E-mail: jin-chong.tan@eng.ox.ac.uk*

[b] *Institute of Physics and Materials Science, Faculty of Natural Sciences and Technology, Riga Technical University, 1048, Riga, Latvia*

† Electronic supplementary information (ESI) available: ATR-FTIR, far-IR, nano-FTIR, AFM and KPFM characterization data. Voltage, current, and power output data. Schematic diagrams of experimental setups and device working mechanisms. See DOI: **https://doi.org/10.1039/d4tc05325g**

mechanism in PDMS remains elusive. The triboelectrification process involves complex surface interactions between materials, and the basic origin of the charge transfer is still being debated. The three proposed theories, including electron transfer, ion transfer, and material transfer, have been observed with experimental and computational studies under various cases,[21–25] but a need for more refined characterization techniques is becoming evident to study these mechanisms.

Herein, we report a method to functionalize the PDMS surface with various siloxane groups to examine the effect of surface functionalization on the triboelectric output performance. Our previous findings have proven the improved charge generation properties by altering the combination of functionalized surfaces under a dielectric-to-dielectric system.[26] In this research, we investigated the actual performance of a TENG device under a dielectric-to-metal condition by measuring the open-circuit voltage and short-circuit current output. The neat PDMS materials are prepared and then functionalized with three different types of self-assembled monolayers (SAM) with different electron-donating/withdrawing behaviour. Our results indicate that the triboelectric properties of PDMS can be tuned through surface functionalization. Moreover, using nanospectroscopy techniques, we observed variations in the work function of functionalized PDMS surfaces and evidence of bond cleavage and charged material transfer to the ITO surface, elucidating the underlying charge transfer mechanisms. The functionalization approach and discussion of mechanisms introduced in this study aimed to link nanoscale characterizations with fundamental triboelectric principles, providing guidelines to advance TENG design for higher output performance.

2. Methods

2.1 Fabrication of functionalized PDMS

Polydimethylsiloxane (PDMS) elastomer and curing agent was obtained from Dow Corning (Sylgard 184). The PDMS samples were prepared by mixing the precursor and curing agent at a mass ratio of 10 : 1. The resulting mixture was poured onto an ITO-coated glass substrate and spun at 2500 rpm for 10 seconds. After curing the PDMS samples at 80 °C for 3 h, the obtained PDMS samples were cut into squares, each with an area of 2.5 × 2.5 cm^2 and a thickness of 100 μm. The PDMS samples were then plasma treated by oxygen to attach hydroxyl groups on the surface. Three different types of functionalized groups, (3-aminopropyl)triethoxysilane (APTES), 3-(trimethoxysilyl)propyl methacrylate (TMSPMA) and vinyltrimethoxysilane (VTMS), were dissolved in ethanol respectively at a concentration of 20 g L^{-1}. The prepared PDMS was immersed in the prepared solutions for 1 h and dried in ambient air for 30 min to yield functionalized PDMS.

2.2 Electrical performance measurements

The triboelectric output of the as-prepared functionalized PDMS was measured under contact-separation mode. A permanent electromagnetic shaker (Brüel & Kjær LDS V201) powered by a voltage-amplified arbitrary function generator (GW Instek AFG-2105) was used to generate the periodic contact-separation motion. The ITO-contacted PDMS was then coupled with another ITO surface as the counter electrode. The TENGs were contacted for 30 minutes to reach stability. The standard electrical output was tested under impact driven by a 2 Hz square wave at a separation distance of 4 mm. The average speed of the moving electrode during contact-separation was 0.4 m s^{-1}. The contact force was monitored by a load cell (RS PRO) connected to the sample holder. The instantaneous force at contact was maintained at 50 N by the controlled separation gap and shaker driving voltage. The voltage output of the samples was measured using a digital oscilloscope (PicoScope 5444B) equipped with a 100 MΩ high voltage probe (Rigol RP1300H). The current output was measured by an electrometer (Keithley 6514).

2.3 Material characterizations

A scanning electron microscope (SEM) was used to reveal the surface morphology of the prepared materials. The Fourier-transform infrared spectra (FTIR) were recorded by a Nicolet iS10 FTIR spectrometer equipped with an attenuated total reflectance (ATR) module. The atomic force microscopic (AFM) surface height topography and the nano-FTIR spectra *via* infrared nanospectroscopy were determined through a scattering-type scanning near-field optical microscope (Neaspec s-SNOM).[27] The nano-FTIR spectra were taken at 20 nm resolution, combining the spectra of two laser sources with ranges from 700 to 1400 cm^{-1} and 1000 to 1600 cm^{-1}. An average of 11 individual interferograms were recorded for each spectrum with a spectral resolution of 12 cm^{-1} and an integration time of 10.2 ms. The far-IR spectra (spectral range 150–650 cm^{-1}) were recorded at the multimode IR imaging and microspectroscopy (MIRIAM) Beamline B22 at the Diamond Light Source synchrotron. A Bruker Vertex 80v FTIR spectrometer equipped with an ATR accessory (Bruker Optics) was used to perform the measurement. The detector was equipped with a liquid helium cooled Si-Bolometer. Post-measurement, the obtained data was processed using the OPUS 7.2 software. The Kelvin-probe force microscopy (KPFM) data were recorded using an Asylum Research Cypher ES with an ASYELEC-01-R2 conductive tip under SKPM mode. The scan area was set to 1 μm × 1 μm, with a scan resolution of 128 × 128 pixels and a scan rate of 2.44 Hz to minimize drift. The KPFM results were processed using Gwyddion software,[28] where the color scale and range were adjusted, and the average surface potential was calculated. The pull-off test was conducted in a nanoindenter (iMicro KLA Tencor). The test employed a cylindrical flat punch with a nominal diameter of 52 μm. Initially, the flat punch was lifted 2 μm above the sample surface. Then, the tip approached the surface at a speed of 100 nm s^{-1}, with surface detection facilitated by monitoring the phase signal. After contact, the punch applied a load at a rate of 0.01 mN s^{-1} until reaching a maximum load of 0.1 mN. The tip was held at this peak load for 2 seconds. Then the tip was unloaded at the same rate and retracted 5 μm from the surface. The pull-off stress was calculated by dividing the measured pull-off force by the nominal contact area. The work of adhesion was calculated by integrating the area under the load-depth curve. A total of 12 tests were performed on a 5 × 5 mm^2 sample area.

2.4 Density functional theory (DFT) calculations

DFT calculations were performed to investigate the electronic properties of SAM molecules for surface functionalization. The molecular structures were first geometrically optimized utilizing the B3LYP functional combined with the 6-31G basis set[29,30] using Gaussian 09.[31] The electrostatic potential maps were then generated to visualize the charge distribution across the molecules.

3. Results

3.1 Materials

Fig. 1 outlines the sample preparation stages in the surface functionalization of PDMS. The pristine PDMS samples are first prepared by spin coating on ITO-coated glass followed by 3 hours of curing. The samples are then plasma treated and immersed in several siloxane-based molecules to attach certain functional groups on the PDMS surface. The surface-functionalized PDMS films show similar surface topography AFM, as shown in Fig. S1 (ESI†), with all functionalized PDMS showing surface roughness less than 1.2 nm, confirming the flatness of PDMS during contact. Fig. 2 shows the schematics of organic molecules that can be covalently linked to the PDMS backbone, including APTES, VTMS, and TMSPMA. Despite their structural similarity, these molecules were selected for their distinct functional properties. The relative electronic characteristics of these molecules are confirmed through *ab initio* density functional theory (DFT) calculations, where their electrostatic potential distributions are shown in Fig. 2. The siloxane groups in these molecules facilitate bonding with the PDMS backbone, while the distinctive parts of each molecule offer unique electronic properties to the overall structure leading to different chemical polarities. In general, the aminopropyl group in APTES offers a strong electron-donating property through the amine group within the molecule, whereas VTMS has a vinyl group that is relatively neutral due to the localized electron density around the C═C bond. On the other hand, the methacrylate bond in TMSPMA possesses a strong electron-withdrawing property resulting from the electronegative oxygen atoms in the carbonyl and ester groups, showing the most negative electrostatic potential.[32]

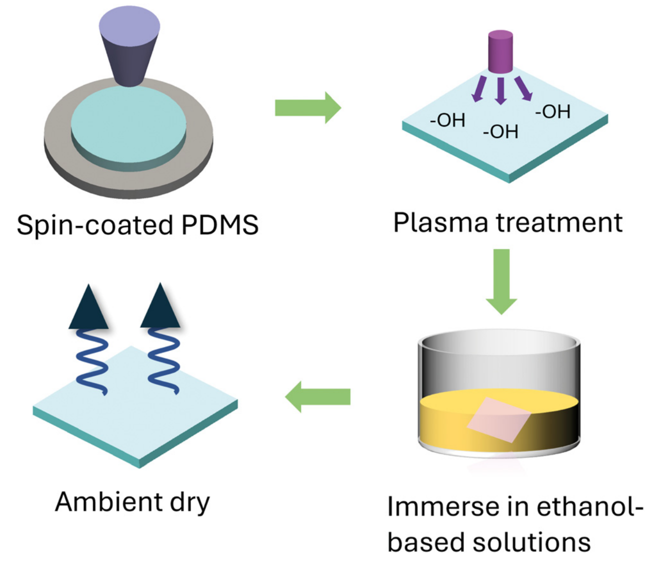

Fig. 1 Schematic of sample preparation steps for the surface functionalized PDMS.

The successful surface functionalization of PDMS with various functional groups has been confirmed through ATR-FTIR spectroscopy. Fig. 3a displays the mid-infrared absorption bands for the different PDMS samples. All PDMS samples show characteristic vibrational bands, including CH_3 rocking mode at 789 cm^{-1}, Si–O–Si stretching mode at 1000–1100 cm^{-1}, and Si–C stretching mode at 1257 cm^{-1}.[33] In addition, the APTES functionalized PDMS shows additional bands at 1561 and 1484 cm^{-1}, representing the N–H bending modes. The TMSPMA–PDMS also shows the C═O stretching mode at 1721 cm^{-1}. The VTMS–PDMS displays less apparent changes in spectra, with a slight signal at 1722 cm^{-1} for C═C stretching, as shown in Fig. S2 (ESI†). The nano-FTIR spectra were also taken to confirm the obtained FTIR results, as displayed in Fig. 3b. The near-field result is well-aligned with ATR-FTIR findings from bulk samples. In the far-IR region as shown in Fig. S3 (ESI†), all functionalized PDMS exhibit similar Terahertz absorption bands, with a dominant peak observed at around 400 cm^{-1} (∼12 THz) for the Si–O–Si backbone bending and 285 cm^{-1} (∼8.5 THz) for Si–C stretching.

3.2 Electrical performance

The triboelectric outputs of the prepared PDMS samples were examined by cyclic contact-separation motion against an ITO surface, acting as the counter tribo-positive material. The experimental setup for the measurement is shown in Fig. S4 (ESI†). The maximum force at contact was maintained at 50 N for all measurements, monitored by a load cell, as shown in Fig. S5 (ESI†). Regarding the open-circuit voltage output, the standard PDMS material reaches a maximum voltage of 136 V and peak-to-peak voltage of 196 V, as shown in Fig. 4a. In contrast, APTES–PDMS and VTMS–PDMS both show reduced voltage output, with peak-to-peak voltages of only 34% that of the neat PDMS. On the other hand, TMSPMA–PDMS, functionalized with a more electronegative functional group, demonstrates a 1.42 times improvement in maximum voltage and 2.25 times improvement in maximum current, showing the highest voltage and current output of 189 ± 6 V and 6.75 ± 0.26 μA, derived from 40 contact-separation cycles. Although APTES–PDMS and VTMS–PDMS show similar voltage output in value, their output profile differs significantly. When looking at a single spike of electric signal generated during contact and separation in Fig. 4b, all PDMS materials, except for APTES–PDMS, show a positive voltage during contact followed by a negative voltage during separation. Typically, PDMS material is considered an excellent tribo-negative material, which means that it withdraws and holds negative charges on its surface in a triboelectric pair. While the PDMS and ITO surfaces are in contact, the surface of PDMS gets negatively charged by taking

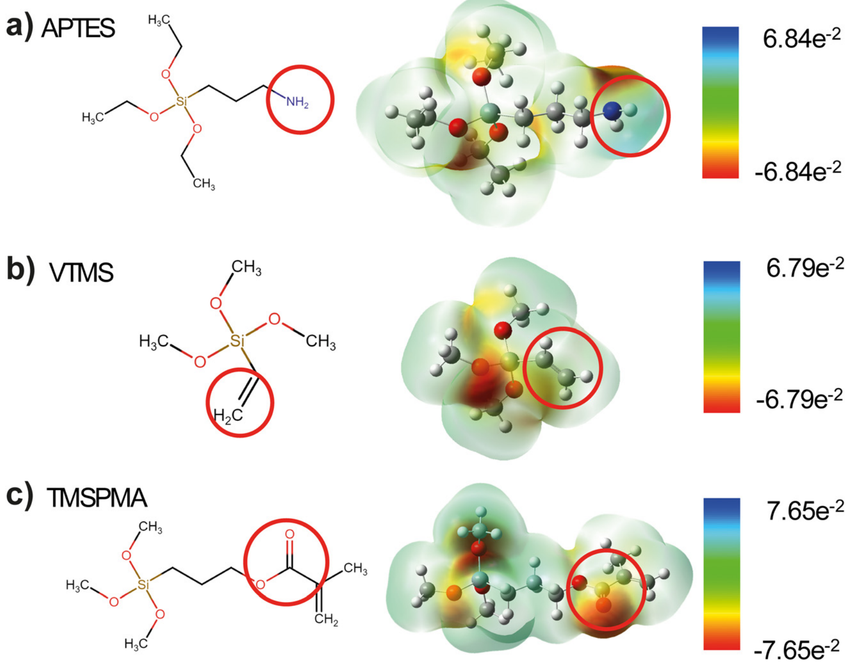

Fig. 2 Molecular structures of the functional groups and electrostatic potential maps predicted by DFT calculations for (a) APTES, (b) VTMS, and (c) TMSPMA. Unit is kcal mol^{-1}.

away the free electrons on the conductive ITO surface. However, an inverted phenomenon was observed for the case of APTES–PDMS, under the premise that the electrical connections during data collection are the same for all samples, indicating that the APTES–PDMS has become a more tribo-positive material relative to ITO. The APTES–PDMS donates electrons to ITO during contact, resulting in the reversed voltage profile exhibited in Fig. 4b. The strong electron-donating effect of the amine group in APTES resulted in changes in the original surface properties of PDMS. Although VTMS–PDMS also reduces the triboelectric output due to the neutral surface alkene groups, the reduction does not alter its relative position in the triboelectric series compared to ITO.

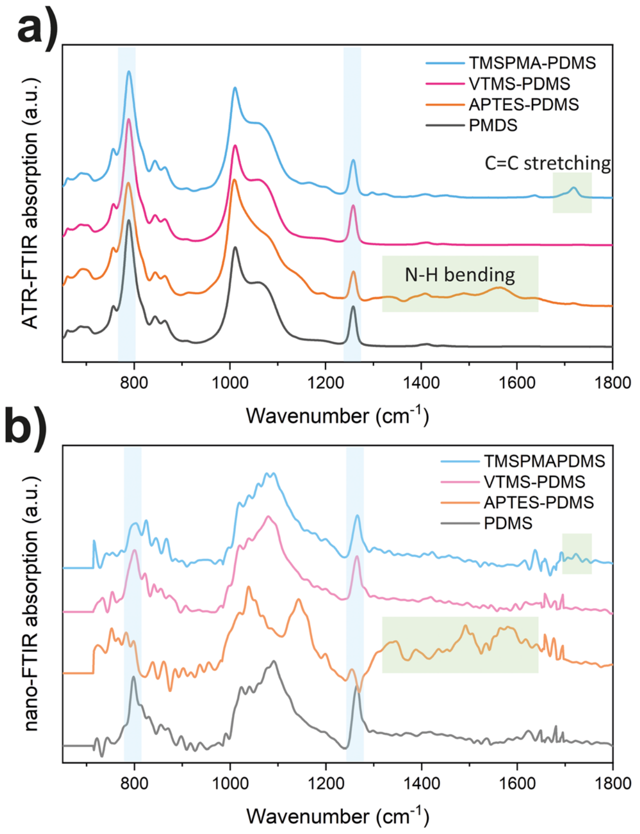

Fig. 3 (a) ATR-FTIR and (b) nano-FTIR spectra of surface-functionalized PDMS.

A similar trend is observed in the closed-circuit current output as shown in Fig. 4c. APTES–PDMS shows the lowest current output, followed by VTMS–PDMS, neat PDMS, and TMSPMA–PDMS. Although APTES–PDMS and VTMS–PDMS have similar voltage output, the current for APTES–PDMS is much lower. While the output voltage reflects the potential difference between the contacting materials, the measured current compensates the induced charges on the electrodes. As ITO is a conductive material abundant with free charge carriers, it has limited ability to hold or transfer more electrons from the APTES–PDMS side, resulting in the low current output of APTES–PDMS. When examining the individual signal peaks in Fig. 4d, APTES–PDMS has the only reversed output peak shape compared to other membranes, confirming our findings in voltage measurements. It is widely accepted that the surface property of a material plays a vital role in its triboelectric performance. While modifying the material surface with various functional groups, the work function of the material compared to the electrode is altered, leading to different charge transfer phenomena. These triboelectric performance results align with our DFT predictions, as shown in Fig. 1c,

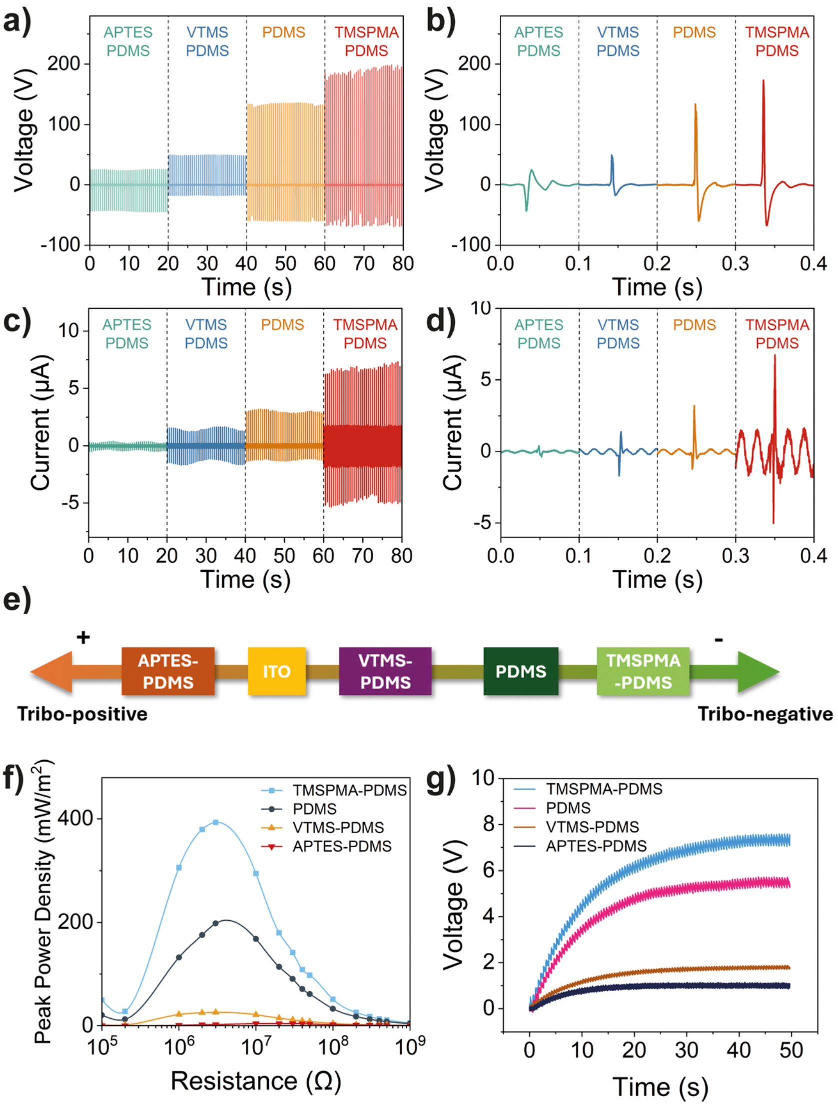

Fig. 4 (a) Open-circuit voltage profile and (b) a single-spike voltage signal of the PDMS-based TENG. (c) Short-circuit current profile and (d) a single spike current signal of the PDMS-based TENG. (e) Triboelectric series summarizing the relative triboelectric properties of functionalized PDMS and the ITO electrode in this study. (f) Peak power densities of different PDMS-based TENGs over a range of load resistances. (g) Voltage profile across a 0.1 μF capacitor while charging by different PDMS-based TENGs.

highlighting the role of surface functionalization in tuning charge transfer characteristics. Summarizing the relative electron-donating and withdrawing propensities of PDMS materials during contact, a triboelectric series can be established for materials studied in this work, as shown in Fig. 4e. Among these, APTES–PDMS is the only material that exhibits stronger electron-donating behaviour compared to conductive ITO, placing it as the most tribo-positive material in the series. On the other hand, through functionalization, TMSPMA–PDMS with enhanced withdrawing ability ranks furthest to the right within the series.

The peak power density of the prepared materials was measured and calculated by connecting the TENG devices to loads with varying resistances. The closed-circuit voltage was measured across the resistors, and the peak power density was calculated using $P_d = V^2/(RA)$. As summarized in Fig. 4f, the TMSPMA-modified PDMS exhibits the highest power density of 393 mW m^{-2}, which has doubled the power output of the neat PDMS attributed to the higher voltage and current output of the former, whereas APTES–PDMS shows the lowest power output. It is worth noticing that all these materials show their highest power density at around 3 MΩ, except for APTES–PDMS, which peaks at 10 MΩ. This optimum resistance at the highest power density denotes the internal resistance of the device.[34] The high internal impedance of the APTES–PDMS device can be explained by the high electron transfer resistance between the surfaces of two tribo-positive materials. Individual measurements of voltage-resistance relationships for functionalized PDMS are shown in Fig. S6 (ESI†). The alternating charge transferred during contact-separation can be rectified into direct current and harvested by capacitors for real-world applications. Fig. S7 (ESI†) shows the charging curves for capacitors ranging from 0.1, 0.47, 1, and 10 μF capacitances. Comparing the charging rates for a 0.1 μF capacitor, we found that TMSPMA–PDMS achieved the fastest charging speed, reaching a voltage of 7.3 V in 50 s, as shown in Fig. 4g.

3.3 Charge transfer mechanism

The charge transfer mechanism of the prepared PDMS-based TENGs is revealed and discussed based on results from various nano-scale characterization techniques. Among the three charge transfer mechanisms, the ion transfer model explains charge transfer by the formation of a water layer on the surface. This model normally applies to ionic and hydrophilic polymers. However, in our case, PDMS has high hydrophobicity where the water layer and amount of charge transfer through ions can be neglected since surface ionization reaction is unlikely to happen between the hydrophobic solid surfaces.[35] We therefore mainly elucidate the role of electron transfer and mass transfer mechanisms during the mechanical interaction between functionalized PDMS and ITO surfaces.

From the electron transfer perspective, electrons are transferred from a material with lower work function to higher, and the amount of charge transfer is proportional to the difference in the work function of the two materials. In this study, the work function of functionalized PDMS (Φ_{sample}) was indirectly measured by KPFM through the measurement of contact potential difference (V_{CPD}):

$$\Phi_{\text{sample}} = \Phi_{\text{tip}} - e\cdot V_{\text{CPD}} \tag{1}$$

where Φ_{tip} is the work function of the KPFM probe tip and e is the charge amount carried by an electron. According to eqn (1), a higher measured contact potential difference corresponds to a lower surface work function. To measure the contact potential difference of PDMS samples, pristine polymers were cut into squares of 5 mm × 5 mm and stabilized for two days after sample preparation to ensure no accumulated charge on the surface. Fig. 5a demonstrates the average V_{CPD} values and surface potential distribution maps of functionalized PDMS samples measured under stabilized conditions. The functionalized PDMS samples exhibited a relatively homogeneous surface potential, with APTES–PDMS showing the highest V_{CPD} and, therefore, the lowest work function, while TMSPMA–PDMS showed the lowest V_{CPD} and highest work function, consistent with the trend in previously summarized triboelectric series in Fig. 4e. The work function of a material is the minimum thermodynamic energy required to remove an electron from a solid to a point just outside the solid surface.[36] Electrons are transferred from the material with a lower work function to higher in order to maintain Fermi level balance, resulting in the material with lower work function being positively charged after contact.[37] This behaviour is illustrated in the surface state model to explain the electron transfer phenomenon as proposed in Fig. 5b. Here, the energy levels of functionalized PDMS are ranked according to the measured V_{CPD} values in comparison to the counter material ITO. While the APTES–PDMS has the lowest work function, its Fermi level exceeds the energy level of ITO, thereby transferring electrons during contact. Conversely, when the PDMS surface is functionalized with TMSPMA, the work function increases, resulting in a lower Fermi level. As a result, this increases the energy gap between TMSPMA–PDMS and the ITO electrode, compared to neat PDMS, thereby driving more electrons to hop from the ITO surface to TMSPMA–PDMS and enhancing charge generation within a TENG device.

On the other hand, evidence of material transfer has been observed *via* nano-FTIR analysis and KPFM scans. The mass transfer or material transfer model proposes that the charge transfer between two materials is due to the transfer of small fragment materials that carry a certain amount of charge that adhere to another surface during contact. As a soft polymer material with relatively low Young's modulus and high surface adhesion, PDMS is more likely to transfer materials during contact from the high contact area and higher density of *van der Waals* intermolecular bonds.[38] To examine the mass transfer between the PDMS film and ITO electrode, pristine materials were clamped together using spring clamps under 6.9 N to ensure conformal surface contact and eliminate potential contamination effects. Then the materials were separated and evaluated under AFM integrated nano-FTIR spectroscopy at a 20-nm spatial resolution.[27] The surface topography of the contacted ITO surface from AFM shows increased surface roughness

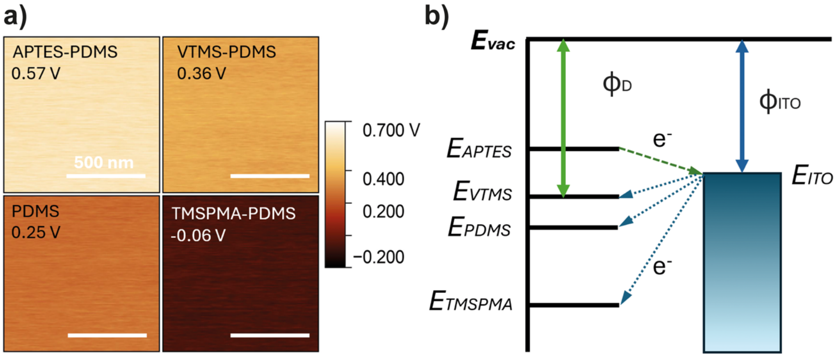

Fig. 5 (a) KPFM surface potential maps and average V_{CPD} values of different functionalized PDMS after stabilization. (b) Schematic diagram of the contact electrification mechanism elucidated by the electron transfer between PDMS and ITO due to different work functions. E_{vac}, vacuum level; E_{X}, Fermi level of the functionalized PDMS; ϕ_{D}, work function of functionalized PDMS; ϕ_{ITO}, work function of the ITO electrode. The relative position of PDMS samples in the energy diagram is determined by the measured V_{CPD} values, where $E_{\text{X}} = E_{\text{vac}} - (\phi_{\text{tip}} - e\cdot V_{\text{CPD\_x}})$.

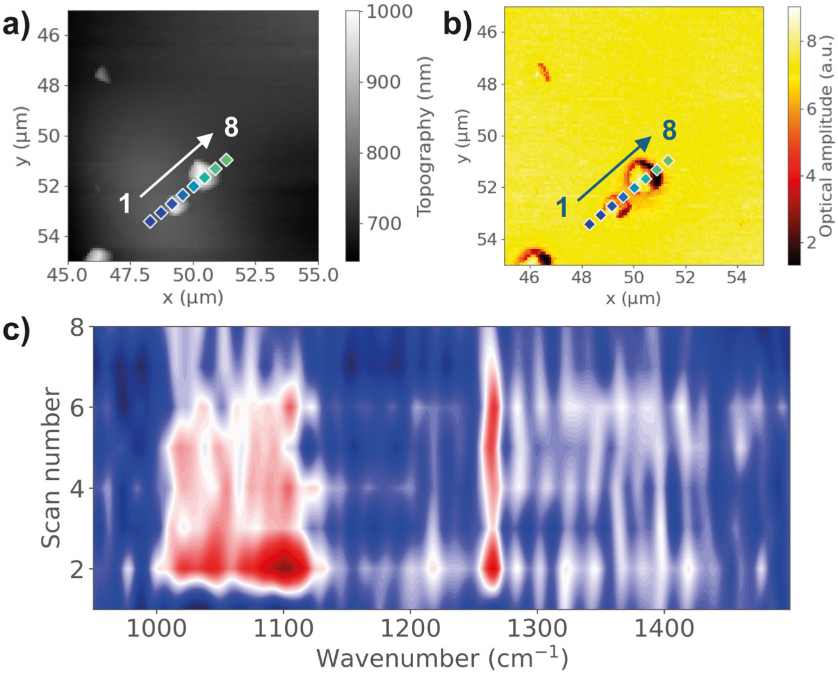

Fig. 6 (a) AFM topography and (b) near-field IR absorption image of nanoscale PDMS residues detected on the ITO surface after contact. (c) Nano-FTIR linescan spectra corresponding to the points marked on the AFM image.

with particles of different sizes. Fig. 6a shows the observation of several nano-sized particles on the ITO surface. By scanning the nano-FTIR spectra across the particles, characteristic peaks at 1265 cm^{-1} and 1091 cm^{-1} representing Si–C stretching and Si–O–Si stretching were observed on the particles, which confirmed the presence of PDMS. The IR absorption peaks are only observable near the particles, but not on the smooth ITO surface, demonstrating the transfer of PDMS residues during contact. In addition to nano-sized PDMS particles, larger transferred fragments, up to 10 μm, are also observed, as shown in Fig. S8 (ESI†). In this case, the absorption peaks are detectable even far away from the particles, indicating a layer of PDMS being transferred to the ITO surface, not only of the large particles but also with cleavage of bonds. The same observation is found

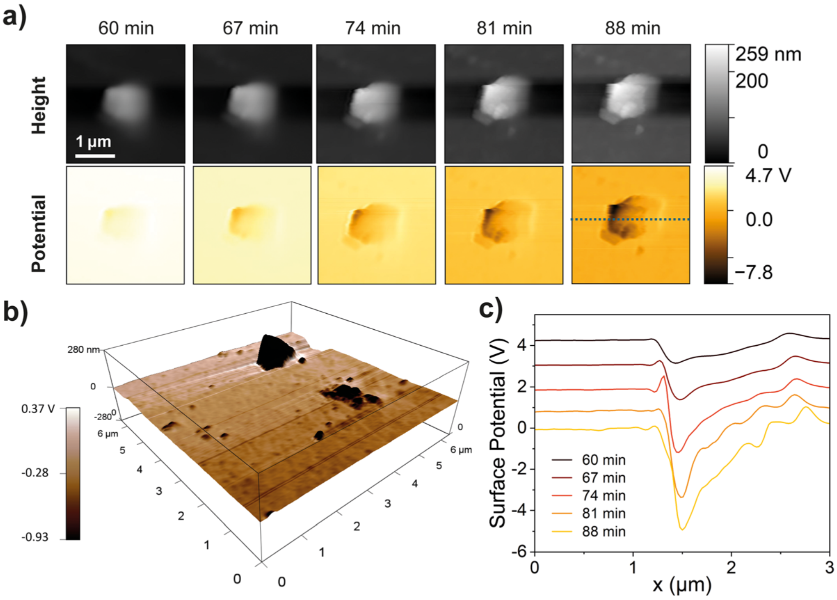

Fig. 7 (a) AFM height topography and KPFM surface potential of a PDMS residue on the ITO surface after contact. (b) 3D maps of the height profile topography with the KPFM surface potential superimposed with corresponding colour scales of PDMS contacted ITO surface. (c) Surface potential profile across the PDMS residue on the ITO surface at different times after contact.

for TMSPMA–PDMS, as shown in Fig. S9 (ESI†). Comparing the relative peak intensity of 1265 cm^{-1} and 1091 cm^{-1}, the Si–O–Si peak shows a lower peak intensity at the ITO surface, compared with bulk TMSPMA–PDMS. This could be an indication of Si–O bond breaking due to physical contact, where the chemical bond breakage on the backbone of functionalized PDMS leads to the transfer of small material fragments across the contact interface.[4] These fragments carry charges due to chemical bond breaking, resulting in the transfer of charges when they come into contact with the counter material.

The KPFM results further support the material transfer mechanism. In Fig. 7a, we detected rounded PDMS residue on the ITO surface immediately after contact, showing a significantly more negative surface potential than the pristine ITO surface. The 3D topography and potential distribution of PDMS residues revealed sizes from 2 μm down to the nanoscale, as shown in Fig. 7b. The surface charge of ITO initially after contact shows a highly positive value due to the withdrawal of electrons from the conductive surface, then gradually drops as it stabilizes and discharges under ambient conditions. However, it can be observed that the PDMS residue retains a much lower surface potential compared to the ITO surface, as shown in Fig. 7c, indicating that these charged tribo-negative counterpart fragments transferred to the surface may contribute importantly to charge transfer during contact. In addition to the observed transferred polymer fragments on the electrode surface, further experiments have revealed the correlation between the surface adhesion properties and triboelectric output of the materials, as shown in Fig. 8. Detailed experimental methods and results are presented in Fig. S10 and S11 (ESI†). TMSPMA–PDMS shows the highest pull-off stress and work of adhesion of 0.11 MPa and 374.4 pJ, respectively, relative to the other functionalized PDMS, indicating a more adhesive surface and thus a higher acceleration during separation. The high pull-off stress and work of adhesion promote more bond cleavage, leading to more material and charge transfer. The functionalization of PDMS alters the surface mechanical properties, further contributing to improved charge transfer efficiency. Together, these observations highlight the critical role of surface adhesion and material transfer in optimizing the triboelectric performance.

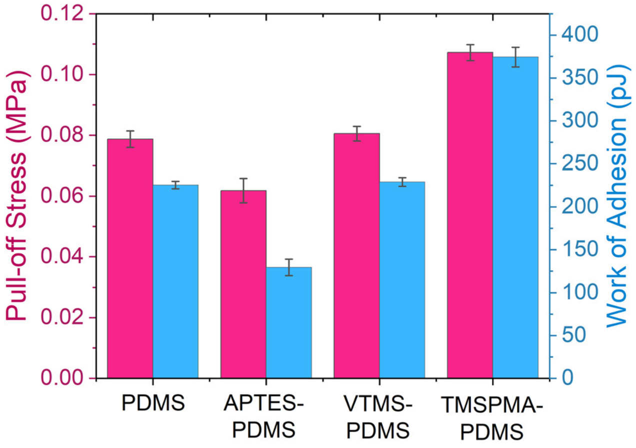

Fig. 8 Comparison of the pull-off stress and work of adhesion for the pristine and functionalized PDMS samples. Work of adhesion values were obtained using a cylindrical flat punch with a nominal diameter of 52 μm. Mean and standard deviation values were derived from 12 measurements shown in Fig. S11 (ESI†).

4. Conclusion

In summary, we introduced a surface functionalization method to tune the surface triboelectric properties of PDMS by self-assembled monolayers of APTES, VTMS and TMSPMA. The functionalized PDMS shows different relative positions on the triboelectric series due to the introduction of surface chemical bonds, validated through molecular simulations and experimental characterizations. The TMSPMA functionalized PDMS shows the highest voltage and current output of 189 ± 6 V and 6.75 ± 0.26 μA, increasing the peak power output density by 2 times compared with the neat PDMS. Moreover, advanced nanoanalytical techniques, including nano-FTIR and KPFM, were employed to investigate the charge transfer mechanisms between the functionalized PDMS and an ITO counter electrode. Our findings indicate that the surface functionalization approach varies the surface work function of PDMS, potentially serving as the driving force for the charge transfer against the ITO electrode. In addition, evidence of material transfer at the nanoscale is observed through surface topographical changes and chemical composition variations, which also significantly contributes to charge transfer. Future studies can leverage these insights in studying the mechanisms under polymer/metal contact electrification and improving the triboelectric performance through strategic surface modification strategies.

Author contributions

Jiahao Ye: conceptualization, methodology, investigation, formal analysis, writing – original draft preparation, writing – review & editing. Tianhuai Xu: methodology, formal analysis, writing – review & editing. Liva Germane: methodology, investigation, funding acquisition. Linards Lapcinskis: methodology, investigation. Andris Šutka: conceptualization, methodology, supervision, funding acquisition, writing – review & editing. Jin-Chong Tan: conceptualization, methodology, supervision, funding acquisition, writing – review & editing.

Data availability

The data supporting this article have been included as part of the ESI.†

Conflicts of interest

The authors declare that they have no known competing financial interests or personal relationships that could have appeared to influence the work reported in this paper.

Acknowledgements

This work was supported by the EPSRC award (TEGMOF EP/Z534146/1) and the ERC Consolidator Grant (PROMOFS grant agreement 771575). We acknowledge the Diamond Light Source for the award of beamtime SM36374, and for the technical support and scientific discussion with Dr Gianfelice Cinque during the far-IR measurements on Beamline B22 MIRIAM. Liva Germane acknowledges the support by the EU Recovery and Resilience Facility within Project No. 5.2.1.1.i.0/2/24/I/CFLA/003 "Implementation of consolidation and management changes at Riga Technical University, Liepaja University, Rezekne Academy of Technology, Latvian Maritime Academy and Liepaja Maritime College for the progress towards excellence in higher education, science and innovation" academic career doctoral grant (ID 1031).

References

1 J. Zhu, M. Zhu, Q. Shi, F. Wen, L. Liu, B. Dong, A. Haroun, Y. Yang, P. Vachon, X. Guo, T. He and C. Lee, Progress in TENG technology—A journey from energy harvesting to nanoenergy and nanosystem, *EcoMat*, 2020, **2**, e12058, DOI: **10.1002/eom2.12058**.

2 D. Choi, Y. Lee, Z.-H. Lin, S. Cho, M. Kim, C. K. Ao, S. Soh, C. Sohn, C. K. Jeong, J. Lee, M. Lee, S. Lee, J. Ryu, P. Parashar, Y. Cho, J. Ahn, I.-D. Kim, F. Jiang, P. S. Lee, G. Khandelwal, S.-J. Kim, H. S. Kim, H.-C. Song, M. Kim, J. Nah, W. Kim, H. G. Menge, Y. T. Park, W. Xu, J. Hao, H. Park, J.-H. Lee, D.-M. Lee, S.-W. Kim, J. Y. Park, H. Zhang, Y. Zi, R. Guo, J. Cheng, Z. Yang, Y. Xie, S. Lee, J. Chung, I.-K. Oh, J.-S. Kim, T. Cheng, Q. Gao, G. Cheng, G. Gu, M. Shim, J. Jung, C. Yun, C. Zhang, G. Liu, Y. Chen, S. Kim, X. Chen, J. Hu, X. Pu, Z. H. Guo, X. Wang, J. Chen, X. Xiao, X. Xie, M. Jarin, H. Zhang, Y.-C. Lai, T. He, H. Kim, I. Park, J. Ahn, N. D. Huynh, Y. Yang, Z. L. Wang, J. M. Baik and D. Choi, Recent Advances in Triboelectric Nanogenerators: From Technological Progress to Commercial Applications, *ACS Nano*, 2023, **17**, 11087–11219, DOI: **10.1021/acsnano.2c12458**.

3 R. Zhang and H. Olin, Material choices for triboelectric nanogenerators: A critical review, *EcoMat*, 2020, **2**, 12062, DOI: **10.1002/eom2.12062**.

4 T. Xu, J. Ye and J.-C. Tan, Unravelling the Ageing Effects of PDMS-Based Triboelectric Nanogenerators, *Adv. Mater. Interfaces*, 2024, 2400094, DOI: **10.1002/admi.202400094**.

5 G.-Z. Li, G.-G. Wang, D.-M. Ye, X.-W. Zhang, Z.-Q. Lin, H.-L. Zhou, F. Li, B.-L. Wang and J.-C. Han, High-Performance Transparent and Flexible Triboelectric Nanogenerators Based on PDMS-PTFE Composite Films, *Adv. Electron. Mater.*, 2019, **5**, 1800846, DOI: **10.1002/aelm.201800846**.

6 W. He, M. Sohn, R. Ma and D. J. Kang, Flexible single-electrode triboelectric nanogenerators with MXene/PDMS composite film for biomechanical motion sensors, *Nano Energy*, 2020, **78**, 105383, DOI: **10.1016/j.nanoen.2020.105383**.

7 Y. Yang, H. Zhang, Z.-H. Lin, Y. S. Zhou, Q. Jing, Y. Su, J. Yang, J. Chen, C. Hu and Z. L. Wang, Human Skin Based Triboelectric Nanogenerators for Harvesting Biomechanical Energy and as Self-Powered Active Tactile Sensor System, *ACS Nano*, 2013, **7**, 9213–9222, DOI: **10.1021/nn403838y**.

8 A. Khan, M. Rashid, G. Grabher and G. Hossain, Autonomous Triboelectric Smart Textile Sensor for Vital Sign Monitoring, *ACS Appl. Mater. Interfaces*, 2024, **16**, 31807–31816, DOI: **10.1021/acsami.4c04689**.

9 Y. Su, G. Chen, C. Chen, Q. Gong, G. Xie, M. Yao, H. Tai, Y. Jiang and J. Chen, Self-Powered Respiration Monitoring Enabled By a Triboelectric Nanogenerator, *Adv. Mater.*, 2021, **33**, 2101262, DOI: **10.1002/adma.202101262**.

10 S. Liu, Y. Li, W. Guo, X. Huang, L. Xu, Y.-C. Lai, C. Zhang and H. Wu, Triboelectric nanogenerators enabled sensing and actuation for robotics, *Nano Energy*, 2019, **65**, 104005, DOI: **10.1016/j.nanoen.2019.104005**.

11 L. Zheng, S. Dong, J. Nie, S. Li, Z. Ren, X. Ma, X. Chen, H. Li and Z. L. Wang, Dual-Stimulus Smart Actuator and Robot Hand Based on a Vapor-Responsive PDMS Film and Triboelectric Nanogenerator, *ACS Appl. Mater. Interfaces*, 2019, **11**, 42504–42511, DOI: **10.1021/acsami.9b15574**.

12 K. V. Vijoy, H. John and K. J. Saji, Self-powered ultra-sensitive millijoule impact sensor using room temperature cured PDMS based triboelectric nanogenerator, *Microelectron. Eng.*, 2022, **251**, 111664, DOI: **10.1016/j.mee.2021.111664**.

13 J. Seo, S. Hajra, M. Sahu and H. J. Kim, Effect of cilia microstructure and ion injection upon single-electrode triboelectric nanogenerator for effective energy harvesting, *Mater. Lett.*, 2021, **304**, 130674, DOI: **10.1016/j.matlet.2021.130674**.

14 S. Wang, Y. Xie, S. Niu, L. Lin, C. Liu, Y. S. Zhou and Z. L. Wang, Maximum Surface Charge Density for Triboelectric Nanogenerators Achieved by Ionized-Air Injection: Methodology and Theoretical Understanding, *Adv. Mater.*, 2014, **26**, 6720–6728, DOI: **10.1002/adma.201402491**.

15 P. Vasandani, B. Gattu, J. Wu, Z.-H. Mao, W. Jia and M. Sun, Triboelectric Nanogenerator Using Microdome-Patterned PDMS as a Wearable Respiratory Energy Harvester, *Adv. Mater. Technol.*, 2017, **2**, 1700014, DOI: **10.1002/admt.201700014**.

16 P. Zhang, L. Deng, H. Zhang, J. He, X. Fan and Y. Ma, Enhanced Performance of Triboelectric Nanogenerator with Micro-Rhombic Patterned PDMS for Self-Powered Wearable Sensing, *Adv. Mater. Interfaces*, 2022, **9**, 2201265, DOI: **10.1002/admi.202201265**.

17 J. Chen, H. Guo, X. He, G. Liu, Y. Xi, H. Shi and C. Hu, Enhancing Performance of Triboelectric Nanogenerator by Filling High Dielectric Nanoparticles into Sponge PDMS Film, *ACS Appl. Mater. Interfaces*, 2016, **8**, 736–744, DOI: **10.1021/acsami.5b09907**.

18 M. Lai, L. Cheng, Y. Xi, Y. Wu, C. Hu, H. Guo, B. Du, G. Liu, Q. Liu and R. Liu, Enhancing the performance of $NaNbO_3$ triboelectric nanogenerators by dielectric modulation and electronegative modification, *J. Phys. D: Appl. Phys.*, 2018, **51**, 015303, DOI: **10.1088/1361-6463/aa9a6c**.

19 M. S. U. Rasel and J.-Y. Park, A sandpaper assisted micro-structured polydimethylsiloxane fabrication for human skin based triboelectric energy harvesting application, *Appl. Energy*, 2017, **206**, 150–158, DOI: **10.1016/j.apenergy.2017.07.109**.

20 K. Shi, H. Zou, B. Sun, P. Jiang, J. He and X. Huang, Dielectric Modulated Cellulose Paper/PDMS-Based Triboelectric

Nanogenerators for Wireless Transmission and Electropolymerization Applications, *Adv. Funct. Mater.*, 2020, **30**, 1904536, DOI: **10.1002/adfm.201904536**.

21 W.-G. Kim, D.-W. Kim, I.-W. Tcho, J.-K. Kim, M.-S. Kim and Y.-K. Choi, Triboelectric Nanogenerator: Structure, Mechanism, and Applications, *ACS Nano*, 2021, **15**, 258–287, DOI: **10.1021/acsnano.0c09803**.

22 H. T. Baytekin, A. Z. Patashinski, M. Branicki, B. Baytekin, S. Soh and B. A. Grzybowski, The Mosaic of Surface Charge in Contact Electrification, *Science*, 2011, **333**, 308–312, DOI: **10.1126/science.1201512**.

23 J. Lowell and A. C. Rose-Innes, Contact electrification, *Adv. Phys.*, 1980, **29**, 947–1023, DOI: **10.1080/00018738000101466**.

24 J. Wu, X. Wang, H. Li, F. Wang, W. Yang and Y. Hu, Insights into the mechanism of metal-polymer contact electrification for triboelectric nanogenerator via first-principles investigations, *Nano Energy*, 2018, **48**, 607–616, DOI: **10.1016/j.nanoen.2018.04.025**.

25 S. Pence, V. J. Novotny and A. F. Diaz, Effect of Surface Moisture on Contact Charge of Polymers Containing Ions, *Langmuir*, 1994, **10**, 592–596, DOI: **10.1021/la00014a042**.

26 L. Ģērmane, L. Lapčinskis, M. Iesalnieks and A. Šutka, Surface engineering of PDMS for improved triboelectrification, *Mater. Adv.*, 2023, **4**, 875–880, DOI: **10.1039/D2MA01015A**.

27 A. F. Möslein, M. Gutiérrez, B. Cohen and J.-C. Tan, Near-Field Infrared Nanospectroscopy Reveals Guest Confinement in Metal–Organic Framework Single Crystals, *Nano Lett.*, 2020, **20**, 7446–7454, DOI: **10.1021/acs.nanolett.0c02839**.

28 D. Nečas and P. Klapetek, Gwyddion: an open-source software for SPM data analysis, *Open Phys.*, 2012, **10**, 181–188, DOI: **10.2478/s11534-011-0096-2**.

29 A. D. Becke, Density-functional exchange-energy approximation with correct asymptotic behavior, *Phys. Rev. A: At., Mol., Opt. Phys.*, 1988, **38**, 3098, DOI: **10.1103/PhysRevA.38.3098**.

30 J. E. Del Bene, W. B. Person and K. Szczepaniak, Properties of Hydrogen-Bonded Complexes Obtained from the B3LYP Functional with 6-31G(d,p) and 6-31+G(d,p) Basis Sets: Comparison with MP2/6-31+ G (d, p) Results and Experimental Data, *J. Phys. Chem.*, 1995, **99**, 10705–10707, DOI: **10.1021/j100027a005**.

31 M. Frisch, *Gaussian 09, Revision D, 01/Gaussian*, 2009.

32 I. Imae, N. Tada and Y. Harima, Tuning of electronic properties of novel donor–acceptor polymers containing oligothiophenes with electron-withdrawing ester groups, *Polym. Bull.*, 2021, **78**, 2341–2355, DOI: **10.1007/s00289-020-03212-5**.

33 J. Lee, J. Kim, H. Kim, Y. M. Bae, K.-H. Lee and H. J. Cho, Effect of thermal treatment on the chemical resistance of polydimethylsiloxane for microfluidic devices, *J. Micromech. Microeng.*, 2013, **23**, 035007, DOI: **10.1088/0960-1317/23/3/035007**.

34 Z. You, S. Wang, Z. Li, Y. Zou, T. Lu, F. Wang, B. Hu, X. Wang, L. Li, W. Fang and Y. Liu, High current output direct-current triboelectric nanogenerator based on organic semiconductor heterojunction, *Nano Energy*, 2022, **91**, 106667, DOI: **10.1016/j.nanoen.2021.106667**.

35 S. Lin, L. Xu, A. Chi Wang and Z. L. Wang, Quantifying electron-transfer in liquid-solid contact electrification and the formation of electric double-layer, *Nat. Commun.*, 2020, **11**, 399, DOI: **10.1038/s41467-019-14278-9**.

36 H. Zou, L. Guo, H. Xue, Y. Zhang, X. Shen, X. Liu, P. Wang, X. He, G. Dai, P. Jiang, H. Zheng, B. Zhang, C. Xu and Z. L. Wang, Quantifying and understanding the triboelectric series of inorganic non-metallic materials, *Nat. Commun.*, 2020, **11**, 2093, DOI: **10.1038/s41467-020-15926-1**.

37 X. Ma, S. Li, S. Dong, J. Nie, M. Iwamoto, S. Lin, L. Zheng and X. Chen, Regulating the output performance of triboelectric nanogenerator by using P(VDF-TrFE) Langmuir monolayers, *Nano Energy*, 2019, **66**, 104090, DOI: **10.1016/j.nanoen.2019.104090**.

38 A. Sutka, K. Malnieks, L. Lapcinskis, M. Timusk, K. Kalnins, A. Kovalovs, J. Bitenieks, M. Knite, D. Stevens and J. Grunlan, Contact electrification between identical polymers as the basis for triboelectric/flexoelectric materials, *Phys. Chem. Chem. Phys.*, 2020, **22**, 13299–13305, DOI: **10.1039/d0cp01947j**.

8

Conclusions and Outlook

This thesis presents the design, development, and optimisation of several TENG systems. Various engineering approaches have been proposed to improve the electrical performance of TENG devices. The research in this thesis focuses on exploring the effects of MOFs with different topologies and ligand functional groups on triboelectric output, as well as investigating both contact-separation mode and noncontact freestanding mode for broader commercial applications. Additionally, the surface functionalisation on conventional polymers was examined to gain insights into the underlying charge transfer mechanisms. The findings contribute to the advancement of design strategies on MOF-based TENG devices and facilitate the exploration of novel applications in energy harvesting and self-powered systems.

In the broader context of triboelectric nanogenerators, a variety of fillers, such as carbon-based nanomaterials (e.g., graphene, carbon nanotubes), metal oxides (e.g., tin oxide, zinc oxide), and conductive polymers, have been widely investigated to enhance output performance. These materials typically function by improving dielectric constant, flexibility, or surface roughness. In comparison, MOFs offer several unique advantages: their highly tuneable structures, high surface area, and diverse chemical and electrical properties, allow for rational design of triboelectric properties at the molecular level. Additional processibility of MOFs, such as functionalisation, guest–host interactions, and post-synthetic modification, make them especially attractive for multi-functional and adaptive TENG systems. While the performance of MOF-based TENGs is generally comparable to conventional fillers, their versatility and customisability provide significant potential for application-specific optimisation. These advantages position MOFs as a promising platform for the design of next-generation energy harvesting devices.

The main conclusions from each chapter presented in this thesis are summarised as follows.

8.1 Chapter 4

This chapter presents findings from Paper I, *Nano Energy*, 114, 108687 (2023), which included:

- Zeolitic MOFs with RHO (ZIF-71) and LCS (ZIF-72) topologies were employed as fillers in PDMS matrices to prepare resilient contact-separation mode TENG devices. ZIF-71 and ZIF-72 exhibited identical chemical composition but drastically different structural morphology, porosity, and dielectric properties owing to their different topologies synthesised under different reaction conditions.
- Triboelectric performance testing revealed that ZIF-72-based TENG generates the highest electrical output of 578 ± 11 V and 19 ± 0.5 μA, with a peak power density of 5 Wm^{-2}, ranking among the highest reported for MOF-based TENGs. Furthermore, the device exhibited excellent durability, maintaining stable performance over 50,000 cycles. The improved performance was attributed to the structural robustness of the nonporous framework structure and improved dielectric properties.
- The mechanism of improved triboelectric performance in ZIF-72-based TENG was revealed through nanoscale-resolved mechanical and chemical studies. Nano-FTIR identified surface chemical heterogeneity as nanoscale charge-generating sites, while mechanical characterisation *via* TFM detected surface adhesion force enhancement due to MOF filler incorporation. This study provided the first insight into how topological modifications on MOF can influence triboelectric performance.

8.2 Chapter 5

This chapter comprised findings from Paper II, *ACS Applied Nano Materials*, 8, 8, 3942–3953 (2025), which included:

- Zeolitic MOFs ZIF-8 were functionalised with halogen groups (-CH_3, -Br, -Cl) *via* solvothermal methods, yielding the same SOD topology. The functionalised MOFs were then incorporated into electrospun PVDF fibres to fabricate composite materials.
- ZIF-8-Cl/PVDF-based TENG exhibited the highest triboelectric performance, with an average voltage of 312.4 ± 2.0 V and current of 4.90 ± 0.07 μA, followed by ZIF-8-Br/PVDF, ZIF-8-CH_3/PVDF and pristine PVDF. Theoretical DFT calculations revealed that halogenation of MOF ligand enhances the electron-withdrawing effects, leading to increased charge transfer efficiency.
- Through nanoscale surface potential characterisation, specifically by KPFM, it was observed that ZIF-8-Cl exhibited the highest work function of 6.8 eV, creating a greater energy gap with the electrode, thus facilitating efficient charge generation during triboelectrification. The correlation between triboelectric output and ligand electronegativity establishes a design principle for tuning MOF-based TENGs, guiding future material optimisation for energy harvesting applications.

8.3 Chapter 6

This chapter comprised findings from Paper III, to be published, which included:

- A noncontact rotational TENG was designed incorporating fluorinated MOFs (ZIF-8-CF_3) within a PVDF matrix. The device operates at high rotational speeds with enhanced stability and durability, while mitigating mechanical wear issues typically observed in contact-mode TENGs. The rational design of the TENG facilitates continuous energy harvesting with minimal wear, making it a promising approach for long-term applications.
- The incorporation of ZIF-8-CF_3 nanofillers significantly improves the triboelectric output, achieving a peak voltage of 280 ± 8 V and a current output of 19 ± 0.4 µA. The superior performance is attributed to the strong electron-trapping capability of fluorine-rich microporous structure and the formation of stable charge-trapping sites in the polymer matrix, further substantiated by DFT calculations of the electrostatic potential distribution and HOCO-LUCO energy level analysis.
- The generated electrical output was successfully harvested and stored in capacitors through a rectifier circuit, demonstrating its potential for powering small electronic devices such as LEDs and calculators. This work broadens the application scope of MOF-based TENGs for self-powered sensors and rotational energy harvesting systems.

8.4 Chapter 7

This chapter comprised findings from Paper IV, *Journal of Materials Chemistry C* (2025), which included:

- The surface functionalisation approach was applied on PDMS material *via* using SAMs of siloxane-based molecules (APTES, VTMS, and TMSPMA) to systematically tune triboelectric properties. The functionalised PDMS films exhibit distinct electron-donating and electron-withdrawing behaviour, as confirmed by molecular simulations and electrical performance analysis.
- TMSPMA-functionalised PDMS achieved a 1.9-fold increase in peak power density output compared to the unmodified PDMS, while the highly electron-donating ATPES-PDMS shifted its relative position on triboelectric series, leading to significantly reduced power output.
- The charge transfer mechanism during the contact-separation operation of functionalised PDMS-based TENG was discussed from both electron transfer and material transfer perspectives. The amount of charge transfer is significantly influenced by the work function difference between functionalised PDMS and ITO, as verified by KPFM surface potential analysis. On the other hand, nano-FTIR, KPFM, and mechanical studies provided direct evidence of material transfer, suggesting that bond cleavage and surface adhesion properties are critical to the overall charge transfer process.

8.5 Outlook

The approaches presented in this thesis summarise the necessary material properties for MOF-based TENG designs, with mechanisms explored through multimodal characterisation techniques bridging the different length scales. These findings open new avenues for further research in this field. Following research can be conducted to deepen the understanding of the role of MOF in TENG and contribute to innovative applications of MOF-based TENG.

- This thesis has studied the effect of MOF topology and ligand functional group on TENG output. The study can be expanded to examine other key factors during MOF-based TENG, such as the effects of metal ions, coordination environments, and electronic structures, on charge transfer dynamics. A comprehensive structure-activity relationship can be developed by integrating these insights with existing literature.
- While this thesis primarily focuses on MOF composites for improved structural robustness and flexibility of prepared TENG devices, there is a significant opportunity to develop reliable fabrication methods for MOF thin film fabrication. Approaches such as electrodeposition and ink-jet printing have potential to yield physically stable and controllable MOF films for TENG applications in future studies.
- The nanoporosity of MOF creates an opportunity for guest@MOF system design where guest molecules with appropriate size can be encapsulated into the MOF cages [210]. The confinement of guest molecules within the MOF pores has been demonstrated to enhance unique properties of the system,

therefore adapted to designated applications such as organic compound capturing and sensing, luminescence, and catalysis. Preliminary work has been done with introduction of polar molecules into MOF pores to enhance the dielectric properties of MOF. The presence of these high-dielectric guests within the crystalline structure increases the overall polarizability of the system, leading to higher triboelectric performance.

- The unique capabilities of MOFs — such as gas absorption, drug delivery, catalysis, and gas sensing — can be leveraged to engineer a broader range of applications beyond traditional energy harvesters. Future studies should focus on integrating MOF-based TENGs into multifunctional sensors and actuators, to fully exploit their potential in emerging technologies such as healthcare and soft robotics.

References

[1] K. Rose, S. Eldridge, L. Chapin, The internet of things: An overview, *The internet society (ISOC)* 80 (2015) 1-50.

[2] Y. Zhou, M. Shen, X. Cui, Y. Shao, L. Li, Y. Zhang, Triboelectric nanogenerator based self-powered sensor for artificial intelligence, *Nano Energy* 84 (2021) 105887.

[3] W. G. Kim, D. W. Kim, I. W. Tcho, J. K. Kim, M. S. Kim, Y. K. Choi, Triboelectric Nanogenerator: Structure, Mechanism, and Applications, *ACS Nano* 15 (2021) 258-287.

[4] F.-R. Fan, Z.-Q. Tian, Z. Lin Wang, Flexible triboelectric generator, *Nano Energy* 1 (2012) 328-334.

[5] Z. L. Wang, Triboelectric Nanogenerators as New Energy Technology for Self-Powered Systems and as Active Mechanical and Chemical Sensors, *ACS Nano* 7 (2013) 9533–9557.

[6] J. Chen, Z. L. Wang, Reviving Vibration Energy Harvesting and Self-Powered Sensing by a Triboelectric Nanogenerator, *Joule* 1 (2017) 480-521.

[7] Z. L. Wang, Triboelectric Nanogenerator (TENG)—Sparking an Energy and Sensor Revolution, *Advanced Energy Materials* 10 (2020)

[8] G. Zhu, Y. Su, P. Bai, J. Chen, Q. Jing, W. Yang, Z. L. Wang, Harvesting Water Wave Energy by Asymmetric Screening of Electrostatic Charges on a Nanostructured Hydrophobic Thin-Film Surface, *ACS Nano* 8 (2014) 6031-6037.

[9] J. S. Kim, J. Kim, J. N. Kim, J. Ahn, J. H. Jeong, I. Park, D. Kim, I. K. Oh, Collectively Exhaustive Hybrid Triboelectric Nanogenerator Based on Flow-Induced Impacting-Sliding Cylinder for Ocean Energy Harvesting, *Advanced Energy Materials* 12 (2021) 2103076.

[10] X. Ren, H. Fan, C. Wang, J. Ma, H. Li, M. Zhang, S. Lei, W. Wang, Wind energy harvester based on coaxial rotatory freestanding triboelectric nanogenerators for self-powered water splitting, *Nano Energy* 50 (2018) 562-570.

[11] J. Bae, J. Lee, S. Kim, J. Ha, B. S. Lee, Y. Park, C. Choong, J. B. Kim, Z. L. Wang, H. Y. Kim, J. J. Park, U. I. Chung, Flutter-driven triboelectrification for harvesting wind energy, *Nature Communications* 5 (2014) 4929.

[12] J. Chen, H. Guo, X. He, G. Liu, Y. Xi, H. Shi, C. Hu, Enhancing Performance of Triboelectric Nanogenerator by Filling High Dielectric Nanoparticles into Sponge PDMS Film, *ACS Applied Materials & Interfaces* 8 (2016) 736-44.

[13] G. Khandelwal, A. Chandrasekhar, N. P. Maria Joseph Raj, S. J. Kim, Metal–Organic Framework: A Novel Material for Triboelectric Nanogenerator–Based Self-Powered Sensors and Systems, *Advanced Energy Materials* 9 (2019) 1803581.

[14] G. Khandelwal, N. P. Maria Joseph Raj, V. Vivekananthan, S. J. Kim, Biodegradable metal-organic framework MIL-88A for triboelectric nanogenerator, *iScience* 24 (2021) 102064.

[15] Y. Guo, Y. Cao, Z. Chen, R. Li, W. Gong, W. Yang, Q. Zhang, H. Wang, Fluorinated metal-organic framework as bifunctional filler toward highly improving output performance of triboelectric nanogenerators, *Nano Energy* 70 (2020) 104517.

[16] Y. M. Wang, X. Zhang, D. Yang, L. Wu, J. Zhang, T. Lei, R. Yang, Highly stable metal-organic framework UiO-66-NH2for high-performance triboelectric nanogenerators, *Nanotechnology* 33 (2021) 065402.

[17] R. A. Shaukat, Q. M. Saqib, J. Kim, H. Song, M. U. Khan, M. Y. Chougale, J. Bae, M. J. Choi, Ultra-robust tribo- and piezo-electric nanogenerator based on metal organic frameworks (MOF-5) with high environmental stability, *Nano Energy* 96 (2022) 107128.

[18] T. Cheng, J. Shao, Z. L. Wang, Triboelectric nanogenerators, *Nature Reviews Methods Primers* 3 (2023) 39.

[19] S. Niu, S. Wang, L. Lin, Y. Liu, Y. S. Zhou, Y. Hu, Z. L. Wang, Theoretical study of contact-mode triboelectric nanogenerators as an effective power source, *Energy & Environmental Science* 6 (2013) 3576-3583.

[20] Y. S. Choi, S. W. Kim, S. Kar-Narayan, Materials-Related Strategies for Highly Efficient Triboelectric Energy Generators, *Advanced Energy Materials* 11 (2021) 2003802.

[21] B. Yang, W. Zeng, Z. H. Peng, S. R. Liu, K. Chen, X. M. Tao, A Fully Verified Theoretical Analysis of Contact-Mode Triboelectric Nanogenerators as a Wearable Power Source, *Advanced Energy Materials* 6 (2016) 1600505.

[22] M. T. Rahman, S. M. S. Rana, M. A. Zahed, S. Lee, E.-S. Yoon, J. Y. Park, Metal-organic framework-derived nanoporous carbon incorporated nanofibers for high-performance triboelectric nanogenerators and self-powered sensors, *Nano Energy* 94 (2022) 106921.

[23] S. Niu, Y. Liu, S. Wang, L. Lin, Y. S. Zhou, Y. Hu, Z. L. Wang, Theory of Sliding-Mode Triboelectric Nanogenerators, *Advanced Materials* 25 (2013) 6184-6193.

[24] G. Zhu, J. Chen, Y. Liu, P. Bai, Y. S. Zhou, Q. Jing, C. Pan, Z. L. Wang, Linear-Grating Triboelectric Generator Based on Sliding Electrification, *Nano Letters* 13 (2013) 2282-2289.

[25] L. Lin, S. Wang, Y. Xie, Q. Jing, S. Niu, Y. Hu, Z. L. Wang, Segmentally Structured Disk Triboelectric Nanogenerator for Harvesting Rotational Mechanical Energy, *Nano Letters* 13 (2013) 2916-2923.

[26] P. Bai, G. Zhu, Y. Liu, J. Chen, Q. Jing, W. Yang, J. Ma, G. Zhang, Z. L. Wang, Cylindrical Rotating Triboelectric Nanogenerator, *ACS Nano* 7 (2013) 6361-6366.

[27] S. Niu, Y. Liu, S. Wang, L. Lin, Y. S. Zhou, Y. Hu, Z. L. Wang, Theoretical Investigation and Structural Optimization of Single-Electrode Triboelectric Nanogenerators, *Advanced Functional Materials* 24 (2014) 3332-3340.

[28] Y. Mao, D. Geng, E. Liang, X. Wang, Single-electrode triboelectric nanogenerator for scavenging friction energy from rolling tires, *Nano Energy* 15 (2015) 227-234.

[29] W. Akram, Q. Chen, G. Xia, J. Fang, A review of single electrode triboelectric nanogenerators, *Nano Energy* 106 (2023) 108043.

[30] S. Niu, Y. Liu, X. Chen, S. Wang, Y. S. Zhou, L. Lin, Y. Xie, Z. L. Wang, Theory of freestanding triboelectric-layer-based nanogenerators, *Nano Energy* 12 (2015) 760-774.

[31] S. Wang, Y. Xie, S. Niu, L. Lin, Z. L. Wang, Freestanding Triboelectric-Layer-Based Nanogenerators for Harvesting Energy from a Moving Object or Human Motion in Contact and Non-contact Modes, *Advanced Materials* 26 (2014) 2818-2824.

[32] Y. Lee, S. G. Kang, J. Jeong, Sliding triboelectric nanogenerator with staggered electrodes, *Nano Energy* 86 (2021) 106062.

[33] Y. Xie, S. Wang, S. Niu, L. Lin, Q. Jing, J. Yang, Z. Wu, Z. L. Wang, Grating-Structured Freestanding Triboelectric-Layer Nanogenerator for Harvesting Mechanical Energy at 85% Total Conversion Efficiency, *Advanced Materials* 26 (2014) 6599-6607.

[34] Z. Li, S. Zhang, H. Guo, B. Wang, Y. Gong, S. Zhong, Y. Peng, J. Zheng, X. Xiao, On the performance of freestanding rolling mode triboelectric nanogenerators from rotational excitations for smart tires, *Nano Energy* 113 (2023) 108595.

[35] X. Xia, H. Wang, H. Guo, C. Xu, Y. Zi, On the material-dependent charge transfer mechanism of the contact electrification, *Nano Energy* 78 (2020) 105343.

[36] J. Lowell, A. C. Rose-Innes, Contact electrification, *Advances in Physics* 29 (1980) 947-1023.

[37] W. R. Harper, G. P. Thomson, The Volta effect as a cause of static electrification, *Proceedings of the Royal Society of London. Series A. Mathematical and Physical Sciences* 205 (1997) 83-103.

[38] Z. L. Wang, From contact electrification to triboelectric nanogenerators, *Reports on Progress in Physics* 84 (2021) 096502.

[39] Z. L. Wang, A. C. Wang, On the origin of contact-electrification, *Materials Today* 30 (2019) 34-51.

[40] D. Li, C. Wu, L. Ruan, J. Wang, Z. Qiu, K. Wang, Y. Liu, Y. Zhang, T. Guo, J. Lin, T. W. Kim, Electron-transfer mechanisms for confirmation of contact-electrification in ZnO/polyimide-based triboelectric nanogenerators, *Nano Energy* 75 (2020) 104818.

[41] H. Zou, L. Guo, H. Xue, Y. Zhang, X. Shen, X. Liu, P. Wang, X. He, G. Dai, P. Jiang, H. Zheng, B. Zhang, C. Xu, Z. L. Wang, Quantifying and understanding the triboelectric series of inorganic non-metallic materials, *Nature Communications* 11 (2020) 2093.

[42] C. Liu, A. J. Bard, Electrostatic electrochemistry at insulators, *Nature Materials* 7 (2008) 505-509.

[43] C.-y. Liu, A. J. Bard, Chemical Redox Reactions Induced by Cryptoelectrons on a PMMA Surface, *Journal of the American Chemical Society* 131 (2009) 6397-6401.

[44] L. S. McCarty, G. M. Whitesides, Electrostatic Charging Due to Separation of Ions at Interfaces: Contact Electrification of Ionic Electrets, *Angewandte Chemie International Edition* 47 (2008) 2188-2207.

[45] H. A. Mizes, E. M. Conwell, D. P. Salamida, Direct observation of ion transfer in contact charging between a metal and a polymer, *Applied Physics Letters* 56 (1990) 1597-1599.

[46] S. Pence, V. J. Novotny, A. F. Diaz, Effect of Surface Moisture on Contact Charge of Polymers Containing Ions, *Langmuir* 10 (1994) 592-596.

[47] A. F. Diaz, R. M. Felix-Navarro, A semi-quantitative tribo-electric series for polymeric materials: the influence of chemical structure and properties, *Journal of Electrostatics* 62 (2004) 277-290.

[48] H. T. Baytekin, B. Baytekin, S. Soh, B. A. Grzybowski, Is Water Necessary for Contact Electrification?, *Angewandte Chemie International Edition* 50 (2011) 6766-6770.

[49] J. Lowell, The role of material transfer in contact electrification, *Journal of Physics D: Applied Physics* 10 (1977) L233.

[50] M. W. Williams, Triboelectric charging of insulating polymers–some new perspectives, *AIP Advances* 2 (2012) 010701.

[51] H. T. Baytekin, A. Z. Patashinski, M. Branicki, B. Baytekin, S. Soh, B. A. Grzybowski, The Mosaic of Surface Charge in Contact Electrification, *Science* 333 (2011) 308-312.

[52] M. M. Apodaca, P. J. Wesson, K. J. M. Bishop, M. A. Ratner, B. A. Grzybowski, Contact Electrification between Identical Materials, *Angewandte Chemie International Edition* 49 (2010) 946-949.

[53] A. Šutka, K. Mālnieks, L. Lapčinskis, P. Kaufelde, A. Linarts, A. Bērziņa, R. Zābels, V. Jurķāns, I. Gorņevs, J. Blūms, M. Knite, The role of intermolecular forces in contact electrification on polymer surfaces and triboelectric nanogenerators, *Energy & Environmental Science* 12 (2019) 2417-2421.

[54] J. Gong, B. Xu, Y. Yang, M. Wu, B. Yang, An Adhesive Surface Enables High-Performance Mechanical Energy Harvesting with Unique Frequency-Insensitive and Pressure-Enhanced Output Characteristics, *Advanced Materials* 32 (2020) 1907948.

[55] R. Zhang, H. Olin, Material choices for triboelectric nanogenerators: A critical review, *EcoMat* 2 (2020) 12062.

[56] G. Khandelwal, N. P. Maria Joseph Raj, S. J. Kim, Materials Beyond Conventional Triboelectric Series for Fabrication and Applications of Triboelectric Nanogenerators, *Advanced Energy Materials* 11 (2021) 2101170.

[57] D. W. Kim, J. H. Lee, J. K. Kim, U. Jeong, Material aspects of triboelectric energy generation and sensors, *NPG Asia Materials* 12 (2020) 6.

[58] Q. Zhang, H. Wang, Z. Chen, Y. Guo, Progress of Inorganic Filler Based Composite Films for Triboelectric Nanogenerators, *J. Inorg. Mater.* 36 (2021) 919.

[59] X. Chen, J. Xiong, K. Parida, M. Guo, C. Wang, C. Wang, X. Li, J. Shao, P. S. Lee, Transparent and stretchable bimodal triboelectric nanogenerators with hierarchical micro-nanostructures for mechanical and water energy harvesting, *Nano Energy* 64 (2019) 103904.

[60] R. Wen, J. Guo, A. Yu, K. Zhang, J. Kou, Y. Zhu, Y. Zhang, B.-W. Li, J. Zhai, Remarkably enhanced triboelectric nanogenerator based on flexible and transparent monolayer titania nanocomposite, *Nano Energy* 50 (2018) 140-147.

[61] O. M. Yaghi, H. Li, Hydrothermal Synthesis of a Metal-Organic Framework Containing Large Rectangular Channels, *Journal of the American Chemical Society* 117 (1995) 10401-10402.

[62] R. Robson, Design and its limitations in the construction of bi- and poly-nuclear coordination complexes and coordination polymers (aka MOFs): a personal view, *Dalton Transactions* (2008) 5113-5131.

[63] Q. Wang, D. Astruc, State of the Art and Prospects in Metal–Organic Framework (MOF)-Based and MOF-Derived Nanocatalysis, *Chemical Reviews* 120 (2020) 1438-1511.

[64] O. K. Farha, J. T. Hupp, Rational Design, Synthesis, Purification, and Activation of Metal−Organic Framework Materials, *Accounts of Chemical Research* 43 (2010) 1166-1175.

[65] A. Phan, C. J. Doonan, F. J. Uribe-Romo, C. B. Knobler, M. O’Keeffe, O. M. Yaghi, Synthesis, Structure, and Carbon Dioxide Capture Properties of Zeolitic Imidazolate Frameworks, *Accounts of Chemical Research* 43 (2010) 58-67.

[66] M. D. Allendorf, C. A. Bauer, R. K. Bhakta, R. J. T. Houk, Luminescent metal-organic frameworks, *Chemical Society Reviews* 38 (2009) 1330-1352.

[67] A. S. Babal, L. Donà, M. R. Ryder, K. Titov, A. K. Chaudhari, Z. Zeng, C. S. Kelley, M. D. Frogley, G. Cinque, B. Civalleri, J.-C. Tan, Impact of Pressure and Temperature on the Broadband Dielectric Response of the HKUST-1 Metal–Organic Framework, *The Journal of Physical Chemistry C* 123 (2019) 29427-29435.

[68] J. Lee, O. K. Farha, J. Roberts, K. A. Scheidt, S. T. Nguyen, J. T. Hupp, Metal-organic framework materials as catalysts, *Chemical Society Reviews* 38 (2009) 1450-1459.

[69] J. R. Li, R. J. Kuppler, H. C. Zhou, Selective gas adsorption and separation in metal-organic frameworks, *Chemical Society Reviews* 38 (2009) 1477-1504.

[70] L. Sun, M. G. Campbell, M. Dinca, Electrically Conductive Porous Metal-Organic Frameworks, *Angewandte Chemie-International Edition* 55 (2016) 3566-3579.

[71] M. X. Wu, Y. W. Yang, Metal-Organic Framework (MOF)-Based Drug/Cargo Delivery and Cancer Therapy, *Advanced Materials* 29 (2017) 1606134.

[72] I. Stassen, N. C. Burtch, A. A. Talin, P. Falcaro, M. D. Allendorf, R. Ameloot, An updated roadmap for the integration of metal-organic frameworks with

electronic devices and chemical sensors, *Chemical Society Reviews* 46 (2017) 3185-3241.

[73] M. Ding, X. Cai, H.-L. Jiang, Improving MOF stability: approaches and applications, *Chemical Science* 10 (2019) 10209-10230.

[74] J. Zhao, H. Li, C. Li, Q. Zhang, J. Sun, X. Wang, J. Guo, L. Xie, J. Xie, B. He, Z. Zhou, C. Lu, W. Lu, G. Zhu, Y. Yao, MOF for template-directed growth of well-oriented nanowire hybrid arrays on carbon nanotube fibers for wearable electronics integrated with triboelectric nanogenerators, *Nano Energy* 45 (2018) 420-431.

[75] Z. C. Shao, J. S. Chen, Q. Xie, L. W. Mi, Functional metal/covalent organic framework materials for triboelectric nanogenerator, *Coordination Chemistry Reviews* 486 (2023) 23.

[76] Z. C. Shao, J. S. Chen, K. X. Gao, Q. Xie, X. J. Xue, S. Y. Zhou, C. Huang, L. W. Mi, H. W. Hou, A Double-Helix Metal-Chain Metal-Organic Framework as a High-Output Triboelectric Nanogenerator Material for Self-Powered Anticorrosion, *Angewandte Chemie-International Edition* 61 (2022) 5.

[77] Y. M. Wang, X. X. Zhang, Y. Ran, C. S. Liu, D. Wang, G. Y. Mao, X. Jiang, S. Wang, X. B. Yin, R. S. Yang, Advances in Metal-Organic Framework-Based Triboelectric Nanogenerators, *ACS Materials Letters* 6 (2024) 3883-3898.

[78] G. Khandelwal, N. P. Maria Joseph Raj, S. J. Kim, Zeolitic Imidazole Framework: Metal–Organic Framework Subfamily Members for Triboelectric Nanogenerators, *Advanced Functional Materials* 30 (2020) 1910162.

[79] G. Khandelwal, N. P. Maria Joseph Raj, S.-J. Kim, ZIF-62: a mixed linker metal–organic framework for triboelectric nanogenerators, *Journal of Materials Chemistry A* 8 (2020) 17817-17825.

[80] N. Jayababu, D. Kim, Co/Zn bimetal organic framework elliptical nanosheets on flexible conductive fabric for energy harvesting and environmental monitoring via triboelectricity, *Nano Energy* 89 (2021) 106355.

[81] X. Li, C. Jiang, Y. Yao, Q. Zhang, S. Dai, Y. Ying, J. Ping, Growth-Controllable Triboelectric Nanogenerator Based on Surface-Attached Metal-Organic Framework Layer on Living Leaf, *Small* (2021) e2103430.

[82] S. Hajra, M. Sahu, A. M. Padhan, I. S. Lee, D. K. Yi, P. Alagarsamy, S. S. Nanda, H. J. Kim, A Green Metal–Organic Framework-Cyclodextrin MOF: A Novel Multifunctional Material Based Triboelectric Nanogenerator for Highly Efficient Mechanical Energy Harvesting, *Advanced Functional Materials* 31 (2021)

[83] S. Hajra, M. Sahu, A. M. Padhan, J. Swain, B. K. Panigrahi, H. G. Kim, S. W. Bang, S. Park, R. Sahu, H. J. Kim, A new insight into the ZIF-67 based triboelectric

nanogenerator for self-powered robot object recognition, *Journal of Materials Chemistry C* 9 (2021) 17319-+.

[84] G. Khandelwal, N. Raj, V. Vivekananthan, S. J. Kim, Biodegradable metal-organic framework MIL-88A for triboelectric nanogenerator, *Iscience* 24 (2021) 18.

[85] J. Sun, K. Tu, S. Büchele, S. M. Koch, Y. Ding, S. N. Ramakrishna, S. Stucki, H. Guo, C. Wu, T. Keplinger, J. Pérez-Ramírez, I. Burgert, G. Panzarasa, Functionalized wood with tunable tribopolarity for efficient triboelectric nanogenerators, *Matter* 4 (2021) 3049-3066.

[86] J. Chen, Z. Shao, Y. Zhao, X. Xue, H. Song, Z. Wu, S. Cui, L. Zhang, C. Huang, L. Mi, H. Hou, Metal-Ion Coupling in Metal-Organic Framework Materials Regulating the Output Performance of a Triboelectric Nanogenerator, *Inorganic Chemistry* 61 (2022) 2490-2498.

[87] S. Hajra, M. Sahu, R. Sahu, A. M. Padhan, P. Alagarsamy, H. G. Kim, H. Lee, S. Oh, Y. Yamauchi, H. J. Kim, Significant effect of synthesis methodologies of metal-organic frameworks upon the additively manufactured dual-mode triboelectric nanogenerator towards self-powered applications, *Nano Energy* 98 (2022) 12.

[88] C. Huang, G. Z. Lu, N. Qin, Z. C. Shao, D. B. Zhang, C. Soutis, Y. Y. Zhang, L. W. Mi, H. W. Hou, Enhancement of Output Performance of Triboelectric Nanogenerator by Switchable Stimuli in Metal-Organic Frameworks for Photocatalysis, *ACS Applied Materials & Interfaces* 14 (2022) 16424-16434.

[89] Q. Li, X. H. An, X. R. Qian, Methyl Orange-Doped Polypyrrole Promoting Growth of ZIF-8 on Cellulose Fiber with Tunable Tribopolarity for Triboelectric Nanogenerator, *Polymers* 14 (2022) 17.

[90] R. Wen, R. Feng, B. Zhao, J. Song, L. Fan, J. Zhai, Controllable design of high-efficiency triboelectric materials by functionalized metal—organic frameworks with a large electron-withdrawing functional group, *Nano Research* 15 (2022) 9386-9391.

[91] A. Babu, L. Bochu, S. Potu, R. Kaja, N. Madathil, M. Velpula, A. Kulandaivel, U. K. Khanapuram, R. K. Rajaboina, H. Divi, P. Kodali, B. Ketharachapalli, R. Ammanabrolu, Facile Direct Growth of ZIF-67 Metal-Organic Framework for Triboelectric Nanogenerators and Their Application in the Internet of Vehicles, *ACS Sustainable Chemistry & Engineering* 11 (2023) 16806-16817.

[92] K. X. Gao, J. S. Chen, M. T. Zhao, R. T. Hu, S. H. Chen, X. J. Xue, Z. C. Shao, H. W. Hou, 3D nanocrystalline metal-organic framework materials for the improved output performance of triboelectric nanogenerators, *Dalton Transactions* 52 (2023) 444-451.

[93] H. Z. Ma, C. Luo, J. N. Zhao, Y. Shao, Y. H. Zhang, X. Liu, S. Li, B. Yin, K. Zhang, K. Ke, L. Zhou, M. B. Yang, Metal-Organic Framework Based Triboelectric Nanogenerator for a Self-Powered Methanol Sensor with High Sensitivity and Selectivity, *ACS Applied Materials & Interfaces* 15 (2023) 37563-37570.

[94] Z. C. Shao, H. R. Cheng, Y. Wei, J. S. Chen, K. X. Gao, Z. Fang, Y. S. Yan, L. W. Mi, H. W. Hou, Cationic metal-organic framework with charge separation effect as a high output triboelectric nanogenerator material for self-powered anticorrosion, *Dalton Transactions* 52 (2023) 13316-13323.

[95] Y. H. Zhang, T. Kang, X. Han, W. F. Yang, W. Gong, K. R. Li, Y. B. Guo, Molecular-functionalized metal-organic frameworks enabling contact-electro-catalytic organic decomposition, *Nano Energy* 111 (2023) 9.

[96] H.-W. Park, N. D. Huynh, W. Kim, C. Lee, Y. Nam, S. Lee, K.-B. Chung, D. Choi, Electron blocking layer-based interfacial design for highly-enhanced triboelectric nanogenerators, *Nano Energy* 50 (2018) 9-15.

[97] H. Jiang, H. Lei, Z. Wen, J. Shi, D. Bao, C. Chen, J. Jiang, Q. Guan, X. Sun, S.-T. Lee, Charge-trapping-blocking layer for enhanced triboelectric nanogenerators, *Nano Energy* 75 (2020) 105011.

[98] R. Wen, J. Guo, A. Yu, J. Zhai, Z. l. Wang, Humidity-Resistive Triboelectric Nanogenerator Fabricated Using Metal Organic Framework Composite, *Advanced Functional Materials* 29 (2019) 1807655.

[99] S. M. S. Rana, M. A. Zahed, M. T. Rahman, M. Salauddin, S. H. Lee, C. Park, P. Maharjan, T. Bhatta, K. Shrestha, J. Y. Park, Cobalt-Nanoporous Carbon Functionalized Nanocomposite-Based Triboelectric Nanogenerator for Contactless and Sustainable Self-Powered Sensor Systems, *Advanced Functional Materials* 31 (2021) 2105110.

[100] R. Wen, L. Fan, Q. Li, J. Zhai, A composite triboelectric nanogenerator based on flexible and transparent film impregnated with ZIF-8 nanocrystals, *Nanotechnology* 32 (2021) 345401.

[101] V. K. Vashistha, D. K. Das, A. Kumar, Metal–organic frameworks-based nanomaterials for nanogenerators: a mini review, *Int. Nano Lett.* 12 (2022) 215-221.

[102] Z. Chen, Y. Cao, W. Yang, L. An, H. Fan, Y. Guo, Embedding in-plane aligned MOF nanoflakes in silk fibroin for highly enhanced output performance of triboelectric nanogenerators, *Journal of Materials Chemistry A* 10 (2022) 799-807.

[103] Q. Fu, Y. H. Liu, T. Liu, J. L. Mo, W. L. Zhang, S. Zhang, B. Luo, J. L. Wang, Y. Qin, S. F. Wang, S. X. Nie, Air-permeable cellulosic triboelectric materials for self-powered healthcare products, *Nano Energy* 102 (2022) 10.

[104] S. M. S. Rana, M. T. Rahman, M. Abu Zahed, S. H. Lee, Y. Do Shin, S. Seonu, D. Kim, M. Salauddin, T. Bhatta, K. Sharstha, J. Y. Park, Zirconium metal-organic framework and hybridized Co-NPC@MXene nanocomposite-coated fabric for stretchable, humidity-resistant triboelectric nanogenerators and self-powered tactile sensors, *Nano Energy* 104 (2022) 17.

[105] M. Salauddin, S. S. Rana, M. Sharifuzzaman, S. H. Lee, M. Abu Zahed, Y. Do Shin, S. Seonu, H. S. Song, T. Bhatta, J. Y. Park, Laser-carbonized MXene/ZiF-67 nanocomposite as an intermediate layer for boosting the output performance of fabric-based triboelectric nanogenerator, *Nano Energy* 100 (2022) 14.

[106] Z. Abbas, M. Anithkumar, A. P. S. Prasanna, N. Hussain, S. J. Kim, S. M. Mobin, Triboelectric nanogenerators enhanced by a metal-organic framework for sustainable power generation and air mouse technology, *Journal of Materials Chemistry A* 11 (2023) 26531-26542.

[107] A. Babu, K. Ruthvik, P. Supraja, M. Navaneeth, K. U. Kumar, R. R. Kumar, K. Prakash, N. Raju, High-performance triboelectric nanogenerator using ZIF-67/PVDF hybrid film for energy harvesting, *Journal of Materials Science-Materials in Electronics* 34 (2023) 11.

[108] N. K. Das, M. Ravipati, S. Badhulika, Nickel Metal-Organic Framework/PVDF Composite Nanofibers based Self-Powered Wireless Sensor for Pulse Monitoring of Underwater Divers via Triboelectrically Generated Maxwell-Displacement Current, *Advanced Functional Materials* 33 (2023) 14.

[109] Y. A. Gui, S. S. He, Y. F. Wang, J. C. Yang, MOF-derived porous Ni/C material for high-performance hybrid nanogenerator and self-powered wearable sensor, *Composites Part a-Applied Science and Manufacturing* 168 (2023) 9.

[110] P. Pandey, K. Thapa, G. P. Ojha, M.-K. Seo, K. H. Shin, S.-W. Kim, J. I. Sohn, Metal-organic frameworks-based triboelectric nanogenerator powered visible light communication system for wireless human-machine interactions, *Chemical Engineering Journal* 452 (2023)

[111] S. Potu, M. Navaneeth, A. Bhadoriya, A. Bora, Y. Sivalingam, A. Babu, M. Velpula, B. Gollapelli, R. K. Rajaboina, U. K. Khanapuram, H. Divi, P. Kodali, L. Bochu, Enhancing Triboelectric Nanogenerator Performance with Metal-Organic-Framework-Modified ZnO Nanosheets for Self-Powered Electronic Devices and Energy Harvesting, *ACS Applied Nano Materials* 6 (2023) 22701-22710.

[112] M. T. Rahman, M. S. Rahman, H. Kumar, K. Kim, S. Kim, Metal-Organic Framework Reinforced Highly Stretchable and Durable Conductive Hydrogel-Based Triboelectric Nanogenerator for Biomotion Sensing and Wearable Human-Machine Interfaces, *Advanced Functional Materials* 33 (2023) 13.

[113] S. M. S. Rana, M. A. Zahed, M. R. Islam, O. Faruk, H. S. Song, S. H. Jeong, J. Y. Park, Metal-organic framework and molybdenum oxide doped highly negative hybridized triboelectric material for self-powered and continuous monitoring of biosignals, *Chemical Engineering Journal* 473 (2023) 13.

[114] G. M. Rani, S. M. Ghoreishian, K. S. Ranjith, S. H. Park, M. Lee, R. Umapathi, Y. K. Han, Y. S. Huh, High Roughness Induced Pearl Necklace-Like ZIF-67@PAN Fiber-Based Triboelectric Nanogenerators for Mechanical Energy Harvesting, *Advanced Materials Technologies* 8 (2023) 14.

[115] A. Sasmal, J. Senthilnathan, A. Arockiarajan, M. Yoshimura, Two-Dimensional Metal-Organic Framework Incorporated Highly Polar PVDF for Dielectric Energy Storage and Mechanical Energy Harvesting, *Nanomaterials* 13 (2023)

[116] S. H. Sohn, G. J. Choi, I. Park, Metal-organic frameworks-induced Self-Poling effect of polyvinylidene fluoride nanofibers for performance enhancement of triboelectric nanogenerator, *Chemical Engineering Journal* 475 (2023) 12.

[117] Y.-M. Wang, X. Zhang, C. Liu, L. Wu, J. Zhang, T. Lei, Y. Wang, X.-B. Yin, R. Yang, Remarkable improvement of MOF-based triboelectric nanogenerators with strong electron-withdrawing groups, *Nano Energy* 107 (2023) 108149.

[118] Q. Q. Xi, Z. X. Chen, Y. W. Li, F. R. Liu, Y. B. Guo, Highly Charge-Trapping MOF Nanofillers Enabling Enhanced Triboelectric Performance, *ACS Applied Electronic Materials* 5 (2023) 5215-5223.

[119] J. H. Zhou, Y. F. Zhang, J. W. Zhang, D. S. Zhang, X. R. Zhou, J. Q. Xiong, Breathable Metal-Organic Framework Enhanced Humidity-Responsive Nanofiber Actuator with Autonomous Triboelectric Perceptivity, *ACS Nano* 17 (2023) 17920-17930.

[120] G. Y. Zhu, X. Y. Li, X. P. Li, A. Wang, T. Li, X. J. Zhu, D. Y. Tang, J. T. Zhu, X. J. He, H. G. Li, S. H. Li, Y. Zhang, B. Wang, S. H. Zhang, H. Xu, Nanopatterned Electroactive Polylactic Acid Nanofibrous MOFilters for Efficient $PM_{0.3}$ Filtration and Bacterial Inhibition, *ACS Applied Materials & Interfaces* 15 (2023) 47145-47157.

[121] X. Lu, Z. Chen, G. M. Chen, Z. X. Liu, Metal-organic framework based self-powered devices for human body energy harvesting, *Chemical Communications* 60 (2024) 7843-7865.

[122] P. Pandey, K. Thapa, G. P. Ojha, M. K. Seo, K. H. Shin, S. W. Kim, J. I. Sohn, Metal-organic frameworks-based triboelectric nanogenerator powered visible light communication system for wireless human-machine interactions, *Chemical Engineering Journal* 452 (2023) 9.

[123] M. N. Liu, T. Chen, F. Yin, W. Z. Song, L. X. Wu, J. Zhang, S. Ramakrishna, Y. Z. Long, Smart Bandage Based on a ZIF-8 Triboelectric Nanogenerator for In Situ Real-Time Monitoring of Drug Concentration, *ACS Applied Materials & Interfaces* 16 (2024) 39079-39089.

[124] A. Kakim, A. Nurkesh, B. Sarsembayev, D. Dauletiya, A. Balapan, Z. Bakenov, A. Yeshmukhametov, G. Kalimuldina, Incorporating MIL-125 Metal-Organic Framework for Flexible Triboelectric Nanogenerators and Self-Powered Sensors for Robotic Grippers, *Advanced Sensor Research* 3 (2024) 11.

[125] G. Wang, Z. K. Ren, L. K. Zheng, Y. J. Kang, N. Luo, Z. H. Qiao, Pulsed Airstream-Driven Hierarchical Micro-Nano Pore Structured Triboelectric Nanogenerator for Wireless Self-Powered Formaldehyde Sensing, *Small* 20 (2024) 13.

[126] V. P. Kallupadi, H. Varghese, U. N. S. Hareesh, A. Chandran, Modulating Contact Electrification With Metal-Organic Frameworks in Flexible Triboelectric Nanogenerators for Kinetic Energy Harvesting and Self-Powered Humidity Sensing Applications, *Advanced Functional Materials* (2024) 15.

[127] Z. H. Hu, F. J. Wang, Y. C. Liu, S. F. Ma, S. Q. Ouyang, M. D. Li, Y. T. Wu, L. Q. Wang, An electrostatically spun cellulose-based self-powered mask with high efficiency air filtration and ammonia sensing, *International Journal of Biological Macromolecules* 282 (2024) 12.

[128] S. Hajra, M. Sahu, A. M. Padhan, I. S. Lee, D. K. Yi, P. Alagarsamy, S. S. Nanda, H. J. Kim, A Green Metal-Organic Framework-Cyclodextrin MOF: A Novel Multifunctional Material Based Triboelectric Nanogenerator for Highly Efficient Mechanical Energy Harvesting, *Advanced Functional Materials* 31 (2021) 11.

[129] X. J. He, C. M. Wang, Y. X. Hao, J. Q. Li, G. Y. Zhu, L. Jiang, J. Shao, M. M. Zhang, X. P. Li, H. G. Li, H. Xu, MOF Nanosheet-Functionalized Poly(lactic acid) Meta-membranes for Long-Term Air Purification and Intelligent Monitoring, *ACS Applied Materials & Interfaces* 16 (2024) 54873-54884.

[130] F. J. Wang, S. Y. Wang, Y. C. Liu, S. Q. Ouyang, D. N. Sun, X. Y. Yang, J. M. Li, Z. Wu, J. Qian, Z. C. Zhao, L. Q. Wang, C. Jia, S. F. Ma, Cellulose Nanofiber-Based Triboelectric Nanogenerators for Efficient Air Filtration in Harsh Environments, *Nano Letters* 24 (2024) 2861-2869.

[131] T. Yang, K. K. Xu, G. Y. Zhu, Y. F. Zhang, X. J. Zhu, X. Li, J. Shao, J. T. Zhu, M. M. Zhang, X. J. He, S. H. Zhang, Y. B. Zhu, J. F. Gao, G. J. Zhong, H. Xu, Hierarchically structured poly(lactic acid) nanofibers by organic-inorganic nanohybridization strategy towards efficient PM removal and respiratory monitoring, *Separation and Purification Technology* 354 (2025) 12.

[132] L. Jiang, X. J. Zhu, J. Q. Li, J. Shao, Y. Zhang, J. T. Zhu, S. H. Li, L. A. Zheng, X. P. Li, S. H. Zhang, H. G. Li, G. J. Zhong, H. Xu, Electroactive and breathable protective membranes by surface engineering of dielectric nanohybrids at poly(lactic acid) nanofibers with excellent self-sterilization and photothermal properties, *Separation and Purification Technology* 339 (2024) 10.

[133] K. Li, L. W. L. Han, J. Y. Zhang, J. Cheng, Metal-Organic Framework Derived Multidimensional Carbon/Multifluorination Epoxy Nanocomposite with Electromagnetic Wave Absorption, Environmentally Adaptive, and Blue Energy Harvesting, *Small Structures* 4 (2023) 16.

[134] P. K. Nitha, A. Chandrasekhar, Fingerprint-Mimicking, ZIF-67 Decorated, Triboelectric Nanogenerator for IoT Cloud-Supported Self-Powered Smart Glove for Paralyzed Patient Care, *ACS Applied Electronic Materials* 6 (2024) 5314-5327.

[135] R. M. Liu, K. Q. Xia, T. Yu, F. Gao, Q. H. Zhang, L. P. Zhu, Z. Z. Ye, S. K. Yang, Y. G. Ma, J. G. Lu, Multifunctional Smart Fabrics with Integration of Self-Cleaning, Energy Harvesting, and Thermal Management Properties, *ACS Nano* 18 (2024) 31085-31097.

[136] X. Peng, X. Wu, M. Zhang, H. Yuan, Metal–Organic Framework Coated Devices for Gas Sensing, *ACS Sensors* 8 (2023) 2471-2492.

[137] G. Khandelwal, A. Chandrasekhar, N. Raj, S. J. Kim, Metal-Organic Framework: A Novel Material for Triboelectric Nanogenerator-Based Self-Powered Sensors and Systems, *Advanced Energy Materials* 9 (2019) 8.

[138] W. Zhou, R. Apkarian, Z. L. Wang, D. Joy, Fundamentals of scanning electron microscopy (SEM), *Scanning microscopy for nanotechnology: techniques and applications* (2007) 1-40.

[139] J. Epp, 4 - X-ray diffraction (XRD) techniques for materials characterization, *Materials Characterization Using Nondestructive Evaluation (NDE) Methods* (2016) 81-124.

[140] C. R. Groom, I. J. Bruno, M. P. Lightfoot, S. C. Ward, The Cambridge Structural Database, *Acta Crystallographica Section B* 72 (2016) 171-179.

[141] H. Kaur, B. Rana, D. Tomar, S. Kaur, K. C. Jena, Fundamentals of ATR-FTIR Spectroscopy and Its Role for Probing In-Situ Molecular-Level Interactions, *Modern Techniques of Spectroscopy: Basics, Instrumentation, and Applications* (2021) 3-37.

[142] Introduction to Vibrational Spectroscopy, *Fourier Transform Infrared Spectrometry* (2007) 1-18.

[143] P. Dumas, M. C. Martin, G. L. Carr, IR Spectroscopy and Spectromicroscopy with Synchrotron Radiation, *Synchrotron Light Sources and Free-Electron Lasers: Accelerator Physics, Instrumentation and Science Applications* (2019) 1-55.

[144] P. Eaton, P. West, Atomic Force Microscopy, (2010)

[145] D. Nečas, P. Klapetek, Gwyddion: an open-source software for SPM data analysis, *Open Physics* 10 (2012) 181-188.

[146] A. F. Möslein, M. Gutiérrez, B. Cohen, J.-C. Tan, Near-Field Infrared Nanospectroscopy Reveals Guest Confinement in Metal–Organic Framework Single Crystals, *Nano Letters* 20 (2020) 7446-7454.

[147] A. Rosa-Zeiser, E. Weilandt, S. Hild, O. Marti, The simultaneous measurement of elastic, electrostatic and adhesive properties by scanning force microscopy: pulsed-force mode operation, *Measurement Science and Technology* 8 (1997) 1333.

[148] K. Xu, W. Sun, Y. Shao, F. Wei, X. Zhang, W. Wang, P. Li, Recent development of PeakForce Tapping mode atomic force microscopy and its applications on nanoscience, 7 (2018) 605-621.

[149] M. Frisch, Gaussian 09, Revision D. 01/Gaussian, (2009)

[150] A. D. Becke, Density-functional exchange-energy approximation with correct asymptotic behavior, *Physical review A* 38 (1988) 3098.

[151] J. E. Del Bene, W. B. Person, K. Szczepaniak, Properties of Hydrogen-Bonded Complexes Obtained from the B3LYP Functional with 6-31G (d, p) and 6-31+ G (d, p) Basis Sets: Comparison with MP2/6-31+ G (d, p) Results and Experimental Data, *The Journal of Physical Chemistry* 99 (1995) 10705-10707.

[152] A. Erba, J. K. Desmarais, S. Casassa, B. Civalleri, L. Donà, I. J. Bush, B. Searle, L. Maschio, L. Edith-Daga, A. Cossard, C. Ribaldone, E. Ascrizzi, N. L. Marana, J.-P. Flament, B. Kirtman, CRYSTAL23: A Program for Computational Solid State Physics and Chemistry, *Journal of Chemical Theory and Computation* 19 (2023) 6891-6932.

[153] L. Doná, J. G. Brandenburg, B. Civalleri, Extending and assessing composite electronic structure methods to the solid state, *The Journal of Chemical Physics* 151 (2019)

[154] R. M. Hanson, X.-J. Lu, DSSR-enhanced visualization of nucleic acid structures in Jmol, *Nucleic acids research* 45 (2017) W528-W533.

[155] N. S. Bobbitt, A. S. Rosen, R. Q. Snurr, Topological effects on separation of alkane isomers in metal−organic frameworks, *Fluid Phase Equilibria* 519 (2020) 112642.

[156] D. Kim, X. Liu, M. S. Lah, Topology analysis of metal–organic frameworks based on metal–organic polyhedra as secondary or tertiary building units, *Inorganic Chemistry Frontiers* 2 (2015) 336-360.

[157] N. Stock, S. Biswas, Synthesis of Metal-Organic Frameworks (MOFs): Routes to Various MOF Topologies, Morphologies, and Composites, *Chemical Reviews* 112 (2012) 933-969.

[158] X. Li, J. Liu, K. Zhou, S. Ullah, H. Wang, J. Zou, T. Thonhauser, J. Li, Tuning Metal–Organic Framework (MOF) Topology by Regulating Ligand and Secondary Building Unit (SBU) Geometry: Structures Built on 8-Connected M6 (M = Zr, Y) Clusters and a Flexible Tetracarboxylate for Propane-Selective Propane/Propylene Separation, *Journal of the American Chemical Society* 144 (2022) 21702-21709.

[159] E. Dziadyk-Stopyra, J. Rogacka, A. Podsiadły-Paszkowska, P. Kawecki, B. Kuchta, B. M. Szyja, Toward rational design of Zr-MOF for CO_2/CH_4 mixture separation, *Separation Science and Technology* 59 (2024) 940-953.

[160] E. Velasco, S. Xian, H. Wang, S. J. Teat, D. H. Olson, K. Tan, S. Ullah, T. M. Osborn Popp, A. D. Bernstein, K. A. Oyekan, A. J. Nieuwkoop, T. Thonhauser, J. Li, Flexible Zn-MOF with Rare Underlying scu Topology for Effective Separation of C6 Alkane Isomers, *ACS Applied Materials & Interfaces* 13 (2021) 51997-52005.

[161] H. Wang, X. Dong, J. Lin, S. J. Teat, S. Jensen, J. Cure, E. V. Alexandrov, Q. Xia, K. Tan, Q. Wang, D. H. Olson, D. M. Proserpio, Y. J. Chabal, T. Thonhauser, J. Sun, Y. Han, J. Li, Topologically guided tuning of Zr-MOF pore structures for highly selective separation of C6 alkane isomers, *Nature Communications* 9 (2018) 1745.

[162] D.-X. Xue, A. Cadiau, Ł. J. Weseliński, H. Jiang, P. M. Bhatt, A. Shkurenko, L. Wojtas, C. Zhijie, Y. Belmabkhout, K. Adil, M. Eddaoudi, Topology meets MOF chemistry for pore-aperture fine tuning: ftw-MOF platform for energy-efficient separations via adsorption kinetics or molecular sieving, *Chemical Communications* 54 (2018) 6404-6407.

[163] M. R. Ryder, L. Donà, J. G. Vitillo, B. Civalleri, Understanding and Controlling the Dielectric Response of Metal–Organic Frameworks, *ChemPlusChem* 83 (2018) 308-316.

[164] M. R. Ryder, Z. Zeng, K. Titov, Y. Sun, E. M. Mahdi, I. Flyagina, T. D. Bennett, B. Civalleri, C. S. Kelley, M. D. Frogley, G. Cinque, J.-C. Tan, Dielectric Properties of Zeolitic Imidazolate Frameworks in the Broad-Band Infrared Regime, *The Journal of Physical Chemistry Letters* 9 (2018) 2678-2684.

[165] J. C. Tan, T. D. Bennett, A. K. Cheetham, Chemical structure, network topology, and porosity effects on the mechanical properties of Zeolitic Imidazolate

Frameworks, *Proceedings of the National Academy of Sciences* 107 (2010) 9938-9943.

[166] Y. Li, Y. Luo, H. Deng, S. Shi, S. Tian, H. Wu, J. Tang, C. Zhang, X. Zhang, J.-W. Zha, S. Xiao, Advanced Dielectric Materials for Triboelectric Nanogenerators: Principles, Methods, and Applications, *Advanced Materials* n/a (2024) 2314380.

[167] T. Xu, J. Ye, J.-C. Tan, Unravelling the Ageing Effects of PDMS-Based Triboelectric Nanogenerators, *Advanced Materials Interfaces* (2024) 2400094.

[168] Z. Shao, J. Chen, K. Gao, Q. Xie, X. Xue, X. Li, H. Hou, L. Mi, A high-spintronic helix metal-organic chain as a high-output triboelectric nanogenerator material for self-powered anticorrosion, *Chemical Engineering Journal* 455 (2023) 140865.

[169] R. M. Wen, R. Feng, B. Zhao, J. F. Song, L. M. Fan, J. Y. Zhai, Controllable design of high-efficiency triboelectric materials by functionalized metal-organic frameworks with a large electron-withdrawing functional group, *Nano Research* 15 (2022) 9386-9391.

[170] Y. D. More, S. Saurabh, S. Mollick, S. K. Singh, S. Dutta, S. Fajal, A. Prathamshetti, M. M. Shirolkar, S. Panchal, M. Wable, S. Ogale, S. K. Ghosh, Highly Stable and End-group Tuneable Metal–Organic Framework/Polymer Composite for Superior Triboelectric Nanogenerator Application, *Advanced Materials Interfaces* 9 (2022) 2201713.

[171] G. Chaplais, G. Fraux, J.-L. Paillaud, C. Marichal, H. Nouali, A. H. Fuchs, F.-X. Coudert, J. Patarin, Impacts of the Imidazolate Linker Substitution (CH3, Cl, or Br) on the Structural and Adsorptive Properties of ZIF-8, *The Journal of Physical Chemistry C* 122 (2018) 26945-26955.

[172] R. Yagi, T. Ueda, Substitution (CH3, Cl, or Br) effects of the imidazolate linker on benzene adsorption kinetics for the zeolitic imidazolate framework (ZIF)-8, *Physical Chemistry Chemical Physics* 25 (2023) 20585-20596.

[173] M. Tu, D. E. Kravchenko, B. Xia, V. Rubio-Gimenez, N. Wauteraerts, R. Verbeke, I. F. J. Vankelecom, T. Stassin, W. Egger, M. Dickmann, H. Amenitsch, R. Ameloot, Template-Mediated Control over Polymorphism in the Vapor-Assisted Formation of Zeolitic Imidazolate Framework Powders and Films, *Angew. Chem. Int. Ed.* 60 (2021) 7553-7558.

[174] J. G. Sun, K. K. Tu, S. Büchele, S. M. Koch, Y. Ding, S. N. Ramakrishna, S. Stucki, H. Y. Guo, C. S. Wu, T. Keplinger, J. Pérez-Ramírez, I. Burgert, G. Panzarasa, Functionalized wood with tunable tribopolarity for efficient triboelectric nanogenerators, *Matter* 4 (2021) 3049-3066.

[175] Y. Zhou, P. Zhang, J. Li, X. Mao, Recent progress of triboelectric nanogenerator-based power management and information processing circuit, *Materials Today Sustainability* 23 (2023) 100426.

[176] C. Fang, T. Tong, T. Bu, Y. Cao, S. Xu, Y. Qi, C. Zhang, Overview of Power Management for Triboelectric Nanogenerators, *Advanced Intelligent Systems* 2 (2020) 1900129.

[177] X. Qu, X. Liu, Y. Yue, Y. Tang, P. Miao, Triboelectric nanogenerator-enabled self-powered strategies for sensing applications, *TrAC Trends in Analytical Chemistry* 185 (2025) 118191.

[178] X. Shi, Y. Shan, M. Du, H. Pang, Synthesis and application of metal-organic framework films, *Coordination Chemistry Reviews* 444 (2021) 214060.

[179] X. Fu, X. Pan, Y. Liu, J. Li, Z. Zhang, H. Liu, M. Gao, Non-Contact Triboelectric Nanogenerator, *Advanced Functional Materials* 33 (2023) 2306749.

[180] S. A. Han, W. Seung, J. H. Kim, S.-W. Kim, Ultrathin Noncontact-Mode Triboelectric Nanogenerator Triggered by Giant Dielectric Material Adaption, *ACS Energy Letters* 6 (2021) 1189-1197.

[181] H. Guo, X. Jia, L. Liu, X. Cao, N. Wang, Z. L. Wang, Freestanding Triboelectric Nanogenerator Enables Noncontact Motion-Tracking and Positioning, *ACS Nano* 12 (2018) 3461-3467.

[182] L. Lin, S. Wang, S. Niu, C. Liu, Y. Xie, Z. L. Wang, Noncontact Free-Rotating Disk Triboelectric Nanogenerator as a Sustainable Energy Harvester and Self-Powered Mechanical Sensor, *ACS Applied Materials & Interfaces* 6 (2014) 3031-3038.

[183] Q. Li, W. Liu, H. Yang, W. He, L. Long, M. Wu, X. Zhang, Y. Xi, C. Hu, Z. L. Wang, Ultra-stability high-voltage triboelectric nanogenerator designed by ternary dielectric triboelectrification with partial soft-contact and non-contact mode, *Nano Energy* 90 (2021) 106585.

[184] Z. Lin, B. Zhang, Y. Xie, Z. Wu, J. Yang, Z. L. Wang, Elastic-Connection and Soft-Contact Triboelectric Nanogenerator with Superior Durability and Efficiency, *Advanced Functional Materials* 31 (2021) 2105237.

[185] T. Jiang, H. Pang, J. An, P. Lu, Y. Feng, X. Liang, W. Zhong, Z. L. Wang, Robust Swing-Structured Triboelectric Nanogenerator for Efficient Blue Energy Harvesting, *Advanced Energy Materials* 10 (2020) 2000064.

[186] X. Ren, H. Fan, C. Wang, J. Ma, S. Lei, Y. Zhao, H. Li, N. Zhao, Magnetic force driven noncontact electromagnetic-triboelectric hybrid nanogenerator for scavenging biomechanical energy, *Nano Energy* 35 (2017) 233-241.

[187] L.-B. Huang, G. Bai, M.-C. Wong, Z. Yang, W. Xu, J. Hao, Magnetic-Assisted Noncontact Triboelectric Nanogenerator Converting Mechanical Energy into Electricity and Light Emissions, *Advanced Materials* 28 (2016) 2744-2751.

[188] G. Zhu, J. Chen, T. Zhang, Q. Jing, Z. L. Wang, Radial-arrayed rotary electrification for high performance triboelectric generator, *Nature Communications* 5 (2014) 3426.

[189] H. Zhou, G. Liu, Y. Gao, Z. Wang, Y. Qin, Y. Wang, Y. Lin, Y. Xie, Y. Chen, C. Zhang, Dual Mode Rotary Triboelectric Nanogenerator for Collecting Kinetic Energy from Bicycle Brake, *Advanced Energy and Sustainability Research* 2 (2021) 2000113.

[190] L. Long, W. Liu, Z. Wang, W. He, G. Li, Q. Tang, H. Guo, X. Pu, Y. Liu, C. Hu, High performance floating self-excited sliding triboelectric nanogenerator for micro mechanical energy harvesting, *Nature Communications* 12 (2021) 4689.

[191] A. Segkos, C. Tsamis, Rotating Triboelectric Nanogenerators for Energy Harvesting and Their Applications, *Nanoenergy Advances* 3 (2023) 170-219.

[192] Y. M. Wang, X. X. Zhang, C. S. Liu, L. T. Wu, J. J. Zhang, T. M. Lei, Y. Wang, X. B. Yin, R. S. Yang, Remarkable improvement of MOF-based triboelectric nanogenerators with strong electron-withdrawing groups, *Nano Energy* 107 (2023) 9.

[193] B. Slater, J.-C. Tan, Triboelectric behaviour of selected zeolitic-imidazolate frameworks: exploring chemical, morphological and topological influences, *Chemical Science* 15 (2024) 10056-10064.

[194] X. Cai, T. Lei, D. Sun, L. Lin, A critical analysis of the α, β and γ phases in poly(vinylidene fluoride) using FTIR, *RSC Advances* 7 (2017) 15382-15389.

[195] G. Liang, D. Zhao, Z. Yan, W. Sun, Z. Wang, T. Tan, A durable non-contact reciprocated triboelectric nanogenerator for low-frequency vibration energy harvesting, *Review of Scientific Instruments* 94 (2023) 115002.

[196] N. Zhang, C. Qin, T. Feng, J. Li, Z. Yang, X. Sun, E. Liang, Y. Mao, X. Wang, Non-contact cylindrical rotating triboelectric nanogenerator for harvesting kinetic energy from hydraulics, *Nano Research* 13 (2020) 1903-1907.

[197] O. Verners, L. Lapčinskis, P. C. Sherrell, A. Šutka, Contact Electrification at Dielectric Polymer Interfaces: On Bond Scission, Material Transfer, and Electron Transfer, *Advanced Materials Interfaces* 10 (2023) 2300562.

[198] V. Nguyen, R. Yang, Effect of humidity and pressure on the triboelectric nanogenerator, *Nano Energy* 2 (2013) 604-608.

[199] T.-C. Hou, Y. Yang, H. Zhang, J. Chen, L.-J. Chen, Z. Lin Wang, Triboelectric nanogenerator built inside shoe insole for harvesting walking energy, *Nano Energy* 2 (2013) 856-862.

[200] M. He, W. Du, Y. Feng, S. Li, W. Wang, X. Zhang, A. Yu, L. Wan, J. Zhai, Flexible and stretchable triboelectric nanogenerator fabric for biomechanical energy harvesting and self-powered dual-mode human motion monitoring, *Nano Energy* 86 (2021) 106058.

[201] F. R. Fan, J. Luo, W. Tang, C. Li, C. Zhang, Z. Tian, Z. L. Wang, Highly transparent and flexible triboelectric nanogenerators: performance improvements and fundamental mechanisms, *Journal of Materials Chemistry A* 2 (2014) 13219-13225.

[202] F. Sarvi, Z. Yue, K. Hourigan, M. C. Thompson, P. P. Y. Chan, Surface-functionalization of PDMS for potential micro-bioreactor and embryonic stem cell culture applications, *Journal of Materials Chemistry B* 1 (2013) 987-996.

[203] Z. Zhou, A. Seif, S. Pourhashem, J. Duan, A. Rashidi, M. Mirzaee, P. L. Silvestrelli, B. Hou, Anti-corrosion and anti-fouling properties of ball-like GQDs hybrided MOFs functionalized with silane in waterborne epoxy-polydimethylsiloxane coatings: Experimental and theoretical studies, *Applied Materials Today* 30 (2023) 101704.

[204] P.-Y. Yeh, N. A. A. Rossi, J. N. Kizhakkedathu, M. Chiao, A silicone-based microfluidic chip grafted with carboxyl functionalized hyperbranched polyglycerols for selective protein capture, *Microfluidics and Nanofluidics* 9 (2010) 199-209.

[205] H. Li, M. Zhao, W. Liu, W. Chu, Y. Guo, Polydimethylsiloxane microfluidic chemiluminescence immunodevice with the signal amplification strategy for sensitive detection of human immunoglobin G, *Talanta* 147 (2016) 430-436.

[206] A. Ulman, Formation and Structure of Self-Assembled Monolayers, *Chemical Reviews* 96 (1996) 1533-1554.

[207] C.-C. Wang, C.-Y. Chang, Enhanced output performance and stability of triboelectric nanogenerators by employing silane-based self-assembled monolayers, *Journal of Materials Chemistry C* 8 (2020) 4542-4548.

[208] Y.-H. Cheng, C.-J. Lee, C.-Y. Chang, Achieving High Power Density and Long-Term Stable Flexible Triboelectric Nanogenerators through Surface Functionalization of High Work-Function Electrode with Cationic Thiol-Based Self-Assembled Monolayer, *Advanced Materials Technologies* 6 (2021) 2000985.

[209] J. H. Ye, J. C. Tan, High-performance triboelectric nanogenerators incorporating chlorinated zeolitic imidazolate frameworks with topologically tunable dielectric and surface adhesion properties, *Nano Energy* 114 (2023) 11.

[210] M. Gutiérrez, Y. Zhang, J.-C. Tan, Confinement of Luminescent Guests in Metal–Organic Frameworks: Understanding Pathways from Synthesis and Multimodal Characterization to Potential Applications of LG@MOF Systems, *Chemical Reviews* 122 (2022) 10438-10483.